Sapienza University of Rome
Department of Mechanical and Aerospace Engineering
Ph.D in Aeronautical and Space Technology - XXIV cycle

Analysis of Heat Transfer Characteristics of Supercritical Fuels in Rocket Cooling Systems by a Space Marching Numerical Technique

by
Annafederica Urbano

Supervisor: Prof. Francesco Nasuti

March 2012

Acknowledgments

I would like to sincerely thank my supervisor, Prof. Francesco Nasuti, for the constant support he gave me during these years and for all his teachings, which have deeply enriched me.

My thanks to Prof. Bernardo Favini for his precious advices, which have been of great help during the final revision of my thesis.

Abstract

Methane and Liquefied Natural Gas (LNG) have been recently considered both for launch and for in-space applications because of several advantages they present if compared with other commonly used fuels. In particular, several studies are dedicated at the use of methane in liquid rocket engines with turbopumb fed systems. In this framework, the present study focuses on the use of methane or LNG as coolant in regenerative cooling systems. The study has two main purposes. The first is to understand what are the differences between using pure methane or LNG in a cooling system. The second purpose is to investigate on the heat transfer deterioration which is a thermodynamic phenomenon that could affect methane or LNG in cooling channels. The idea is to fulfill these objectives by numerical studies. The test cases that have to be analyzed are straight channels with circular cross section, a length of the order of the meter and a diameter of the order of the millimeter. The Reynolds number is of the order of $10^5 - 10^6$, which implies that the flow is turbulent. The coolant enters the channels with a supercritical pressure ($\sim$10 MPa) and a subcritical temperature ($\sim$ 110 K), which correspond to a very low compressibility. As a consequence, the inlet Mach number are very low ($\sim$ 0.01). High heat fluxes up to 10 MW/m^2 are enforced along the channel. The temperature variations along the channel cause a change in all the thermophysical properties that strongly influence the coolant behavior.

Thermophysical properties of real fluids and mixtures of real fluids are used to carry out the present investigations. An equation of state based on the Helmholtz free energy is used for the thermodynamic properties. Transport property models are based on the extended corresponding states approach used in combination with accurate models for the transport properties of each considered species. A numerical code is developed specifically to deal with the test cases of interest. It is based on parabolized Navier Stokes equations which can be solved with a space marching approach. The numerical model, used together with the selected thermophysical models, is validated against experimental data. Finally the developed code is used to obtain the desired results. First a comparison between LNG and pure methane behavior is carried out which permits to emphasize their different properties. In particular, the influence of the LNG composition on the coolant flow is analyzed. Subsequently, study of the deterioration of the heat transfer is addressed both with methane and LNG. Parametric studies permit to understand what are the main parameters involved in the phenomenon and how it can be handled.

Contents

Nomenclature

a reduced Helmholtz free energy

$\mathbf{A}$ Jacobian matrix $\dfrac{\partial \mathbf{G}}{\partial \mathbf{F}}$

$\tilde{\mathbf{A}}$ Roe's matrix

$\mathbf{A_v}$ Jacobian matrix for the system written in quasi linear form with respect to the primitive variable vector

$\mathcal{A}_x$ area of the cell-face surface perpendicular to the longitudinal direction [m^2]

$\mathbf{B}$ Jacobian matrix $\dfrac{\partial \mathbf{F_e}}{\partial \mathbf{V}}$

$\mathbf{C}$ Jacobian matrix $\dfrac{\partial \mathbf{G_e}}{\partial \mathbf{V}}$

c_p specific heat at constant pressure [J/kg/K]

d smaller distance from the closest wall [m]

D channel cross section diameter [m]

f friction coefficient

$\mathbf{F_e}$ vector of Eulerian fluxes in the streamwise direction

G specific mass flow rate: mass flow rate per unit area [kg/s/m^2]

$\mathbf{G_e}$, $\mathbf{H_e}$ vectors of Eulerian fluxes in the transverse directions

Gr Grashof number $\dfrac{g(\rho_b - \rho_w)D^3}{\rho_b \nu_b^2}$

$\mathbf{G_v}$, $\mathbf{H_v}$ vectors of viscous fluxes in the transverse directions

h enthalpy [J/kg]

I_{sp} specific impulse

k thermal conductivity [W/m/K]

L channel length [m]

M	Mach number
n	direction normal to the longitudinal lateral surface
p	pressure [Pa]
$\mathbf{P}$	pressure term vector for PNS
Pr	Prandtl number
R	gas constant [J/K/kg]
$\Re$	universal gas constant = 8.31434 J/K/mol
Re	Reynolds number $(\rho_b u_b D)/\mu_b$
$\mathbf{Q}$	source terms vector
q_w	heat flux [MW/m^2]
S	vorticity module [1/s]
$\tilde{S}$	corrected vorticity module [1/s]
$\mathcal{S}$	surface
$\mathcal{S}_{c,i}$	channel cross sections surface at x_i
$\mathcal{S}_l$	cell-face surface parallel to the longitudinal direction between the integration abscissas x_i and x_{i+1}
$\mathcal{S}_{w,i}$	channel wall surface spanning between the cross sections at x_i and x_{i+1}
$\mathcal{S}_x$	cell-face surface perpendicular to the longitudinal direction
T	temperature [K]
u	streamwise velocity component [m/s]
u^+	velocity wall coordinate
v, w	transverse velocity components [m/s]
$\mathbf{V}$	primitive variable vector
w_s	speed of sound [m/s]
x	streamwise direction and coordinate
$\mathbf{x}$	molar composition vector $\mathbf{x} = (x_1, x_2, \ldots, x_N)$
y, z	transverse directions and coordinates
y^+	distance wall coordinate

Acronyms

BL	boundary layer
EoS	equation of state
FNS	full Navier-Stokes equations
HC	hydrocarbons
LCH4	liquid methane
LH2	liquid hydrogen
LNG	liquefied natural gas
LO2	liquid oxygen
LRE	liquid rocket engine
PNS	parabolized Navier-Stokes equations
PPNS	partially Parabolized Navier-Stokes equations
RP-1	rocket propellant-1
TC	test case

Greek symbols

δ	reduced density $\tau = \rho/\rho_c$
μ	viscosity [Pa.s]
$\tilde{\mu}$	integration variable of the turbulence model equation [Pa.s]
$\tilde{\nu}$	corrected kinematic turbulent viscosity used in the turbulence model equation [m^2/s]
Ω	vorticity vector components
ω	Vigneron parameter
ω_a	acentric factor
ρ	density [kg/m^3]
τ	reduced temperature $\tau = T_c/T$
τ_w	wall shear stress [Pa]

Subscripts

$1, \ldots 5$	first, ... fifth component of flux vectors
6	turbulence model equation component of flux vectors (sixth component)

b	bulk
c	critical value
co	coking
i	cell index in the streamwise direction x
in	inlet
j	cell index in the transverse direction y
k	cell index in the transverse direction z
r	reduced variable
s	saturation value
t	turbulent viscosity, conductivity and Prandtl number
w	wall

Chapter 1

Introduction

The history of liquid rocket engines started slightly more than a century ago, in 1903, when Konstantin Tsiolkovsky published his work "The Exploration of Cosmic Space by Means of Reaction Devices" [70]. Even though solid rockets were known since the tenth century a.d., the new idea of using liquid propellants rockets was a fundamental step towards the beginning of space exploration. The first liquid rocket engine will be realized by Robert Goddard 28 years later, March 1926, and flew for 2.5 s. A new era begun, which led to the access to space in 1957, when Sputnik, the first artificial satellite, was put into an earth orbit by the two stage R7-launcher marking the start of the space age. Liquid rocket engines have been successfully used since then for launch and space propulsion, and in the last thirty years rocket propulsion has become a relatively mature field. Nowadays, research is devoted to a better understanding of subsystems with the aim to improve overall engine performance and to find out propellants that could be advantageous for specific goals. For instance, several studies have been recently carried out on the use of methane, or liquefied natural gas (LNG), as fuel in liquid rocket engines. Actually, these propellants have been taken into consideration to be used in the next launcher generation together with liquid oxygen as oxidizer. Consequently, it is mandatory to understand the behavior of each subsystem of an engine when using methane based fuels. Focusing on the use of such fuels in launch system engines, the present study addresses the regenerative cooling system which is expected to be part of any engine of this class. In the following a basic description of a generic liquid rocket engine is carried out. In particular, attention is devoted to the cooling system and to the propellants used in different types of engines. Then, attention is devoted to methane and LNG. The goal of the work being to understand the influence of the thermophysical properties of these fuels on the regenerative cooling system, two more topics are introduced. One topic is the definition and description of a transcritical fluid, as methane is likely to be in a regenerative cooling system. The other topic is the description of cooling channels and of the techniques generally adopted for their study. The chapter ends with the objectives of the work and with a detailed presentation of each chapter contents.

1.1 Liquid rocket engines

The basic principle of liquid rocket engines [1] rely in the combustion of liquid propellants at high pressure and on the subsequent acceleration and exhaust of the combustion gas. The gas is ejected at high velocity and as a consequence, by reaction, the engine is pushed in the opposite direction, providing the thrust required by the launcher or the spacecraft. Three main subsystems compose a liquid rocket engine that are the propellant tanks, the feed system and the thrust chamber. The tanks are needed to store the propellants: in case of bi-propellant systems there are at least one tank for the oxidizer and one for the fuel. The feed system ensures that the propellants taken from the tanks are delivered under high pressure to the combustion chamber. This can be realized either with gas pressure or turbopump feed systems. The thrust chamber is the assembly of injectors, combustion chamber and nozzle (see Fig. 1.1). The injectors ensure the correct atomization and mixing of the propellants so as to permit a efficient combustion. Finally, the nozzle, which has a convergent-divergent form, provides the expansion of the combustion gas to supersonic exhaust velocities. Both the combustion efficiency and the nozzle design contribute to the specific impulse I_{sp} value which is a determinant parameter for engine performance. An high specific impulse implies a minor propellant consumption for a given thrust and therefore the specific impulse represents a determinant performance parameter for an rocket engine.

Several other subsystems can be individuated in a liquid rocket engine. In particular the present study focuses on bi-propellant engines of large size with tubopump feed system. In regard to this, one fundamental subsystem for engines of large size is the cooling system. In fact, in these engines the combustion temperatures can exceed 3600 K and the heat transfer rate peak value can reach value of the order of 100 MW/m^2.[2] These huge values demonstrate how the cooling of the combustion chamber and of the nozzle is a mandatory task. Cooling is necessary to prevent the walls to warm excessively. In fact, high temperatures could cause a structural weakening, and thus a loss of elasticity or creep problems, and in the worst case a failure due to the material melting.

Steady-state and unsteady techniques can be used to cool a liquid rocket engine [145]. When a steady state technique is used, a thermal equilibrium is reached. Therefore, for the operating duration a constant heat transfer rate and a constant wall temperature are obtained. Differently, if an unsteady method is used, the thermal equilibrium is never reached. Rather, the temperatures increase for the whole operating duration. Therefore, the system must be designed in such a way that the structure temperature never exceeds the limit value during that time. Consequently, the maximum operating duration depends on the heat absorbing capacity of the hardware. From these techniques four basic cooling approaches can be identified (for engine of large size that are addressed):

- **Radiation cooling**. The thrust chamber heats up during the combustion until the structure gets red or white hot and heat radiates to space thus keeping the

[1] The aim of this section is to briefly introduce the liquid rocket engines putting the attention only on some basic concepts that are necessary in the follows. For a complete description see [145].

[2] For instance the heat flux per unit area reached in the throat region of the SSME is around 160 MW/m^2 [107].

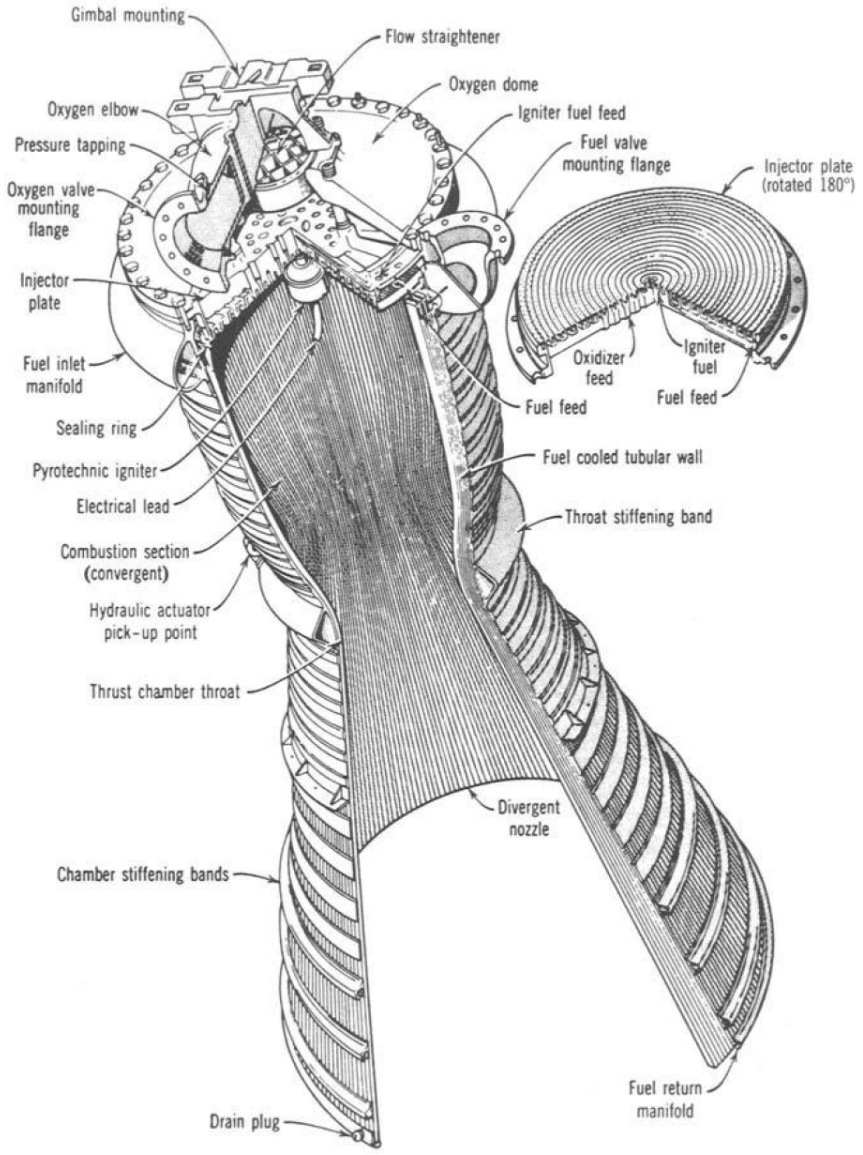

Figure 1.1: Regeneratively cooled tubular thrust chamber. Taken from [145].

structure at a reasonable temperature.

- **Ablative cooling**. An inner liner made of ablative material covers the wall chamber and essentially burns thus protecting the wall.

- **Regenerative and dump cooling**. One of the propellant flow through passages in the chamber wall. The cold propellant absorbs the heat coming from the hot gases thus keeping the wall temperature under the limit. In dump cooling this is done with a little amount of propellant which is then dumped overboard. In a regenerative cooling system the propellant remains in the system and contributes to the whole engine performance.

- **Film and transpiration cooling**. Film cooling is usually used in combination with regenerative cooling and consists in a thin layer of cold propellant injected near the chamber wall, parallel to the wall, so as to avoid the direct contact of the hot gases and the wall. Following the same basic idea, in transpiration cooling liquid or gaseous propellant is introduced in the chamber via a porous wall.

Radiation, regenerative and film cooling are steady state techniques while ablative cooling is an unsteady technique. Another common distinction is made between active cooling (regenerative, film) and passive cooling (radiation, ablative) [32].

Another fundamental aspect in a liquid rocket engine is the propellant. Focusing on bi-propellant systems, among the most widely used propellants, the combination of liquid hydrogen and liquid oxygen gives the highest specific impulse followed by hydrocarbons/oxygen and other storable propellants like for example the hypergolic propellant combinations of nitrogen-tetroxide (N_2O_4) and mixtures of hydrazine (N_2H_4) and unsymmetrical dymethylhydrazine (UDMH) or monomethylhydrazine (MMH).[3]

1.2 Methane and liquefied natural gas (LNG)

For the next launcher generation hydrocarbons/oxygen combinations have been considered to be used both for first and upper stages. In particular, among the hydrocarbons there is a large interest in using methane or the liquefied natural gas (from which methane can be extracted). The reasons of this interest are outlined in the following.

1.2.1 Methane as a rocket engine fuel

Methane owns several advantages compared to storable propellants, to hydrogen and to other hydrocarbons, as discussed in numerous works [18, 33, 64, 91, 125, 139].

Compared to storable propellants methane, used with oxygen, can provide an higher specific impulse. Moreover, the combination methane/oxygen is cleaner than common storable propellants which are toxic. Indeed, methane and more in general hydrocarbons are referred to as "green propellants". This is one of the aspects making methane well suited for reusable engines [23, 57].

On another hand, methane has three main advantages if compared with hydrogen. First, it has a higher density, which implies smaller tanks. Consequently, there is a positive impact on the structural weight and also a reduction of the low atmosphere drag (first stages). Second, methane is less cryogenic than hydrogen. In fact, methane is stored at a temperature of 111 K in the tanks, whereas hydrogen is stored at the very low temperature of 20 K. This also implies that for methane the production, operational and management costs are lower. Third, methane is a safer fluid than hydrogen because the risk of an explosion is lower. This also have an impact on the

[3] The interest in hypergolic propellant combinations is principally based on their chemical reactivity which makes unnecessary the ignition system. Moreover, they are storable at room temperature which is a great advantage. Conversely, they present several drawbacks: they have a comparatively small specific impulse, are toxic and due to their aggressiveness cause problems during storage and handling.

cost. For these reasons methane results and interesting alternative to hydrogen to be used with oxygen, even though at the cost of a lower specific impulse.

Most of the methane advantages listed above are own also by the other hydrocarbons. However, among the hydrocarbons methane could be preferred because of several aspects. First of all methane is the most energetic: for instance the specific impulse with methane is 10 s higher than with RP-1[4]. Besides the energetic aspect, one of the greater advantages of methane compared to other hydrocarbons is its higher coking temperature[5], due too its lower carbon content [21,34,97]. Methane coking temperature is $T_{co} = 970$ K, which is higher than the temperature typically reached in an expander cycle. This implies that methane can be considered as a possible coolant in the regenerative cooling system of an expander cycle [33]. Regarding a regenerative cooling system, among hydrocarbons methane has the best cooling efficiency. For instance, if compared to kerosene, the same heat flux can be taken away by twice smaller methane flow rate [22, 73]. Other important advantages of methane are its lower cost (three times lower than kerosene for example) and the higher ecological clearness of combustion products. To summarize, the comparison of some characteristics of methane, hydrogen and other hydrocarbons when used as fuels with liquid oxygen, are reported in Tab. 1.1. In particular, in the table are reported the specific impulse in vacuum (I_{sp}), the normal boiling temperature [6] T_s, the storage density and the coking temperature T_{co}.

Besides launchers, methane has also been considered as an interesting option for in-space applications [150]. In fact, methane is space-storable and less evaporable in space than hydrogen. Therefore, methane is suitable for a vehicle that travels in space for a prolonged period, such as an inter-orbit transporter or a planetary probe. Another attractive feature is that methane is abundant in the outer solar system. Methane can also be obtained for carbon dioxide and with only a small amount of hydrogen, for instance via the Sabatier process. Therefore considering, for example, a possible future mission to Mars, which has an atmosphere rich in CO_2, methane could be produced in-situ, which should allow a great reduction of the propellant to be carried from earth and hence a reduction of the mission cost [172].

1.2.2 Liquefied natural gas

In nature the major source of methane is the natural gas. Row natural gas is a mixture composed by more than 80% mole fraction of methane, and for the remaining part by heavier hydrocarbons (primarily ethane, propane), nitrogen, water, carbon dioxide and elemental sulfur. Actually the natural gas composition varies with extraction location. Anyway its liquefaction process requires removal of carbon dioxide, water, oxygen and sulfur compounds to prevent them from forming solids when the gas is cooled. As a result commercial LNG is typically made up of 90% or more of methane and of ethane, propane, butane and nitrogen in different percentages for the remaining part. Further processing LNG allows to increase methane molar fraction with the

[4]Rocket propulsion-1. It is a blend of different hydrocarbons (kerosene) that has been widely used in US for liquid rocket engines. Atomic ratio: $CH_{1.952}$

[5]Coking represents one of the main problem in the cooling process of LRE when using hydrocarbons in cooling channels: it is the carbon deposition after thermal cracking which causes an insulation of the wall and thus a sharp drop of the heat transfer rate.

[6]The normal boiling temperature T_s is the boiling temperature at a pressure of $p = 1$ bar.

Propellant	Formula	I_{sp} [s]	T_s [K]	ρ[kg/m^3]	T_{co} [K]
Hydrogen	H_2	455	20	70 (T=20 K)	-
Methane	CH_4	369	112	422 (T=112 K)	970
Propane	C_3H_8	360	231	584 (T=230 K)	700-730
RP-1	$CH_{1.952}$ (atomic ratio)	358	450-547	810 (T=293 K)	560

Table 1.1: Comparison between hydrogen and hydrocarbons propellants. Data taken from [22, 50, 88, 101].

obvious increase of propellant cost. In fact, the cost of the production and handling technology necessary to yell the desired liquid methane composition up to get pure methane, must be taken into account [37, 38]. The cheaper LNG has therefore been considered as a possible rocket engine fuel instead of pure methane [45, 51, 57, 111]. In fact, because of the large amount of methane contained, LNG should have the same advantages as methane. For this reason in the literature about the liquid rocket engine field, methane or LNG are often discussed together, or even confused, and LNG is frequently referred to as methane [31, 57, 73]. However using LNG rather than methane may affect the behavior of the different subsystems in such a way to yield changes of the overall rocket performance that have to be correctly predicted.

1.2.3 Methane and LNG liquid rocket engines

The different LRE subsystems can be differently affected by the selected propellants. As a consequence, focusing on methane and LNG, suitable studies have been carried out for the different subsystems. Particularly most of the works are devoted to the combustion chamber (combustion [141], injection [92]) and the cooling system (regenerative cooling system, film cooling). Different system analysis can be found [33, 139]. To date, none methane/oxygen engine has ever flown, yet several demonstrators have been built (for example 3M9, 5M12 and 5M15 XCOR first stages, or the JAXA full size prototype engine: LE-8).

Among the different subsystems the present work focuses on LRE regenerative cooling system, and in particular attention will be devoted to two main aspects. The first is to understand what are the differences between pure methane and LNG if they are used as coolants in a regenerative cooling system. The second is to investigate on the heat transfer deterioration phenomenon. In fact this phenomenon is likely to occur in the thermodynamic conditions at which methane and LNG should operate in cooling channels. An introduction of the deterioration phenomenon is given in the following section so as to demonstrate the need of its study.

1.3 Thermodynamic conditions of methane based fuels in the cooling system: the heat transfer deterioration in supercritical coolants

The thermodynamic conditions that methane and LNG can encounter in a regenerative cooling system of turbopump fed engines deserve a careful consideration. In fact, because of the coolant pressure and temperature and of the large amount of heat flux, the phenomenon of heat transfer deterioration may occur. Typical operating conditions and the phenomenon of heat transfer deterioration are thus shortly described below.

1.3.1 Transcritical fluid

Critical parameters[7] of propellants strongly influence both their storage and their evolution in the cooling system. For example the critical temperature and pressure of several LRE propellants are reported in Tab. 1.2.

Propellant	Formula	T_c [K]	p_c[MPa]
Ammonia	NH_3	405	11.3
Fluorine	F_2	144	5.2
Hydrazine	N_2H_4	654	14.7
Hydrogen	H_2	33	1.29
RP-1	$CH_{1.952}$ (atomic ratio)	622	2.2
Nitrogen tetroxide	H_2O_4	432	10.1
Oxygen	O_2	155	5.04
UDMH	$(CH_3)_2NNH_2$	524	8.9
Methane	CH_4	190.6	4.6

Table 1.2: Liquid propellants critical parameters from [32] (round off values).

Earth storable fuels like UDMH and RP-1 have high critical temperatures and hence can be stored in a liquid phase at ambient conditions, whereas cryogenic fuels like hydrogen or methane, have lower critical temperatures. Therefore to enable their storage in a liquid phase their temperature must be decreased under their saturation temperature at the tank pressure, which for a turbopump fed engine is slightly greater than the atmospheric pressure. Before entering the cooling channel the propellant passes in the turbopump thus its pressure increases: at the channel inlet the propellant pressure is either subcritical or supercritical depending both on the propellant critical pressure and on the application. In any case the coolant temperature at the channel inlet is generally subcritical[8]. If the coolant has a subcritical pressure, increasing its temperature in the cooling channels can bring to a phase change. This

[7] see appendix A for the definition of critical point

[8] Except for hydrogen as it will be pointed out in the following

can be observed in Fig 1.2, in which a generic (p, T) phase diagram is reported: if a liquid is heated up and its temperature exceeds the saturation temperature T_s, then it undergoes a phase change from liquid to vapor. Conversely, if the coolant has a supercritical pressure, it cannot undergo phase changes. Nevertheless, at subcritical temperatures it is much similar to a liquid (high density low compressible fluid), whereas at supercritical temperatures it is much similar to a gas (low density high compressible fluid). More precisely for supercritical pressures a *pseudocritical* temperature T_{ps} is defined for which fluid properties undergo large changes [48, 61, 120]. As an example in Fig. 1.3(a) isobaric curves of the constant pressure specific heat c_p for methane are reported versus temperature, for different supercritical pressures. For each pressure the temperature at which the c_p exhibits a peak is called pseudocritical temperature T_{ps}. The pseuodcritical temperature is an increasing function of pressure as shown in Fig. 1.3(a) and for pressure converging towards the critical pressure, T_{ps} converges towards the critical temperature. Also isobaric curves for density, viscosity and conductivity are reported in Fig. 1.3. It can observed how passing from $T < T_{ps}$ to $T > T_{ps}$ the density drops, whereas viscosity and conductivity reach a minimum and then start to increase. This behavior has some similarity with a phase passage except that all the variations occur gradually in a temperature range around the pseudocritical temperature rather than at the constant saturation temperature of subcritical fluids. From these similarities comes the use to say that a supercritical fluid with a $T < T_{ps}$ is a *liquid-like* fluid that undergoes a *pseudo phase change* when its temperature exceeds the pseudocritical value thus becoming a *gas-like* fluid [138]. With analogy with subcritical fluids the term *pseudoboiling* is sometimes used referring to the pseudo phase change [76]. Fig. 1.3 also shows that increasing the pressure the pseudo phase change occurs with milder variations. In the following, a propellant with a supercritical pressure and a temperature crossing the pseuodcritical value will be referred to as a "transcritical fluid" flow[9].

Having put in evidence the difference in the cooling system between supercritical or subcritical pressure propellants, Tab. 1.2 is considered again. Liquid hydrogen has a low critical temperature ($T_c = 33$ K) and a low critical pressure ($p_c = 1.3$ MPa). Consequently, dealing with engine in the medium-high thrust range, in the cooling channels its pressure is usually far enough from the critical pressure to undergo only mild variation during the pseudo phase change. Moreover, because of its very low critical temperature, the losses in the turbopump are in general sufficient to make the hydrogen reach a temperature greater than the pseudocritical temperature at the cooling channel entrance or in a very short distance. A different situation occurs if methane is used as a coolant because methane has a critical pressure of $p_c = 4.6$ MPa and a critical temperature of $T_c = 190.6$ K. This means that, if compared to hydrogen at a same pressure level, methane will be much closer to its critical pressure as schematically reported in Fig. 1.2 [125]. Therefore, because the pseudo phase change occurs at lower pressure, all the property variations are much stronger for methane and LNG than for hydrogen. It can be concluded that pseudo phase change in cooling channels is an important aspect if methane is considered and hence it must be taken into account in the analysis because it may strongly influence

[9]The term "transcritical" is used in analogy with the definition introduced in the field of combustion which identifies a "transcritical fluid" as a fluid which is injected in the combustion chamber at supercritical pressure and subcritical temperature [141]

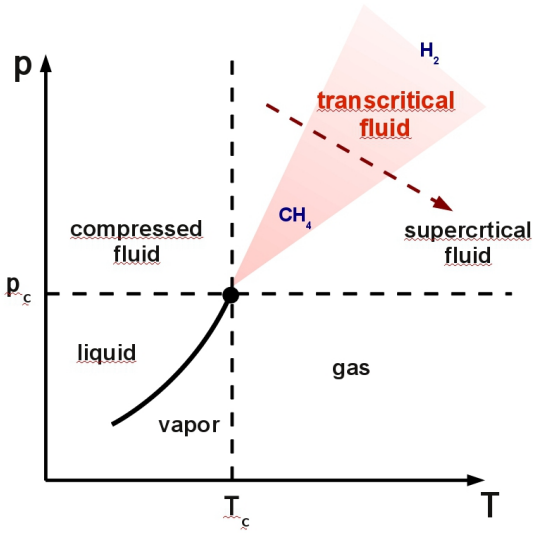

Figure 1.2: Schematic of a pressure temperature phase diagram

the coolant heat transfer capability.

1.3.2 Heat transfer deterioration

Dealing with forced convection heat transfer to supercritical pressure fluids in channels, two characteristics modes of heat transfer can occur [119, 131, 154]:

- **Normal heat transfer**: the values of the temperature field always increase in a monotone trend as heat is enforced along the channel.
- **Deteriorated heat transfer**: a thermal spike is present at a certain location along the channel. More precisely the wall temperature exhibits a peak and in the same axial location the heat transfer coefficient h_c has a minimum value[10].

Deteriorated heat transfer can occur both at low mass flow rates, where buoyancy forces are still important despite the forced convection mode, and high mass flow rates for which buoyancy forces are not relevant [76]. In cooling channel applications buoyancy forces are not relevant and hence in the following attention is devoted only to the heat transfer deterioration occurring without buoyancy forces.[11]

Several experimental works have been carried out trying to understand and explain the phenomenon of heat transfer deterioration. In particular, most of the works available in literature use water as fluid because they are related with supercritical pressure water cooled reactor (SCPR) [27, 119]. However, the deterioration has been experimentally studied also for other fluids among which, for example, carbon dioxide [25, 140], toluene (C_7H_8) [131], hydrocarbons [68] and the refrigerant

[10] The convective heat transfer coefficient is a characteristic of the cooling capabilities of a flow and is defined as: $h_c = q_w/(T_w - T_b)$. Its definition will be discussed in the following of the chapter.

[11] Buoyancy effects have to be taken into account if $Gr/Re^2 > 10^{-3}$ for horizontal tubes and $Gr/Re^{2.7} > 10^{-5}$ for vertical tubes [83, 142], with $Gr/Re = (g(\rho_b - \rho_w)D^2)/(\mu_b u_b)$. For the test cases of interest, even at sea level (g=9.81 m/s^2) $Gr \sim 10^6$ and hence being $Re \sim 10^6$ these limits are far to be reached, hence buoyancy effect can be neglected.

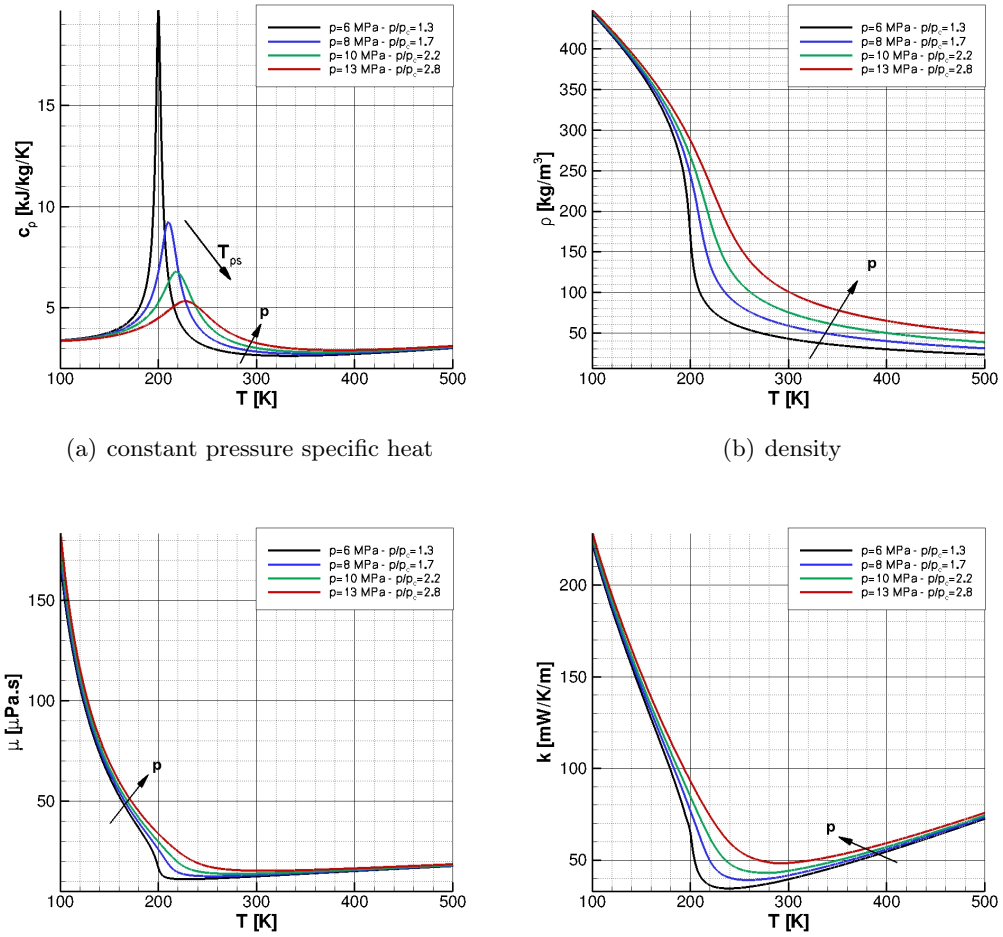

(a) constant pressure specific heat

(b) density

(c) viscosity

(d) conductivity

Figure 1.3: Properties variations of methane passing from $T < T_{ps}$ to $T > T_{ps}$

HCFC22 [154]. All these experimental works show that the deterioration occurs when the bulk and wall temperature are respectively lower and higher than the pseudocritical value. Moreover, for a given mass flow rate, the heat flux must be higher than a threshold value which depends on the pressure level. In these works the heat transfer deterioration is associated with the pseudoboiling occurring near the wall, where the temperature crosses the pseudocritical value. As a consequence, a thin layer of low density fluid is created near the wall thus bringing to a drop in the heat transfer capabilities, which is analogous of the film boiling phenomena occurring at subcritical pressures. Moreover, the low density layer accelerates while the cold core of the fluid is still slow.[12]

[12]This brings to the formation of M-shaped velocity profiles which are characterized by a flat gradient near the wall. Consequently the turbulent diffusion is locally deteriorated and this also has a negative influence over the heat transfer capabilities.

From the modeling point of view, it has to be underlined that the classical semi empirical correlations for the normal heat transfer do not work in the deteriorated mode. Therefore several works have been carried out with the purpose of modify existing correlations, or find out new correlations, for the deteriorated heat transfer [120, 156].

Numerical works focusing on the heat transfer deterioration phenomenon have also been carried out. Generally RANS approaches, with different closure models, are used to simulate heated supercritical pressure flows in two dimensional axisymmetric configurations. Most of these works deals with water [26, 27, 76, 102, 113] or carbon dioxide [53,102]. Actually, these works focus on the ability to describe the phenomena with the proposed numerical models and to reproduce experimental data.

Focusing on liquid rocket engines, heat transfer deterioration has been observed in several experimental investigations on rocket propellants flowing in cooling channels. In particular, the deterioration has been outlined with hydrogen [55], methane, propane and LNG [45,88]. However, these studies were not carried out to investigate the deterioration phenomenon, rather their purpose was to investigate the cooling capabilities and coking characteristics of the coolant fluid (coking for hydrocarbons). Nevertheless, these experimental works demonstrate the risk of a deteriorated heat transfer in regenerative cooling channel configurations. In spite of the above experimental evidences, only a few numerical works on the deterioration in LRE cooling channels can be found in literature, dealing with either methane [123, 163], n-heptane [61] or hydrogen [60]. These works underline the possible occurrence of heat transfer deterioration in a regenerative cooling system. In these works parametric studies are carried out varying the heat flux and the thermodynamic conditions at the channel entrance with the aim of better understanding the phenomenon peculiarities and find suitable heat transfer correlations.

From the above considerations it comes out that the heat transfer deterioration is an important phenomenon that has to be investigated if methane or LNG are to be used in cooling channels. Actually a work which clearly investigate on all the parameters of interest and give information on the phenomenon onset cannot be found in the literature, and therefore there is a large interest in carrying out such study. In particular one of the main aspects that have to be taken into account if the deterioration heat transfer is to be studied numerically is the correct description of the thermophysical properties: accurate equations of state and transport property models have to be used.

1.4 Regenerative cooling channels

Among the different cooling systems the regenerative one is the most efficient in applications with high chamber pressures and high heat transfer rates and is usually adopted for the engines in the medium to high thrust range. Other advantages of the regenerative cooling system, if compared with other cooling systems, include no changing in wall contour, an indefinite firing duration (except for coking problems) and a relatively light weight construction. Nevertheless, also some disadvantages must be considered among which a limited throttling with most coolants, the pressure

losses[13] in the channels and limits due to the maximum allowable coolant temperature. In the present work cooling channels of regenerative cooling systems are taken into consideration. Therefore, in the following a general description is given so as to introduce the problem of heat transfer in cooling channels. Then the methodologies typically applied to study cooling channels are presented.

1.4.1 General description

In a regeneratively cooled engine one of the propellants passes in cooling channels surrounding the thrust chamber and the nozzle before entering either the main combustion chamber, a preburner or a turbine depending on the cycle. The internal energy of the coolant rises along the channels prior to reach the injection plate and thus the heat absorbed by the coolant is not wasted: from this feature comes the name *regenerative* because of similarity to steam regenerators. A steady state condition is reached for which the temperatures of the structures are kept under the limit value. Actually, this thermal equilibrium results from a coupled problem between the forced convective heat transfer from the hot gas flow to the combustion chamber internal wall, the conductive heat transfer through the solid wall and the forced convection heat transfer from the cooling channel wall to the coolant flow.[14] The thermal problem is schematically represented in Fig. 1.4. The aim of a regenerative cooling system is to keep the resulting chamber wall temperature at steady state under the limit value, with a minimum pressure loss. This is why in the system design phase the main parameters that have to be controlled in the cooling system are the pressure losses, that influence the turbopump design and hence the whole system, and the heat transfer capabilities, or rather the ability to keep a low wall temperature with high heat fluxes[15]. These requirements influence both the selection of the coolant and the channels configuration as discussed in the following.

Channels configuration

Historically, the first chambers were made of tubular walls with circular or elliptic section passages for the coolant. Then with the increasing operating pressures and heat transfer rates and also the development of fabrication techniques, more robust configurations have been developed. In more recent configurations the channels, with a rectangular cross section, are aligned with the chamber axis and in fact constitute the wall chamber or rather a *cooling jacket*: they can be either brazed together or milled in the liner (see Fig. 1.5). The cooling jacket material should have a high conductivity to facilitate the heat transfer but it should also be sufficiently elastic

[13] A suitable pressure level must be provided at the channel inlet considering the high pressure losses in the channels and the requirement at the channel exit. Moreover, the pressure level is linked to the propellant feed system and high pressure levels are associated with turbopump fed systems. This is why regenerative cooling systems are applied with turbopums fed systems.

[14] If a rigorous balance is done the radiative heat transfer to the ambient must also be taken into account. However in a regenerative cooling system the outer wall of the engine is cold and hence the radiative heat flux to the space should be very small. Consequently radiative heat flux can be neglected if compared with the other heat fluxes involved in the thermal balance.

[15] The pressure losses are caused both by the shear stress and the heat load: in this sense a minimum pressure loss requirement results in a maximum heat load that can be absorbed by the coolant. Generally a maximum heat load that the coolant can absorb is identified as a constraint in the design phase [56, 88, 101].

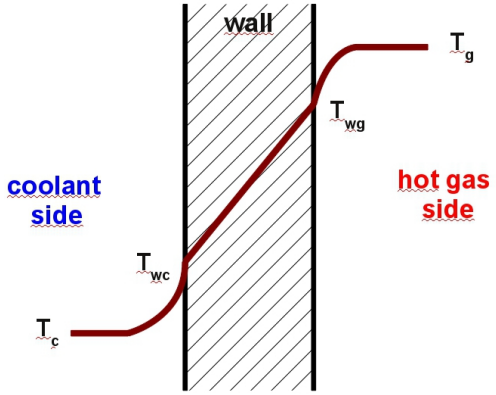

Figure 1.4: coupled thermal problem in a regenerative cooling system

and able to withstand high pressures and high temperature gradients. For these reasons copper alloy is usually selected for the liner. In the case of milled channels on the slotted liner, a shell, usually in nickel, is applied to bear hydraulic, thermal and mechanical loads (see Fig. 1.8).

(a) formed tubes brazed or soldered together

(b) milled channels

Figure 1.5: Brazed and milled channels configurations. Taken from [145].

In some applications, the channel cross section can be rectangular and in some cases it also features a high aspect ratio (the ratio between the height and the width), because of several advantages it provides if compared to circular section. The material between two channels gives a fin effect which increases with the aspect ratio, the pressure drops are smaller and vortex are generated with a benefit on the heat transfer [67, 167]. The fin effect increases with aspect ratio but also the pressure drop hence an optimal configuration has to be selected depending on the particular application [116, 165, 166, 168, 169]. In Fig. 1.8 a photography of a cut through a combustion chamber wall is reported and shows the cooling channels milled in the wall.

The number of channels and their crosswise dimension depend both on the system requirements (mass flow rate, maximum allowable pressure drop, heat loads) and on the technological constraints (the channel diameter cannot be too small). The channels are curved because of the convergent-divergent thrust chamber geometry and in some configuration U-turn are implemented [74][16]. Moreover, the heat flux is

[16]The curvature increases the pressure drop but brings also to the formation of vortex which

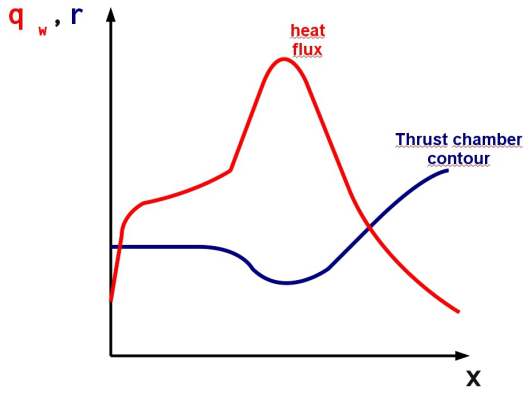

Figure 1.6: Typical axial heat transfer rate distribution for liquid propellant thrust chamber.

not constant along the chamber axis but reaches a maximum at the throat region, as schematically shown in Fig. 1.6. Therefore, the channel crosswise area usually changes along the axis with a smaller value in the throat region. In fact, decreasing the area increases the velocity and hence the cooling capabilities. However, increasing the velocity also brings an increase of the pressure drop which must be controlled because it is directly connected with the final chamber pressure, especially for closed cycle. Another aspect taken into account in the design of the variable cross area of the channels is that it has to permit the same number of tubes at the throat and exit diameters as schematically shown in the Fig. 1.7. Even though the design is strongly related with the particular engine, it can be said that cooling channels feature hydraulic diameter of the order of the millimeter and length of the order of the meter (related with the thrust chamber size).

At last, but not least, pressure losses in the channels are strongly influenced by the wall roughness: attention must be devoted to the manufacturing so as to obtain a suitable roughness level and at a design level suitable models must be considered to take roughness into account.

Coolant fluid

Between the two propellants the fuel is usually preferred as a coolant because of its high heat capacity. Another problem associated with oxidizers is that at high temperatures they tend to become corrosive. However, also for hydrocarbons fuels care must be devoted to the corrosion of channel surfaces that deteriorate fuel cooling capabilities. The corrosion problem is due to the presence of oxygen and sulfur molecules that can respectively oxidize and sulphurize copper. Therefore the content of these species in the hydrocarbon fuels must be limited under certain values [88]. A further problem associated with hydrocarbons is the carbon deposition because of thermal cracking called *coking*: the phenomenon occurs if the temperature exceeds a threshold value, the coking temperature, which increases with the hydrogen to carbon atomic ratio (see Tab. 1.1) [134–136]. Also coking can cause the channel

enhance the heat transfer [100, 116, 168].

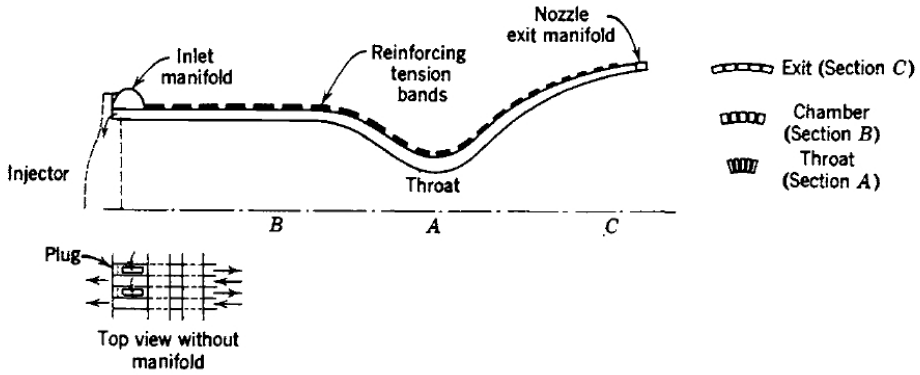

Figure 1.7: Diagram of a tubular cooling jacket. Taken from [145]

wall corrosion. Actually the main problem with coking is the resulting insulation of the wall which brings to a drastic drop of the fuel cooling capabilities. Generally, a maximum heat load that the coolant can absorb is identified as a constraint in the design phase [56, 88, 101]. Dealing with chemical characterization, coking due to hydrocarbons thermal cracking limits both the temperature reachable in the channels and the operational duration. Coking is one of the main reason that prevent the use kerosene and heavy hydrocarbons in expander cycles.

The coolant thermophysical properties can also strongly affect the heat transfer capabilities as shown in section 1.3.2. In particular if the coolant is subcritical attention must be given to the possible phase passage that could occur if the temperature exceeds the saturation temperature. If the phase passage is controlled and bounded near the wall it can enhance the heat transfer: small vapor bubbles form at the wall surface, cause local turbulence, break away from the wall and collapse in the cooler liquid. This phenomenon is known as *nucleate boiling*, but if the temperature is further increased nucleate boiling can degenerate in *film boiling*: a vapor film is created near the wall forming an insulation barrier [145]. Nucleate and film boiling cannot occur if the coolant is supercritical. Nevertheless, even at supercritical pressures passing from subcritical to supercritical temperatures the gradients of fluid properties could affect the heat transfer characteristics and bring to the deterioration, as shown in section 1.3.2.

1.4.2 Analysis of cooling channels

Regenerative cooling channels have been investigated in a large number of works, both experimentally and numerically. A large number of experimental works have been carried out since the sixties on straight channels with circular cross section electrically heated with the purpose of investigating both the heat transfer capabilities of the propellants and the pressure losses. Often experimental data are analyzed and correlated to find suitable coefficients for semi-empirical correlations to be used in the design phase [31, 54, 55, 125, 149]. Circular cross section test cases are also used in experimental studies dealing with hydrocarbons coking. The aim of these studies is to find the threshold wall temperature for which the thermal cracking occurs and to find corrections in standard heat transfer correlations to account for the diminishing

Figure 1.8: Cut through a combustion chamber wall with CuAgZr liner and galvanic deposited Ni outer shell. Taken from [50].

of cooling capabilities [56, 88, 125]. Moreover, when focusing on corrosion, these studies also investigate on the propellant and material compatibility and eventually give information over the maximum allowable percentage of hydrogen, sulfur and oxygen to prevent corrosion [134–136]. On the other hand, geometrical effects have been considered in a number of works focusing on the channel curvature and on the rectangular cross section and generally correction factors for empirical correlation are provided [100, 165, 166].

Experimental investigations permitted to acquire experience in the problems characterizing cooling channels. Moreover, the obtained semi-empirical correlations are largely used in the cooling channels analysis. In fact, to carry out a correct cooling system analysis a coupled problem must be considered between the coolant flow, the heat transfer in the wall and the hot gas flows in the chamber. Consequently several iterations are needed until the suitable configuration is found. This is why one dimensional numerical approaches are often used to describe the coolant flow evolution in channels and these approaches need the use of semi-empirical correlations to relate the one dimensional variables, which represent the bulk flow behavior, and wall variables.

More precisely bulk and wall temperatures (T_b and T_w) are correlated to the heat flux q_w by the heat transfer coefficient defined by Newton law:

$$q_w = h_c(T_w - T_b) \tag{1.1}$$

Nusselt number Nu and h_c are related by:

$$Nu = \frac{h_c D}{k_b} \tag{1.2}$$

which can be correlated to the Prandtl (Pr) and Reynolds (Re) numbers by correlations which are modifications of the Dittus-Bolter equation [115]:

$$Nu = KRe^a Pr^b \left(\frac{T_b}{T_w}\right)^c \left(\frac{\mu_b}{\mu_w}\right)^d \left(\frac{k_b}{k_w}\right)^e \left(\frac{c_{p,b}}{\overline{c}_p}\right)^f \left(\frac{p_c}{p_b}\right)^g \left(1 + 2\frac{L}{D}\right)^m \tag{1.3}$$

where $\overline{c}_p = (h_w - h_b)/(T_w - T_b)$. The coefficients K, a, b, d, e, f, g and m are related to one particular fluid and are determined from a least squares fit of the experimental data. Several correlations of the type of Eq (1.3) and similar can be found in literature and a summary of the most used for straight cooling channels with a circular cross section can be found in [50, 88–90, 155]. To account for three dimensional effects on heat transfer, efficiencies are introduced which multiply the right hand side of Eq. (1.3) [100, 109, 139]. In particular curvature terms depend on the geometry parameters and fin effect terms depend on the aspect ratio.

To correlate the shear stress to the pressure losses in the momentum equation the cooling passage is considered as a hydraulic pipe and hence the friction loss can be calculated according to the following expression valid for a straight channel:

$$\frac{\Delta p}{\rho_b} = \frac{1}{2} f u_b^2 (\frac{L}{D}) \tag{1.4}$$

where Δp is the pressure drop. Semi-empirical correlations permit to relate the friction loss coefficient f to the Reynolds number. To account for further local losses that occur when the flow direction is changed (like in bends) or the cross section changes, further pressure losses are added [139].

These approaches permit to study the whole system in a coupled manner with a low computational cost. Nevertheless semi-empirical correlations are known to carry a high level of uncertainty, around 20%, in particular if the conditions are not in the range of the experimental data from which correlations are derived. Moreover these uncertainties become very high in the transcritical thermodynamic region where the high property variations make the use of semi-empirical relations unacceptable [60]. To obtain more general results (out of the thermodynamic range of the correlations) and when some three dimensional aspect, physical or geometrical, have to be studied, three dimensional CFD tools are used. Reynolds Averaged Navier Stokes equations (RANS) are considered to simulate the turbulent flow in cooling channels either with pressure-based or density-based approaches with attention to account that propellant flowing in cooling channel is a high compressible low Mach number flow. Therefore density-based codes are usually preconditioned [67, 110], whereas compressibility corrections are included in the pressure-based approaches [60]. DNS or LES methodologies have not been applied to investigate on cooling channels, the Reynolds numbers being too high. Even with RANS approaches the high computational cost does not permit to carry out parametric studies on a whole engine in a coupled manner. Hence fully coupled approach between hot gas side, chamber wall heat transfer and coolant side simulated with a three dimensional CFD code are limited to small regions [99]. Another approach is to consider only the conjugated coolant flow and heat conduction simulations without the coupling with the hot gas side [110]. Three dimensional CFD computations are rather used to investigate on some particular aspect like for example the effect of the curvature [116, 121], the aspect ratio effect on the heat transfer

capabilities [67,168]. These geometrical aspects are inherently three dimensional and moreover induce secondary flows which must be described by the numerical methods to account for their influence. Other investigated aspects are the wall channel roughness, the thermal stratification due to near-critical property behavior and asymmetry heating with high heat flux, and in general the effect of the variation of the fluid thermodynamic properties on the heat transfer [60, 116]. In particular, when the study focuses on some peculiar physical aspects, like the effect of thermodynamic property variations, simpler configurations of the channels are often selected. Often no coupling is considered and a the heat load is given to the coolant flow as a boundary condition. In particular when the study focuses on the chemical characterization of the fluid rather than on geometrical aspects, straight channels with a circular cross section can be suitable test cases [60, 123, 163].

To summarize, if regenerative cooling channels have to be numerically studied two possibilities are available: one dimensional semi-empirical approaches with semi-empirical correlations modified to account for three dimensional effects and others peculiar aspects (channel roughness, coking, etc...) or three dimensional CFD codes, based on a RANS approach to account for turbulence. Attempts have also been made to adopt space marching techniques [11]: it can be demonstrated that with suitable approximations the problem can be described with a system of equations, called Parabolized Navier Stokes equations (PNS), well posed for a space marching solving technique. Applying this technique, investigations on curved cooling channels with high aspect ratio have been carried out [81], together with a comparison against experimental data, thus demonstrating the validity of the PNS approach to study cooling channels flows.

1.5 Objectives

The main objective of the present work is to study the behavior of methane and LNG in cooling channels. In particular two aspects have to be investigated. Firstly, LNG being a mixture of hydrocarbons and nitrogen, it is interesting to understand the influence of each species over its cooling capabilities and the entity of the foreseeable loss of cooling capabilities if compared to pure methane with respect to the economical gain (LNG is cheaper than methane). Second, the heat transfer deterioration phenomenon, which is likely to occur at the thermodynamic conditions that should characterize methane and LNG used as coolants, is investigated. In fact it is important to understand if deterioration is a real risk in cooling channels applications, and to understand what are its consequences and its onset conditions so as to be able to handle it. All the aspects that have to be considered to fulfill these objectives are exposed in the following. Then the contents of each chapter are presented.

1.5.1 Features of the work

The idea is to numerically study the above LNG and methane propellant aspects. To this aim one of the main challenges is to find suitable thermophysical models able to accurately describe a mixture of supercritical real fluids, with a particular attention devoted to the pseudocritical region.

The thermophysical models have to be implemented in a computational fluid dy-

namic code suitable to do parametric studies either with respect to thermodynamic conditions and mixture composition or with respect to boundary conditions. 1D approaches are clearly insufficient to analyze thermodynamic phenomena which cannot be described by averages but rather induce local effects in a channel cross section, hence a CFD approach must be used. Among the possibilities the use of a space marching approach, which should be suitable to describe these channel flows, present several advantages compared to more common time marching CFD approaches: principally a saving of computational time and a facility in carrying out parametric studies. The numerical problem is further complicated because of the very low Mach number (of the order of 0.01) that characterizes cooling channels flows hence the numerical tool has to be able to describe low Mach number compressible flows.

The regenerative system is characterized by several geometrical and physical aspects which affect the flow in the cooling channels and make its analysis complicated if all the aspects are to be taken into account. However, the present study focuses exclusively on the thermophysical property influence both with respect to the LNG composition and with respect to the strong property variations in the pseudocritical region. To deeply study these physical aspects and understand their influence on the coolant heat transfer capabilities it should be better to investigate simple configurations which permit to understand the influence of each parameter over the coolant flow. For this reason the present study relies only on straight channels, with smooth walls, with circular cross section, without any coupling with the hot gas side.

The results have to be analyzed mainly considering the main performance parameters of a cooling system, that are the pressure drop[17] in the cooling channels and the temperature fields. The pressure drop is related both to the wall shear stress and to the heat flux, which also make the temperature increases. The wall temperature, which is a critical quantity that has to satisfy cooling system constraints, depends both on the bulk temperature and on the heat transfer capabilities. The limit to the highest acceptable T_w is set by either structural requirements or coolant thermal cracking temperature, which depend on the wall channel material and on the selected propellant properties, respectively. The relation between bulk temperature, wall temperature and the heat transfer capabilities, is described by the convective heat transfer coefficient h_c, as defined in Eq. (1.1). The heat transfer coefficient is useful to compare the heat transfer efficiency of the coolant in different situations. In fact, for an assigned temperature difference $(T_w - T_b)$ the greater h_c the higher the heat flux that can be absorbed by the coolant flow, or for an assigned heat flux and bulk temperature, the higher h_c the lower the corresponding T_w.

1.5.2 Outline

The thesis is organized in two main parts: in the the first part physical and mathematical models are presented whereas the second part addresses the investigations carried out implementing the above models.

[17] In fact, reducing the pressure drop in the cooling channels is mandatory because if target chamber pressure is assigned, the losses in the cooling channels influence the turbopump design and hence the whole system.

First part: mathematical and physical models

In Chapter 2 an overview of the possible suitable EoS and equations for transport properties to describe mixtures of real fluids is presented. The most accurate models for the thermodynamic conditions of interest are selected. To demonstrate the adequacy of the selected models, comparisons are carried out with the National Institute of Standards and Technology data.

The possible numerical approaches available to investigate flows of supercritical fluids in cooling channels are considered in Chapter 3. In particular, the problem of a low Mach number compressible flow is taken into consideration. A parabolized form of the Navier stokes equations (PNS) is chosen to describe the flow in cooling channels, at very low Mach number, and a mathematical justification of the suitability of the selected equations to describe the test cases of interest is reported. Then a detailed demonstration of the hyperbolic nature of the system of equations is carried out. In fact, the main interest in using the PNS to mathematically describe the problem is that a space marching approach can be used to numerically solve them, because of their demonstrated hyperbolic nature. The chapter ends with the development of an approximate Riemann solver. In particular, it is an extension of the Roe's Riemann solver for the PNS with a generic equation of state.

In Chapter 4 a complete description of the mathematical and numerical model is reported. The flow is turbulent, indeed a Parabolized form of the Reynolds Averaged Navier-Stokes approach is actually considered with an eddy viscosity model to close the problem. In particular, the one equation model of Spalart-Allmars is adapted to fit the PNS hypothesis. The numerical model is based on a finite volume approach with a Godunov-type scheme which includes the developed approximate Riemann solver to obtain the Eulerian fluxes.

Before using the numerical code to fulfill the objectives, it has do be validated. Indeed, in Chapter 5 several numerical studies permit to acquire confidence in the code. In particular, a grid convergence analysis on a significant test case demonstrate the second order of accuracy of the code. Moreover, these studies demonstrate that the code is suitable to describe very low Mach number flows. A validation is then carried out. First a comparison with a full Navier-Stokes (FNS) solver is carried out so as to demonstrate that the terms neglected in the PNS equations are of minor importance in the test cases of interest. Then experimental data are reproduced with low discrepancies. Furthermore the experimental test case is characterized by the heat transfer deterioration phenomenon which is very well reproduced numerically.

Second part: results

Parametric investigation are carried out with the numerical code together with the selected thermophysical models. In Chapter 6 a study on the LNG composition influence over the coolant capabilities is carried out showing the influence of each species. Then in Chapter 7 the heat transfer deterioration phenomenon is studied. Parametric studies are done considering as parameters the inlet pressure, inlet temperature and the ratio between the heat transfer and the mass flow rate. In particular, a threshold value of heat flux to specific mass flow rate ratio is found and its dependence over the pressure is put in evidence. A comparison between LNG and pure methane is also carried out for a deteriorated heat transfer test case.

Part I

Physical and mathematical model

Chapter 2

Thermodynamic and transport properties

A suitable thermophysical characterization of the propellant flowing in the cooling channels is mandatory for the purpose of the present study. In fact the aim is to understand how the variation of the propellant thermophysical properties affect the performance parameters in cooling channels (that is the cooling capability and pressure losses). In particular we are interested in supercritical fluids with a temperature varying from low subcritical values (liquid-like region) to high supercritical values (gas-like region) and thus passing in the transcritical region where all the properties strongly vary both with temperature and pressure. The requirement is to find a model that can accurately describe these strong variations. Moreover with the aim of investigating the influence of LNG composition on the cooling capabilities and eventually compare LNG with pure methane, the thermophysical models must permit a coherent variation of the properties passing from a LNG mixture to pure methane. This implies that we need a mixture model able to reduce to very accurate models for each single species. Available models for the characterization of real fluids are first presented. Then an accurate description of the selected equation of state and transport property models is reported together with a comparison with National Institute of Standard Technologies (NIST) data [1] as a validation. In Appendix A are given several basic definitions that are useful for a complete understanding of the present chapter. Finally a discussion of other models available in the literature which have been discarded in the present study is carried out for the sake of comparison.

2.1 Overview of the thermophysical characterization of real fluids and mixtures of real fluids

2.1.1 Equations of state

Before addressing mixtures of real fluids it is worthwhile to remind some aspects that have brought to the formulation of a wide number of thermal Equations of State (EoS) for the description of real fluids. A fluid by definition is a thermodynamic system that in equilibrium conditions can be identified with two independent variables. If pressure, density and temperature are taken as independent variables for the fluid

description, a generic thermal EoS can be implicitly expressed by:

$$f(\rho, p, T) = 0 \tag{2.1}$$

The form of Eq. (2.1) is strictly related to the thermodynamic region of interest and in particular with the distance from the critical point: in fact it is common use to refer to reduced thermodynamic variables with respect to the critical values to identify different thermodynamic regions (p/p_c and T/T_c). In the present work attention is devoted to supercritical fluids ($p/p_c > 1$) that are single phase fluids.

It is common use to distinguish between *real* and *ideal* fluids. An ideal fluid can be described with the perfect gas law, which is the simplest thermal equation of state for a pure substance:

$$p = \rho R T \tag{2.2}$$

where p is the pressure, ρ is the density, R is the gas constant, with $R = \Re/W$, where $\Re = 8.31434$ J/K/mol is the universal gas constant and W is the molar weight, and T is the temperature. This law can be derived from the kinetic theory of gas and is based on the hypothesis that the molecules are rigid, pointwise particles that interact with each other only by means of collisions. This hypothesis is verified for a rarefied gas; in this state the molecules are so far one from each other that no attractive/repulsive force arises and they interact only by collisions. For a *real fluid* this molecular regime occurs at high temperature (i.e., high kinetic energy) and low pressure (i.e., low intermolecular interaction energy):

$$\frac{p}{p_c} \ll 1 \qquad \frac{T}{T_c} \gg 1 \tag{2.3}$$

Nevertheless perfect gas equation (Eq. 2.2) can also be suitably applied for supercritical pressures and high temperatures much greater than the critical, that is where the kinetic energy is predominant over the intermolecular interaction energy. A different situation occurs decreasing the temperature, where intermolecular forces become important and cannot be neglected: perfect gas EoS is not longer valid. To describe a real fluid the simpler EoS that have been historically proposed are two parameters *cubic equations of state*. Many of the common equations of this group can be expressed by:

$$p = \frac{\rho R T}{1 - \rho B} - \frac{\rho^2 A}{1 + \rho U B + \rho^2 V B^2} \tag{2.4}$$

where U and V are integers values, while A and B are two parameters that are chosen to verify some conditions. The two parameters where selected so as to verify the two critical point conditions:

$$\begin{aligned} \left(\frac{\partial p}{\partial \rho}\right)_{T_c} &= 0 \\ \left(\frac{\partial^2 p}{\partial \rho^2}\right)_{T_c} &= 0 \end{aligned} \tag{2.5}$$

and then eventually make them function of the temperature and acentric factor ω_a to reproduce vapor pressure.[1] Four well-known cubic equations which follow this approach are the van der Waals, Redlich-Kwong (RK), Soave (SRK) and Peng-Robinson

[1] The acentric factor ω_a gives an indication of the deviation from spherical symmetry in a molecule. See appendix A for the definition

(PR) equations [118,130,143]: the corresponding parameters are reported in Tab. 2.1. Another approach to get the parameters is to assume A and B functions of temperature suitably set so as to reproduce some selected experimental data. There have been numerous extensions and modifications of these cubic EoS, most of which introduce a third parameter, and even nowadays this represents an open research field [39,78,129]. The advantage of these equations is their relative simplicity if compared to other real fluids EoS but unfortunately they are low accurate in the transcritical region.

Equation	U	V	A	B
Van Der Walls (VDW)	0	0	$\frac{RT_c}{8p_c}$	$\frac{27}{64}\frac{R^2T_c^2}{p_c}$
Redlich-Kwong (RK)	1	0	$\frac{0.08664RT_c}{p_c}$	$\frac{0.42748R^2T^{2.5}}{p_cT^{1/2}}$
Soave (SRK)	1	0	$\frac{0.08664RT_c}{p_c}$	$\frac{0.42748R^2T_c^2}{p_c}[1+f_\omega(1-(T/T_c)^{1/2}]^2$ $f_\omega = 0.48+1.574\omega_a-0.176\omega_a^2$
Peng-Robinson (PG)	2	-1	$\frac{0.07780RT_c}{p_c}$	$\frac{0.45724R^2T_c^2}{p_c}[1+f_\omega(1-(T/T_c)^{1/2}]^2$ $f_\omega = 0.37464+1.54226\omega_a-0.26992\omega_a^2$

Table 2.1: Parameters for four cubic equations of state [118, 130, 143]

Another approach to describe real fluids comes from statistical mechanics and expresses the compressibility factor Z in terms of a series in the density ρ [2] :

$$Z = \frac{p}{\rho RT} = 1 + C_2\rho + C_3\rho^2 + \cdots \tag{2.6}$$

where the *virial coefficients* C_i are functions of temperature for a given fluid and are evaluated from empirical data (C_i is the $i-th$ virial coefficient). An important EoS derived from this approach is the Benedict-Webb-Rubin equation (BWR) [12] which is explicit in pressure:

$$p = \rho RT + [B_0RT - A_0 - \frac{C_0}{T^2}]\rho^2 + [bRT - a]\rho^3 + [a\alpha]\rho^6 + \frac{c}{T^2}(1+\gamma\rho^2)e^{-\gamma\rho^2}\rho^3 \tag{2.7}$$

with A_0, B_0, C_0, a, b, c, α and γ constant parameters determined from experimental data and hence related to a particular fluid. Since its introduction in 1940 this equation has been widely applied and modified increasing the number of parameters to reach a higher accuracy. In particular Jacobsen et al. [65] introduced the well known

[2] see appendix A for the definition of the compressibility factor

Modified Benedict-Webb-Rubin equation (MBWR) for nitrogen, then extended to a number of fluids among which methane [171]. The MBWR equation has the following form:

$$p(\rho,T) = \sum_{k=1}^{N} A_k(T)\cdot\rho^k + \left(\sum_{k=N+1}^{M} A_k(T)\cdot\rho^{ik-j}\right)\cdot e^{-(\rho/\rho_c)^2} \tag{2.8}$$

where $A_k(T)$ are simple functions of temperature determined by parameters which are computed by least-squares interpolation of experimental data. These equations are known to provide accurate representation of thermodynamic properties even in proximity of the critical point.

BWR equation has been also used by Lee and Kesler [82] to develop a *generalized* equation based on a three parameters corresponding states theory[3]. The three parameters are reduced temperature $T_r = T/T_c$, reduced pressure $p_r = p/p_c$ and acentric factor ω_a and the compressibility factor for a generic fluid is given by:

$$Z = Z^0 + \omega_a Z^1 \tag{2.9}$$

where Z^0 is the compressibility factor of a simple fluid ($\omega_a = 0$) and Z^1 is the deviation of the compressibility factor of the real fluid from Z^0. Both Z^0 and Z^1 are functions of p_r and T_r. In the Lee-Kesler equation the compressibility factor of any fluid is written in terms of a simple fluid and a reference fluid as follows:

$$Z = Z^0 + \frac{\omega_a}{\omega_a^R}(Z^R - Z^0) \tag{2.10}$$

where Z^0 and Z^R are represented as generalized equations of the BWR form (Eq. 2.7) in terms of reduced temperature and pressure.

Besides cubic and virial equations, other complex EoS have been developed for the description of real fluids. In particular, the more accurate approaches nowadays, namely most of the models used by NIST [1], rely on the assumption of a departure behavior of the real fluid with respect to the perfect gas regime through the definition of excess thermodynamic properties. An excess property is the difference between the actual property value of a fluid and the ideal value at the same temperature and pressure. Following this idea the reduced Helmholtz free energy a, is the Helmholtz free energy A normalized with respect to the product between the gas constant R and the temperature T, and is expressed as:

$$a(\delta,\tau) = \frac{A}{RT} = a^0(\delta,\tau) + a^r(\delta,\tau) \tag{2.11}$$

where the residual term a^r, also referred to as departure function is a correction, in the real fluid regime of the perfect gas term a^0. δ and τ are, respectively, the fluid reduced density and temperature:

$$\delta = \frac{\rho}{\rho_c} \qquad \text{and} \qquad \tau = \frac{T_c}{T} \tag{2.12}$$

A large number of experimental data are used to obtain accurate expressions for a^r which is in general a polynomial of δ and τ.

[3] see appendix A for the introduction of the corresponding state principle

To describe a mixture of fluids the composition has to be considered as a third variable together with pressure and temperature, hence a generic equation of state will have the implicit form:

$$f(\rho, p, T, \mathbf{x}) = 0 \tag{2.13}$$

where $\mathbf{x} = \{x_1, \cdots, x_N\}$ is the composition vector of a N component mixture with x_i molar fraction of the $i-th$ species. Hence the problem of describe a real fluid is further complicated for mixtures: in fact each species has to be accurately described as a real fluid and also the interaction between one species and the others differs from that of a perfect gas mixture. Indeed mixture rules which describe the behavior of one species with respect to the others are necessary: generally binary parameters, which relate one species to another, are combined for mixtures with more than two species (see Appendix A).

Available EoS to describe mixtures of real fluids are extensions of the EoS briefly described above for pure fluids: cubic, virial equations and their generalized form through the corresponding states principle and EoS in terms of the Helmholtz free energy.

Cubic EoS are extended to mixtures through the definition of suitable mixing rules which permit to consider the mixture as if it was a pure fluid. For all two parameters cubic EoS the following mixing rules can be applied to evaluate the two mixture parameters a_m and b_m:

$$\begin{aligned} a_m &= \sum_i \sum_j x_i x_j (a_i a_j)^{1/2} (1 - k_{ij}) \\ b_m &= \sum_i x_i b_i \end{aligned} \tag{2.14}$$

where x_i and x_j are the molar fraction of the $i-th$ and $j-th$ species, and k_{ij} is a mixture interaction parameter (see appendix A for more details on the mixing rules). Once a_m and b_m are evaluated it is possible to proceed as for a pure fluid, except if derivatives with respect to composition are needed. More complex mixing rules have also been proposed both for two and three parameters cubic equations: they usually take into account local composition and require other parameters. Among the cubic EoS extensions of SRK and PR are widely used for mixtures [157].

Following the same idea *virial equations* can be extended to mixtures: for example BWR coefficients in Eq. (2.7) can be evaluated from the coefficients of each species through suitable mixing rules [14]. Nevertheless these mixing rules have not been widely developed in recent years. Conversely recent works on generalized virial EoS for mixtures can be found [40]. Among generalized virial EoS the Lee-Kesler EoS (Eq. (2.10) for a pure fluid) is extended to mixtures defining pseudocritical properties from which the necessary reduced mixture properties can be evaluated. In particular

Lee and Kesler proposed the following mixing rules in their work [82]:

$$\begin{aligned} T_{cm} &= \rho_{cm}^{1/4} \sum_i \sum_j x_i x_j \frac{T_{cij}}{(\rho_{cij})^{1/4}} \\ \frac{1}{\rho_{cm}} &= \sum_i \sum_j x_i x_j \frac{1}{\rho_{cij}} \\ \omega_{am} &= \sum_i x_i \omega_{ai} \\ p_{cm} &= [0.2905 - 0.085\omega_{am}]\rho_{cm} R_m T_{cm} \end{aligned} \tag{2.15}$$

with T_{cij} and ρ_{cij} combining the critical parameters of the components i and j:

$$\begin{aligned} T_{cij} &= (T_{ci}T_{cj})^{1/2} k_{ij} \\ \frac{1}{\rho_{cij}} &= \frac{1}{8}\left[\left(\frac{1}{\rho_{ci}}\right)^{1/3} + \left(\frac{1}{\rho_{cj}}\right)^{1/3}\right]^3 \end{aligned} \tag{2.16}$$

Extensions of these mixing rules for LK equation can be found in literature, but with the same basic formulation.

Helmholtz free energy EoS for mixtures have the same basic form of Eq. (2.11) with a departure function to take the real gas behavior into account either for any components and for the different binary mixtures. Each binary mixture is related to another with binary parameters. These approaches need a very large number of experimental data. In particular the most accurate models are extensions of the mixture model developed independently by Tillner-Roth [151] and Lemmon [86] which expresses *Helmholtz free energy* of a mixture of N components as:

$$a = \sum_{j=1}^{N} [x_j (a_j^0 + a_j^r) + x_j \ln x_j] + \sum_{p=1}^{N-1} \sum_{q=p+1}^{N} x_p x_q F_{pq} a_{pq}^{excess} \tag{2.17}$$

The first term summation in Eq. (2.17) arises from an ideal mixing: the real fluid behavior is described for each single species ($a = a^0 + a^r$) but the components are mixed as if they were perfect gas. In fact the term $x_j \ln x_j$ arises from the entropy of mixing of ideal gases. Hence the second summation account for the interaction between the different mixture components which bring a departure from the ideal mixing solution. The excess contribution due the real mixing is accounted for each binary mixture by the term a_{pq}^{excess} (for the components p and q), and the different binary mixtures are related to each other through the generalizing parameters F_{pq}: both F_{pq} and a_{pq}^{excess} are based on a large number of experimental data. Moreover both a_j^r and a_{pq}^{excess} are evaluated at residual density and temperature, with pseudocritical values as reducing parameters. It has to be noticed that the mixing rule of Eq. (2.17) could in general be applied with any EoS: either directly to an Helmholtz EoS or with BWR, cubic EoS, etc. (with a suitable caloric equation for the perfect gas c_p for all the models except the Helmholtz one). It should be even possible to model different species with different type of EoS. If composition approaches a mole fraction of unity the model reduces exactly to the pure component EoS and this represents a great

advantage. Hence it appears how the accuracy of the final mixture EoS will depend both on the single species model and on the mixture model.

Either for single species and mixtures it is important to point out that there is an intrinsic difference between Helmholtz free energy EoS and the other equations previously discussed. In fact both perfect gas, cubic and virial equations are thermal equations of state which correlate three thermodynamic variables, namely pressure, density and temperature. To obtain a complete description of the fluid energetic quantities (like enthalpy, entropy, Helmholtz free energy) a thermal equation is not sufficient: rather a caloric equation must be provided to correlate an energetic quantity to two thermodynamic variables. Usually, this is done with an expression for the specific heat at constant pressure. Conversely, an EoS in terms of the Helmholtz free energy is a *fundamental* equation and is self-sufficient to provide all the thermodynamic variables that are needed. The term *fundamental* comes for the fact that from it a number of thermodynamic properties of the fluid can be derived none of which alone would permit the computation of all the others.

2.1.2 Transport properties

Differently from the case of thermal EoS, all the transport property models to describe real fluids are based on the same basic assumption of an excess behavior of a real fluid with respect to perfect gas. Indeed, following the same principle described above for Helmholtz free energy EoS, excess property models are also used to describe the transport properties of real fluids, namely, if Λ is either the viscosity μ or the thermal conductivity k, the real fluid property is expressed as:

$$\Lambda(\rho, T) = \Lambda_{id}(T) + \Lambda_{ex}(\rho, T) \tag{2.18}$$

where Λ_{ex} is the excess property from the dilute gas term Λ_{id}. Different terms compose the excess viscosity and conductivity. Excess viscosity is usually the sum of two terms:

$$\mu_{ex} = \rho\mu^1(T) + \mu^r(\rho, T) \tag{2.19}$$

where $\mu^1(T)$ is the initial density dependence term, accounting for low density real behavior, and μ^r is the residual viscosity which becomes important at high densities. The excess thermal conductivity is given by:

$$k_{ex} = k^r(\rho, T) + \Delta k_c(\rho, T) \tag{2.20}$$

where k^r is the residual conductivity and Δk_c is the critical enhancement which is important only near the critical region. The different models available in the literature differ in the way the excess property is treated. In particular, for the residual part, semi empirical correlations are proposed, provided a sufficient number of experimental data is available. Conversely, when, for a given fluid, only few experimental data are available, corresponding state models can provide a good approximation. The residual property of the fluid at a given temperature and density (T and ρ) is considered equal to the residual property of a reference fluid, for which an accurate correlation is available, evaluated at a *conformal* temperature and density (T_0 and ρ_0) given by the solution of the following system:

$$\begin{cases} a^r(T, \rho) = a_0^r(T_0, \rho_0) \\ \\ Z(T, \rho) = Z_0(T_0, \rho_0) \end{cases} \tag{2.21}$$

where a^r is the residual part of the reduced Helmholtz free energy ($a = A/RT$) and Z the compressibility factor of the fluid, whereas a_0^r and Z_0 are the corresponding functions for the reference fluid.

2.1.3 Selection of suitable mixture models

In the selection of the models for the present study different aspects have been considered. First of all the need of high accurate EoS for supercritical pressures and temperature in the whole range from low subcritical to high supercritical temperatures, with particular attention devoted to the pseudocritical region: this requirement makes inadequate cubic EoS, which are known to be highly inaccurate just in the transcritical region. Moreover, the model has to be able to consider high number of components and therefore also Lee-Kelser equations are not suitable. Another requirement in the selection of EoS for the present work is the possbility to compare mixtures and single species: in this sense a Helmholtz mixture model, which relies on highly accurate EoS for each single species, reduces to a highly accurate EoS for a pure fluid in case of single species. For the description of each single fluid both virial EoS, like the MBWR, and Helmholtz based EoS should be suitable in terms of accuracy, even though the most recently developed EoS are of the Helmholtz type. Beyond all these considerations it is important to put the attention on the specific mixtures we are interested in which are Liquefied Natural Gas mixtures. In this framework, an accurate model based on a very large number of experimental data has been developed by the Groupe Européen de Recherche Gazière (GERG) purposely for the description of natural gas mixtures [79]: the model was first presented in 2004. The mixture model is an extension of Lemmon model (see Eq.(2.17)) with parameters for the departure functions based on a large number of experimental data. Moreover, for each species an accurate Helmholtz based EoS is proposed, with particular attention on the main components of natural gas, first of all methane. Considering all the aspects previously discussed, GERG mixture equation together with EoS proposed for the different species have been selected for the present work.

The selection of transport property mixture models is straightforward the Extended Corresponding States (ECS) model being the only available accurate option. Nevertheless, care must be given to the selection of the transport property models for each single species, whose accuracy strongly influences the accuracy of the mixture property. Note also that the ECS model relies on the Helmholtz free energy equation of the mixture (see Eq. 2.21) and of each single species (as it will be pointed out in the following): also for this reason the selection of EoS based on Helmholtz free energy have been preferred.

2.2 Equation of state for mixtures

The mixing rules selected are valid for a mixture made of any number of species, provided data relevant to each species are available. In the present study attention has been focused only on a limited number of species namely methane, ethane, propane and nitrogen (which are the main LNG components). However the model can be extended to any number of components. First the thermodynamic models used in the perfect gas regimes are presented, which also are used in the real fluid regime

models that follow.

2.2.1 Perfect gas regime

In the perfect gas regime, each species in the mixture behave according to the perfect gas law:

$$p_i = \rho_i R_i T \quad (i = 1, \dots N) \tag{2.22}$$

where subscript i refers to $i-th$ of the N species of the mixture. In particular p_i is the partial pressure of the $i-th$ species. R_i is the gas constant of the species defined by $R_i = \Re/W_i$, where $\Re = 8.31434$ J/K/mol is the universal gas constant and W_i is the molar weight of the $i-th$ species. The mixing rule for the perfect gas EoS is given by Dalton's law:

$$p = \sum_{i=1}^{N} p_i = \rho R T \tag{2.23}$$

where p, ρ and T are values relevant to the mixture.

The perfect gas law is the EoS sufficient to correlate pressure, temperature and density, whereas to have a complete description of the thermodynamic state a caloric equation of state is also needed which allows to correlate enthalpy, internal energy, Helmholtz free energy and Gibbs free energy to other two independent thermodynamic variables. One of the ways to get a caloric EoS is to provide an expression for the specific heat at constant pressure, c_p. In the general case of a thermally perfect gas the value of constant pressure specific heat cannot be considered as a constant (the latter is the simplest case of calorically perfect gas), although as long as a perfect gas is considered, the c_p only depends on temperature. To take into account for the variation of c_p with temperature many studies have been carried out in the past for the different substances which led to the development of polynomials interpolating experimental data and which can represent the behavior of the selected substance in a given temperature range. In the present work the NASA standard polynomials have been selected [94, 95]. In particular, they express constant pressure specific heat of the mixture as an average of the contribution of each species, weighted with its molar fraction, as given from perfect gas mixture theory:

$$\begin{aligned}\frac{c_p}{R} &= \sum_{i=1}^{N} x_i \frac{c_{p,i}}{R_i} = \\ &= \sum_{i=1}^{N} x_i \left(a_{1,i}T^{-2} + a_{2,i}T^{-1} + a_{3,i} + a_{4,i}T + a_{5,i}T^2 + a_{6,i}T^3 + a_{7,i}T^4\right)\end{aligned} \tag{2.24}$$

For each species two further integration constants are necessary to provide the values of the standard-state enthalpy and entropy (the reference state is defined by $p = 1.01325 \cdot 10^5$ Pa and $T = 298.15$ K). Enthalpy and entropy at the reference pressure are therefore expressed as:

$$\begin{aligned}\frac{h}{RT} = \sum_{i=1}^{N} x_i \Bigg(&-a_{1,i}T^{-2} + a_{2,i}T^{-1}\ln T + a_{3,i} + a_{4,i}\frac{T}{2} + \\ &+ a_{5,i}\frac{T^2}{3} + a_{6,i}\frac{T^3}{4} + a_{7,i}\frac{T^4}{5} + \frac{a_{8,i}}{T}\Bigg)\end{aligned} \tag{2.25}$$

$$\frac{s^0}{R} = \sum_{i=1}^{N} x_i \left(-a_{1,i}\frac{T^{-2}}{2} - a_{2,i}T^{-1} + a_{3,i}\ln T + a_{4,i}T + \right.$$
$$\left. + a_{5,i}\frac{T^2}{2} + a_{6,i}\frac{T^3}{3} + a_{7,i}\frac{T^4}{4} + a_{9,i} \right) \quad (2.26)$$

The mixture entropy can be computed according to Eq. (2.27):

$$\frac{s}{R} = \frac{s^0}{R} - \ln(p) - \sum_{i=1}^{N} x_i \ln(x_i) \quad (2.27)$$

The coefficients for the four species ($N = 4$) considered are listed in Tables B.1–B.2 in Appendix B. Also enthalpy and entropy at the reference state for each species are reported in Table B.11.

2.2.2 Real fluid regime

Dealing with methane based mixtures, the most recent and reliable equations of state are those presented in [79] which have been built especially to describe natural gas mixtures. They belong to the group based on the Helmholtz free energy, which takes into account the real behavior of fluids with some kind of departure functions from the perfect gas solution. In particular, the GERG EoS is based on pure substances equations of state for each considered mixture component and correlation equations for binary mixtures consisting of these components. The current number of considered components is N=18, which include the 4 selected species considered in the present study, even if the mixture model is obviously valid for a generic N. It is important to underline that out of the 153 possible combinations of binary mixtures consisting of the 18 considered natural gas components, data for a total of 98 binary mixtures is available for the development and evaluation of the presented EoS. Moreover, since methane is the most important natural gas component, the data situation for mixtures containing methane is of primary interest for the development of the GERG EoS and has been largely investigated. The range of validity of GERG EoS covers temperatures of 60 K$\leq T \leq$ 700 K and pressures of $p \leq$ 70 MPa, with an uncertainty in density lower than 0.5%.

Mixing rules are applied to obtain the reduced Helmholtz free energy a of the mixture which can be expressed as the sum of the ideal and residual term, as previously shown in Eq. 2.11 for a single species and in Eq. 2.17 for a mixture [4]. For the sake of clearness the equation is rewritten here in the following form:

$$a(\delta, \tau, \mathbf{x}) = \frac{A}{RT} = a^0(\rho, T, \mathbf{x}) + a^r(\delta, \tau, \mathbf{x}) \quad (2.28)$$

with ρ and T being respectively the mixture density and temperature, R the gas constant of the mixture, A the mass specific Helmholtz free energy, and $\mathbf{x} = (x_1, x_2, \ldots, x_N)$ the molar composition. The residual term a^r, which corrects in the real fluid regime the perfect gas term a^0, is expressed in terms of reduced mixture density δ and

[4] As previously emphasized the present GERG model uses a mixing rule which is an extention of the Lemmon mixing rule given in Eq. (2.17)

reduced mixture temperature τ, according to:

$$\delta = \frac{\rho}{\rho_r(\mathbf{x})} \qquad \text{and} \qquad \tau = \frac{T_r(\mathbf{x})}{T} \tag{2.29}$$

This fundamental equation is sufficient to provide a complete description of the thermodynamic properties of the mixture. It is necessary to provide relationships for the terms a^0, a^r, ρ_r and T_r which appear in Eqs. (2.28)–(2.29).

Perfect gas mixture term

The perfect gas mixture term takes into account the perfect gas behavior of the mixture. At first, the perfect gas mixture rule for the Helmholtz free energy has to be considered:

$$a^0(\rho, T, \mathbf{x}) = \sum_{i=1}^{N} x_i [a_i^0(\rho, T) + \ln\, x_i] \tag{2.30}$$

In this equation the terms $a_i^0(\rho, T)$ are the Helmholtz free energy EoS for each of the considered species. While in the range of higher temperatures the NASA polynomials given in Sec. 2.2.1 are considered, in the range of real fluid the following relationship is assumed:

$$\begin{aligned} a_i^0 = \frac{R^*}{R}\Bigg[&\ln\left(\frac{\rho}{\rho_{c,i}}\right) + n_{i,1}^0 + n_{i,2}^0 \frac{T_{c,i}}{T} + n_{i,3}^0 \ln\left(\frac{T_{c,i}}{T}\right) + \\ &+ \sum_{k=4,6} n_{i,k}^0 \ln\left|\sinh\left(\theta_{i,k}^0 \frac{T_{c,i}}{T}\right)\right| - \sum_{k=5,7} n_{i,k}^0 \ln\left|\cosh\left(\theta_{i,k}^0 \frac{T_{c,i}}{T}\right)\right| \Bigg] \end{aligned} \tag{2.31}$$

where $\rho_{c,i}$ and $T_{c,i}$ are the critical values of the pure species given in Table B.12, $n_{i,k}^0$ and $\theta_{i,k}^0$ are the empirical coefficients listed in Table B.3, R is the current internationally molar gas constant, and R^* is a former gas constant for which relationships have been calibrated:

$$R = 8.314\,472\,\mathrm{J \cdot mol^{-1} \cdot K^{-1}} \qquad R^* = 8.314\,510\,\mathrm{J \cdot mol^{-1} \cdot K^{-1}} \tag{2.32}$$

The perfect gas terms of Eq. (2.31) are obtained combining the perfect gas law and Jaeschke and Schley [5] equation for the specific heat at constant pressure.

Residual part term

The residual part of the reduced Helmholtz free energy takes into account the departure from the perfect gas mixture behavior. It includes both the departure Helmholtz free energy of each species linearly combined using the mole fraction x_i and the residual behavior of the mixture (the double summation is called departure function):

$$a^r(\delta, \tau, \overline{x}) = \sum_{i=1}^{N} x_i a_i^r(\delta, \tau) + \sum_{i=1}^{N-1} \sum_{j=i+1}^{N} x_i x_j F_{ij} a_{ij}^r(\delta, \tau) \tag{2.33}$$

Referring to Eq. (2.33) the residual part of the reduced Helmholtz free energy of the $i-th$ species is given by the pure substance equation of state:

$$a_i^r(\delta,\tau) = \sum_{k=1}^{K_{Pol,i}} n_{i,k}\delta^{d_{i,k}}\tau^{t_{i,k}} + \sum_{k=K_{Pol,i}+1}^{K_{Pol,i}+K_{Exp,i}} n_{i,k}\delta^{d_{i,k}}\tau^{t_{i,k}}e^{-\delta^{c_{i,k}}} \tag{2.34}$$

The coefficients $n_{i,k}$, $d_{i,k}$, $t_{i,k}$ and $c_{i,k}$ for the species of interest are listed in Tables B.4–B.7. In the departure function (double summation in Eq. (2.33)) F_{ij} is an adjustable factor which relates the behavior of one binary mixture to the whole which is reported in Table B.8 for the species of interest in the present work. The remaining part of the departure term is the function $a_{ij}^r(\delta,\tau)$ which is given for each specific binary mixture as:

$$\begin{aligned} a_{ij}^r(\delta,\tau) = &\sum_{k=1}^{K_{Pol,ij}} n_{ij,k}\delta^{d_{ij,k}}\tau^{t_{ij,k}} + \\ &+ \sum_{k=K_{Pol,ij}+1}^{K_{Pol,ij}+K_{Exp,ij}} n_{ij,k}\delta^{d_{ij,k}}\tau^{t_{ij,k}}e^{-\eta_{ij,k}(\delta-\epsilon_{ij,k})^2-\beta_{ij,k}(\delta-\gamma_{ij,k})} \end{aligned} \tag{2.35}$$

The values for the coefficients $n_{ij,k}$ and the exponents $d_{ij,k}$, $t_{ij,k}$, $\eta_{ij,k}$, $\epsilon_{ij,k}$, $\beta_{ij,k}$ and $\gamma_{ij,k}$ are also given in Table B.8.

Reduced density and temperature

The reduced density δ and temperature τ are calculated by means of the composition-dependent reducing functions which do not correspond with the mixture critical parameters, rather they are combinations of the critical parameters of the single species and are expressed as follows:

$$\begin{aligned} \frac{1}{\rho_r(\overline{x})} &= \sum_{i=1}^{N} x_i^2\frac{1}{\rho_{c,i}} + \sum_{i=1}^{N-1}\sum_{j=i+1}^{N} 2x_ix_j\beta_{\nu,ij}\gamma_{\nu,ij}\frac{x_i+x_j}{\beta_{\nu,ij}^2x_i+x_j}\frac{1}{8}\left(\frac{1}{\rho_{c,i}^{1/3}}+\frac{1}{\rho_{c,j}^{1/3}}\right)^3 \\ T_r(\overline{x}) &= \sum_{i=1}^{N} x_i^2T_{c,i} + \sum_{i=1}^{N-1}\sum_{j=i+1}^{N} 2x_ix_j\beta_{T,ij}\gamma_{T,ij}\frac{x_i+x_j}{\beta_{T,ij}^2x_i+x_j}(T_{c,i}\cdot T_{c,j})^{0.5} \end{aligned} \tag{2.36}$$

The binary parameters $\beta_{\nu,ij}$, $\gamma_{\nu,ij}$, $\beta_{T,ij}$ and $\gamma_{\nu,ij}$ are listed in Table B.10.

2.2.3 Other thermodynamic variables

Once the equation of state for the reduced Helmholtz free energy is available, the other thermodynamic properties of the mixture can be obtained from its derivatives with respect to reduced temperature and density. In particular, the compressibility factor Z can be obtained as:

$$Z(\delta,\tau,\overline{x}) = 1 + \delta\left(\frac{\partial a^r}{\partial\delta}\right)_{\tau,\overline{x}} \tag{2.37}$$

pressure as:

$$p(T, \rho, \overline{x}) = Z\rho RT \tag{2.38}$$

enthalpy as:

$$\frac{h(\delta, \tau, \overline{x})}{RT} = 1 + \tau \left[\left(\frac{\partial a^0}{\partial \tau} \right)_{\delta, \overline{x}} + \left(\frac{\partial a^r}{\partial \tau} \right)_{\delta, \overline{x}} \right] + \delta \left(\frac{\partial a^r}{\partial \delta} \right)_{\tau, \overline{x}} \tag{2.39}$$

constant pressure specific heat as:

$$\begin{aligned} \frac{c_p}{R} = -\tau^2 \left[\left(\frac{\partial^2 a^0}{\partial \tau^2} \right)_{\delta, \overline{x}} + \left(\frac{\partial^2 a^r}{\partial \tau^2} \right)_{\delta, \overline{x}} \right] + \\ + \frac{\left[1 + \delta \left(\frac{\partial a^r}{\partial \delta} \right)_{\tau, \overline{x}} - \delta\tau \left(\frac{\partial^2 a^r}{\partial \delta \partial \tau} \right)_{\overline{x}} \right]^2}{1 + 2\delta \left(\frac{\partial a^r}{\partial \delta} \right)_{\tau, \overline{x}} + \delta^2 \left(\frac{\partial^2 a^r}{\partial \delta^2} \right)_{\tau, \overline{x}}} \end{aligned} \tag{2.40}$$

Further interesting thermodynamic variables, and details on their derivation from the Helmholtz free energy, can be found in Appendix A.

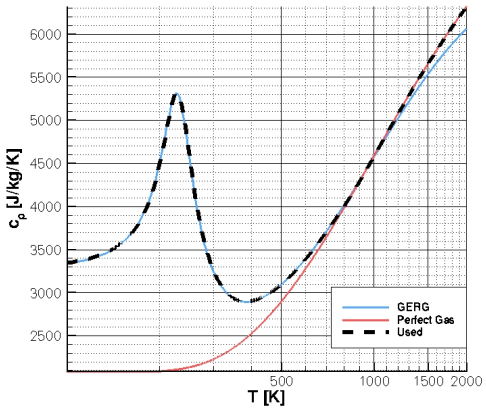

Figure 2.1: CH_4 constant pressure specific heat for $p = 13\,MPa$

2.2.4 From real fluid to perfect gas

At high temperatures fluid mixtures can be considered as mixtures of perfect gases and the perfect gas EoS can be used, whereas at low temperature real fluid mixture EoS must be used. For pure methane and LNG the passage between the real fluid and perfect gas regime occurs for temperatures between 600 K and 1000 K. Nevertheless in this temperature range GERG and perfect gas EoS give slightly different results: to pass from one equation to another without discontinuities a linear interpolation

between the two equations has been considered when the temperatures fall in this range. Moreover, the same reference values for enthalpy and entropy at the standard state must be used for both EoS: these values are listed in Table B.11 for each of the 4 considered species. To show the smooth passage between the two EoS an example is given in Fig. 2.1 for the methane c_p, at a pressure of $p = 13$ MPa. The switch between GERG and perfect gas models takes place at about 900 K without discontinuities.

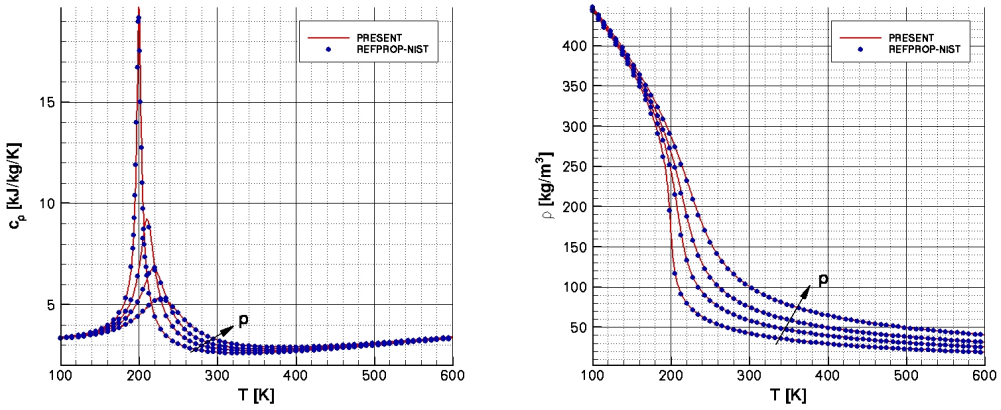

Figure 2.2: Computed isobaric specific heat and density as a function of temperature for different pressures: $6, 8, 10$ and 13 MPa. Species: methane.

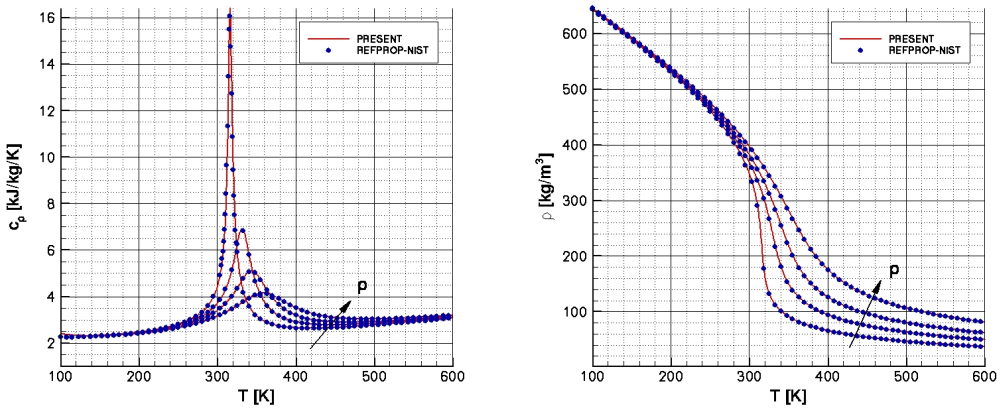

Figure 2.3: Computed isobaric specific heat and density as a function of temperature for different pressures: $6, 8, 10$ and 13 MPa. Species: ethane.

2.2.5 Validation

First a validation of the pure fluid equations of state used in the proposed mixture model has been carried out by comparison of thermodynamic properties with those provided by the National Institute of Standard Technologies (NIST) [1] (obtained

with the REFPROP software released by NIST), for each of the 4 selected species considered separately: the comparison is shown in Fig. 2.3-2.5 for the c_p and density.

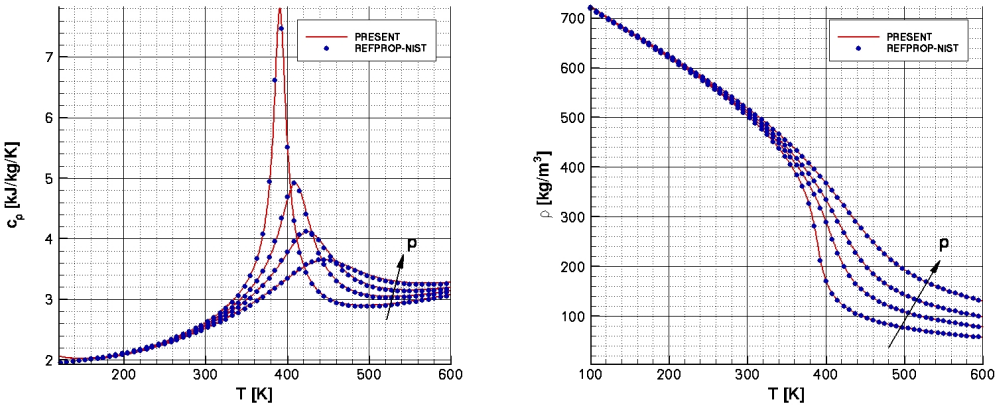

Figure 2.4: Computed isobaric specific heat and density as a function of temperature for different pressures: $6, 8, 10$ and 13 MPa. Species: propane.

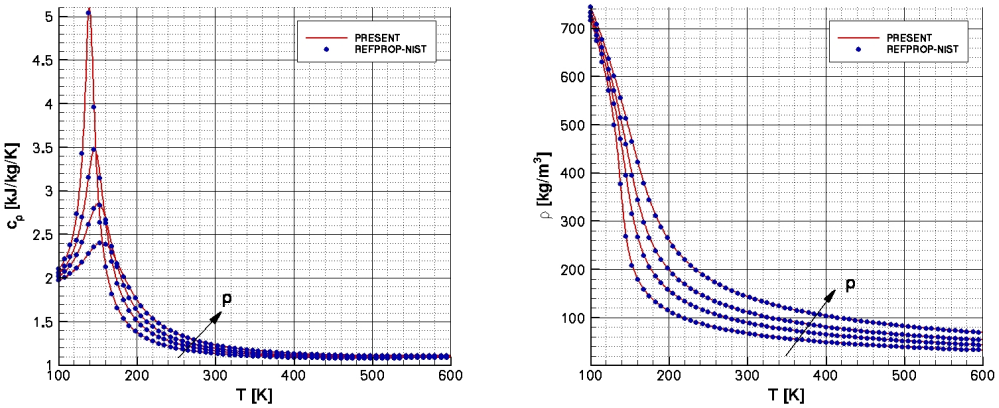

Figure 2.5: Computed isobaric specific heat and density as a function of temperature for different pressures: $6, 8, 10$ and 13 MPa. Species: nitrogen.

The Helmholtz EoS for each pure species is Eq.(2.28) when $x_i = 1$ and $x_j = 0$ for $j \neq i$, reduces to $a_i(\delta, \tau) = a_i^0(\rho, T) + a_i^r(\delta, \tau)$, with a_i^0 and a_i^r given by Eqs. (2.31) and (2.34). The reducing parameters for a single species are the critical temperature T_c and critical density ρ_c, consistently with Eq. (2.36).

Once asserted that the single pure fluid equations of state are correctly implemented and able to describe the state of the art of thermophysical fluid properties, a validation of the mixture model presented above has been carried out by a comparison of the results with those obtained by the NIST software REFPROP. For this purpose the binary mixtures methane-ethane, methane-propane and methane-nitrogen have been investigated comparing all the thermodynamic properties at several supercriti-

cal pressure, in a temperature range containing the pseudocritical value and varying the species molar fraction. As an example in Figs. (2.6) computed density and specific heat at constant pressure are shown for a pressure of $p = 13$ MPa and different molar fractions: for each binary mixtures 4 values are considered with methane molar fraction being $x_{CH4} = 0./0.25/0.5/0.75/1$ ($x_\alpha = 1 - x_{CH4}$ with α either C_2H_6, C_3H_8 or N_2). In these comparisons the investigated range of temperatures includes the pseudocritical temperatures, corresponding to the c_p peaks. The accordance between the present model and REFPROP results is satisfactory for all the pressures and compositions investigated.

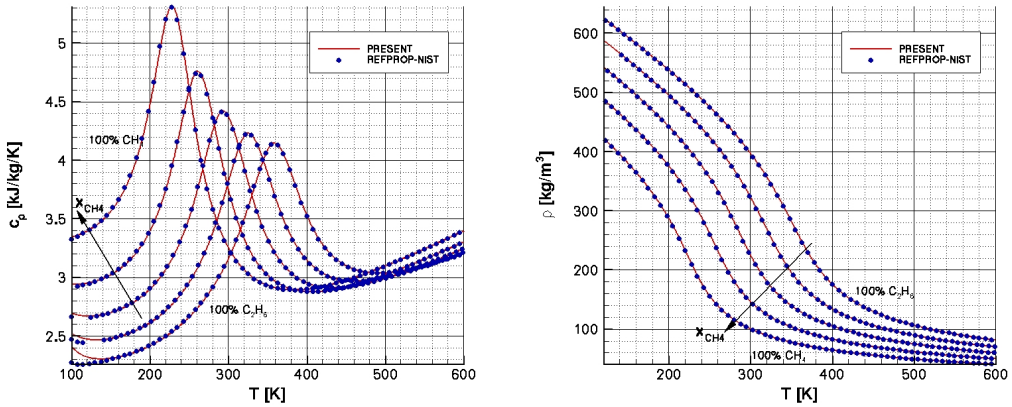

Figure 2.6: Computed isobaric specific heat and density as a function of temperature for $p = 13$ MPa. Species of the binary mixture: methane and ethane.

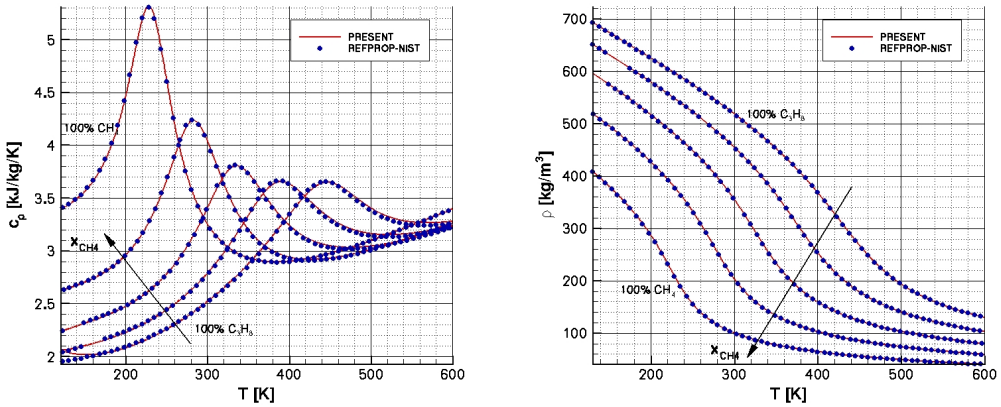

Figure 2.7: Computed isobaric specific heat and density as a function of temperature for $p = 13$ MPa. Species of the binary mixture: methane and propane.

Finally also a typical LNG composition is investigated with the following molar fractions: $x_{CH_4} = 0.92$, $x_{C_2H_6} = 0.04$, $x_{C_3H_8} = 0.022$ and $x_{N_2} = 0.018$. Computed

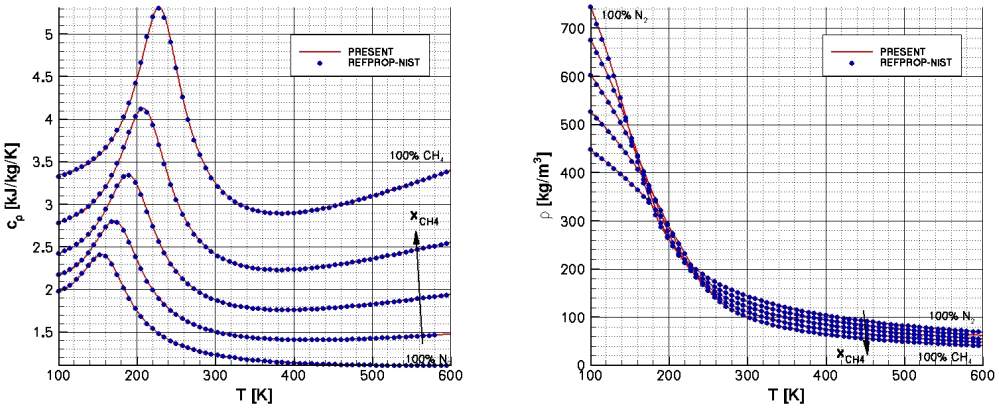

Figure 2.8: Computed isobaric specific heat and density as a function of temperature for $p = 13$ MPa. Species of the binary mixture: methane and nitrogen.

c_p and density are compared for different supercritical pressures with those obtained with NIST REFPROP software showing a satisfactory agreement.

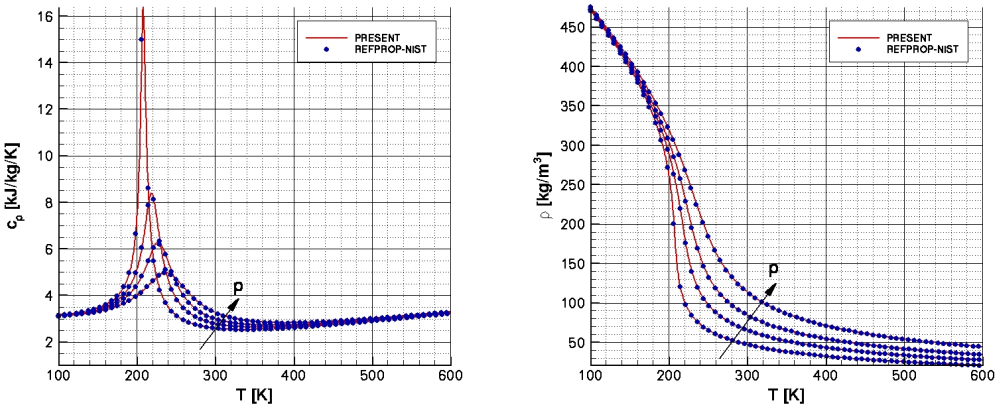

Figure 2.9: Computed isobaric specific heat and density as a function of temperature for different pressures: $6, 8, 10$ and 13 MPa. LNG composition: $x_{CH_4} = 0.92$, $x_{C_2H_6} = 0.04$, $x_{C_3H_8} = 0.022$ and $x_{N_2} = 0.018$

2.3 Transport properties for mixtures

Transport properties models for mixtures are discussed: models used in the perfect gas and real fluid regimes are presented and a comparison with NIST data is carried out.

2.3.1 Perfect gas regime

A common way to obtain the viscosity and thermal conductivity of a mixture of perfect gases is to rely on empirical mixture rules which provide the values of the mixture transport properties as a weighted average of those of the species in the mixture.

Viscosity and thermal conductivity expressions for methane, ethane and nitrogen are taken from [94], according to the empirical relations provided in [15, 146]. The dependence of transport properties on temperature is in the form:

$$\mu_i^0(T) = 10^{-7} \cdot \exp[a_{\mu,1,i} \log(T) + a_{\mu,2,i} T^{-1} + a_{\mu,3,i} T^{-2} + a_{\mu,4,i}] \tag{2.41}$$

$$k_i^0(T) = 10^{-4} \cdot \exp[a_{k,1,i} \log(T) + a_{k,2,i} T^{-1} + a_{k,3,i} T^{-2} + a_{k,4,i}] \tag{2.42}$$

whose coefficients necessary to get values in the SI for each of considered species are listed in Table B.13 for viscosity and in Table B.14 for thermal conductivity. Data for propane are not available in [15, 146]: hence the dilute gas part of the viscosity model presented in [160] and of the thermal conductivity model presented in [93] have been considered for propane in the perfect gas regime. Once data for the species are available, perfect gas mixture viscosity μ^0 and thermal conductivity k^0 are computed according to [94, 95] as:

$$\mu^0(T, \overline{x}) = \sum_{i=1}^{5} x_i \mu_i^0 \left(x_i + \sum_{\substack{i=1 \\ j \neq i}}^{5} x_j \phi_{ij} \right)^{-1} \tag{2.43}$$

and

$$k^0(T, \overline{x}) = \sum_{i=1}^{5} x_i k_i^0 \left(x_i + \sum_{\substack{i=1 \\ j \neq i}}^{5} x_j \psi_{ij} \right)^{-1} \tag{2.44}$$

where the coefficients ϕ_{ij} depends on the values of μ_i, μ_j and on the molar weights of the species:

$$\phi_{ij} = \frac{1}{2\sqrt{2}} \left[1 + \left(\frac{\mu_i}{\mu_j} \right)^{1/2} \left(\frac{W_j}{W_i} \right)^{1/4} \right]^2 \left(1 + \frac{W_i}{W_j} \right)^{-1/2} \tag{2.45}$$

and the coefficients ψ_{ij} necessary to evaluate the thermal conductivity are computed by a suitable correction of ϕ_{ij}:

$$\psi_{ij} = \phi_{ij} \left[1 + \frac{2.41\,(W_i - W_j)(W_i - 0.142\,W_j)}{(W_i + W_j)^2} \right] \tag{2.46}$$

2.3.2 Real fluid regime

In the field of real fluids the most commonly used approach followed in the literature to get mixture viscosity and thermal conductivity is that of ECS theory. In the present study, resorting to equations of state given in Sec. 2.2 and on prefect gas contribution to viscosity and thermal conductivity given in Sec. 2.3.1, transport

properties have been evaluated according to ECS theory presented in [72,96]. In this theory viscosity and thermal conductivity are accurately evaluated for reference fluid, nitrogen, whose properties are taken from [85]. In general, the viscosity of the fluid mixture is expressed (according to [62]) as:

$$\mu = \mu^0(T, \overline{x}) + \mu^r(T, \rho, \overline{x}) + \mu^m(T, \rho, \overline{x}) \tag{2.47}$$

where μ^0 is the diluted gas term (that is taken as equal to the perfect gas mixture viscosity given in Eq. (2.43)), μ^r is the residual viscosity, and μ^m is a correction term for mixtures. The latter term will be neglected in the present study as is usually done for many of the fluid conditions of interest. The basic assumption of the ECS model is that:

$$\mu^r(T, \rho, \overline{x}) = \mu_0^r(T_0, \rho_0) F_\mu^r \tag{2.48}$$

namely, the residual viscosity of the mixture is equal to the residual viscosity of the reference fluid μ_0^r evaluated at the conformal temperature T_0 and density ρ_0 and modified for a correction factor F_μ^r. Assuming that the residual viscosity of the reference fluid as a function of temperature and density is known, it is only necessary to evaluate conformal temperature and density and the reducing factor F_μ^r which also depends on the single species residual viscosity μ_j^r. The conformal temperature and density are defined as such that:

$$\begin{cases} a^r(T, \rho, \overline{x}) = a_0^r(T_0, \rho_0) \\ \\ Z(T, \rho, \overline{x}) = Z_0(T_0, \rho_0) \end{cases} \tag{2.49}$$

where a^r is the residual part of the reduced Helmholtz free energy ($a = A/RT$) and Z the compressibility factor of the mixture, whereas a_0^r and Z_0 are the corresponding functions for the reference fluid that is nitrogen. Both the mixture and reference fluid values are obtained by Eq. (2.33) and Eq. (2.37). The system of equations (2.49) is then solved for T_0 and ρ_0 and the residual viscosity μ_0^r is evaluated. On the basis of the conformal values the following equivalent reducing ratios are defined:

$$f_x = \frac{T}{T_0}; \qquad h_x = \frac{\rho_0}{\rho} \tag{2.50}$$

Following the same procedure conformal values are calculated also for each species ($i = 1, 2, \ldots, 5$) from the system:

$$\begin{cases} a^r(T, \rho, \overline{x}) = a_j^r(T_j, \rho_j) \\ \\ Z(T, \rho, \overline{x}) = Z_j(T_j, \rho_j) \end{cases} \tag{2.51}$$

which is identical to Eq. (2.49) with the j species considered instead of the reference fluid. Residual viscosity for each single species μ_j^r are computed at the conformal values ρ_j and T_j. Also reducing factors for each species are computed according to:

$$f_j = f_x \frac{T_j}{T}; \qquad h_j = h_x \frac{\rho}{\rho_j} \tag{2.52}$$

Finally the reducing factor F_μ^r necessary to get the value of viscosity can be computed. The reducing factor is then expressed as:

$$F_\mu^r = \frac{g_{x,\mu}}{h_x^2} \tag{2.53}$$

where $g_{x,\mu}$ is an equivalent mass for the mixture:

$$g_{x,\mu} = \sum_{i=1}^{N}\sum_{j=1}^{N} x_i x_j f_{ij}^{1/2} h_{ij}^{4/3} \left(\frac{W_{ij}}{W_0}\right)^{1/2} \tag{2.54}$$

The latter expression for $g_{x,\mu}$ requires the introduction of the three terms W_{ij}, f_{ij} and h_{ij}. The first term is computed as the following average of equivalent molar weights g_j:

$$W_{ij} = \frac{2 g_i g_j}{g_i + g_j} \tag{2.55}$$

where g_j for each species is given by:

$$g_j = \left(\frac{\mu_j^r}{\mu_0^r} h_j^{2/3} f_j^{-1/2}\right)^2 W_0 \tag{2.56}$$

The second and third terms rely only on the species values f_i, f_j, h_i and h_j:

$$f_{ij} = \sqrt{f_i f_j} \tag{2.57}$$

$$h_{ij} = \frac{1}{8}\left(h_i^{1/3} + h_j^{1/3}\right)^3 \tag{2.58}$$

The evaluation of thermal conductivity follows the same procedure as for viscosity. In general the thermal conductivity of the fluid mixture will be expressed (according to [63]) as:

$$k = k^0(T, \overline{x}) + k^r(T, \rho, \overline{x}) + k^c(T, \rho, \overline{x}) \tag{2.59}$$

where k^0 is the diluted gas term (that is taken as equal to the perfect gas mixture viscosity given in Eq. (2.44)), k^r is the residual viscosity, and k^c is the so-called critical enhancement which allows to predict the thermal conductivity peak in the vicinity of the critical point.

ECS model is used to compute the residual part k^r. The basic assumption of the ECS model is as in case of viscosity:

$$k^r(T, \rho, \overline{x}) = k_0^r(T_0, \rho_0) F_k^r \tag{2.60}$$

namely, the residual thermal conductivity of the mixture is equal to the residual thermal conductivity of the reference fluid k_0^r evaluated at the conformal temperature T_0 and density ρ_0 and modified for a correction factor F_k^r. Because the reference fluid is the same as for viscosity (nitrogen) conformal temperature and density are those given by Eqs. (2.49) and already available from the computation of viscosity. Also conformal temperature and density for each species are those computed for viscosity from Eqs. (2.51). Therefore, it is only necessary to evaluate the reducing factor F_k^r.

The reducing factor has the same expression as Eq. (2.53), except for the value of $g_{x,k}$ instead of $g_{x,\mu}$:

$$F_k^r = \frac{g_{x,k}}{h_x^2} \tag{2.61}$$

The reducing ratios f_x and h_x are those computed for viscosity in Eq. (2.50), whereas $g_{x,k}$ can be computed by:

$$g_{x,k} = \sum_{i=1}^{N}\sum_{j=1}^{N} x_i x_j f_{ij}^{1/2} h_{ij}^{4/3} \left(\frac{W_0}{W_{ij}}\right)^{1/2} \tag{2.62}$$

where f_{ij} and h_{ij} are evaluated on the basis of species conformal temperatures and densities according to Eq. (2.51) like for viscosity, and W_{ij} is given by Eq. (2.55) but each equivalent molar weight g_j has a different expression than for viscosity:

$$g_j = \left(\frac{k_0^r}{k_j^r} h_j^{-2/3} f_j^{1/2}\right)^2 W_0 \tag{2.63}$$

The critical enhancement is evaluated according to a theoretical model [112, 158] developed for pure fluids:

$$\Delta k_c = \rho c_p \frac{R_0 k_{bol} T}{6\pi\mu\xi}(\Omega - \Omega_0) \tag{2.64}$$

where

$$\Omega = \frac{2}{\pi}\left[\left(\frac{c_p - c_v}{c_p}\right)\arctan(q_D\xi) + \frac{c_v}{c_p} q_D \xi\right] \tag{2.65}$$

and

$$\Omega_0 = \frac{2}{\pi}\left\{1 - \exp\left[-\frac{1}{(q_D\xi)^{-1} + \frac{1}{3}(q_D\xi\rho_c/\rho)^2}\right]\right\} \tag{2.66}$$

The correlation length ξ is given by:

$$\xi = \xi_0 \left[\frac{\chi(T,\rho) - \chi(T_{ref},\rho)\dfrac{T_{ref}}{T}}{\Gamma}\right]^{g/\gamma} \tag{2.67}$$

where

$$\chi(T,\rho) = \frac{p_c \rho}{(\rho_c)^2}\left(\frac{\partial\rho}{\partial p}\right)_T \tag{2.68}$$

In Eq. (2.64)-(2.68) R_0, g and γ are theoretically based constants whereas q_D, ξ_0 and Γ are fluid-specific fitted terms; T_{ref} is a reference temperature greater than the critical temperature (usually $T_{ref} = 1.5T_c$); k_{bol} is the Boltzmann constant; μ is the real fluid viscosity. For mixtures the model is extended considering averages terms weighted with the molar fractions for R_0, g, γ, q_D, ξ_0, Γ and T_{ref}. As an example $R_{0,x}$ of the mixture is evaluated by:

$$R_{0,x} = \sum_{i=1}^{5} x_i R_{0,i} \tag{2.69}$$

with $R_{0,i}$ referring to the $i-th$ species. Mixture critical parameters are approximated with the reducing density and temperature of Eq. (2.36) used in the thermodynamic model. Finally the pressure derivative with respect to pressure in Eq. (2.68) and the specific heats are evaluated with the EoS model presented in Sec. 2.2. The parameters involved in the critical enhancement model for each of the considered 4 species are reported in Appendix B.

2.3.3 Single species models

It has been pointed out that it is mandatory to describe accurately the transport properties of each single species to obtain an accurate description of the mixture properties. In this framework it is worthwhile to notice that two different kinds of models have been considered in the description of the excess viscosity and conductivity for the 4 species, trying to select for each species the most accurate model available in the open literature. More precisely all the models, except the methane viscosity one, are rational polynomial in the reduced density ($\delta = \rho/\rho_c$) and temperature ($\tau = T_c/T$) which have an expression of the type:

$$\Lambda^r(\tau,\delta) = \sum_{i=1}^{n} N_i \tau^{t_i} \delta^{d_i} \exp(-\gamma_i \delta^{l_i}) \tag{2.70}$$

with N_i, t_i, d_i, l_i and γ_i , with $i = 1, \cdots, n$, parameters fitted to experimental data. More details can be found in the references of Table 2.2

The excess viscosity has been evaluated according to the friction theory presented by Quiñones-Cisneros et al. [128], which relates the viscosity of a fluid to its EoS. In this approach the pressure $p = p(\rho, T)$ is expressed as the sum of a repulsive term p_r and an attractive term p_a:

$$p = p_r + p_a = p^0 + \Delta p_r + p_a \tag{2.71}$$

where $p^0 = \rho RT$ is the perfect gas pressure, and Δp_r is the real part of the repulsive pressure term. Once the pressure and its derivatives are computed the evaluation of p_r, p_a and Δp_r is straightforward:

$$\begin{cases} p_r & = T\left(\dfrac{\partial p}{\partial T}\right)_\rho \\ p_a & = p - p_r \\ \Delta p_r & = p_r - p^0 \end{cases} \tag{2.72}$$

Once these variables have been evaluated, the excess viscosity is obtained by the quadratic expression:

$$\mu_{ex} = c_i p^0 + c_r \Delta p_r + c_a p_a + c_{ii} p_0^2 + c_{rr} \Delta p_r^2 + c_{aa} p_a^2 \tag{2.73}$$

where the c_j and c_{jj} (j being i, a or r) coefficients depend on the reduced temperature $\tau = T_c/T$ and are reported in [128].

Species	Viscosity	Conductivity
Methane	Quiñones-Cisneros et al. [128]	Friend et al. [42]
Nitrogen	Lemmon et al. [85]	Lemmon et al. [85]
Ethane	Friend et al. [43]	Friend et al. [43]
Propane	Vogel et al. [160]	Marsh et al. [93]

Table 2.2: Single species transport property models for the excess viscosity and conductivity

2.3.4 From real fluid to perfect gas

For temperatures between 600 K and 1000 K real and perfect gas transport models equations give slightly different results: following the same procedure adopted for the thermodynamic properties, to pass from one equation to another without discontinuities a linear interpolation between the two equations has been considered when the temperatures fall in this range. An example is given in Fig. 2.10 for the methane viscosity, for a pressure of $p = 13$ MPa. The switch between Klein ECS and perfect gas models takes place at about 900 K without discontinuities.

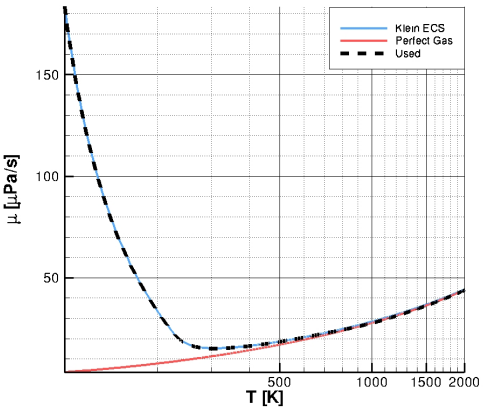

Figure 2.10: CH_4 dynamic viscosity for $p = 13$ MPa

2.3.5 Validation

To validate the models adopted in the transport property description, comparisons with REFPROP-NIST data have been carried out. First the pure fluids models are investigated: in Figs. 2.11-2.14 viscosity and conductivity for each of the 4 species

considered separately are reported for different supercritical pressures. Then mixtures are addressed: in particular viscosity and conductivity are compared for the same mixtures as in the EoS validations. In Figs. 2.15-2.17 results referring to several binary mixtures at a pressure of 13 MPa can be observed, whereas in Fig. 2.18 the transport properties are compared at different pressure for a typical LNG mixture. From the analysis of these figures it can be concluded that the agreement between the present and REFPROP-NIST data is satisfactory

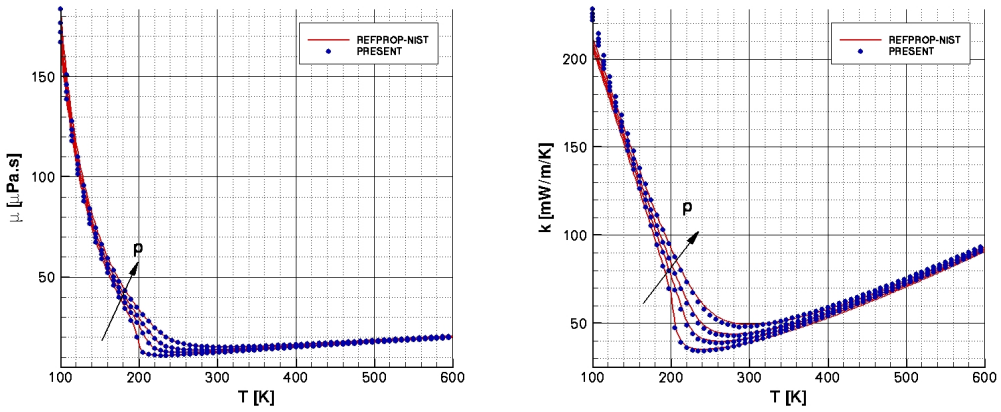

Figure 2.11: Dynamic viscosity and thermal conductivity as function of temperature for different pressures: 6, 8, 10 and 13 MPa. Species: methane.

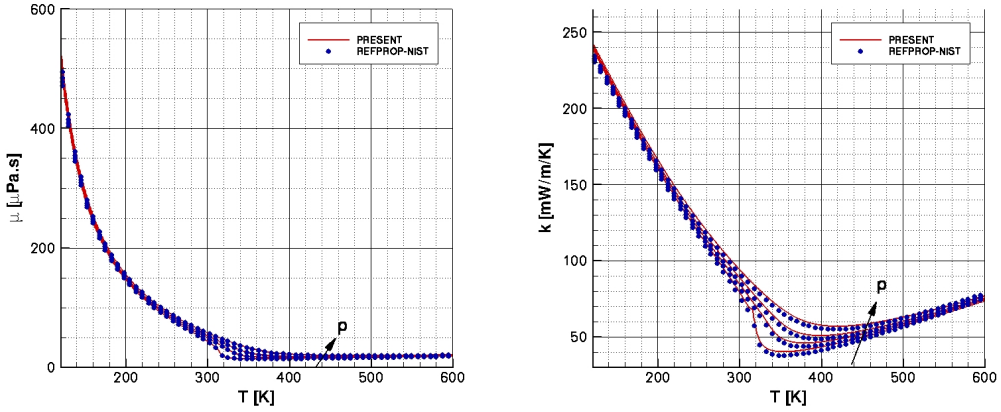

Figure 2.12: Dynamic viscosity and thermal conductivity as function of temperature for different pressures: 6, 8, 10 and 13 MPa. Species: ethane.

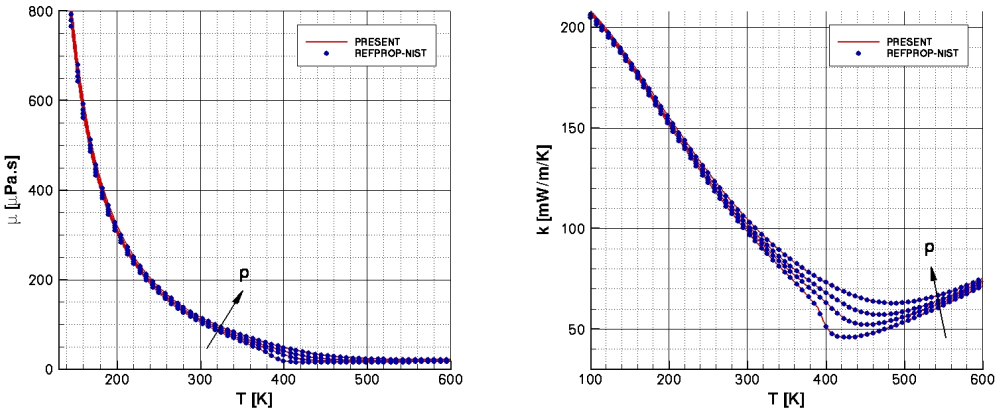

Figure 2.13: Dynamic viscosity and thermal conductivity as function of temperature for different pressures: $6, 8, 10$ and 13 MPa. Species: propane.

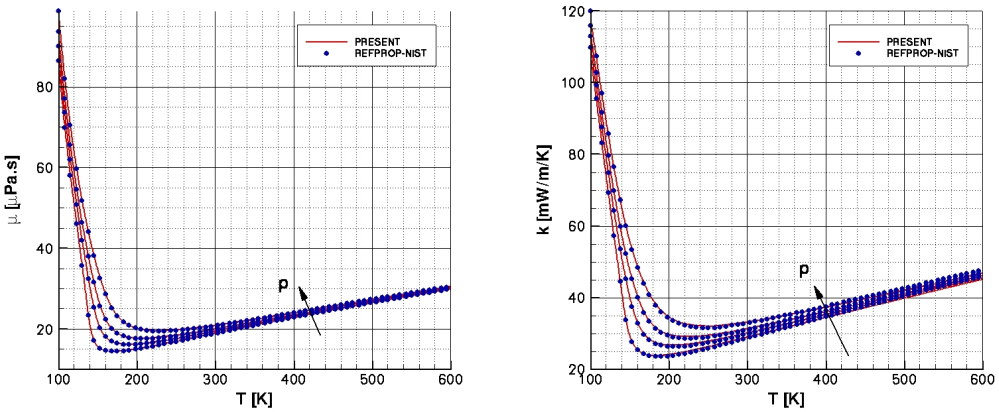

Figure 2.14: Dynamic viscosity and thermal conductivity as function of temperature for different pressures: $6, 8, 10$ and 13 MPa. Species: nitrogen.

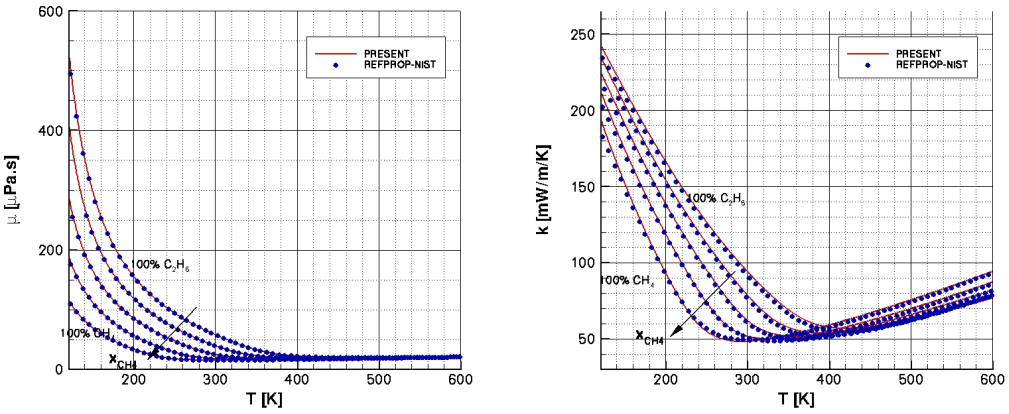

Figure 2.15: Dynamic viscosity and thermal conductivity as a function of temperature for $p = 13$ MPa. Binary mixture: methane-ethane.

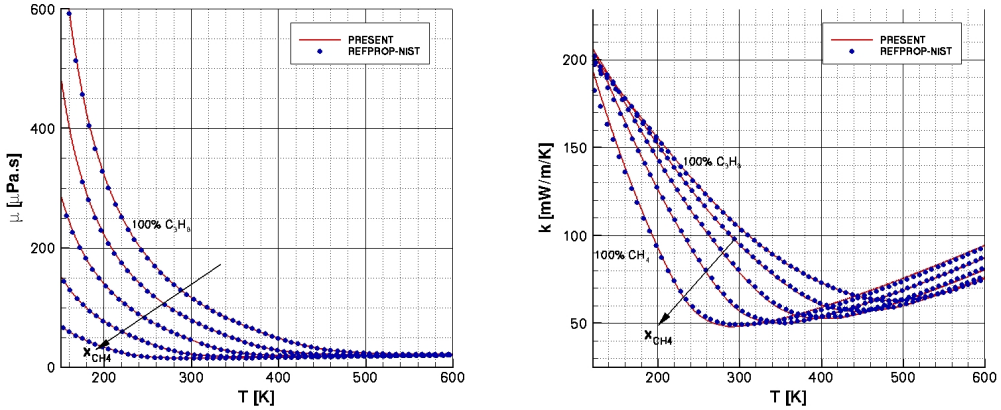

Figure 2.16: Dynamic viscosity and thermal conductivity as a function of temperature for $p = 13$ MPa. Binary mixture: methane-propane.

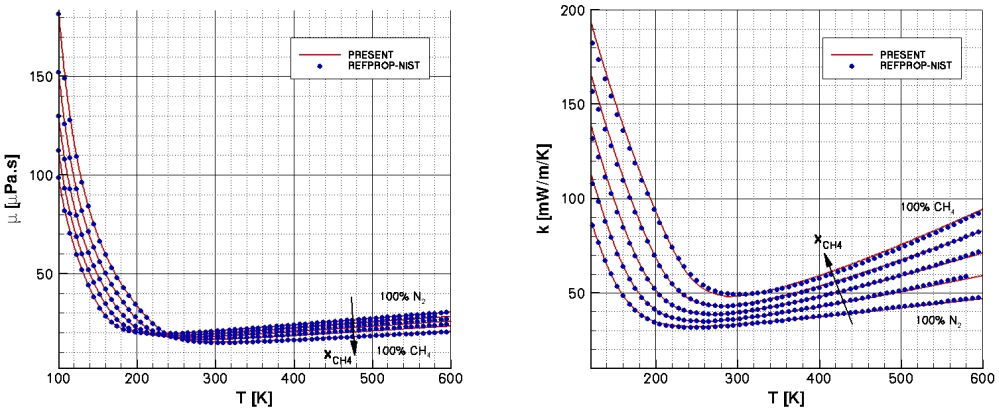

Figure 2.17: Dynamic viscosity and thermal conductivity as a function of temperature for $p = 13$ MPa. Binary mixture: methane-nitrogen.

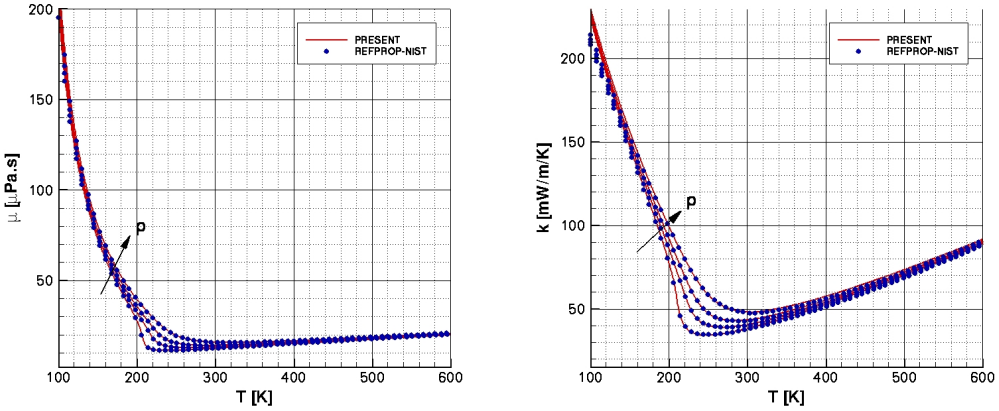

Figure 2.18: Dynamic viscosity and thermal conductivity as a function of temperature for different pressures: $6, 8, 10$ and 13 MPa. LNG composition:$x_{CH_4} = 0.92$, $x_{C_2H_6} = 0.04$, $x_{C_3H_8} = 0.022$ and $x_{N_2} = 0.018$

Chapter 3

Parabolized Navier Stokes equations

A suitable numerical tool has to be developed to carry out the investigations that are the objectives of the work and that have been introduced in Chapter 1. Before developing the numerical code two different aspects have to be analyzed. The first aspect is that the flow of interest is an highly compressible and low Mach number flow. Therefore the numerical model has to be able to handle such kind of flows. The second aspect is the need of a fast but accurate tool to carry out parametric studies. This need has brought to consider parabolized Navier-Stokes (PNS) equations that allow the use of a space marching approach.

In the present chapter first the problem of numerically describe low Mach number flows is introduced. Then attention is devoted to the parabolized Navier-Stokes equations.

3.1 On the numerical analysis of compressible flows with low Mach number

To investigate on the behavior of heated turbulent flows of supercritical fluids in liquid rocket engine cooling channels, a suitable numerical model able to manage its peculiarities has to be found. It is useful therefore to summarize and discuss these peculiarities. From the thermophysical point of view the fluid to be studied is supercritical, with a pressure close to the critical pressure ($p/p_c \sim 2$) and a temperature varying from $T < T_{ps}$ to $T > T_{ps}$, thus spanning a thermodynamic region characterized by steep variations of all the thermophysical properties. In particular, the propellant is a compressed fluid, with a very low compressibility, when it enters the channels. Then it is heated up along the channel and as its temperature increases its compressibility is largely increased: in the neighborhood of the pseudocritical temperature density changes respect to temperature and pressure are very high [46, 84]. The high values of the density gradients $(\partial\rho/\partial p)_T$ and $(\partial\rho/\partial T)_p$ in the transcritical region can be observed in Figs. 3.1(a)-3.1(b) where, for methane, their evolution with temperature have been computed, with the EOS presented in Chap. 2, for different supercritical pressures: as a consequence density strongly vary both with temperature and pressure as shown in Fig. 3.1(c). The high compressibility of the fluid in this

thermodynamic region can also be observed in Fig. 3.1(d) where methane speed of sound evolution with temperature is reported for the different supercritical pressures: a minimum value is reached at the pseudocritical temperature showing that for those thermodynamic conditions the fluid is either more compressible than in a perfect gas condition (reached for higher temperatures). Also the transport properties exhibit strong variations with respect to pressure and density in this region. Even though

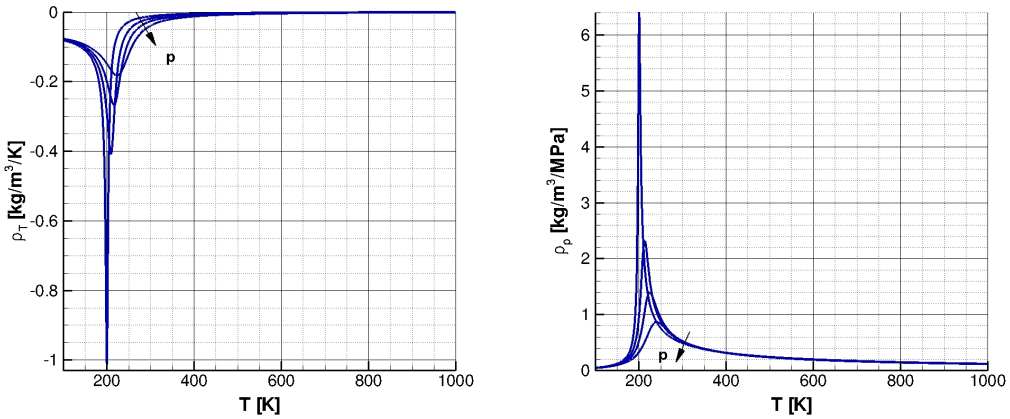

(a) $(\partial\rho/\partial T)_p$

(b) $(\partial\rho/\partial p)_T$

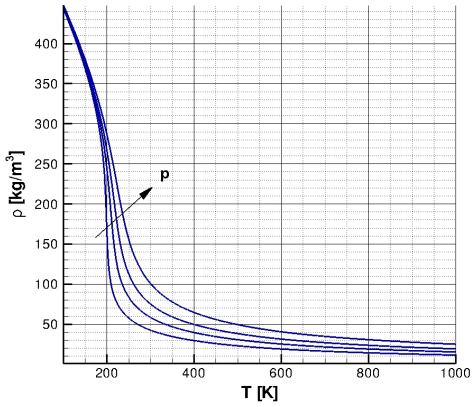

(c) density

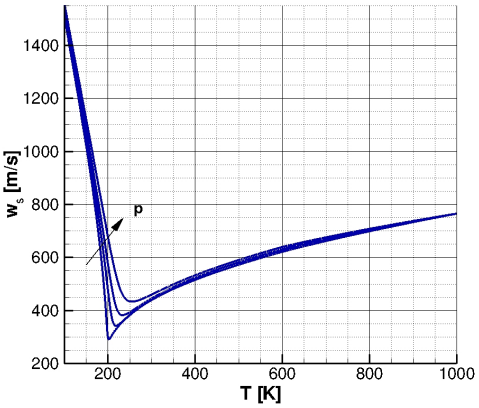

(d) speed of sound

Figure 3.1: Methane density and speed of sound evolution with temperature for different pressure in the range 6-13 MPa

the fluid is highly compressible, it flows in cooling channels with a low velocity, of the order of 10 m/s, and thus is characterized by a low Mach number. It comes out that for this kind of fluid the Mach number is not a suitable parameter to characterize the flow compressibility [98]. Moreover along the channels the heated flow accelerates while the speed of sound decreases thus the Mach number vary along the channel from $M < 0.01$ up to $M \sim 0.3$. To study the present physical problem the numerical tool has to be able to describe very low Mach number flows with a high compress-

ibility which face high density and temperature gradients. Additionally, a desirable feature of the numerical model is the ability to describe flows with a higher Mach number. In fact this could be important in a parametric study. Moreover, being able to investigate a larger range of conditions rather to be limited to a narrow range is a desirable feature for a numerical tool.

The numerical study of low Mach number flows has been deeply investigated in the last thirty years and continue to be an intense research field especially in the case of large density variations. In fact, historically, different computational fluid dynamics models have been developed to study either incompressible ($M = 0$) or high compressible flows ($M > 0.3$) and this because of the different influence of the pressure in these two distinct regimes [10]:

- For incompressible flows the pressure influences the velocity via the momentum equation, whereas the density does not depend on the pressure: following this characteristic **pressure-based** numerical models have been developed;

- For high compressible flows the pressure strongly influences the density via the equation of state: **density-based** numerical models have been initially created to deal with these flows.

If for very low and high Mach number the methods are stable and work well, problems arise in the intermediate Mach number range, that is for $0 < M < 0.3$ where pressure influences both the velocity and the density. This is one of the reasons that has brought to the extension of density-based solvers for low Mach number flows, and pressure-based solvers for weakly compressible low Mach number flows. Another reason that has brought to these attempts is the need of numerical models able to describe large Mach number range flows and also flows with low and high Mach number regions. In the following a brief review of these methods is presented.

3.1.1 Pressure based methods

Pressure based models were developed for incompressible flow problems for which the density is considered constant and hence the continuity equation reduces to the velocity divergence free equation. Hence only pressure and velocity are coupled with the momentum equation. The basic idea of pressure based method is to start with an initial guess for the pressure which permits to find an initial velocity field which will not satisfy the continuity equation [114]. Hence the pressure is iteratively corrected to find the correct velocity. A detailed review of pressure-based algorithms can be found in [10]. The most popular pressure-based method is the pressure-correction SIMPLE algorithm (Semi-Implicit Methods for the Pressure Linked Equations) initially developed by Pantakar [114]: the continuity equation is used to find a pressure correction equation which is solved. The SIMPLE algorithm developed for incompressible flows have be extended to account for compressibility [52, 66, 69]. Pressure based methods use a staggered grid to avoid for check-board pressure solutions and are based on an iterative methodology and this make the algorithm quite complex [126]. Because pressure is used as a primary variable in these methods pressure variations are always finite irrespective of the flow Mach number.

3.1.2 Density based methods

Density based methods have been originally developed to deal with high compressible flows. The continuity equation is regarded as an evolution equation for the density which is related to the pressure and temperature with an equation of state. It has been largely proved in the literature that these methods suffer from accuracy and convergence problems when the Mach number is lowered and cannot be applied (without some modifications) if $M < 0.3$. From the accuracy point of view it has been demonstrated that for a fixed mesh size, the error is proportional to $1/M^2$ when lowering the Mach number toward a 0 value [104, 161]: this error can be reduced lowering the mesh size but this also brings to very long computational time because of the corresponding reduced iteration time step. Guillard and Viozat [49] explained the accuracy problem showing that there is a different behavior of the discretized and continue Navier-Stokes equations in the limit $M \to 0$. In particular while it is well known that for $M \to 0$ the pressure perturbations are $O(M^2)$, the discretized equations result in pressure perturbations of the order $O(M)$. Differently the convergence problem arises from the stiffness of the problem which is ill-conditioned because of the large difference between the eigenvalues: from a physical point of view this reflects the presence of high speed acoustic waves traveling with a velocity $u + w_s$, w_s being the sound speed and u the fluid velocity and for low Mach number flows ($M = u/w_s \ll 1$) it is $u \ll u + w_s$. As a consequence very small iteration time steps are used with a deterioration of the convergence.

Preconditioning techniques have been largely applied to extend density based methods to low Mach number problems. The basic idea is to reduce the stiffness: this is obtained by premultiplying the Jacobian matrix by a preconditioning matrix so as to obtain all the eigenvalues of the same order. As explained by Turkel [153] let us consider an ill-conditioned algebraic system:

$$Av = b \tag{3.1}$$

where A is positive definite and has a very large condition number $k(A) = max\dfrac{\lambda_i}{\lambda_j}$, with λ_i eigenvalues of A. If we premultiply left and right hand side of Eq. (3.1) by a non singular matrix P we obtain the following system:

$$PAv = Pb \tag{3.2}$$

which is equivalent to Eq. (3.1) and so have the same solution. If P is chosen so as to obtain $k(PA) << k(A)$ then the problem will not be stiff anymore: P is called the preconditioning matrix. To extend density based methods to low compressible flows, preconditioning is applied to the flux Jacobian matrix [13, 153] and the preconditioning matrix can be chosen to permit an accurate description both of compressible and incompressible flows [98, 164]. For stability reasons preconditioning schemes have to be implicit.

3.1.3 Asymptotic analysis

The asymptotic analysis of the Navier-Stokes equations when $M \to 0$ brings to the identification of different terms in the pressure. In particular following a single scale

asymptotic analysis (in time and in space) [104] the pressure can be expressed as:

$$p(x,t) = p_0(t) + \tilde{M}^2 p_2(x,t) + O(\tilde{M}^3) \tag{3.3}$$

with $p_0(t) = O(1)$ and $\tilde{M} \propto M$. The leading pressure term $p_0(t)$ is called the *thermodynamic pressure* and only depends on the time t whereas $p' = \tilde{M}^2 p_2$ is the very low *incompressible pressure* which varies both with time t and in the space x. Thus the pressure gradient Δp in the momentum equation reduces to the incompressible pressure gradient $\Delta p'$. With the same analysis the conservative variables can be expressed in the low Mach number limit as the sum of a stagnation term and a perturbation term. Following this analysis *perturbation techniques* to extend density based methods to low Mach number, have been developed: the Navier-Stokes equations are reformulated in terms of the perturbed variables thus avoiding the stiffness problem [29, 71, 152]. Also *multi pressure variables* methods are developed following the pressure asymptotic decomposition: the basic idea is that the different pressure terms are accounted separately, and for example only the incompressible pressure will appear in the momentum equation [105, 133] whereas the thermodynamic pressure has to satisfy the equation of state.

3.2 Selection of a space marching technique

Difficulties in dealing with low Mach number flows with compressibility effects, like transcritical fluids flowing in cooling channels are, have been pointed out in the previous section. These aspects have to be taken into consideration in the development of the numerical code. Other aspects characterizing cooling channel flows are presently considered. Cooling channels have a long length with respect to their section and no reverse flow is expected because the streamwise velocity is always a positive quantity and much greater than the crosswise velocity. Moreover, we are interested in steady state flows. Considering these features reduced forms of the Navier-Stokes equations can be taken into consideration. In fact streamwise diffusion of momentum and energy can be neglected for the present cooling channels, so as to obtain the so-called *parabolized Navier-Stokes equations*. The interest in considering such reduced system is that it can be numerically solved with a space marching approach, if the streamwise pressure gradient is suitably treated, thus alloying a simplification on the problem. In the following first a literature review on numerical methods for PNS is carried out. It will come out that the same methods applied for full Navier-Stokes equations (FNS) are used for PNS. In particular pressure-based methods are usually used for incompressible flows whereas density based methods are used for compressible flows. A mathematical formulation of the system of equations presently considered is then done together with the demonstration of the hyperbolic nature of the system Eulerian part.

3.2.1 Literature review on PNS numerical methods

Parabolized Navier-Stokes equations have been introduced in the literature since the seventies to describe both subsonic-incompressible and supersonic-hypersonic flows. Several methodologies have been developed and all the approaches share three common characteristics:

- the steady form of the governing equations is employed;
- streamwise diffusive terms are neglected;
- some assumptions have to be made to treat the streamwise pressure gradient in the subsonic region.

With these assumptions the solution can be "marched" in space, so that a typical problem is reduced from four (three space dimensions and time) to three dimensions. PNS equations are suitable to describe flows with a predominant direction, but for which crosswise momentum equation is important as for example channel flows with curvature or high crosswise gradients of the thermodynamic properties, or external supersonic flows for which the interaction between inviscid flow and boundary layer is important. For this kind of flows boundary layer equations are not suitable because they require that the crosswise momentum equation reduces to $\partial p/\partial y = 0$. PNS equations are intermediate between full Navier-Stokes equations (FNS) and boundary-layer equation (BL). Nevertheless, BL numerical methods cannot be applied to PNS, rather FNS methods have to be suitably modified to solve PNS. Therefore for PNS different approaches have been developed to describe incompressible and weakly compressible or supersonic-hypersonic flows, as for FNS. Consequently a first classification can be made between pressure-based PNS solvers developed for incompressible flows and density-based approaches for highly compressible flows.

Incompressible and subsonic flows

Implicit pressure-based algorithms developed to solve PNS equations for subsonic flows differ in the way the pressure gradient is treated. As it will be mathematically pointed out in the following, once the streamwise diffusion terms have been neglected, the streamwise pressure gradient is the only elliptic term which permits information to propagate from downstream to upstream and hence must be suitable treated to permit a space marching approach. If the pressure gradient is somehow assigned, *initial value methods*, also referred as fully parabolic methods, are developed for which the solution is obtained marching from initial values until the end of the domain is reached. Conversely for *global iteration methods* referred to as Partially Parabolized Navier-Stokes (PPNS) the streamwise pressure gradient is an unknown: iteration algorithms are used for which multiple domain sweeps are necessary until convergence is reached [77, 114, 147].

Pantakar and Spalding [117] were among the first to introduce a fully parabolic algorithm to describe laminar incompressible, internal and external flows. They assume that the streamwise pressure gradient $d\overline{p}/dx$ is constant in the crosswise direction and evaluate it separately imposing the mass conservation for internal flows, or from the inviscid external solution for external flows. Differently none assumption is made on the crosswise pressure gradients $\partial p/\partial y$ and $\partial p/\partial z$, which are included in the equations and permit a pressure variation in crosswise planes. To allow the description of curved geometries, Briely [16] further divided the pressure in multiple contributions: an inviscid pressure field is obtained from a potential flow solution through the given geometry, which is then corrected with the viscous pressure field. This last field is calculated with the space marching algorithm in which streamwise and pressure gradients are treated separately following Pantakar and Spalding approach.

Starting from this basic idea of dividing the solution in a viscous and inviscid part, primary-secondary flows algorithms were developed afterward and largely employed in particular to describe situations with large secondary flows [17, 47, 77, 87].

Global iteration methods have been developed [28, 106]: in these approaches the equations are only *partially* parabolized because the elliptic influence has been only partially eliminated neglecting streamwise diffusion terms while upstream influences can still be transmitted through the pressure field. Hence in global iterations methods an initial pressure field is prescribed, and multiple sweeps of a marching integration method across the domain are carried out until the correct pressure field is reached.

Although simpler than the corresponding FNS, these parabolic pressure based algorithm are computationally heavy because of the sequential solving of the equations which are then coupled. Differently, space-marching methods developed for supersonic flows solve the governing equations in steady form as a coupled system by marching in space in the streamwise direction. These methods are economical, elegant and straightforward. For these reasons Pougare and Lakshminarayana [124] developed a method for incompressible flows based on ideas used in space-marching methods for supersonic flows with the pressure streamwise gradient treated as a source term evaluated from an inviscid solution of the flow field.

Regarding LRE cooling channels, Frölich et al [11] developed a suitable code based on the SIMPLE algorithm adapted to a co-located variable arrangement: numerical results obtained with this tool were validated against experimental and other numerical results [81] demonstrating the validity of the PNS approach to study cooling channels configurations.

Supersonic and hypersonic flows

Also for supersonic flows parabolic methods, more often referred as space marching methods, where developed mostly for external flows: a complete review of these methods can be found in the work of Rubin at al. [137] and in Chapter 8 of the text by Tannehill et al. [147]. Initially these methods were introduced to compute supersonic flows over circular cones at angle of attack, and then have been extended for generic shapes [159]. For supersonic flows the streamwise pressure gradient problem comes out only in the confined subsonic regions near the wall. Where the flow is supersonic neglecting streamwise diffusion is sufficient to the flow to be parabolic and the solution can be marched in space. Conversely if the flowfield includes subsonic regions the pressure gradient must be correctly handled. The common applied strategy follows Vigneron et al. analysis [159] which demonstrates that if only a portion of the streamwise gradient is retained in the equations the system is still well posed for a space marching resolution technique. The remaining streamwise pressure gradient is usually neglected [35, 159] or evaluated with a backward difference [44]. However, different studies have demonstrated that a backward difference gives stability problems unless the space marching step is greater than a minimum value, which is in contrast with the CFL requirement condition [75, 147]. Because of the hyperbolic-parabolic nature of PNS equations upwind schemes have been efficiently applied. Initially a switch between central differences and upwind differences were made passing from subsonic to supersonic regions [80], then methods based on upwind schemes in all the flow regions where developed. In particular, schemes based on the Roe's approximate Riemann solver for a perfect gas can be found [75, 162] as well as the essentially non

oscillatory (ENO) scheme based on a linearized approximated Riemann solver [35]. Moreover, also finite volume schemes based on unsteady Riemann problems have been developed [44]: the invariants and characteristics directions are obtained from unsteady Euler equations, though they are not consistent with the equations that are actually integrated. Real gas effects have also be taken into account in few works: Vigneron analysis has been extended to chemically reacting flows [19, 36, 148] and Gerbsh et al. [44] scheme is based on a general equation of state.

3.3 Parabolized Navier-Stokes equations

Before mathematically approaching the equations let us briefly outline what is meant by parabolized Navier-Stokes equations (PNS). In appendix C the mathematical definitions of the terms elliptic, parabolic, hyperbolic can be found. These concepts are here applied to the Navier-Stokes equations. The steady state full Navier-Stokes equations (FNS) for subsonic flows form an elliptic-parabolic system: all the variables in a certain point depend upon the solution in the whole integration domain. Let us consider a channel flow with a length much longer than the hydraulic diameter and a streamwise velocity which is much greater than the crosswise velocity and always positive. In these conditions the diffusive effect in the streamwise direction is negligible compared to the convective effect therefore diffusive terms do not influence the solution and they can be neglected. Because the flow is subsonic, pressure waves traveling with the speed of sound are faster than the fluid velocity and this permits the information to travel also upstream. If the evolution of the pressure along the streamwise direction is supposed to be known then the solution in a point will depend only on upstream influence and the system is said to be parabolized in the streamwise direction. Parabolized Navier-Stokes equations are a mixed hyperbolic-parabolic system in the streamwise direction. This means that, with suitable initial and boundary conditions, the mathematical problem is well posed for a space marching solution methodology in the streamwise direction.

3.3.1 From full Navier-Stokes to parabolized Navier-Stokes equations

In the following the mathematical passages that permit to obtain the parabolized Navier-Stokes equations for channel flows are reported. For the sake of clarity the equation are written considering a Cartesian reference system (x, y, z) but all the reasoning that follows can be equally carried out in generalized coordinates. The three dimensional Navier-Stokes equations for a steady state flow can be written in the following conservative form:

$$\frac{\partial \mathbf{F_e}}{\partial x} - \frac{\partial \mathbf{F_v}}{\partial y} + \frac{\partial \mathbf{G_e}}{\partial y} - \frac{\partial \mathbf{G_v}}{\partial y} + \frac{\partial \mathbf{H_e}}{\partial z} - \frac{\partial \mathbf{H_v}}{\partial z} = \mathbf{Q} \tag{3.4}$$

where the subscripts $()_e$ and $()_v$ indicate the Eulerian and viscous flux vectors, respectively. A source term vector $\mathbf{Q}$ has been emphasized in Eq. (4.1) for the sake of

generality. The expressions of the flux vectors are:

$$\mathbf{F_e} = \begin{Bmatrix} \rho u \\ \rho u^2 + p \\ \rho uv \\ \rho uw \\ \rho u h_0 \end{Bmatrix} \qquad \mathbf{G_e} = \begin{Bmatrix} \rho v \\ \rho uv \\ \rho v^2 + p \\ \rho vw \\ \rho v h_0 \end{Bmatrix} \qquad \mathbf{H_e} = \begin{Bmatrix} \rho w \\ \rho uw \\ \rho vw \\ \rho w^2 + p \\ \rho w h_0 \end{Bmatrix} \tag{3.5}$$

$$\mathbf{F_v} = \begin{Bmatrix} 0 \\ \frac{2}{3}\mu\left(2\frac{\partial u}{\partial x} - \frac{\partial v}{\partial y} - \frac{\partial w}{\partial z}\right) \\ \mu\left(\frac{\partial u}{\partial y} + \frac{\partial v}{\partial x}\right) \\ \mu\left(\frac{\partial u}{\partial z} + \frac{\partial w}{\partial x}\right) \\ uF_{v,2} + vF_{v,3} + wF_{v,4} + k\frac{\partial T}{\partial x} \end{Bmatrix} \tag{3.6}$$

$$\mathbf{G_v} = \begin{Bmatrix} 0 \\ \mu\left(\frac{\partial u}{\partial y} + \frac{\partial v}{\partial x}\right) \\ \frac{2}{3}\mu\left(2\frac{\partial v}{\partial y} - \frac{\partial u}{\partial x} - \frac{\partial w}{\partial z}\right) \\ \mu\left(\frac{\partial v}{\partial z} + \frac{\partial w}{\partial y}\right) \\ uG_{v,2} + vG_{v,3} + wG_{v,4} + k\frac{\partial T}{\partial y} \end{Bmatrix} \quad \mathbf{H_v} = \begin{Bmatrix} 0 \\ \mu\left(\frac{\partial u}{\partial z} + \frac{\partial w}{\partial x}\right) \\ \mu\left(\frac{\partial v}{\partial z} + \frac{\partial w}{\partial y}\right) \\ \frac{2}{3}\mu\left(2\frac{\partial w}{\partial z} - \frac{\partial v}{\partial y} - \frac{\partial w}{\partial z}\right) \\ uH_{v,2} + vH_{v,3} + wH_{v,4} + k\frac{\partial T}{\partial z} \end{Bmatrix} \tag{3.7}$$

In the above flux vectors u,v and w are the components of the velocity in x, y and z directions respectively; ρ is the density, T is the temperature and p is the pressure; μ and k are the dynamic viscosity and thermal conductivity; h_0 is the total enthalpy defined by:

$$h_0 = h + \frac{u^2}{2} + \frac{v^2}{2} + \frac{w^2}{2} \tag{3.8}$$

The Navier-Stokes equations system (3.4) can be used to describe the flow in a cooling channel. So a straight channel of length L and hydraulic diameter D, with the streamwise direction aligned with the x coordinate, is presently taken into consideration. A schematic of the channel is shown in Fig. 3.2.

Assuming that it is $L >> D$ and $u >> v$ (u always positive) a dimensional analysis of the equation system (3.4) can be carried out defining the following non dimensional quantities:

$$\bar{\rho} = \frac{\rho}{\rho_r}\,,\ \bar{u} = \frac{u}{u_r}\,,\ \bar{v} = \frac{v}{v_r}\,,\ \bar{w} = \frac{w}{w_r}\,,\ \bar{p} = \frac{p}{\rho_r u_r^2}\,,\ \bar{\mu} = \frac{\mu}{\mu_r}\,, \tag{3.9}$$

$$\bar{x} = \frac{x}{L}\,,\ \bar{y} = \frac{y}{D}\,,\ \bar{z} = \frac{z}{D} \tag{3.10}$$

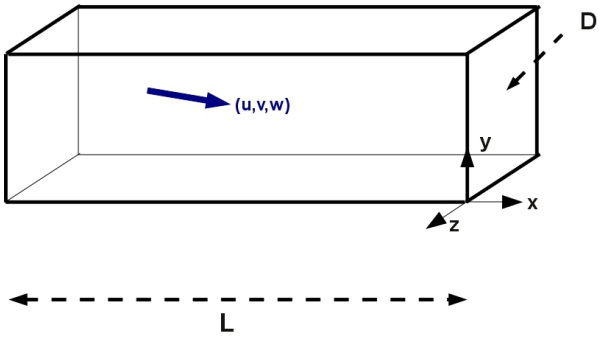

Figure 3.2: Integration domain: straight channel with $L >> D$ and $u >> v$, $u >> v$

where the reference quantities have been indicated with subscript r and non dimensional quantities with an overbar. Reference quantities are chosen so as to obtain non dimensional quantities of order $O(1)$. With this reference quantities let us consider the non dimensional form of the first momentum equation of Eq.(3.4) having multiplied by the factor $\dfrac{LD}{u_r \mu_r}$:

$$\begin{aligned} &\frac{\rho_r u_r D}{\mu_r}\left(\frac{\partial(\bar{\rho}\bar{u}^2)}{\partial\bar{x}}+\frac{\partial\bar{p}}{\partial\bar{x}}+\frac{v_r}{u_r}\frac{L}{D}\frac{\partial(\rho\bar{u}\bar{v})}{\partial\bar{y}}+\frac{w_r}{u_r}\frac{L}{D}\frac{\partial(\bar{\rho}\bar{u}\bar{w})}{\partial\bar{z}}\right)- \\ &\mu\left(\frac{4}{3}\frac{D}{L}\frac{\partial^2\bar{u}}{\partial\bar{x}^2}+\frac{L}{D}\frac{\partial^2\bar{u}}{\partial\bar{y}^2}+\frac{L}{D}\frac{\partial^2\bar{u}}{\partial\bar{z}^2}+\frac{1}{3}\frac{v_r}{u_r}\frac{\partial^2\bar{v}}{\partial\bar{x}\partial\bar{y}}+\frac{1}{3}\frac{w_r}{u_r}\frac{\partial^2\bar{w}}{\partial\bar{x}\partial\bar{z}}\right)=0 \end{aligned} \tag{3.11}$$

The Reynolds number based on the channel diameter $Re = \dfrac{\rho_r u_r D}{\mu}$, appears in the convective terms: we recall that for the flow of interest we have high Reynolds numbers of the order of $10^5 - 10^6$. On the other hand we can introduce the little parameter ϵ defined as the order of the ratio D/L. Let us analyze the order of the other non dimensional numbers appearing in Eq. (3.11). We can suppose that the ratio between crosswise and streamwise velocities is at least of order $O(\epsilon)$ or even smaller. With this assumption it results that:

- $\dfrac{v_r}{u_r}\dfrac{L}{D} = O(1)$ and $\dfrac{w_r}{u_r}\dfrac{L}{D} = O(1)$
  hence all the convective terms are multiplied by Re
- $\dfrac{D}{L} = O(\epsilon)$
- $\dfrac{L}{D} = O\left(\dfrac{1}{\epsilon}\right)$
- $\dfrac{v_r}{u_r} = O(\epsilon)$ and $\dfrac{w_r}{u_r} = O(\epsilon)$

So with the above hypothesis this analysis indicates that the terms of order $O(\epsilon)$, which are all the diffusive terms that involve a streamwise derivative, can be neglected

in a first approximation. The same non dimensional analysis can be carried out for all the equations and leads to similar results. Neglecting all the streamwise derivatives in the viscous fluxes of Eq. (3.4), the following simplified system is obtained:

$$\frac{\partial \mathbf{F_e}}{\partial x} + \frac{\partial \mathbf{G_e}}{\partial y} - \frac{\partial \mathbf{G_v}}{\partial y} + \frac{\partial \mathbf{H_e}}{\partial z} - \frac{\partial \mathbf{H_v}}{\partial z} = \mathbf{Q} \tag{3.12}$$

where $\mathbf{F_v}$ is no longer present and the $\mathbf{G_v}$ and $\mathbf{H_v}$ viscous fluxes are simplified as follows:

$$\mathbf{G_v} = \begin{Bmatrix} 0 \\ \mu \dfrac{\partial u}{\partial y} \\ \dfrac{2}{3}\mu \left(2\dfrac{\partial v}{\partial y} - \dfrac{\partial w}{\partial z} \right) \\ \mu \left(\dfrac{\partial v}{\partial z} + \dfrac{\partial w}{\partial y} \right) \\ uG_{v,2} + vG_{v,3} + wG_{v,4} + k\dfrac{\partial T}{\partial y} \end{Bmatrix} \quad \mathbf{H_v} = \begin{Bmatrix} 0 \\ \mu \dfrac{\partial u}{\partial z} \\ \mu \left(\dfrac{\partial v}{\partial z} + \dfrac{\partial w}{\partial y} \right) \\ \dfrac{2}{3}\mu \left(2\dfrac{\partial w}{\partial z} - \dfrac{\partial v}{\partial y} \right) \\ uH_{v,2} + vH_{v,3} + wH_{v,4} + k\dfrac{\partial T}{\partial z} \end{Bmatrix} \tag{3.13}$$

The main question at this point is to understand what is the mathematical nature of the reduced Navier-Stokes equation system (3.12). As it will be mathematically demonstrated in the following, system (3.12) is an hyperbolic-parabolic system only for supersonic flows. For subsonic flows the streamwise pressure gradient permits information to propagate upstream and therefore the system is elliptic. Nevertheless Vigneron et al. [159] showed that if only a fraction ω ($0 \leq \omega \leq 1$) of the streamwise pressure gradient ($\partial p/\partial x$) is retained in the equations, the system becomes hyperbolic-parabolic in the streamwise direction also in the case of subsonic flows. This is done by splitting the pressure term in the Eulerian flux $\mathbf{F_e}$ in two parts:

$$p = \omega p + (1 - \omega)p \tag{3.14}$$

Then ωp is retained in $\mathbf{F_e}$ whereas $(1-\omega)p$ is considered as a source term thus yielding to the following system:

$$\frac{\partial \overline{\mathbf{F}}_\mathbf{e}}{\partial x} + \frac{\partial \mathbf{G_e}}{\partial y} - \frac{\partial \mathbf{G_v}}{\partial y} + \frac{\partial \mathbf{H_e}}{\partial z} - \frac{\partial \mathbf{H_v}}{\partial z} = \mathbf{Q} + \frac{\partial \mathbf{P}}{\partial x} \tag{3.15}$$

The vectors $\overline{\mathbf{F}}_\mathbf{e}$ and $\mathbf{P}$ are given by:

$$\overline{\mathbf{F}}_\mathbf{e} = \begin{Bmatrix} \rho u \\ \rho u^2 + \omega p \\ \rho uv \\ \rho uw \\ \rho u h_0 \end{Bmatrix} \qquad \mathbf{P} = \begin{Bmatrix} 0 \\ (\omega - 1)p \\ 0 \\ 0 \\ 0 \end{Bmatrix} \tag{3.16}$$

Vigneron et al. [159] carried out an eigenvalues analysis on system (3.15) with the simplified assumption of calorically and thermally perfect gas with constant transport properties and showed that the system is hyperbolic-parabolic if:

- $\omega < \dfrac{\gamma M_x^2}{1+(\gamma-1)M_x^2} < 1$ for $M_x < 1$ and $\omega = 1$ for $M_x \geq 1$, with $M_x = u/w_s$. Hence all the pressure can be included in $\overline{\mathbf{F}}_\mathbf{e}$ for supersonic flows ($\omega = 1$) whereas only a portion can be considered for subsonic flows. Moreover it comes out that in the incompressible limit ($M_x \to 0$) all the pressure gradient must be in the source term ($\omega = 0$)
- $u > 0$ that is no reverse flow occurs. This condition is essential to have non negative viscous eigenvalues and thus a dumping effect for a positive viscosity.

If these conditions are verified the inviscid eigenvalues are all real, and viscous eigenvalues are real and non negative. This analysis has been extended for chemically reacting flows [36] and real gas described by a generic equation of state [44]: the resulting constraint on ω is still the same replacing γ by a parameter depending on the equation of state. In the present work an eigenvalues analysis has also been carried out to verify what is the constraint on ω for a real gas. In particular the hyperbolic nature of the PNS system has been addressed considering the Eulerian part of the PNS system (3.15). The existence of characteristic directions is demonstrated in a two dimensional case. A generic equation of state is considered $h = h(p, \rho)$, which permits to extend the results to any kind of EoS. The main results are reported in this chapter whereas a detailed demonstration can be found in Appendix D. Let us consider the following system:

$$\frac{\partial \overline{\mathbf{F}}_\mathbf{e}}{\partial x} + \frac{\partial \mathbf{G}_\mathbf{e}}{\partial y} = 0 \tag{3.17}$$

where the two dimensional Eulerian fluxes are given by:

$$\overline{\mathbf{F}}_\mathbf{e} = \begin{Bmatrix} \rho u \\ \rho u^2 + \omega p \\ \rho uv \\ \rho u h_0 \end{Bmatrix} \qquad \mathbf{G}_\mathbf{e} = \begin{Bmatrix} \rho v \\ \rho uv \\ \rho v^2 + p \\ \rho v h_0 \end{Bmatrix} \tag{3.18}$$

The system (3.17) can be written in quasi linear form introducing the Jacobian matrix of the fluxes with respect to the primitive variable vector $\mathbf{V}$ defined by:

$$\mathbf{V} = \begin{Bmatrix} \rho \\ u \\ v \\ p \end{Bmatrix} \tag{3.19}$$

The Jacobian matrix of the fluxes are:

$$\mathbf{B} = \frac{\partial \overline{\mathbf{F}}_\mathbf{e}}{\partial \mathbf{V}} = \begin{pmatrix} u & \rho & 0 & 0 \\ u^2 & 2\rho u & 0 & \omega \\ uv & \rho v & \rho u & 0 \\ u(h_0 + \rho h_\rho) & \rho(h_0 + u^2) & \rho uv & \rho u h_p \end{pmatrix} \tag{3.20}$$

$$\mathbf{C} = \frac{\partial \mathbf{G}_\mathbf{e}}{\partial \mathbf{V}} = \begin{pmatrix} v & 0 & \rho & 0 \\ uv & \rho v & \rho u & 0 \\ v^2 & 0 & 2\rho v & 1 \\ v(h_0 + \rho h_\rho) & \rho uv & \rho(h_0 + v^2) & \rho v h_p \end{pmatrix} \tag{3.21}$$

where the following contracted notations for the thermodynamic derivatives have been used:

$$\begin{aligned} h_p &= \left(\frac{\partial h}{\partial p}\right)_\rho \\ h_\rho &= \left(\frac{\partial h}{\partial \rho}\right)_p \end{aligned} \tag{3.22}$$

Hence, defining the matrix $\mathbf{A_v} = \mathbf{B^{-1}C}$, the system (3.17) can be written in a quasi linear form:

$$\frac{\partial \mathbf{V}}{\partial x} + \mathbf{A_v}\frac{\partial \mathbf{V}}{\partial y} = 0 \tag{3.23}$$

To understand the mathematical nature of this system $\mathbf{A_v}$ eigenvalues must be calculated solving the problem:

$$det(\mathbf{A_v} - \lambda \mathbf{I}) = 0 \tag{3.24}$$

where $\mathbf{I}$ is the identity matrix and λ the generic eigenvalue. This problem is equivalent to:

$$det(\mathbf{C} - \lambda \mathbf{B}) = 0 \tag{3.25}$$

which will be considered. Two parameters are introduced for the clearness of notation:

$$\hat{x} = \rho h_p \qquad \hat{y} = \rho h_\rho \tag{3.26}$$

Hence the computed four eigenvalues are:

$$\lambda_{1,2} = \frac{v}{u} \qquad \lambda_{3,4} = \frac{[2\hat{x} - (\omega + 1)]uv \pm \sqrt{\Delta}}{2[(\hat{x} - \omega)u^2 + \omega\hat{y}]} \tag{3.27}$$

with Δ given by:

$$\Delta = (\omega - 1)^2 u^2 v^2 - 4[(\hat{x} - \omega)u^2 + \omega(\hat{x} - 1)v^2]\hat{y} - 4\omega\hat{y}^2 \tag{3.28}$$

The system is hyperbolic if all the eigenvalues are real. $\lambda_{1,2}$ are always real and are defined if $u \neq 0$: this last condition is included in the previous hypothesis $u > 0$. The two others eigenvalues $\lambda_{3,4}$ are real if Δ is positive and hence its sign must be investigated. First the hypothesis $u \gg v$ can be used to simplify the expression of Δ, neglecting the terms multiplied by the crosswise velocity v thus yielding to:

$$\Delta \backsimeq -4y[(\hat{x} - \omega)u^2 + \omega\hat{y}] \tag{3.29}$$

Furthermore using some basic thermodynamic relations it can be shown that:

$$\begin{aligned} \hat{x} &= \rho e_p + 1 \\ \hat{y} &= -w_s^2 \rho e_p \end{aligned} \tag{3.30}$$

where w_s is as usual the speed of sound, and $e_p = \left(\frac{\partial e}{\partial p}\right)_\rho$. Thus the sign of $\hat{y}$ is related to the sign of e_p which can also be expressed as:

$$e_p = \frac{c_v}{\left(\frac{\partial p}{\partial T}\right)_\rho} \tag{3.31}$$

where c_v is the specific heat at constant volume which is always positive. Also the derivative $\left(\frac{\partial p}{\partial T}\right)_\rho$ is a positive quantity for any generic equation of state. To confirm this obvious statement the computed above derivative with the thermodynamic models presented in Chap. 2 is reported in Fig. 3.3 versus temperature for different supercritical pressures. The temperature range covers different regimes going from the liquid-like condition to perfect gas condition, and the observed quantity is always positive.

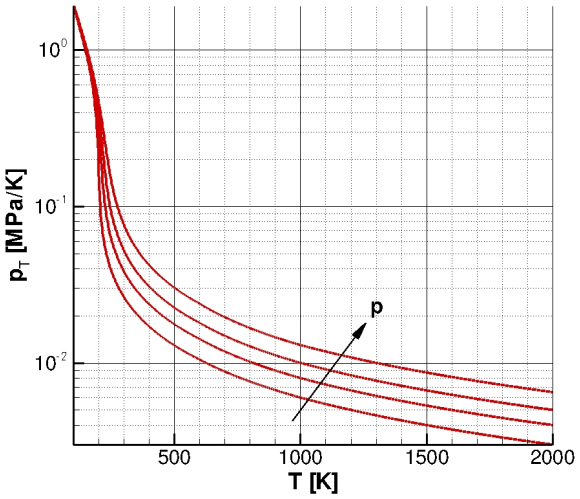

Figure 3.3: Evolution of $\left(\frac{\partial p}{\partial T}\right)_\rho$ with the temperature for different supercritical pressures (6 MPa$< p <$ 13 MPa) for methane. (logarithmic scale)

The previous conditions imply that $\hat{y} < 0$. Thus Δ is positive if the term between square brackets in Eq. (3.29) is positive which reduces to the following condition on ω:

$$\omega < \frac{[1 + \rho e_p] M_x^2}{M_x^2 + \rho e_p} \tag{3.32}$$

where $M_x = u/w_s$ is the Mach number in the streamwise direction. This condition is equivalent to the perfect gas one if γ is replaced with an equivalent parameter defined as:

$$\overline{\gamma} = 1 + \frac{1}{\rho e_p} \tag{3.33}$$

The internal energy derivative e_p is always positive and hence it results that the right hand side of Eq. (3.32) is always positive. Moreover it is an increasing function of the Mach number and it tends towards zero when $M_x \to 0$. Hence, despite the foregoing demonstration that would allow to retain part of the pressure gradient in the Eulerian flux, considering that we are interested in very low Mach number flows, in the present approach the ω parameter has been taken null. Therefore the streamwise pressure gradient is considered as a source term and so the expressions of $\overline{\mathbf{F}}_\mathbf{e}$ and $\mathbf{P}$

in Eq. (3.15) become:

$$\overline{\mathbf{F}}_{\mathbf{e}} = \begin{Bmatrix} \rho u \\ \rho u^2 \\ \rho uv \\ \rho uw \\ \rho u h_0 \end{Bmatrix} \qquad \mathbf{P} = \begin{Bmatrix} 0 \\ -p \\ 0 \\ 0 \\ 0 \end{Bmatrix} \tag{3.34}$$

With these expressions Eq. (3.15) is a hyperbolic-parabolic system that can be called a system of Parabolized Navier-Stokes equations (PNS) in the streamwise direction. The corresponding eigenvalues can be obtained replacing $\omega = 0$ in Eq. (3.27):

$$\lambda_{1,2} = \frac{v}{u} \qquad \lambda_{3,4} = \frac{[2\hat{x} - 1]\, v \pm \sqrt{\Delta}}{2\hat{x}u} \tag{3.35}$$

with Δ given by:

$$\Delta = v^2 - 4\hat{x}\hat{y} \tag{3.36}$$

As was expected the eigenvalues defined in Eq. (3.35) are always real: in fact as it as been demonstrated $\hat{x} > 1$ and $\hat{y} < 0$. This analysis permits to conclude that the obtained PNS system of Eq. (3.15) has a hyperbolic nature. This means that characteristic directions exist and this will permit to numerically solve the PNS problem with methods based on existence of characteristic directions.

3.4 Riemann problem for PNS

The Eulerian system (3.17) with $\omega = 0$ is a hyperbolic system. This implies that the solution has a propagation nature. The system is well posed if initial conditions are assigned. In particular a Riemann problem arises if initial conditions are discontinuous [7]. This special initial value problem can be written as:

$$\begin{aligned} &\frac{\partial \mathbf{F}}{\partial x} + \mathbf{A}\frac{\partial \mathbf{F}}{\partial y} = 0 \qquad -\infty < y < +\infty,\ x > 0 \\ &\mathbf{F}(0, y) \equiv \mathbf{F}_L(y > 0) \quad \mathbf{F}(x, y) \equiv \mathbf{F}_R(y < 0) \end{aligned} \tag{3.37}$$

where the subscript e and the overbar on $\mathbf{F}$ have been omitted to simplify the notation. The Jacobian matrix $\mathbf{A}$ is defined as:

$$\mathbf{A} = \frac{\partial \mathbf{G}}{\partial \mathbf{F}} \tag{3.38}$$

The Riemann problem of Eq. (3.37) is represented in Fig. 3.4. The structure of its solution consists of four waves emanating from the origin, one for each eigenvalue. The solution at the left of λ_3 is simply $\mathbf{F_L}$ and on the right of λ_4 is $\mathbf{F_R}$. The task of a Riemann problem is to find the solution in the wedges between the waves. In particular for the present work we are interested in finding the solution for $y = 0$. For this purpose an approximate Riemann solver is developed. This is the well known Roe's Riemann solver which has been modified for the PNS and for a generic EoS. Also Korte [75] developed a Roe's Riemann solver for the PNS equations but considering a perfect gas equation of state whereas in the present work a generic equation of state has been considered $h = h(p, \rho)$.

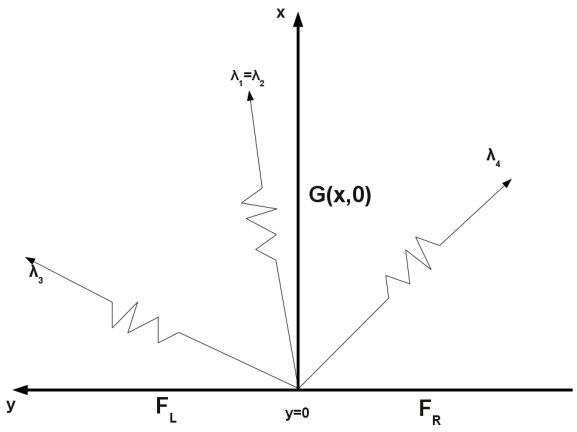

Figure 3.4: Schematic of a Riemann problem

3.4.1 Roe's approximate Riemann solver

The method of Roe [132] to solve the problem of Eq. (3.37) considers approximate solutions which are exact solutions to the following approximate problem:

$$\frac{\partial \mathbf{F}}{\partial x} + \tilde{\mathbf{A}} \frac{\partial \mathbf{F}}{\partial y} = 0 \tag{3.39}$$

where $\tilde{\mathbf{A}}$ is a constant matrix, representative of local conditions. $\tilde{\mathbf{A}}$ has to satisfy the following properties which form the so called *U property*:

(i) it constitutes a linear mapping from vector space $\mathbf{F}$ to the vector space $\mathbf{G}$

(ii) as $\mathbf{F_L} \to \mathbf{F_R} \to \mathbf{F}$, $\tilde{\mathbf{A}}(\mathbf{F_L}, \mathbf{F_R}) \to \mathbf{A}(\mathbf{F}) = \dfrac{\partial \mathbf{G}}{\partial \mathbf{F}}$

(iii) for any $\mathbf{F_L}$,$\mathbf{F_R}$, $\tilde{\mathbf{A}}(\mathbf{F_L}, \mathbf{F_R}) \times (\mathbf{F_L} - \mathbf{F_R}) = \mathbf{G_L} - \mathbf{G_R}$

(iv) the eigenvectors of $\tilde{\mathbf{A}}$ are linear independent

Once $\tilde{\mathbf{A}}$ is known, the evaluation of her eigenvalues λ_i and corresponding eigenvectors $\mathbf{r}^{(i)}$ permit to get an approximate solution of the Riemann problem which can be written in terms of the transverse flux $\mathbf{G}$ in y=0:

$$\mathbf{G}(x,0) = \frac{1}{2}(\mathbf{G_R} + \mathbf{G_L}) - \frac{1}{2}\sum_{i=1}^{4} |\lambda_i| a_i \mathbf{r}^{(i)} \tag{3.40}$$

where a_i are the projections of the jump $\Delta\mathbf{F} = \mathbf{F}_L - \mathbf{F}_R$ on the eigenvectors as a basis:

$$\Delta\mathbf{F} = \sum_{i=1}^{4} a_i \mathbf{r}^{(i)}. \tag{3.41}$$

In the present work the same approach followed in [132] is used to find the matrix $\tilde{\mathbf{A}}$ which verify the above properties. Moreover a generic equation of state will be considered in the implicit form

$$p = p(\rho, \rho h) \tag{3.42}$$

The searched matrix $\tilde{\mathbf{A}}$ must verify property (iii) that is it must be a mapping between jumps $\Delta\mathbf{F} = \mathbf{F_L} - \mathbf{F_R}$ and $\Delta\mathbf{G} = \mathbf{G_L} - \mathbf{G_R}$. To find such a matrix the parameter vector $\mathbf{w} = \sqrt{\rho}[1, u, v, h_0]$ is defined following the idea introduced by Roe. The jump of any variable, scalar or vector, is here indicated with the notation $\Delta(\cdot) = (\cdot)_L - (\cdot)_R$. Also for the parameter vector it is $\Delta\mathbf{w} = \mathbf{w_L} - \mathbf{w_R}$. The flux vectors $\mathbf{F}$ and $\mathbf{G}$ can then be expressed in terms of the $\mathbf{w}$ components:

$$\mathbf{F} = \begin{Bmatrix} w_1 w_2 \\ w_2^2 \\ w_2 w_3 \\ w_2 w_4 \end{Bmatrix} \qquad \mathbf{G} = \begin{Bmatrix} w_1 w_3 \\ w_2 w_3 \\ w_3^2 + p(w_1^2, \sigma) \\ w_3 w_4 \end{Bmatrix} \tag{3.43}$$

where the pressure p has been reported as an implicit function of density $\rho = w_1^2$ and the thermodynamic variable $\sigma = \rho h = \rho(h_0 - \frac{1}{2}u^2 - \frac{1}{2}v^2) = w_1 w_4 - \frac{1}{2}w_2^2 - \frac{1}{2}w_3^2$. At this point it is useful two introduce two more symbols, α and β, to indicate the thermodynamic derivatives of p to respect to ρ and σ:

$$\alpha = \left(\frac{\partial p}{\partial \rho}\right)_\sigma \qquad \beta = \left(\frac{\partial p}{\partial \sigma}\right)_\rho \tag{3.44}$$

The mapping $\Delta\mathbf{w} \to \Delta\mathbf{F}$ and $\Delta\mathbf{w} \to \Delta\mathbf{G}$ can be expressed with two matrix $\tilde{\mathbf{B}}$ and $\tilde{\mathbf{C}}$ respectively, evaluated at the arithmetic mean $\bar{\mathbf{w}} = 0.5(\mathbf{w_L} + \mathbf{w_R})$:

$$\tilde{\mathbf{B}} = \begin{bmatrix} \bar{w_2} & \bar{w_1} & 0 & 0 \\ 0 & 2\bar{w_2} & 0 & 0 \\ 0 & \bar{w_3} & \bar{w_2} & 0 \\ 0 & \bar{w_4} & 0 & \bar{w_3} \end{bmatrix} \qquad \tilde{\mathbf{C}} = \begin{bmatrix} \bar{w_3} & 0 & \bar{w_1} & 0 \\ 0 & \bar{w_3} & \bar{w_2} & 0 \\ 2\alpha\bar{w_1} + \beta\bar{w_4} & -\beta\bar{w_2} & \bar{w_3}(2-\beta) & \beta\bar{w_4} \\ 0 & 0 & \bar{w_4} & \bar{w_3} \end{bmatrix} \tag{3.45}$$

To obtain $\tilde{\mathbf{C}}$ the pressure jump Δp has been written in terms of $\Delta\mathbf{w}$, α and β according to:

$$\begin{aligned} \Delta p &= 2\alpha\bar{w_1}\Delta\bar{w_1} + \beta\Delta\sigma \\ \Delta\sigma &= \bar{w_1}\Delta w_4 + \bar{w_4}\Delta w_1 - \bar{w_2}\Delta w_2 - \bar{w_3}\Delta w_3 \end{aligned} \tag{3.46}$$

The matrix $\tilde{\mathbf{A}}$ can be straightforward evaluated from $\tilde{\mathbf{B}}$ and $\tilde{\mathbf{C}}$, in fact:

$$\left.\begin{aligned} \Delta\mathbf{F} &= \tilde{\mathbf{B}}\Delta\mathbf{w} \\ \Delta\mathbf{G} &= \tilde{\mathbf{C}}\Delta\mathbf{w} = \tilde{\mathbf{C}}\tilde{\mathbf{B}}^{-1}\Delta\mathbf{F} \end{aligned}\right\} \tilde{\mathbf{A}} = \tilde{\mathbf{C}}\tilde{\mathbf{B}}^{-1} \tag{3.47}$$

Nevertheless to evaluate the eigenvalues and eigenvectors of $\tilde{\mathbf{A}}$ it is not necessary to compute $\tilde{\mathbf{A}}$: they can be evaluated from $\tilde{\mathbf{B}}$ and $\tilde{\mathbf{C}}$ as it will be demonstrated.

Eigenvalues

The eigenvalues of $\tilde{\mathbf{A}}$ can be computed according to

$$det(\tilde{\mathbf{C}} - \lambda\tilde{\mathbf{B}}) = 0$$

demonstration:

$$\begin{aligned} & & det(\tilde{\mathbf{A}} - \lambda\mathbf{I}) &= 0 \\ \tilde{\mathbf{A}} = \tilde{\mathbf{C}}\tilde{\mathbf{B}}^{-1} &\Rightarrow & det(\tilde{\mathbf{C}}\tilde{\mathbf{B}}^{-1} - \lambda\mathbf{I}) &= 0 \\ \mathbf{I} = \tilde{\mathbf{B}}\tilde{\mathbf{B}}^{-1} &\Rightarrow & det([\tilde{\mathbf{C}} - \lambda\tilde{\mathbf{B}}]\tilde{\mathbf{B}}^{-1}) &= 0 \\ Binet\ Theorem &\Rightarrow & det(\tilde{\mathbf{C}} - \lambda\tilde{\mathbf{B}})det(\tilde{\mathbf{B}}^{-1}) &= 0 \end{aligned}$$

Eigenvectors

If $\mathbf{s}$ and $\mathbf{r}$ are the eigenvectors associated with the eigenvalues problems:

$$(\tilde{\mathbf{C}} - \lambda\tilde{\mathbf{B}})\mathbf{s} = 0$$
$$(\tilde{\mathbf{A}} - \lambda\mathbf{I})\mathbf{r} = 0$$

it results that

$$\mathbf{r} = \tilde{\mathbf{B}}\mathbf{s}$$

demonstration:

$$\begin{array}{ll} & (\tilde{\mathbf{A}} - \lambda\mathbf{I})\mathbf{r} = 0 \\ \tilde{\mathbf{A}} = \tilde{\mathbf{C}}\tilde{\mathbf{B}}^{-1} \Rightarrow & (\tilde{\mathbf{C}}\tilde{\mathbf{B}}^{-1} - \lambda\mathbf{I})\mathbf{r} = 0 \\ \mathbf{I} = \tilde{\mathbf{B}}\tilde{\mathbf{B}}^{-1} \Rightarrow & (\tilde{\mathbf{C}} - \lambda\tilde{\mathbf{B}})\tilde{\mathbf{B}}^{-1}\mathbf{r} = 0 \\ (\tilde{\mathbf{C}} - \lambda\tilde{\mathbf{B}})\mathbf{s} = 0 \Rightarrow & \mathbf{s} = \tilde{\mathbf{B}}^{-1}\mathbf{r} \end{array}$$

At this stage it is convenient to divide all the components of $\tilde{\mathbf{B}}$ and $\tilde{\mathbf{C}}$ by $\bar{w}_1$ and do adopt the following notation:

$$\varphi = \frac{\rho_R^{1/2}\varphi_R + \rho_L^{1/2}\varphi_L}{\rho_R^{1/2} + \rho_L^{1/2}} \tag{3.48}$$

with φ being u, v, h_0 or p. Hence it will be $u = \bar{w}_2/\bar{w}_1$, $v = \bar{w}_3/\bar{w}_1$ and $h_0 = \bar{w}_4/\bar{w}_1$. With these notations the eigenvalues problem can be expressed as:

$$det(\tilde{\mathbf{C}} - \lambda\tilde{\mathbf{B}}) = det\begin{pmatrix} v - \lambda u & -\lambda & 1 & 0 \\ 0 & v - 2\lambda u & u & 0 \\ 2\alpha + \beta h_0 & -\beta u - \lambda v & (2-\beta)v - \lambda u & \beta \\ 0 & -\lambda h_0 & h_0 & v - \lambda u \end{pmatrix} = 0 \tag{3.49}$$

The resultants eigenvalues are:

$$\tilde{\lambda_{1,2}} = \frac{v}{u} \qquad \tilde{\lambda_{3,4}} = \frac{(2-\beta)v}{2u} \pm \frac{\sqrt{\tilde{\Delta}}}{2u} \tag{3.50}$$

$$\tilde{\Delta} = \beta^2 v^2 + 4(\beta h + \alpha) \tag{3.51}$$

The corresponding eigenvectors are:

$$\mathbf{r^{(1)}} = \begin{Bmatrix} 1 \\ 0 \\ 0 \\ -2\dfrac{\alpha}{\beta} - h_0 \end{Bmatrix} \quad \mathbf{r^{(2)}} = \begin{Bmatrix} q^2/(2(2\dfrac{\alpha}{\beta} + h_0)) + 1 \\ 2u \\ 2v \\ h_0 + \dfrac{q^2}{2} \end{Bmatrix} \quad \mathbf{r^{(3,4)}} = \begin{Bmatrix} u \\ u^2 \\ \tilde{\lambda}_{3,4}u^2 \\ uh_0 \end{Bmatrix} \tag{3.52}$$

where $q^2 = u^2 + v^2$.

3.4.2 The real fluid EoS in the Riemann solver

The originality of the developed Riemann solver relies on the fact that a generic EoS is considered. Hence any fluid can be theoretically considered provided that the two parameters α and β are suitably evaluated. It can be shown that α and β can be computed from the enthalpy h and its derivatives h_p h_ρ. To demonstrate this statement let us consider a linearization of the enthalpy $h = h(\rho, p)$ around a constant state $\tilde{h} = h(\tilde{\rho}, \tilde{p})$:

$$h = \tilde{h} + \tilde{h_p}(p - \tilde{p}) + \tilde{h_\rho}(\rho - \tilde{\rho}) \tag{3.53}$$

Therefore the pressure can be expressed as:

$$\begin{aligned} p &= \tilde{p} + \frac{h - \tilde{h}}{h_p} - \frac{\tilde{h_\rho}}{\tilde{h_p}}(\rho - \tilde{\rho}) \\ p &= \tilde{p} + \frac{1}{\tilde{\rho}\tilde{h_p}}[\tilde{\rho}h - \tilde{\rho}\tilde{h} + \rho h - \rho h] - \frac{\tilde{h_\rho}}{\tilde{h_p}}(\rho - \tilde{\rho}) \\ p &= \tilde{p} + \frac{1}{\tilde{\rho}\tilde{h_p}}(\rho h - \tilde{\rho}\tilde{h}) - \frac{\tilde{h} + \tilde{\rho}\tilde{h_\rho}}{\tilde{\rho}\tilde{h_p}}(\rho - \tilde{\rho}) \end{aligned} \tag{3.54}$$

Hence from this truncated expansion series the pressure jump Δp between the left and right states can be expressed as:

$$\Delta p = \frac{1}{\rho h_p}\Delta(\rho h) - \frac{h + \rho h_\rho}{\rho h_p}\Delta\rho \tag{3.55}$$

in which the terms which multiply the jumps are evaluated at the average Roe state defined by Eq. (3.48). Comparing the last relation with Eqs. (3.44) and (3.46) it can be concluded that α and β can be provided by:

$$\alpha = -\frac{h + \rho h_\rho}{\rho h_p} \qquad \beta = \frac{1}{\rho h_p} \tag{3.56}$$

For a calorically and thermally perfect gas α and β have simple expressions. In fact from the perfect gas law it results:

$$p = \rho h \frac{\gamma - 1}{\gamma} = \sigma \frac{\gamma - 1}{\gamma} \tag{3.57}$$

with $\gamma = c_p/c_v = const.$ Hence it results:

$$\alpha = 0 \qquad \beta = \frac{(\gamma - 1)}{\gamma} \tag{3.58}$$

3.4.3 U property for the Roe matrix

The matrix $\tilde{\mathbf{A}}$ appearing in Eq. (3.39) must verify the *U property*. In the following the check of each property is carried out. It has to be noticed that although $\tilde{\mathbf{A}}$ is never wrote explicitly it is represented by its eigenvalues written in Eq. (3.50).

First of all the matrix $\tilde{\mathbf{A}}$ has been constructed as a linear mapping between the vector spaces $\mathbf{F}$ and $\mathbf{G}$ which was a request from property (i). Moreover, the parameter vector has been introduced precisely to find a matrix which verifies property (iii) which is essential for the algorithm to be conservative. Also property (iv), which requires the linearly independence of the eigenvalues, is verified because the eigenvectors has been chosen to be independent. Anyway, this property is further demonstrated analyzing the determinant of the eigenvectors matrix:

$$det(\mathbf{r^1}, \mathbf{r^2}, \mathbf{r^3}, \mathbf{r^4}) \tag{3.59}$$

which is always non null. Finally property (ii) requires that $\tilde{\mathbf{A}}$ tends toward the Jacobian matrix when the right and left states tend one towards each other. This condition is essential to recover smoothly the linearized algorithm to the original system. The first observation is that when $\varphi_R \to \bar{\varphi}$ and $\varphi_L \to \bar{\varphi}$ also the Roe average $\varphi \to \bar{\varphi}$ by definition (see Eq. (3.48)). Therefore, the eigenvalues of $\tilde{\mathbf{A}}$ when $\mathbf{F_L} \to \mathbf{F_R} \to \mathbf{F}$ are obtained from Eq. (3.50) replacing the Roe averages with the actual state corresponding with $\mathbf{F}$. On the other side, the Jacobian matrix $\mathbf{A} = \dfrac{\partial \mathbf{G}}{\partial \mathbf{F}}$ has been analyzed in Sec. 3.3.1. In fact it is:

$$\left(\frac{\partial \mathbf{G}}{\partial \mathbf{F}}\right) = \left(\frac{\partial \mathbf{G}}{\partial \mathbf{V}}\right)\left(\frac{\partial \mathbf{F}}{\partial \mathbf{V}}\right)^{-1} \qquad \to \qquad \mathbf{A} = \mathbf{C}\mathbf{B}^{-1} \tag{3.60}$$

Hence $\mathbf{A}$ eigenvalues can be computed from

$$det(\mathbf{C} - \lambda \mathbf{B}) = 0 \tag{3.61}$$

which has been evaluated and are given by Eq. (3.35). If $\hat{x}$ and $\hat{y}$ are replaced by the equivalent:

$$\hat{x} = \frac{1}{\beta} \qquad \hat{y} = -\frac{\alpha}{\beta} - h \tag{3.62}$$

It is easy to verify that when the right and left states tend one towards each other $\tilde{\mathbf{A}}$ eigenvalues of Eq. (4.45) tend towards $\mathbf{A}$ eigenvalues of Eq. (3.35) which demonstrates that $\tilde{\mathbf{A}} \to \mathbf{A}$

3.5 PNS model to study low Mach number compressible flows

It has been demonstrated that PNS are suitable to be numerically solved with a space marching approach and this permits to simplify the original problem: in fact marching in space instead of marching in time permits to reduce the problem dimensions from four (t, x, y, z) to three (x, y, z). Nevertheless the issue of solving low Mach number compressible flow is still present: how PNS equations deal with this particular regime? This may of course depend on the way these equations are numerically solved. Anyway, to answer this question we have to analyze the low Mach number problems that were exposed in Section 3.1 for the PNS system of equations (3.15) with Vigneron parameter $\omega = 0$.

- **Accuracy problem**. The streamwise pressure gradient is completely considered as a source term, that has to be correctly evaluated (and this is a delicate issue that will be faced in the next chapter), and for this reason the problem of errors in the solution of the order $O(1/M^2)$ that were precisely connected with the pressure divergence term in momentum equations does not subsist anymore. Nevertheless, it has to be pointed out that the crosswise pressure gradients are retained in the equations.

- **Convergence problem**. The PNS system at low velocity continues to be a stiff problem because of the small values of $\lambda_{1,2}$ compared to the large $\lambda_{3,4}$. In fact $\lambda_{1,2}$ will always be very small in a channel because the crosswise velocity are very small. However this characteristic is inherent of the PNS approach because $u \gg v$ is one of the hypothesis that has permitted to obtain these simplified equations. So the stiffness problem is no longer a low Mach number problem but much more a price to pay to use this set of simplified equations. Nevertheless, having simplified the problem, small space steps, and hence a lengthening of the computational time, can be taken into consideration so as to reach a correct solution.

These last considerations have just the aim to conclude the reasoning that has been conducted in this chapter and that has brought to the selection of PNS to face the numerical simulation of supercritical propellants flows in heated cooling channels: in the development and validation of the numerical method these aspects will be more deeply investigated so as to demonstrate the accuracy of the numerical method.

Chapter 4

Analytical and Numerical Model

PNS equations are suitable to describe flows in cooling channels with a high ratio L/D, as discussed in Chap. 3, under the two main assumptions:

- the derivatives in the streamwise direction in the diffusive terms are of lower order of magnitude than the same derivatives in the transverse directions;
- the velocity in the streamwise direction is always positive: no reverse flow occurs.

Considering these assumptions all the streamwise diffusing terms in the Navier-Stokes equations have been neglected. Moreover, the streamwise pressure gradient has been considered as a source term. This last condition is essential for the system to be hyperbolic-parabolic when the Mach number has very low values. The PNS system equations obtained after these simplifications are reported here in divergence form. A Cartesian reference system for a straight tube is considered where x is the streamwise direction and y,z are the transverse directions. The proposed PNS system is:

$$\frac{\partial \mathbf{F_e}}{\partial x} + \frac{\partial \mathbf{G_e}}{\partial y} - \frac{\partial \mathbf{G_v}}{\partial y} + \frac{\partial \mathbf{H_e}}{\partial z} - \frac{\partial \mathbf{H_v}}{\partial z} = \frac{\partial \mathbf{P}}{\partial x} + \mathbf{Q} \tag{4.1}$$

where the subscripts $()_e$ and $()_v$ indicate the Eulerian and viscous flux vectors, respectively, after the PNS approximations have been applied. Therefore this system of equations corresponds to Eq. (3.15) with $\omega = 0$. The corresponding fluxes are:

$$\mathbf{F_e} = \begin{Bmatrix} \rho u \\ \rho u^2 \\ \rho uv \\ \rho uw \\ \rho u h_0 \end{Bmatrix} \qquad \mathbf{G_e} = \begin{Bmatrix} \rho v \\ \rho uv \\ \rho v^2 + p \\ \rho vw \\ \rho v h_0 \end{Bmatrix} \qquad \mathbf{H_e} = \begin{Bmatrix} \rho w \\ \rho uw \\ \rho vw \\ \rho w^2 + p \\ \rho w h_0 \end{Bmatrix} \tag{4.2}$$

$$\mathbf{G_v} = \begin{Bmatrix} 0 \\ \mu\dfrac{\partial u}{\partial y} \\ \dfrac{2}{3}\mu\left(2\dfrac{\partial v}{\partial y} - \dfrac{\partial w}{\partial z}\right) \\ \mu\left(\dfrac{\partial v}{\partial z} + \dfrac{\partial w}{\partial y}\right) \\ uG_{v,2} + vG_{v,3} + wG_{v,4} + k\dfrac{\partial T}{\partial y} \end{Bmatrix} \qquad \mathbf{H_v} = \begin{Bmatrix} 0 \\ \mu\dfrac{\partial u}{\partial z} \\ \mu\left(\dfrac{\partial v}{\partial z} + \dfrac{\partial w}{\partial y}\right) \\ \dfrac{2}{3}\mu\left(2\dfrac{\partial w}{\partial z} - \dfrac{\partial v}{\partial y}\right) \\ uH_{v,2} + vH_{v,3} + wH_{v,4} + k\dfrac{\partial T}{\partial z} \end{Bmatrix} \tag{4.3}$$

where subscripts $()_2$, $()_3$, $()_4$, indicate the second, third and fourth component of vectors, respectively. Pressure does not appear in the streamwise Eulerian flux vectors because it has been moved to the pressure source vector given by Eq. (3.16) with $\omega = 0$:

$$\mathbf{P} = \begin{Bmatrix} 0 \\ -p \\ 0 \\ 0 \\ 0 \end{Bmatrix} \tag{4.4}$$

A source term vector $\mathbf{Q}$ has also been emphasized in Eq. (4.1) for the sake of generality.

An important peculiarity of the cooling channel flows of interest is their high Reynolds number of the order of $10^5 - 10^6$. The consequence is that these flows are turbulent. In the present study the Reynolds-averaged Navier-Stokes (RANS) approach has been used to describe these turbulent flows [8]. In the following the parabolized form of the RANS equations is presented together with the eddy viscosity closure model of Spalart-Allmaras suitably modified to account for PNS hypothesis. Then attention is devoted to the present numerical model. The hyperbolic-parabolic nature of the PNS system has been demonstrated and this allows to use a space marching method in particular relying on the existence of the characteristics. Therefore, a Godunov type finite volume scheme has been selected for the numerical model. The core of the scheme is the approximate Roe's Riemann solver developed for PNS and a generic EoS, that has been presented in Chap. 3. Other important characteristics of the code are the initial and boundary conditions, the treatment of the streamwise pressure gradient and the thermophysical property models implementation through suitable look-up table.

4.1 Turbulence model

Reynolds averaged Navier-Stokes equations (RANS) have the same form of the Navier-Stokes equations except that local instantaneous variables are replaced with averaged variables. Further stresses, referred to as turbulent stresses, are added in the diffusive terms. Closure models are then necessary to provide a link between the Reynolds-Stresses and the other variables. Among closure models the basic class of Eddy Viscosity/Diffusivity Models, are based on the Boussinesq assumption that the turbulent stress tensor $\tau_{t,ij}$ can be expressed in terms of the mean rate of strain S_{ij} in the

same way as viscous stresses for Newtonian isotropic fluid, except that the coefficient of the molecular viscosity is replaced by eddy viscosity [8]. Boussinesq hypothesis is:

$$\begin{aligned} \tau_{t,ij} &= 2\mu_T S_{ij} \\ S_{ij} &= \frac{1}{2}\left(\frac{\partial u_i}{\partial x_j} + \frac{\partial u_j}{\partial x_i}\right) \end{aligned} \tag{4.5}$$

where μ_T is called eddy viscosity or turbulent viscosity. In Eq. (4.5) u_i are u, v, w average velocities and x_i are x, y, z coordinates. Applying Boussinesq hypothesis reduces to replace the transport property coefficients with the sum of laminar and turbulent coefficients, that is:

$$\mu = \mu_\ell + \mu_t \qquad k = k_\ell + k_t \tag{4.6}$$

where subscript ℓ refers to laminar values (given from transport property models) and subscript t refers to turbulent values. It is necessary to provide μ_t and k_t and several methods are available for this purpose. Dealing with wall turbulence (which is our interest in channel flows) the more simple models are algebraic and provide algebraic expressions for μ_t and k_t as functions of different local parameter as for example the distance from the wall. More complex models include convection-diffusion equations to be solved together with the other equations. In the present work the one equation model of Spalart-Allmaras (SA) has been selected. In fact, this model is suitable to describe wall turbulence and is widely used in literature for this purpose. Moreover, thought more complicated than algebraic models, the one equation model of SA is obviously lighter than two equations models. In the following the SA model is presented and then suitably modified for the PNS.

4.1.1 Spalart-Allmaras one equation model

Spalart-Allmaras [144] introduced a convection-diffusion equation for the turbulent viscosity. The idea is to treat μ_t as an additional transported variable. Whereas the turbulent conductivity k_t is considered to be simply related to the turbulent viscosity through:

$$k_t = \mu_t c_p / \mathrm{Pr_t} \tag{4.7}$$

where $\mathrm{Pr_t}$ is the turbulent Prandtl number that has been introduced by analogy with molecular transport. Actually to account for the viscous effect of the wall the transported variable is an equivalent turbulent viscosity rather than μ_t defined by:

$$\begin{aligned} \tilde{\mu} &= \frac{\mu_t}{f_{v1}} \\ f_{v1} &= \frac{\chi^3}{\chi^3 + c_{v1}^3} \\ \chi &= \frac{\tilde{\mu}}{\mu_\ell} \end{aligned} \tag{4.8}$$

where $c_{v1} = 7.1$ is a constant whereas both the viscous function f_{v1} and the viscosity ratio χ depend on the local variables. The original SA equation for $\tilde{\mu}$ for a

compressible flow for the non stationary RANS [24] has been adopted here:

$$\frac{D\tilde{\mu}}{Dt} = \frac{1}{\sigma}(\nabla((\mu_\ell + \tilde{\mu})\nabla\tilde{\nu})) + P_{prod} - P_{dest} + P_{diff} \tag{4.9}$$

where $\sigma \in [0.6 \div 1]$ is a constant and $\tilde{\nu} = \tilde{\mu}/\rho$. The left hand side of Eq (4.9) is the material derivative accounting for the convective transport, whereas on the right hand side the term between brackets is a classical diffusive term, with ∇ given by:

$$\nabla = \frac{\partial()}{\partial x} + \frac{\partial()}{\partial y} + \frac{\partial()}{\partial z} \tag{4.10}$$

Finally three source terms are also present on the right hand side to account for production and destruction and non conservative diffusion of $\tilde{\mu}$. In particular, the source terms are modeled as discussed in the following.

Production term $\mathbf{P_{prod}}$. The production term expression comes from the requirement that for a simple shear stress it has to be proportional to the mean rate of strain $S_{ij} = \dfrac{\partial u}{\partial y}$. Therefore the production term could be expressed as:

$$P_{prod} = c_{b1} S \nu_T \tag{4.11}$$

where S must be chosen so as to reduce to S_{ij} for a simple shear flow. One suitable choice is to consider the vorticity $S = \sqrt{\Omega_x^2 + \Omega_y^2 + \Omega_z^2}$ with:

$$\Omega_x = \frac{\partial v}{\partial z} - \frac{\partial w}{\partial y} \qquad \Omega_y = \frac{\partial w}{\partial x} - \frac{\partial u}{\partial z} \qquad \Omega_z = \frac{\partial u}{\partial y} - \frac{\partial v}{\partial x} \tag{4.12}$$

Following the same basic idea that has bring to consider $\tilde{\mu}$ instead of μ_T as transported variable, $\tilde{S}$ is then introduced instead of S in the production term which becomes:

$$\begin{aligned} P_{prod} &= c_{b1}\tilde{S}\tilde{\nu} \\ \tilde{S} &= S + \frac{\tilde{\nu}}{\kappa^2 d^2} f_{v2} \end{aligned} \tag{4.13}$$

where $\kappa = 0.41$ is the Von-Karman constant, $c_{b1} \in [0.13 \div 0.14]$ is a constant, d is the distance from the wall and f_{v2} is a local viscous function given by:

$$f_{v2} = 1 - \frac{\chi}{1 + \chi f_{v1}} \tag{4.14}$$

Diffusive term $\mathbf{P_{diff}}$. This non conservative diffusive term is totally empirical and introduces another constant c_{b2} that can be suitable tuned. The term is given by:

$$P_{diff} = \rho c_{b2} (\nabla\tilde{\nu})^2 \tag{4.15}$$

with $c_{b2} \in [0.6 \div 0.7]$.

Destruction term $\mathbf{P_{dest}}$. This term is introduced to account for the near-wall but non viscous "blocking" effect. Dimensional analysis considerations bring to the following expression:

$$P_{dest} = \frac{c_{w1} f_w}{\rho} \left(\frac{\tilde{\mu}}{d} \right)^2 \tag{4.16}$$

The constant c_{w1} is evaluated with the equilibrium requirement between P_{prod}, P_{diff} and P_{dest}:

$$c_{w1} = \frac{c_{b1}}{\kappa^2} + \frac{1 + c_{b2}}{\sigma} \tag{4.17}$$

The wall function f_w is introduced so as to get the correct friction coefficient at the wall, which without it was smaller than the experimental data. This last function is evaluated locally from:

$$\begin{aligned} f_w &= g \left[\frac{1 + c_{w3}^6}{g^6 + c_{w3}^6} \right]^{1/6} \\ g &= r + c_w (r^6 - r) \\ r &= min \left(\frac{\tilde{\mu}}{\tilde{S} \kappa^2 d^2}, 10 \right) \end{aligned} \tag{4.18}$$

with c_{w2} and c_{w3} calibration constants.

4.1.2 Spalart-Almaras equation for the PNS

The PNS system (4.1) is now considered, replacing μ and k with the effective viscosity and conductivity given by Eq (4.6). The PNS hypothesis have been applied to the SA Eq. (4.9) in stationary condition, that is without time derivative. Therefore all the streamwise derivatives have been neglected in the diffusive and source terms. The equation is then included in system of Eq. (4.1) as the following sixth scalar equation:

$$\frac{\partial \tilde{\mu} u}{\partial x} + \frac{\partial \tilde{\mu} v}{\partial y} + \frac{\partial \tilde{\mu} w}{\partial z} = \frac{1}{\sigma} \left(\frac{\partial}{\partial y} \left[(\mu_\ell + \tilde{\mu}) \frac{\partial \tilde{\nu}}{\partial y} \right] + \frac{\partial}{\partial z} \left[(\mu_\ell + \tilde{\mu}) \frac{\partial \tilde{\nu}}{\partial z} \right] \right) + P_{prod} - P_{dest} + P_{diff} \tag{4.19}$$

where:

- the *production* term is: $P_{prod} = c_{b1} \tilde{S} \tilde{\mu}$;
- the *destruction* term is: $P_{dest} = \dfrac{c_{w1} f_w}{\rho} \left(\dfrac{\tilde{\mu}}{d} \right)^2$;
- the *diffusion* term is: $P_{diff} = \dfrac{\rho c_{b2}}{\sigma} \left[\left(\dfrac{\partial \tilde{\nu}}{\partial y} \right)^2 + \left(\dfrac{\partial \tilde{\nu}}{\partial z} \right)^2 \right]$.

In the evaluation of the diffusion terms (conservative and non conservative) the difference with respect to the standard model is that the streamwise derivatives are neglected. For the production and destruction terms the corrected vorticity module

$\tilde{S}$ is computed according to Eq. (4.13) except that the vorticity module S is computed neglecting the streamwise velocity derivatives. The components of the vorticity vector are therefore:

$$\Omega_x = \frac{\partial v}{\partial z} - \frac{\partial w}{\partial y} \qquad \Omega_y = -\frac{\partial u}{\partial z} \qquad \Omega_z = \frac{\partial u}{\partial y} \tag{4.20}$$

The above closure model contains several coefficients that can be tuned to reproduce experimental data. In the present model the standard values proposed in [144] have been used and are reported in Table 4.1.

Coefficient	**Value**
κ	0.41
c_{b1}	0.1355
c_{b2}	0.622
c_{v1}	7.1
c_{w2}	0.3
c_{w3}	2
σ	2/3
Pr_t	0.9

Table 4.1: Values for the Spalart-Allmaras coefficients taken from [144]

4.2 PNS finite volume scheme

Before facing the numerical model it is convenient to finally write the complete analytical model that has been obtained for the description of the turbulent cooling channel flows. Therefore the parabolized RANS equations are reported in integral form considering a generic control volume $\bar{\mathcal{V}}$ bounded by a surface $\bar{\mathcal{S}}$:

$$\int_{\bar{\mathcal{V}}} \frac{\partial \mathbf{F_e}}{\partial x} = -\oint_{\bar{\mathcal{S}}} (\mathbf{G}n_y + \mathbf{H}n_z) d\mathcal{S} + \int_{\bar{\mathcal{V}}} \frac{\partial \mathbf{P}}{\partial x} d\mathcal{V} + \int_{\bar{\mathcal{V}}} \mathbf{Q} d\mathcal{V} \tag{4.21}$$

where $\mathbf{G} = \mathbf{G_e} - \mathbf{G_v}$ and $\mathbf{H} = \mathbf{H_e} - \mathbf{H_v}$ whereas n_y, n_z are the components in the y and z directions, respectively, of the outward unit vector normal to the surface $\bar{\mathcal{S}}$. The Eulerian and viscous fluxes are given by:

$$\mathbf{F_e} = \begin{Bmatrix} \rho u \\ \rho u^2 \\ \rho uv \\ \rho uw \\ \rho u h_0 \\ u\tilde{\mu} \end{Bmatrix} \qquad \mathbf{G_e} = \begin{Bmatrix} \rho v \\ \rho uv \\ \rho v^2 + p \\ \rho vw \\ \rho v h_0 \\ v\tilde{\mu} \end{Bmatrix} \qquad \mathbf{H_e} = \begin{Bmatrix} \rho w \\ \rho uw \\ \rho vw \\ \rho w^2 + p \\ \rho w h_0 \\ w\tilde{\mu} \end{Bmatrix} \tag{4.22}$$

$$\mathbf{G_v} = \begin{Bmatrix} 0 \\ \mu\dfrac{\partial u}{\partial y} \\ \dfrac{2}{3}\mu\left(2\dfrac{\partial v}{\partial y} - \dfrac{\partial w}{\partial z}\right) \\ \mu\left(\dfrac{\partial v}{\partial z} + \dfrac{\partial w}{\partial y}\right) \\ uG_{v,2} + vG_{v,3} + wG_{v,4} + k\dfrac{\partial T}{\partial y} \\ \dfrac{1}{\sigma}(\mu_\ell + \tilde{\mu})\dfrac{\partial \tilde{\nu}}{\partial y} \end{Bmatrix} \qquad \mathbf{H_v} = \begin{Bmatrix} 0 \\ \mu\dfrac{\partial u}{\partial z} \\ \mu\left(\dfrac{\partial v}{\partial z} + \dfrac{\partial w}{\partial y}\right) \\ \dfrac{2}{3}\mu\left(2\dfrac{\partial w}{\partial z} - \dfrac{\partial v}{\partial y}\right) \\ uH_{v,2} + vH_{v,3} + wH_{v,4} + k\dfrac{\partial T}{\partial z} \\ \dfrac{1}{\sigma}(\mu_\ell + \tilde{\mu})\dfrac{\partial \tilde{\nu}}{\partial y} \end{Bmatrix} \tag{4.23}$$

The source terms are:

$$\mathbf{P} = \begin{Bmatrix} 0 \\ -p \\ 0 \\ 0 \\ 0 \\ 0 \end{Bmatrix} \qquad \mathbf{Q} = \begin{Bmatrix} 0 \\ 0 \\ 0 \\ 0 \\ 0 \\ P_{prod} - P_{dest} + P_{diff} \end{Bmatrix} \tag{4.24}$$

The numerical solution of Eq. (4.21) can be carried out considering that the system of equations is hyperbolic-parabolic in the streamwise direction. Therefore the equations can be solved using a space-marching method in the streamwise direction. Moreover upwind schemes must be used for the Eulerian part because of its hyperbolic nature. Upwind finite volume schemes are largely used in compressible density based numerical codes to solve the unsteady form of the compressible Navier-Stokes equations marching in time [4]. The computational domain is divided into volumes, also called cells. The integration in time arises after the evaluation of the fluxes at each interface. In particular in upwind schemes the Eulerian fluxes are obtained as solutions of Riemann problems at each interface. Hence these methods rely on the existence of characteristic directions which has in fact been demonstrated for the PNS system in Chap. 3. Therefore such approach is suitable for the PNS system of interest. Given these considerations the present space-marching method relies on a finite volume scheme in which the unknown $\mathbf{F_e}$ fluxes are integrated in the x direction with an Euler explicit scheme once the $\mathbf{G_e}$, $\mathbf{G_v}$, $\mathbf{H_e}$, and $\mathbf{H_v}$ fluxes have been evaluated at the cell interfaces. The developed scheme is first order in the streamwise direction and second order in the crosswise direction.

Geometries that will be investigated are straight channels with the axis aligned with the x coordinate, which is therefore the streamwise coordinate. Each crosswise section is perpendicular to the streamwise direction as shown in Fig. 4.1. The generic crosswise section is divided in control volumes. These volumes are genuinely areas and are called "volumes" only because of the analogy with unsteady finite volume schemes. In the following they will be called cells. Hence there are N cells in the y direction and M cells in the z direction and each cell is individuated with a pair of indexes (j, k) with $j = \{1, \cdots, N\}$ and $k = \{1, \cdots, M\}$. The the index i is associated with the streamwise direction. In a finite volume approach, the integrated variables are averages over each cell. Hence in the present case at each integration step i the

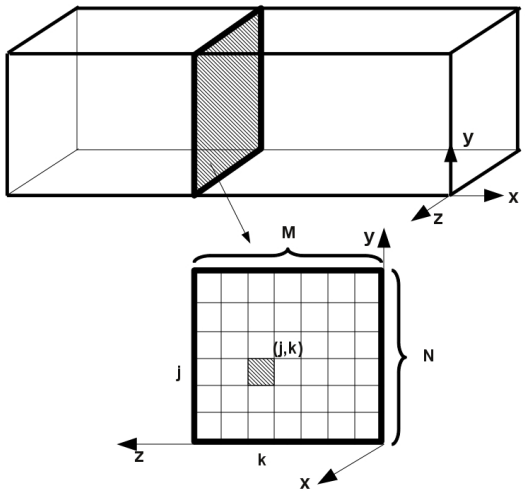

Figure 4.1: Schematic of a generic 3D control volume and discretization of the crosswise section in $(N \times M)$ cells

integrated variable in the cell (j,k), located in the cell center, is defined as:

$$\widetilde{\mathbf{F}}^{\mathbf{i}}_{\mathbf{e,jk}} = \frac{1}{\mathcal{A}_{x,jk}} \int_{\mathcal{S}_{x,jk}} \mathbf{F}^{\mathbf{i}}_{\mathbf{e}}(\mathbf{y},\mathbf{z}) d\mathcal{S} \tag{4.25}$$

where $\mathcal{S}_{x,jk}$ is the surface of the cell (j,k) and $\mathcal{A}_{x,jk}$ is its area. In the following a lighter notation is assumed omitting the (j,k) indexes in the fluxes subscripts. For example it is:

$$\widetilde{\mathbf{F}}^{\mathbf{i}}_{\mathbf{e}} \equiv \widetilde{\mathbf{F}}^{\mathbf{i}}_{\mathbf{e,jk}} \tag{4.26}$$

Following the basic finite volume approach the system of Eq. (4.21) is considered for the volume $\mathcal{V}_{i,j,k}$ represented in Fig. 4.2 that is the volume formed from the cell (j,k) over the streamwise step $\Delta x = x_{i+1} - x_i$:

$$\int_{\mathcal{V}_{i,j,k}} \frac{\partial \mathbf{F_e}}{\partial x} = -\int_{\mathcal{S}_l} (\mathbf{G}n_y + \mathbf{H}n_z) d\mathcal{S} + \int_{\mathcal{V}_{i,j,k}} \frac{\partial \mathbf{P}}{\partial x} d\mathcal{V} + \int_{\mathcal{V}_{i,j,k}} \mathbf{Q} d\mathcal{V} \tag{4.27}$$

where n_y, n_z are the components in the y and z directions, respectively, of the outward unit vector normal to the longitudinal surface $\mathcal{S}_l$ of the volume $\mathcal{V}_{i,j,k}$. At this stage an explicit Euler scheme is chosen for the streamwise integration. Introducing the averages of Eq. (4.26) and considering that $\mathbf{Q}$ and the streamwise pressure gradients are source terms, the above equation becomes:

$$\widetilde{\mathbf{F}}^{\mathbf{i+1}}_{\mathbf{e}} = \widetilde{\mathbf{F}}^{\mathbf{i}}_{\mathbf{e}} - \frac{1}{\mathcal{A}_x} \int_{\mathcal{S}_l} (\mathbf{G}n_y + \mathbf{H}n_z) d\mathcal{S} + \mathbf{Q}\Delta x + \Delta \mathbf{P} \tag{4.28}$$

where $\Delta P = P_{i+1} - P_i$. Hence for each cell, if $\widetilde{\mathbf{F}}^{\mathbf{i}}_{\mathbf{e}}$ is known, the rest of the right hand side must be evaluated to compute $\widetilde{\mathbf{F}}^{\mathbf{i+1}}_{\mathbf{e}}$. In this explicit scheme all the terms are evaluated in x_i and considered constant over the space step Δx. This requires the estimation of the source terms in each cell (j,k) and the transverse fluxes on the

boundary of the cell which is called interface. To this aim several points must be addresses:

- The thermophysical models described in Chap. 2 are necessary. Nevertheless their complex analytical form make them not usable in their direct form because of the consequent high computational cost. Rather, all the thermodynamic and transport properties of interest are discretized in a data base. During the solving process the properties are taken from the data base which also includes the necessary thermodynamic derivatives.

- Suitable initial and boundary conditions are provided.

- The accuracy order of the scheme is strictly related on the way it is built. A explicit Euler scheme has been adopted in the streamwise direction thus yielding to a first order accurate scheme in this direction. A *CFL* condition permits to choose a Δx integration step which provides a stable scheme. A linear reconstruction of the solution over each cell has been adopted to obtain a second order in the transverse direction.

- Transverse Eulerian fluxes are obtained as solution of Riemann problems at each interface, whereas central differences are used for the viscous fluxes. A suitable Riemann solver has been developed in this work. It is a modified version of the Roe's approximate Riemann solver [132] for Eq. (4.1) with a generic equation of state.

- The streamwise pressure gradient is evaluated with an algorithm requiring the global conservation of the integral momentum equation.

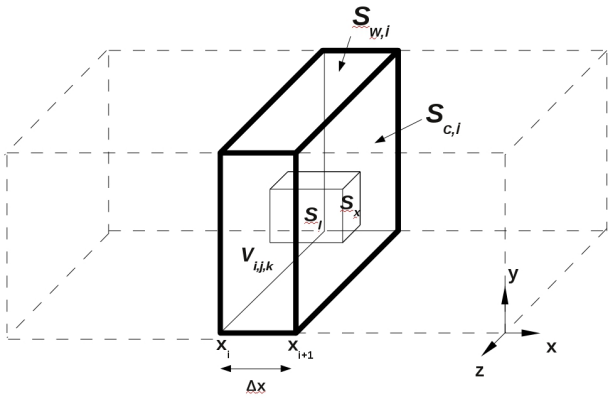

Figure 4.2: Schematic of a generic 3D control volume

4.2.1 Implementation of the thermophysical models

In the numerical resolution thermodynamic and transport properties must be computed and related to the primitive variables. Suitable thermophysical models have been selected and validated in Chap. 2. However these algebraic models are complex

polynomials and hence their direct use in a numerical model would bring a high computational cost. For this reason a cheaper method has been adopted. The properties are provided to the numerical model through look up tables.

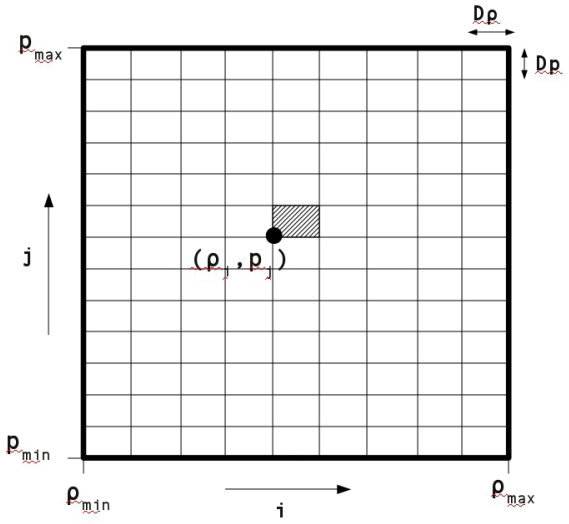

Figure 4.3: Two dimensional rectilinear grid for the property database

A two dimensional rectilinear grid is generated for pressure and density. Considering the ranges of density $[\rho_{min}, \rho_{max}]$ and pressure $[p_{min}, p_{max}]$ each node of the grid is defined by:

$$\begin{aligned} \rho_i \quad & i = 1, \cdots, N_\rho \quad \rho_{i+1} > \rho_i \\ p_j \quad & j = 1, \cdots, N_p \quad p_{j+1} > p_j \end{aligned} \tag{4.29}$$

Moreover $\Delta\rho = (\rho_{i+1} - \rho_i)$ and $\Delta p = (p_{j+1} - p_j)$ are constant over the grid. A schematic of the grid is reported in Fig. 4.3. A property database is then obtained computing all the property of interest in the above grid nodes (ρ_i, p_j) with the models of Chap. 2. Bicubic splines are used to evaluate the value of a generic property $\mathcal{F}$ in a thermodynamic state $(\bar{\rho}, \bar{p})$, which in general does not correspond with any of the grid nodes. Bicubic splines are piecewise cubic functions that pass through a set of given data points. They are continuous and continuously twice differentiable. Hence they permit to have a very accurate approximation of the property that would have been evaluated directly with the thermophysical model equation. Moreover the differentiability ensure a smooth passage between subregions of the grid. If $\rho_i < \bar{\rho} < \rho_{i+1}$ and $p_j < \bar{p} < p_{j+1}$, then the generic property $\mathcal{F}$ is evaluated with:

$$\mathcal{F}(\bar{\rho}, \bar{p}) = \sum_{m=0}^{3} \sum_{n=0}^{3} c(i,j)_{mn} \delta\rho^m \delta p^n \tag{4.30}$$

where $\delta\rho = \bar{\rho} - \rho_i$ and $\delta p = \bar{p} - p_j$, as depicted in the schematic of Fig 4.4. The $c(i,j)_{mn}$ are 16 coefficients associated to the grid subregion $[\rho_i, \rho_{i+1}] \times [p_j, p_{j+1}]$ containing $(\bar{\rho}, \bar{p})$. These coefficients are related with the four following values for each of the four nodes of the subgrid:

$$\mathcal{F}, \ \frac{\partial^2 \mathcal{F}}{\partial \rho^2}, \ \frac{\partial^2 \mathcal{F}}{\partial p^2}, \ \frac{\partial^4 \mathcal{F}}{\partial^2 \rho \partial^2 p} \tag{4.31}$$

and can be computed in several ways. In any case for a given choice of $N_\rho \times N_p$ data points $\mathcal{F}(i,j)$ and $2N_\rho + 2N_p$ boundary conditions, it can be demonstrated that there is exactly one bicubic spline function which is continuously twice differentiable over the entire domain [2]. In the present numerical model the bicubic spline coefficients for each property of interest have been evaluated with the NTCC PSPLINE library [2], which adopt periodic boundary conditions. These libraries are used in a preprocessor and for each data point a 4×4 array of 16 coefficients is retained. Then, at run time when it is necessary, suitable subroutines permit to compute the needed property $\mathcal{F}$ and its derivatives with respect to pressure and density. If $c_{11}, \cdots, c_{44}$ are the 16 coefficients associated with (i,j), the generic $\mathcal{F}$ in the subregion $[\rho_i, \rho_{i+1}] \times [p_j, p_{j+1}]$ is computed from:

$$\begin{aligned}\mathcal{F}(\bar{\rho},\bar{p}) =& c_{11} + c_{21}\cdot\delta\rho + c_{31}\cdot\delta\rho^2 + c_{41}\cdot\delta\rho^3 + \\ & \delta p(c_{12} + c_{22}\cdot\delta\rho + c_{32}\cdot\delta\rho^2 + c_{42}\cdot\delta\rho^3) + \\ & \delta p^2(c_{13} + c_{23}\cdot\delta\rho + c_{33}\cdot\delta\rho^2 + c_{43}\cdot\delta\rho^3) + \\ & \delta p^3(c_{14} + c_{24}\cdot\delta\rho + c_{34}\cdot\delta\rho^2 + c_{44}\cdot\delta\rho^3)\end{aligned} \tag{4.32}$$

Therefore the formula for the derivatives are:

$$\begin{aligned}\mathcal{F}_\rho(\bar{\rho},\bar{p}) =& c_{21} + c_{31}\cdot 2\delta\rho + c_{41}\cdot 3\delta\rho^2 + \\ & \delta p(c_{22} + c_{32}\cdot 2\delta\rho + c_{42}\cdot 3\delta\rho^2) + \\ & \delta p^2(c_{23} + c_{33}\cdot 2\delta\rho + c_{43}\cdot 3\delta\rho^2) + \\ & \delta p^3(c_{24} + c_{34}\cdot 2\delta\rho + c_{44}\cdot 3\delta\rho^2)\end{aligned} \tag{4.33}$$

$$\begin{aligned}\mathcal{F}_p(\bar{\rho},\bar{p}) =& c_{12} + c_{22}\cdot\delta\rho + c_{32}\cdot\delta\rho^2 + c_{42}\cdot\delta\rho^3 + \\ & 2\delta p(c_{13} + c_{23}\cdot\delta\rho + c_{33}\cdot\delta\rho^2 + c_{43}\cdot\delta\rho^3) + \\ & 3\delta p^2(c_{14} + c_{24}\cdot\delta\rho + c_{34}\cdot\delta\rho^2 + c_{44}\cdot\delta\rho^3)\end{aligned} \tag{4.34}$$

with $\mathcal{F}_\rho$ and $\mathcal{F}_p$:

$$\mathcal{F}_\rho = \left(\frac{\partial\mathcal{F}}{\partial\rho}\right)_p \qquad \mathcal{F}_p = \left(\frac{\partial\mathcal{F}}{\partial p}\right)_\rho \tag{4.35}$$

4.2.2 Initial and boundary conditions

Initial and boundary conditions must be provided to carry out the integration. These conditions are applied on the primitive variable vector $\mathbf{V} = \{\rho, u, v, w, p, \tilde{\mu}\}$, where also $\tilde{\mu}$ has been included for a uniform notation. Hence the number of condition must be 6.

Initial conditions are necessary to start the integration. The vector $\mathbf{V}$ is assigned at the channel entrance and the corresponding initial $\tilde{F}_e$ can be computed.

Boundary conditions are necessary to provide the transverse fluxes on the computational domain boundary. If the vector $\mathbf{V}$ is assigned on the boundary the corresponding transverse fluxes can be computed. Two conditions are taken into consideration: a viscous or an Eulerian wall (symmetry condition).

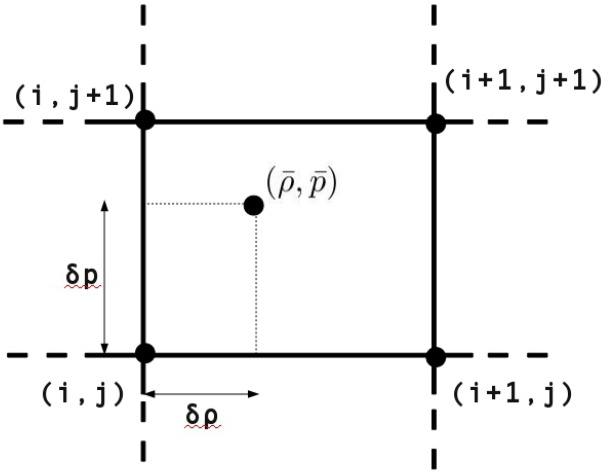

Figure 4.4: Subregion of the two dimensional grid of Fig. 4.3

- *Viscous wall.* The no slip and impermeability conditions imply respectively that the tangential and normal velocities are null. Moreover for the impermeability condition also the pressure gradient normal to the wall has to be null. Finally the temperature gradient at the wall can be evaluated from an assigned heat flux (which is zero in the adiabatic case), or the wall temperature is assigned for an isothermal condition. In any case the conditions on pressure and temperature involve a condition on the density. Finally the turbulent viscosity at the wall is zero by definition. These boundary conditions can be expressed mathematically as follows:

$$\begin{cases} u = v = w = 0 \\ \dfrac{\partial p}{\partial n} = 0 \\ k_\ell \dfrac{\partial T}{\partial n} = \bar{q}_w \text{ or } T = T_w \\ \tilde{\mu} = 0 \end{cases} \tag{4.36}$$

- *Symmetry condition.* The normal derivatives of the thermodynamic variables p and ρ, of the turbulent viscosity and of the velocity tangential to the wall are null, and the normal velocity component is null. Hence introducing the normal and tangential unit vectors at the wall $\mathbf{n}$ and $\mathbf{t}$, and indicating the vector velocity $\mathbf{U} = \{u, v, w\}$, these conditions can be expressed as:

$$\begin{cases} \mathbf{U} \cdot \mathbf{n} = 0 \text{ and } \dfrac{\partial \mathbf{U} \cdot \mathbf{t}}{\partial n} = 0 \\ \dfrac{\partial p}{\partial n} = 0 \\ \dfrac{\partial \rho}{\partial n} = 0 \\ \dfrac{\partial \tilde{\mu}}{\partial n} = 0 \end{cases} \tag{4.37}$$

The boundary conditions are fundamental to obtain the correct solution of the test case of interest. For example a straight channel with a circular cross section can be investigated with a 2D axisymmetric configuration which is obtained considering a suitable geometry and suitable boundary conditions. The 2D axisymmetric integration domain is a cylinder slice, as shown in Fig. 4.5. A symmetry boundary condition is imposed on the lateral surfaces S_1 and S_2, and a viscous wall boundary condition on the channel surface $S_{w,i}$. The symmetry axis (x-axis in Fig. 4.5) is a degenerate surface that is with a null area. This implies that all the fluxes at the symmetry axis must be assigned null.

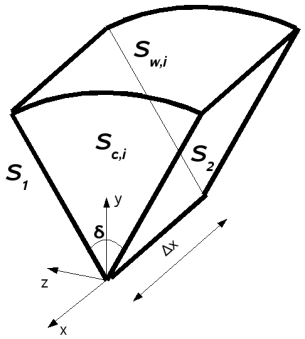

Figure 4.5: Schematic of a 2D axisymmetric integration domain

4.2.3 Eulerian fluxes

In the present Godunov type scheme the Eulerian fluxes $\mathbf{G_e}$ and $\mathbf{H_e}$ are obtained at each cell interface as solutions of Riemann problems. The simplest approach is to consider that over each cell the primitive variable vector $\mathbf{V} = \{\rho, u, v, w, p, \tilde{\mu}\}$ is constant. This situation is schematically depicted in Fig. 4.6 for a two dimensional case. Therefore, there is a discontinuity at each intercell $j + 1/2$ from which arises a Riemann problem. The Riemann problem solution gives the unknown fluxes at the interface. This approach, in which a piecewise constant solution is considered at each integration step, gives a first order accurate scheme. Rather to obtain a second order accurate scheme linear reconstructions of the solution over each cell must be considered. This is the followed approach in the developed scheme. Unfortunately linear reconstructions can bring to spurious oscillations in the solution and hence a further trick must be considered to obtain a Total Variation Diminishing (TVD) scheme. This is done considering a slope limiter which permits to suitably choose the reconstruction slope over each cell so to avoid oscillations. In particular the *Minmod* slope limiter have been selected. For example if we consider a two dimensional case at each integration step i linear reconstruction of $\mathbf{V}$ must be considered in the y direction for every j cell. To obtain a linear reconstruction two information must be provided:

1. a value in a point in the cell: the average over the cell is associated with the cell center

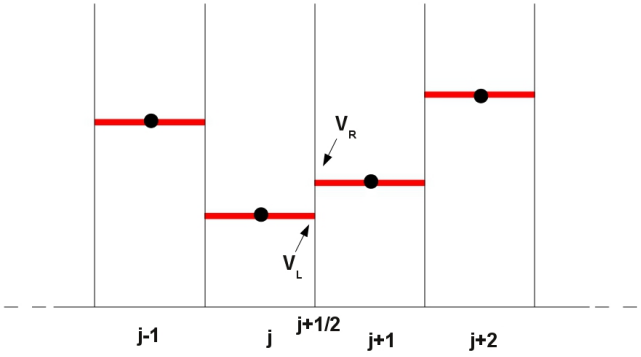

Figure 4.6: Discontinuity between left and right states arising at each intercell $j+1/2$ with constant reconstruction of the primitive variable vector $\mathbf{V}$

2. the slope of the line: there are two possible slopes $\Delta\mathbf{V}_0 = \mathbf{V}_j - \mathbf{V}_{j-1}$ and $\Delta\mathbf{V}_1 = \mathbf{V}_j - \mathbf{V}_{j+1}$

the Minmod slope limiter permits to select the slope in the following manner:

$$\Delta\mathbf{V} = \begin{cases} \min(\Delta\mathbf{V}_0, \Delta\mathbf{V}_1) \text{ if } \Delta\mathbf{V}_0 > 0 \text{ and } \Delta\mathbf{V}_1 > 0 \\ \max(\Delta\mathbf{V}_0, \Delta\mathbf{V}_1) \text{ if } \Delta\mathbf{V}_0 < 0 \text{ and } \Delta\mathbf{V}_1 < 0 \\ 0 \text{ if } \Delta\mathbf{V}_0 \cdot \Delta\mathbf{V}_1 < 0 \end{cases} \tag{4.38}$$

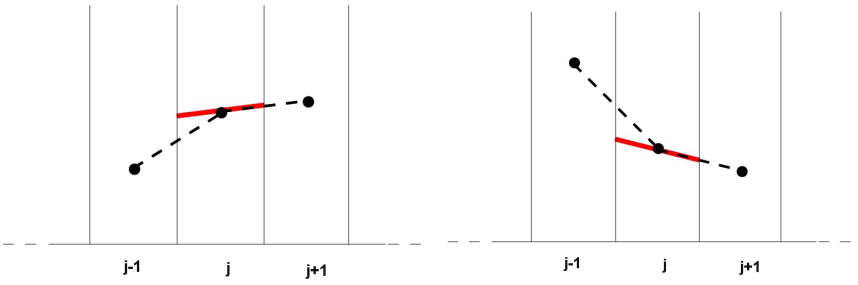

(a) $\Delta\mathbf{V}_0 > 0,\ \Delta\mathbf{V}_1 > 0$ (b) $\Delta\mathbf{V}_0 > 0,\ \Delta\mathbf{V}_1 < 0$

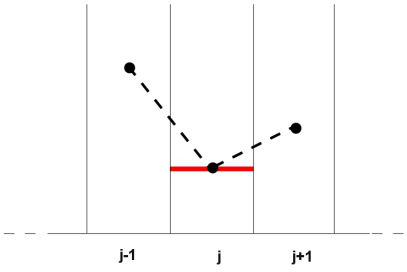

(c) $\Delta\mathbf{V}_0 \cdot \Delta\mathbf{V}_1 < 0$

Figure 4.7: Linear reconstruction with *Minmod* slope limiter

Minmod slope limiter effect on the linear reconstruction is schematically represented in Fig. 4.7 for a generic variable which is one of the $\mathbf{V}$ vector components. If

both the slopes have the same sign, the Minmod slope limiter select the smaller slope in absolute value. This situation is depicted in Fig. 4.7(a)-4.7(b) for positive and negative slopes respectively. On the contrary if the slopes have different signs a zero value is selected as it is the case in Fig. 4.7(c). Finally an example of the discontinuity that arises at each interface with these linear reconstructions is reported in Fig. 4.8.

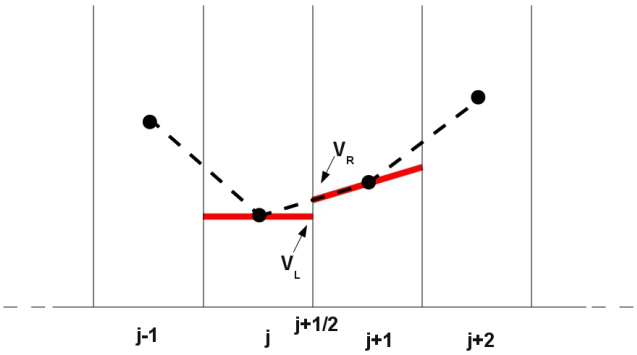

Figure 4.8: Discontinuity between left and right states arising at each intercell $j+1/2$ with linear reconstruction of the primitive variable vector $\mathbf{V}$ using a Minmod slope limiter

Once the linear reconstructions of the solution have been carried out the transverse Eulerian fluxes $\mathbf{G_e}$ and $\mathbf{H_e}$ have to be evaluated on the boundary S_l through the solution of the above mentioned Riemann problems. Multidimensional Riemann problems can always be reduced to 1D problems in the normal direction to the surface [4]. Therefore the Roe's Riemann solver presented in Section 3.4 for a 2D PNS system is used. The Riemann solver has been developed for PNS and a generic EoS $h = h(p, \rho)$. The main steps necessary to provide the approximate solution of the Riemann problem are reported. To this aim the Eulerian part of the PNS system is written in divergence form for a 2D case (omitting the subscript which are not necessary here):

$$\frac{\partial \mathbf{F}}{\partial x} + \frac{\partial \mathbf{G}}{\partial y} = 0 \tag{4.39}$$

with

$$\mathbf{F} = \begin{Bmatrix} \rho u \\ \rho u^2 \\ \rho uv \\ \rho u h_0 \end{Bmatrix} \qquad \mathbf{G} = \begin{Bmatrix} \rho v \\ \rho uv \\ \rho v^2 + p \\ \rho v h_0 \end{Bmatrix} \tag{4.40}$$

The Riemann problem occurring at each interface $(j + 1/2)$ between the cells j and $j+1$ is schematically reported in Fig. 4.9: the solution of the problem should provide the fluxes $\mathbf{G}_{j+1/2}$ at the interface necessary to update the solution from the step i to the step $i + 1$ in the x streamwise direction.

The system (4.39) can be written in a linear form using the constant Roe's matrix $\tilde{\mathbf{A}}$:

$$\frac{\partial \mathbf{F}}{\partial x} + \tilde{\mathbf{A}} \frac{\partial \mathbf{F}}{\partial y} = 0 \tag{4.41}$$

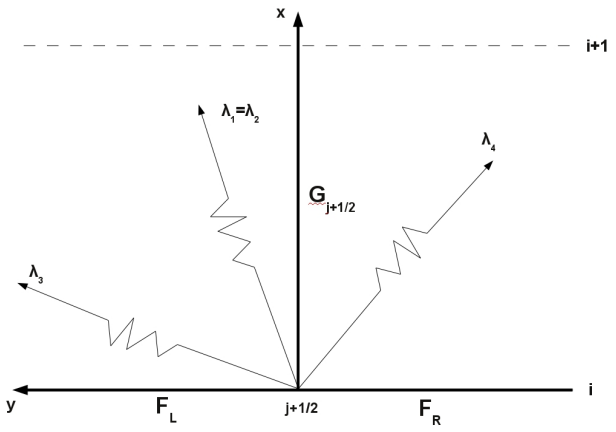

Figure 4.9: Schematic of a Riemann problem at a cell interface

If $\tilde{\lambda_i}$ are the eigenvalues of $\tilde{\mathbf{A}}$ and $\mathbf{r}^{(i)}$ the corresponding eigenvectors, the solution of the Riemman problem is given by:

$$\mathbf{G}_{j+1/2} = \frac{1}{2}(\mathbf{G_R} + \mathbf{G_L}) - \frac{1}{2}\sum_{i=1}^{4} |\tilde{\lambda_i}| a_i \mathbf{r}^{(i)} \tag{4.42}$$

In Eq. (4.42) a_i are the projections of the jump $\Delta\mathbf{F} = \mathbf{F}_L - \mathbf{F}_R$ on the eigenvectors as a basis:

$$\Delta\mathbf{F} = \sum_{i=1}^{4} a_i \mathbf{r}^{(i)} \tag{4.43}$$

The matrix $\tilde{\mathbf{A}}$ is expressed in terms of an average state defined by the following equation:

$$\varphi = \frac{\rho_R^{1/2}\varphi_R + \rho_L^{1/2}\varphi_L}{\rho_R^{1/2} + \rho_L^{1/2}} \tag{4.44}$$

with φ being u, v ,h_0 or p. With these notations the eigenvalues of the matrix $\tilde{\mathbf{A}}$ are:

$$\tilde{\lambda_{1,2}} = \frac{v}{u} \qquad \tilde{\lambda_{3,4}} = \frac{(2-\beta)v}{2u} \pm \frac{\sqrt{\tilde{\Delta}}}{2u} \tag{4.45}$$

$$\tilde{\Delta} = \beta^2 v^2 + 4(\beta h + \alpha) \tag{4.46}$$

The corresponding eigenvectors are:

$$\mathbf{r^{(1)}} = \begin{Bmatrix} 1 \\ 0 \\ 0 \\ -2\dfrac{\alpha}{\beta} - h_0 \end{Bmatrix} \quad \mathbf{r^{(2)}} = \begin{Bmatrix} q^2/(2(2\dfrac{\alpha}{\beta} + h_0)) + 1 \\ 2u \\ 2v \\ h_0 + \dfrac{q^2}{2} \end{Bmatrix} \quad \mathbf{r^{(3,4)}} = \begin{Bmatrix} u \\ u^2 \\ \tilde{\lambda_{3,4}} u^2 \\ uh_0 \end{Bmatrix} \tag{4.47}$$

Finally α and β are two parameters computed according to the used EoS and are expressed in terms of density, static enthalpy and its derivatives to respect to pressure

and density evaluated, as all the other variables, in the average state of Eq. (4.44), with the following expressions:

$$\alpha = -\frac{h + \rho h_\rho}{\rho h_p} \qquad \beta = \frac{1}{\rho h_p} \tag{4.48}$$

with h_p and h_ρ defined by Eq. (3.22). The projections a_i of the jumps along the eigenvectors are computed solving the linear system of Eq. (4.43) with the LAPACK routine DGESV.

4.2.4 Viscous fluxes

Second order accurate evaluations must be used also for the viscous fluxes $\mathbf{G_v}$ and $\mathbf{H_v}$. This is obtained considering central differences between adjacent cells for the primitive variable vector $\mathbf{V}$. Hence the first order derivatives appearing in these fluxes are simply evaluated as ratios between the jumps $\Delta(\cdot) = (\cdot)_L - (\cdot)_R$, whereas the local value is evaluated as an arithmetic mean: $(\cdot)_m = 0.5((\cdot)_L + (\cdot)_R)$. As an example in a two dimensional case the viscous flux $\mathbf{G_v}$ at each intercell $j + 1/2$ is evaluated according to:

$$\mathbf{G_v} = \left\{ \begin{array}{c} 0 \\ \mu \dfrac{\partial u}{\partial y} \\ \dfrac{4}{3}\mu \dfrac{\partial v}{\partial y} \\ uG_{v,2} + vG_{v,3} + k\dfrac{\partial T}{\partial y} \\ \dfrac{1}{\sigma}(\mu_\ell + \tilde{\mu})\dfrac{\partial \tilde{\nu}}{\partial y} \end{array} \right\} \quad \rightarrow \quad \left\{ \begin{array}{c} 0 \\ \mu_m \dfrac{\Delta u}{\Delta y} \\ \dfrac{4}{3}\mu_m \dfrac{\Delta v}{\Delta y} \\ uG_{v,2} + vG_{v,3} + k_m\dfrac{\Delta T}{\Delta y} \\ \dfrac{1}{\sigma}(\mu_{\ell,m} + \tilde{\mu}_m)\dfrac{\Delta \tilde{\nu}}{\Delta y} \end{array} \right\} \tag{4.49}$$

4.2.5 The streamwise pressure gradient

How to treat the streamwise pressure gradient is one of the more delicate and critical points in all the PNS approaches present in literature. In the present approach the whole streamwise pressure gradient is considered as a source term which has to be evaluated at each integration step. To this aim it is assumed that the pressure gradient in the streamwise direction is constant along each transverse plane, namely it does not depend on the position in the transverse plane. This is a good approximation in a straight channel, whereas if curved channels have to be investigated further assumptions should be made. Nevertheless it is important to note that only the streamwise pressure gradient is assumed constant over the crosswise section while the pressure can vary: in fact none hypothesis has been made on the crosswise pressure gradients $\dfrac{\partial p}{\partial y}$ and $\dfrac{\partial p}{\partial z}$ which allow the pressure to vary over the section.

The $\dfrac{\partial \mathbf{P}}{\partial x}$ term in Eq. (4.1) is evaluated with an iteration process, imposing the conservation of the integral momentum equation for each step of channel of length Δx. Referring to Fig. 4.2 the pressure variation has to verify the following balance

equation:

$$\int_{\mathcal{S}_{c,i+1}} (\rho u^2 + p) dS = \int_{\mathcal{S}_{c,i}} (\rho u^2 + p) dS - \int_{\mathcal{S}_{w,i}} \mu \frac{\partial u}{\partial n} d\mathcal{S} \tag{4.50}$$

in which $\mathcal{S}_{c,i+1}$ indicates the channel cross section surface, and $\mathcal{S}_{w,i}$ the wall surface of channel in the length Δx. For example, for a 2D planar channel Eq. (4.50) becomes:

$$\frac{d}{dx}\left(\int_0^H (\rho u^2 + p) dy\right) - \left(\mu \frac{\partial u}{\partial y}\bigg|_H - \mu \frac{\partial u}{\partial y}\bigg|_0\right) = 0 \tag{4.51}$$

where H is the height of the channel.

Thus the evaluation of the streamwise pressure gradient implies an iteration process. If the solution $\widetilde{\mathbf{F}}_{\mathbf{e,i}}$ is known at a certain streamwise step i, once the Eulerian and viscous fluxes have been evaluated and an initial value is given for the source term $\mathbf{\Delta P}$ it is possible to march in space and evaluate the solution $\widetilde{\mathbf{F}}_{\mathbf{e,i+1}}$ at $i+1$ according to Eq. (4.28), except that the momentum balance of Eq. (4.50) will not be verified. Therefore an iteration process is started looking for the value of $\mathbf{\Delta P}$, considered constant for each integration cell, which will permit to verify Eq. (4.50). A secant iteration method algorithm permits to find the correct $\mathbf{\Delta P}$ in a few iterations: as starting value the $\mathbf{\Delta P}$ at the previous space marching step is considered. Note that only the second component of the $\mathbf{F_e}$ flux is involved in this iteration process, since it is in fact the only flux influenced by the streamwise pressure gradient within the hypothesis that have been made (namely that the streamwise pressure gradient is constant in the transverse direction). This makes the iteration process to find the pressure gradient rather cheap in terms of computational cost.

Chapter 5

Validation of the Numerical Method

The numerical model has been tested and validated for 2D axisymmetric configurations so as to demonstrate its suitability for the cooling channel flows analysis. In the following the results of a numerical simulation carried out on a supercritical methane adiabatic flow are first exposed and analyzed. In particular, the turbulence model is investigated and a convergence analysis is carried out. The purpose of these investigations is to demonstrate the capability of the numerical method to study the configurations of interest. Then validation is carried out by making comparisons with numerical results obtained with a standard density based full Navier-Stokes solver and with experimental data.

5.1 Numerical investigations

5.1.1 Supercritical methane flow

A numerical investigation has been carried out on a turbulent flow of supercritical methane in a straight channel with a high length over diameter ratio. The dimensions are within the expected range for liquid rocket cooling channels (see Chap. 1). More precisely the channel has a diameter of $D = 4$ mm and a length of $L = 100\ D$. A length of $50\ D$ is sufficient to obtain a turbulent developed flow and therefore a developed flow is expected in the second half of the present channel. At the channel inlet methane has a supercritical pressure of $p = 13$ MPa and a subcritical temperature of $T = 118$ K. These values correspond to a reduced pressure $p_r = 2.83$ and a reduced temperature $T_r = 0.62$ and therefore it is a compressed fluid which has a liquid-like behavior and hence a very low compressibility. Moreover, the flow inlet velocity is low ($u_{in} = 20$ m/s) and hence the inlet Mach number is also very low: $M_{in} = 0.014$. The solution can be analyzed both observing the two-dimensional field and the bulk variables. Different definitions of bulk variables can be found in literature: the definitions that have been used in the present study are reported in Appendix F. In Fig. 5.1 the velocity profiles at different streamwise stations along the channel are reported in a schematic of the channel: to help figure readability no unit is reported for the velocity whereas the same velocity profiles with a scale for the velocity are reported in Fig. 5.2(a). Because constant inlet conditions are enforced, the first space

marching steps cannot be considered physically correct. Nevertheless, this initial incorrectness is soon overcome along the channel. Indeed the boundary layer correctly grows and a developed flow is obtained at 50 diameters, as it is expected for a turbulent flow. In fact, as can be observed in Fig. 5.2(a) the velocity profiles at $x/D \geq 50$ are nearly superimposed. The boundary layer development can also be deduced by the wall shear stress behavior depicted in Fig. 5.2(b). It can be observed that the shear stress initially decreases because of the increase of the boundary layer thickness then, once the influence of the wall reaches the whole channel, it starts to grow, and finally reaches a constant value in the developed region. Of course, the flow is never truly developed as it should be for ideal incompressible flow and in fact the velocity profile continues to slightly variate also for $x/D > 50$ (see Fig. 5.2(a)). However, the fact that the shear stress can be considered constant in the second half of the channel demonstrates that the present supercritical fluid is very similar to a liquid (and this is why is referred to as "liquid-like"). These results confirm the validity of the developed methodology, especially with respect to the following delicate aspects:

1. capability of describing a liquid-like flow with a very low Mach number with a density based solver;

2. capability to get a correct flow evolution by enforcing uniform initial conditions in the radial direction. In the algorithm results stable despite the very strong gradients just downstream the inlet. This is a very interesting feature for the developed numerical tool because it permits to easily choose the dynamic and thermodynamic inlet conditions and hence facilitates parametric studies.

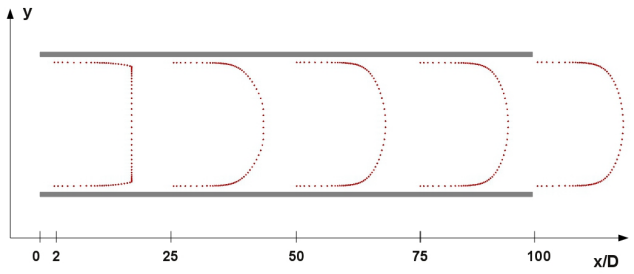

Figure 5.1: Schematic of velocity profiles for an adiabatic, turbulent methane channel flow (not to scale)

5.1.2 Turbulent law of the wall

In the present simulations turbulence has been modeled with a RANS approach together with the Spalart-Allmaras closure model modified to suit PNS hypothesis. It is well known that the original Spalart-Allmaras model [144] is build precisely to fit the wall logarithmic law: to verify that the modifications that have been made for the PNS model do not change this behavior, a comparison of a velocity profile in *wall coordinates*, $u^+ = u/u_\tau$ and $y^+ = y/y_\tau$, with what is expected from the law of the wall theory has been carried out. The friction velocity u_τ and the characteristic

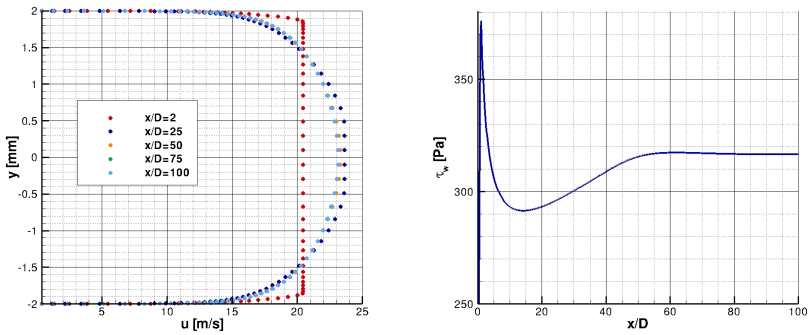

(a) velocity (b) wall shear stress

Figure 5.2: Velocity profiles at different streamwise stations, and wall shear stress for an adiabatic flow of turbulent methane

length y_τ are defined as:

$$u_\tau = \sqrt{\frac{\tau_w}{\rho}} \qquad y_\tau = \frac{\nu}{u_\tau} \tag{5.1}$$

where the kinetic viscosity ν and the density ρ are evaluated at the wall together with the wall shear stress τ_w. For turbulent flow conditions the velocity profile can be split into three different regions: the viscous sublayer, the logarithmic layer and the defect layer [8]. From the law of the wall theory the form of the solution in the viscous sublayer is linear in wall coordinates:

$$u^+ = y^+ \tag{5.2}$$

whereas in the logarithmic region the following logarithmic law should be valid:

$$u^+ = \frac{1}{\kappa} log(y^+) + B \tag{5.3}$$

with $\kappa = 0.41$ (von Kàrmàn constant) and B a constant ($B \sim 5$). In Fig. 5.3 a velocity profile in wall coordinates at the end of the channel is compared with Eq. (5.2) in the viscous sublayer region and with Eq. (5.3) in the logarithmic layer with $B = 5.1$: a perfect agreement is found. This demonstrates the validity and good implementation of the parabolized version of the Spalart-Allmaras closure model.

5.1.3 Grid convergence

Attention must be devoted on the grid generation which is an important part of any numerical study. Detail on the grid used for the test cases of the present work are given in Appendix E.

To verify if the number of cells is sufficient to get the solution of the PNS equations, a grid convergence analysis has been carried out on the test case analyzed in the previous section. In particular the same test case has been simulated with three different grids having 20, 40 and 80 cells in the radial direction. The results are

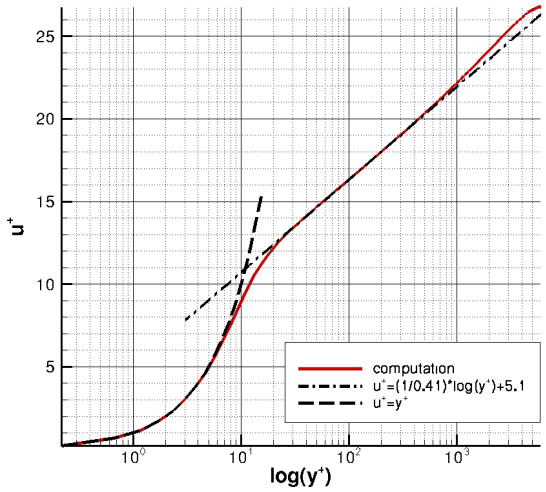

Figure 5.3: Comparison between numerical and theoretical velocity profiles in wall coordinates.

reported in Fig. 5.4 for the wall shear stress and the bulk pressure. The transverse spatial order of accuracy r_s for the variable s can be evaluated according to Richardson method [6, 20] by the following expression:

$$r_s = \ln\left(\frac{s_c - s_m}{s_m - s_f}\right)\frac{1}{\ln(\bar{h})} \tag{5.4}$$

where $\bar{h}$ is the refinement factor between one grid and another ($\bar{h} = 2$ in the present convergence analysis). The subscript (c), (m) and (f) refer respectively to the coarse, medium and fine solution. The computed order of accuracy is close to the formal one (which is 2, see Chap. 4) for all the solution quantities as can be observed for the bulk pressure and the wall shear stress in Fig. 5.4. As an example in Tab. 5.1 the order of accuracy is calculated with Eq. (5.4) in the streamwise station $x/D = 100$. An estimation of the solution s_{ex} that could be obtained in the limit $N \to \infty$ is given by the Richardson extrapolation:

$$s_{ex} = \frac{\bar{h}^{r_s} s_f - s_m}{\bar{h}^{r_s} - 1} \tag{5.5}$$

An estimation of the numerical error can be carried out comparing the Richarson extrapolation with the computed solution. The errors analyzed with this method for the local variables are of the order of 1% for the coarse grid, 0.2% for the medium grid and 0.1% for the fine grid. Note that the errors for the bulk variables are smaller and this is mainly due to the fact that the averages reduce the difference between one grid and another (see Appendix F for the details of the bulk variables evaluation). As an example of the above estimated numerical error the extrapolated wall shear stress and bulk pressure are reported for $x/D = 100$ in Tab. 5.1.

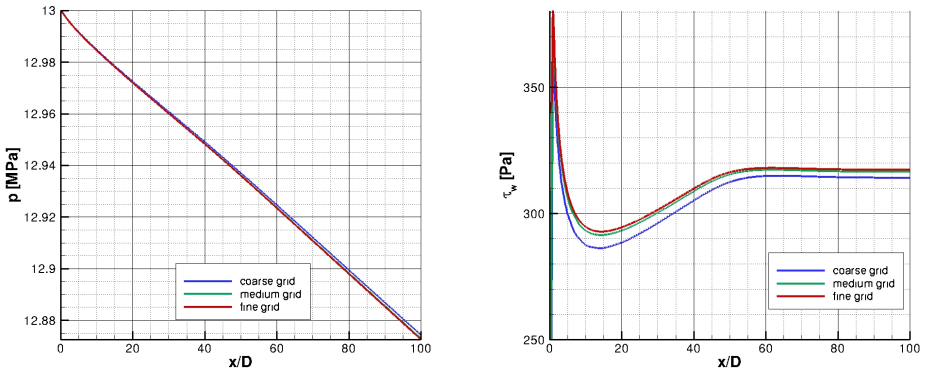

(a) bulk pressure

(b) wall shear stress

Figure 5.4: Results obtained with three different grid levels in the radial direction: coarse grid (N=20), medium grid (N=40) and fine grid (N=80)

	coarse	medium	fine	extrapolated	r
τ_w[Pa]	314.156	316.564	317.343	317.719	**1.62**
p_b[MPa]	12.8743	12.8729	12.8725	12.8723	**1.7**

Table 5.1: Grid convergence analysis: calculation of the spatial order of accuracy and Richardson extrapolation.

5.2 Validation: comparison between PNS and FNS results

To validate the PNS solver for a perfect gas, either in a laminar or turbulent condition, comparisons have been made with the results obtained with the full Navier-Stokes solver presented in [122], for a 2D planar flow and a 2D axisymmetric flow. The fluid is air in a perfect gas condition. The parameters of all the test cases presented in the following are listed in Table 5.2.

Test case	Geometry	Flow	p_{in} [MPa]	T_{in} [K]	M_{in}	q_w [MW/m^2]	D or H [mm]	L [cm]
TC1	planar	laminar	0.164	424	0.60	0.00	5	100
TC2	planar	turbulent	0.234	412	0.21	0.10	5	25
TC3	axisymmetric	laminar	0.243	311	0.14	0.01	4	50
TC4	axisymmetric	turbulent	0.244	304	0.12	0.00	4	10
TC5	axisymmetric	turbulent	0.244	312	0.12	0.01	4	10
TC6	axisymmetric	turbulent	0.245	422	0.10	0.10	4	10

Table 5.2: Test case inlet conditions and geometric parameters . Fluid: air

5.2.1 2D planar flow

Results obtained with the FNS and PNS solvers for 2D planar channels are compared for the following two test cases:

1. Laminar adiabatic flow (TC1);
2. Turbulent non adiabatic flow (TC2).

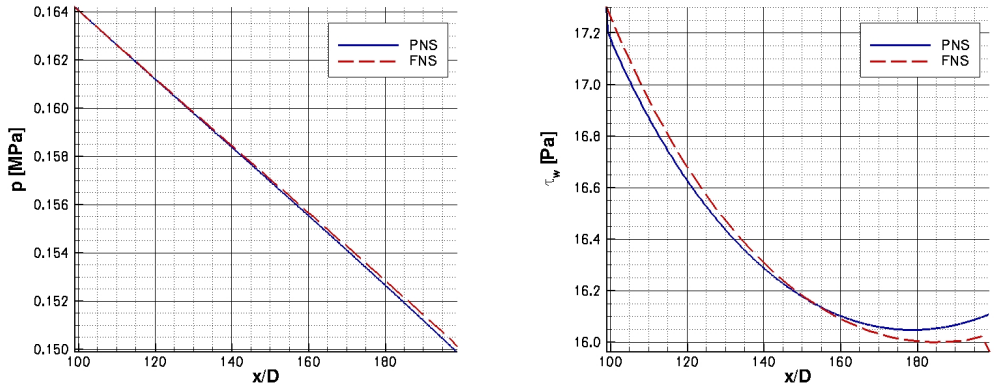

(a) pressure (b) wall shear stress

Figure 5.5: Comparisons between FNS and PNS for a 2D planar adiabatic laminar flow (TC1)

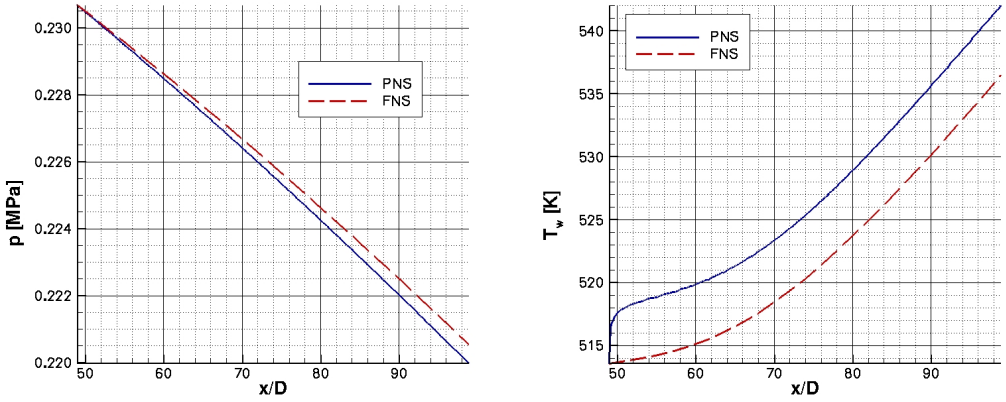

(a) pressure (b) wall temperature

Figure 5.6: Comparisons between FNS and PNS for a 2D planar heated turbulent flow of air in perfect gas conditions (TC2)

Inlet and outlet boundary conditions have to be imposed in the full Navier-Stokes code: the stagnation state at the entrance (pressure and temperature) and the static

exit pressure. The geometric parameters of the computational domain (L is the length of the channel) are reported in Table 5.2. The density, pressure and velocity profiles at a distance $L/2$ from the entrance ($x = 0$) are enforced as the initial condition of the PNS simulations: the results are compared in the remaining $L/2$ length of the channel. Pressure, temperature and Mach number at the entrance of the channel of the PNS simulations are also reported in Table 5.2. The bulk pressure and the wall shear stress obtained with the two codes are compared in the Fig. 5.5 for the laminar test case. The displacement of the PNS solution with respect to the FNS solution is quite small: the maximum discrepancy is of 0.15% on the bulk pressure and 0.5% on the wall shear stress. For the turbulent heated flow test case TC2 (Fig. 5.6) the comparison on the wall temperature T_w is displayed instead of the wall shear stress. As can be seen also in this case the discrepancies are very small: the biggest discrepancy is on the wall temperature with a difference of 1% (Fig. 5.6(b)).

5.2.2 2D axisymmetric flow

As for the 2D planar test cases, for the 2D axisymmetric flow validation comparisons have been made between the results obtained with the FNS and the PNS codes. The following test cases are analyzed:

1. Laminar non adiabatic flow (TC3);
2. Turbulent adiabatic and non adiabatic flows (TC4,TC5 and TC6).

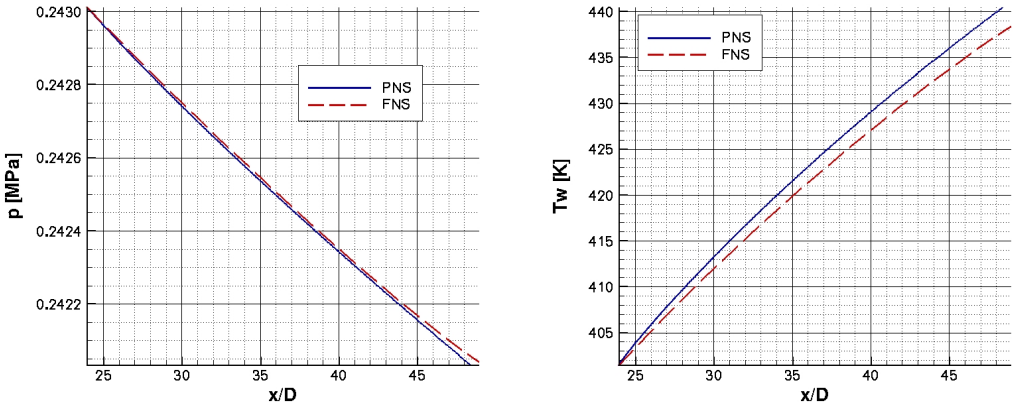

(a) pressure

(b) wall temperature

Figure 5.7: Comparisons between FNS and PNS for a 2D axisymmetric heated laminar flow of air in perfect gas conditions (TC3)

Figure 5.7 illustrates the comparisons for the bulk pressure and the wall temperature for the laminar test case: it is a non adiabatic flow with constant heat load along the channel $q_w = 10^4 \mathrm{W/m^2}$ (TC3 of Table 5.2). As can be seen the discrepancies are as small as in the 2D planar cases: the biggest discrepancy is on the wall temperature with a difference of 0.5%. The comparisons for the turbulent test cases are

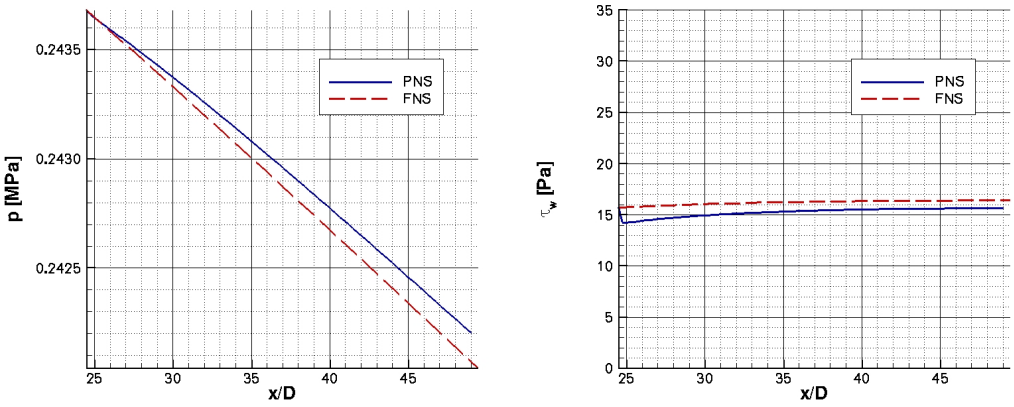

(a) pressure (b) wall shear stress

Figure 5.8: Comparisons between FNS and PNS for a 2D axisymmetric adiabatic turbulent flow of air in perfect gas conditions (TC4)

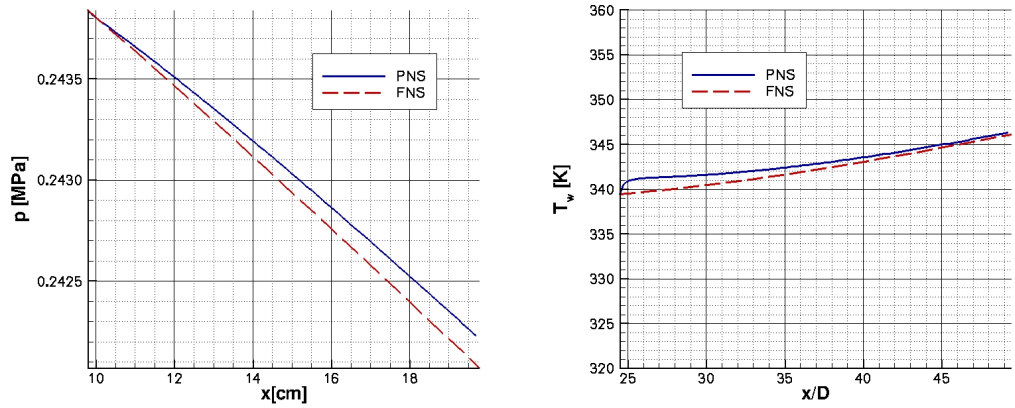

(a) pressure (b) wall temperature

Figure 5.9: Comparisons between FNS and PNS for a 2D axisymmetric heated turbulent flow of air in perfect gas conditions (TC5)

presented in Figs. 5.8, 5.9 and 5.10: TC4 is an adiabatic test case, whereas TC5 and TC6 are heated flows with a constant heat load along the channel of $q_w = 10^4 \mathrm{W/m^2}$ and $q_w = 10^5 \mathrm{W/m^2}$ respectively. The analysis of these solutions evidences a very good agreement for the bulk pressure, with discrepancies smaller than 0.05%. The differences on the wall shear stress and temperature are smaller than 5% and the trends of the PNS and FNS results are the same.

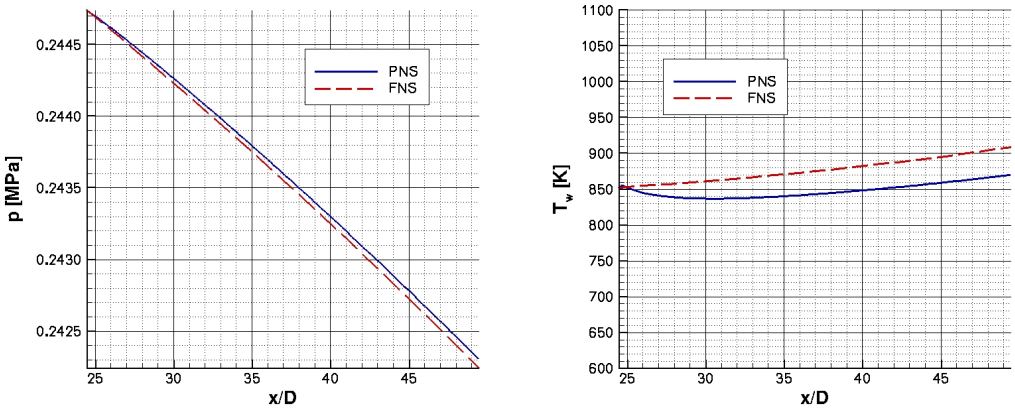

(a) pressure

(b) wall temperature

Figure 5.10: Comparisons between FNS and PNS for a 2D axisymmetric heated turbulent flow of air in perfect gas conditions (TC6)

5.2.3 Computational time

One of the advantages of the PNS approach with respect to the FNS consists in a saving of computational time. A quantification of the saving has been carried out by comparing the time it takes to compute the same flow-field with the two approaches. The test case is the TC4 of Table 5.2 except for the length which is $L = 20$ cm, that is 50 diameters. The same mesh in the transverse direction has been adopted for both the computations. The end of the computation with the two codes is obviously established by different criteria: the FNS simulation is continued until iterative convergence to the steady-state is achieved; the PNS simulation finishes when the end of the tube is reached. The computations have been carried out on an Intel (R) processor, Core(TM)2, quad core, with a 2.5 GHz CPU. The FNS computation took $\Delta t_{FNS} = 7895\ s$, whereas the PNS one only took $\Delta t_{PNS} = 299\ s$, that is more than 25 times less. This is an illustrative case but the the same order of computational time saving was obtained in all the configurations.

5.3 Validation: comparison with experimental data

The good agreement between the results obtained with the PNS and the FNS solvers demonstrates that the terms neglected because of the PNS hypothesis are of minor importance in channel test cases. However, to extend the analysis to other possible situations occurring inside rocket engine cooling channels, the case of heating of a supercritical-pressure/subcritical-temperature fluid has been considered as a further validation test. Moreover, longer channel than those studied in the foregoing section should be considered. To reach this goal, for a correct validation of the PNS solver, a test case has been selected for which experimental data are available in the open literature. In particular, the selected test case is one of those presented in [54], which is a detailed experimental study of para-hydrogen flow in heated tubes at

sub- and super-critical pressures. Among all the test cases, the "64_706" has been selected because of the particular thermodynamic condition of the hydrogen which can be of great interest in the field of rocket cooling channels. Test case inlet and exit temperature are 25 and 53 K, respectively, and the inlet pressure is 5 MPa. Consequently hydrogen operative condition is transcritical: in fact the pressure is supercritical ($T_r \simeq 3.8$) and the inlet temperature is subcritical ($T_r \simeq 0.8$) while the exit temperature is supercritical ($T_r \simeq 1.8$).

This test case is of particular interest because it presents heat transfer deterioration and one of the aim of the present work is to study such phenomena in LRE cooling channels. The heat transfer deterioration phenomena has been introduced in Chapter 1 and will be deeply studied in the following, hence no further details are given in this chapter.

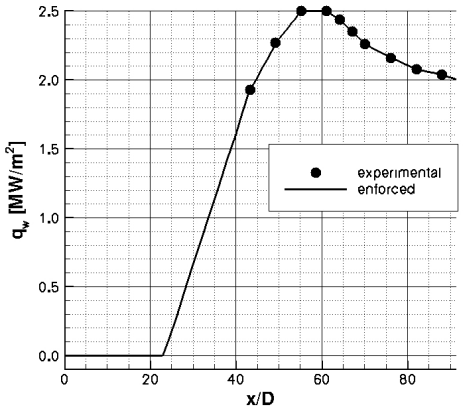

Figure 5.11: Enforced and experimental heat flux.

Some detail on the experiments are given. The mass flow rate per unit area of the tube cross section is 1324 kg/m^{2}s. The experimental apparatus, reported in Fig. 5.12, is composed by a straight tube which has a length of 91.44 cm and an internal diameter of 8.51 mm. It is electrically heated (the nominal heat flux is 2.35 MW/m^2) in the last part of the tube, whereas the first third of the tube is unheated in order to have a developed flow-field in the heated region [54]. The experimental results are measured in the heated part of the tube by means of surface thermocouples, pressure taps and voltage measurement devices, as can be observed in Fig. 5.13 where a schematic of the test-section is reported.

Computations of the 2D axisymmetric configuration are made by enforcing the following inlet boundary conditions inferred from experimental data: static pressure $p_{in} = 5.0012$ MPa, density $\rho_{in} = 71.65$ kg/m^3, velocity $u_{in} = 18.5045$ m/s and $v_{in} = 0$ m/s. These conditions provide the same values as in the experimental test of static temperature and static pressure at the first instrumented test section and mass flow rate. Moreover, zero heat flux has been imposed in the first part of the tube and a non-constant heat flux distribution in the remaining length, as reported in [54]. In fact, the measured heat flux is different than that theoretically enforced because of the dependence of the channel material electric resistance on temperature and because of heat conduction through channel walls. For the latter reason, the

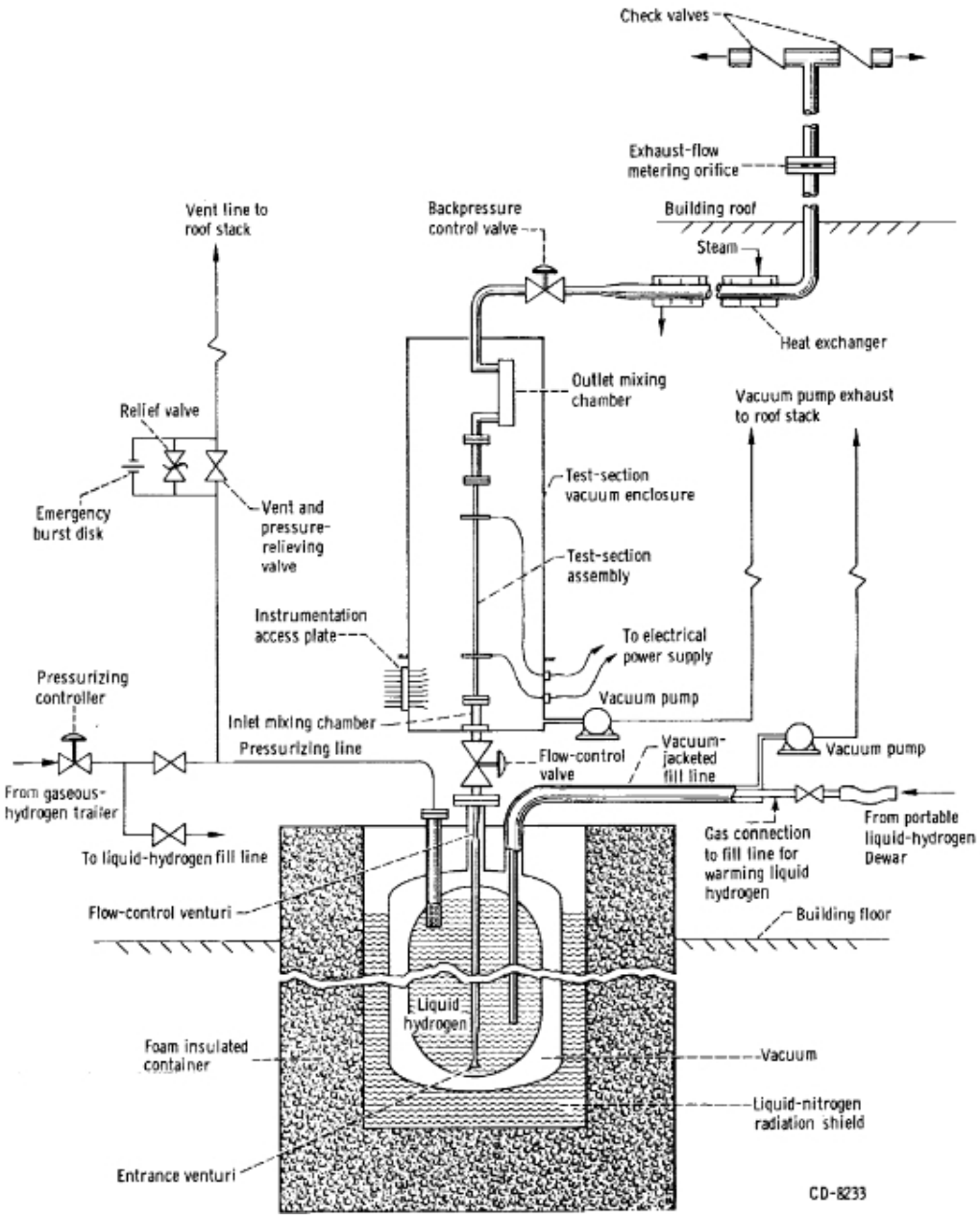

Figure 5.12: Experimental apparatus [54]

heat flux is non-zero also in the nominal unheated region and a linear interpolation has been assumed to enforce the smooth transition between the adiabatic and heated part of the channel (Fig. 5.11). The thermophysical properties of hydrogen has been evaluated according to accurate models that can be found in [170].

The numerical results are compared with the experimental data in Fig. 5.14 in terms of wall temperature and bulk temperature, pressure and velocity. Note that the heat flux deterioration is showed by the large peak of wall temperature (see Fig. 5.14(a)) occurring at $x \simeq 50$ cm. As can be seen in Fig. 5.14(b), the bulk temperature behavior is very well reproduced by the numerical simulation with a

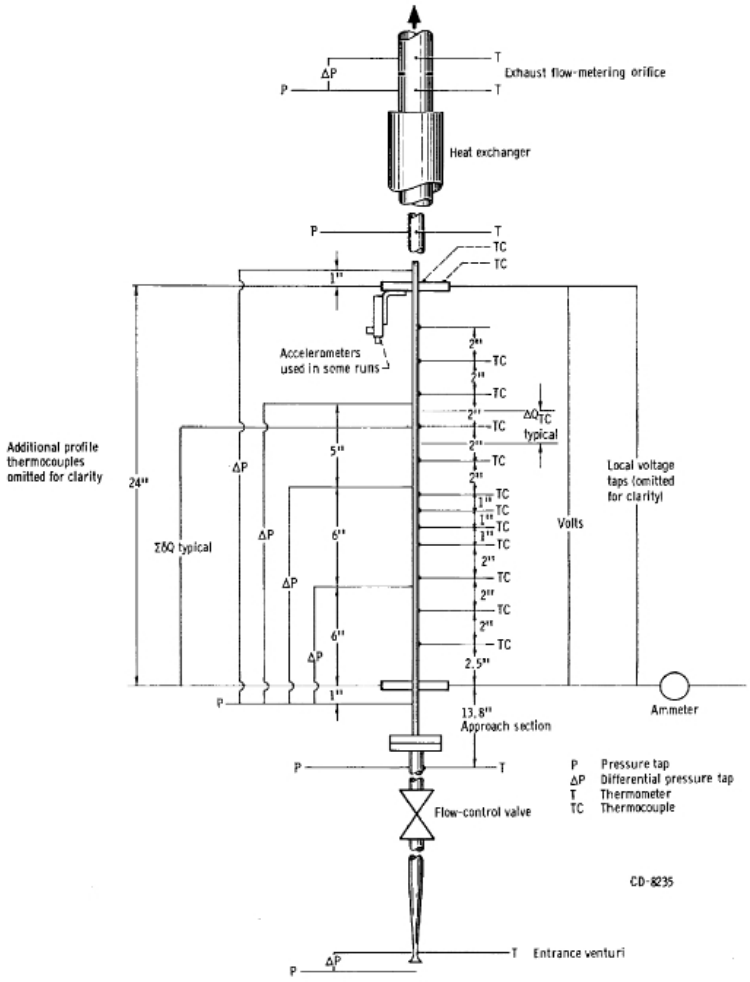

Figure 5.13: Test section [54]

discrepancy smaller than 0.2%. Also computed bulk pressure (Fig. 5.14(c)), velocity (Fig. 5.14(d)) and density (not shown here) fall in the range of experimental test results, as the maximum discrepancy is only 0.1% for pressure, 0.5% for the density and 0.6% for the velocity. The wall temperature (Fig. 5.14(a)) shows a larger discrepancy, which however remains smaller than 6%. These comparisons are very satisfactory. In fact, the data of [54] are affected by an estimated experimental error of 3% for the mass flow rate, 4% for the inlet fluid temperature and 1% for the fluid pressure. Moreover, because the value of material electric resistance is considered no better than 10% accurate, the same uncertainty affects the estimate of the heat flux as it is a function of the electric power supplied and the wall material resistance.

For the sake of completeness, the results presented in Fig. 5.14 are also compared with grid converged FNS simulations carried out for this test case in [123]. As seen in the foregoing section, there are differences between PNS and FNS results. However, if compared to experimental data, both results are included within the data uncertainty. In particular, a good agreement is found on the bulk properties, whereas there

is a greater discrepancy in the evaluation of wall properties (see for instance the wall temperature in Fig. 5.14(a)). It is interesting to note that in this case PNS results are even closer to experimental data than FNS results. Although the extremely high resolution in the streamwise direction of PNS and the different way of enforcing inlet and outlet boundary conditions could provide a partial explanation, the greater closeness of PNS results to experimental data with respect to FNS should be considered as fortuitous. The overall result is, however, that both approaches can be used to reasonably predict the flows of interest, as confirmed by comparison with experimental data. Besides, the most important result for the objectives of the present study is that the PNS approach provides solutions close to FNS also in the case of turbulent heated flow of a near critical fluid.

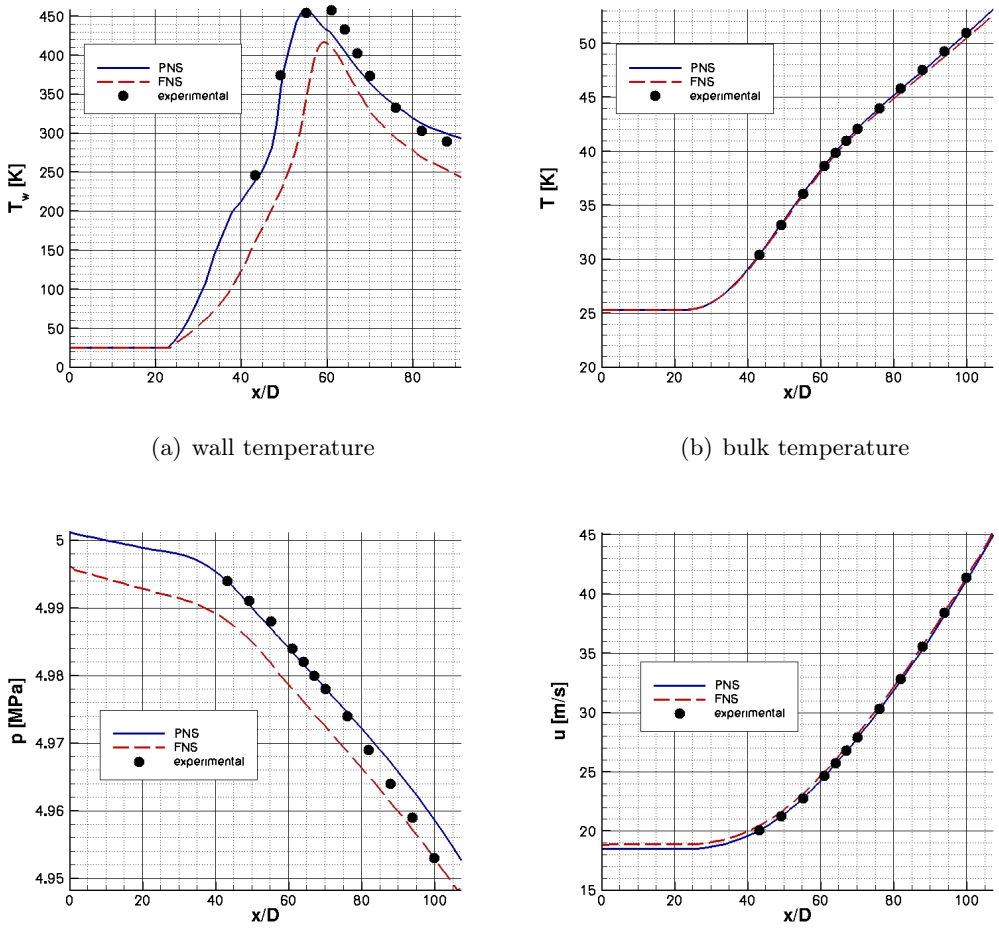

(a) wall temperature

(b) bulk temperature

(c) bulk pressure

(d) bulk velocity

Figure 5.14: Comparisons between experimental data and numerical results

The good agreement between experimental data and numerical results on this test case proves therefore that the PNS solver could be a suitable tool to study complex thermodynamic phenomena, and among all the heat transfer deterioration.

Part II

Results

Chapter 6

Numerical Analysis of LNG as a Coolant in Liquid Rocket Engines

In the recent years an interest toward methane as a rocket engine fuel (together with oxygen as oxidizer) has grown up again because of several advantages it presents if compared with other commonly used fuels. A discussion on this subject has been done in Chapter 1. It has also been emphasized that in nature the major source of methane is the natural gas. Commercial LNG is typically made up of 90% or more of methane and of ethane, propane, butane and nitrogen in different percentages for the remaining part. Further processing LNG allows one to increase methane molar fraction with the obvious increase of propellant cost. The cheaper LNG has therefore been considered as a possible rocket engine fuel instead of pure methane: in fact, due to the large amount of methane contained, LNG should have the same kind of advantages as methane. However, using LNG rather than methane may affect the behavior of the different subsystems in such a way to yield changes of overall rocket performance that have to be correctly predicted. In the present chapter attention will be devoted to the influence of the LNG composition on the regenerative cooling capability, which may strongly affect the whole system performance. To this goal an accurate thermodynamic description of LNG is important and therefore it has to be described as a gas mixture by appropriate thermodynamic models. The most important parameters useful to analyze cooling system performance are the pressure drop and the temperature increase along the channel and also their local behavior or rather their evolution along the channel. In particular, it is interesting to observe how the pressure drop and heat transfer characteristics in the cooling channels change with LNG composition. To pursue this objective the PNS solver presented in Chapter 4, together with the thermophysical models and suitable mixing rules presented in Chapter 2, is used to carry out a parametric investigation on the LNG composition influence on the propellant heat transfer behavior in cooling channels. The test case is a 2D straight axisymmetric channel, with constant heat load and a parametric study has been carried out, varying the LNG composition. The role of the percentage of the main components of LNG mixture on cooling system performance is presented on the basis of the numerical results obtained.

6.1 Test case parameters

6.1.1 Geometry and boundary conditions

To investigate the influence of the LNG composition on the heat transfer behavior in the cooling channels of a liquid rocket engine, different numerical simulations have been carried out on a 2D axisymmetric geometry, that is a straight channel with a circular cross section of diameter $D = 4$ mm. In Fig. 6.1 a schematic of the test case with the enforced boundary conditions is shown: in the first 100 diameters no heat flux is applied so as to obtain a developed flow before heating in the last 200 diameters with a constant heat load of 5 MW/m^2. The parametric study has been carried out keeping constant the following parameters:

- inlet pressure $p_{in} = 13$ MPa
- inlet temperature $T_{in} = 118$ K
- mass flow rate per unit area $G = 8500$ kg/s/m^2

Both the geometry and the boundary conditions have been selected so as to get reliable thermodynamic conditions for a rocket engine cooling channel. In particular the work of Schuff et al. [139] has been used as a reference for this purpose.

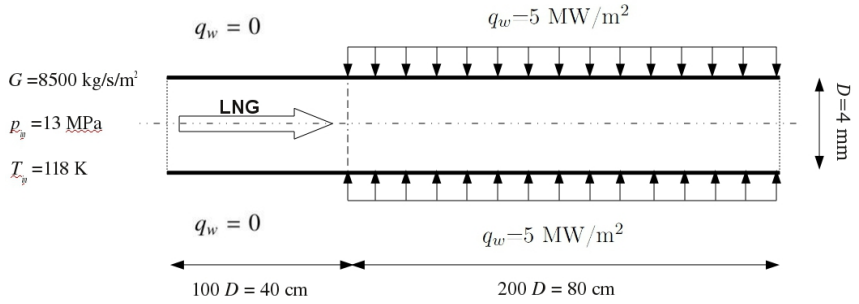

Figure 6.1: Schematic of the computational domain with the enforced boundary conditions (not to scale)

6.1.2 LNG compositions

LNG is natural gas that has been condensed to a liquid through a cooling process. Natural gas composition varies with its source (location and climate) and processing history. Raw natural gas is a mixture of up to 21 components: methane (CH_4) is the primary component with a molar fraction of at least 80%. Among the other components there are heavier hydrocarbons (ethane (C_2H_6), propane (C_3H_8),...), carbon dioxide (CO_2), nitrogen (N_2) and water (H_2O) [3,41]. Before the liquefaction process starts, hydrates, CO_2 and other components that will freeze are removed. Also hydrogen sulphide (H_2S) and mercury (Hg) are removed to ensure that the gas is neither corrosive nor toxic [79]. The LNG composition will depend on the quality specification, and is quite variable around the world, but in general the main components molar fractions vary in the ranges reported in Tab. 6.1 [9, 30, 31, 37, 51, 59, 108, 127]:

CH_4	$80 - 99\%$
C_2H_6	$1 - 17\%$
C_3H_8	$0.1 - 5\%$
C_4H_{10}	$0.1 - 2\%$
C_5H_{12} and heavier	$\leq 1\%$
N_2	$0 - 5\%$

Table 6.1: LNG composition range [9, 30, 31, 37, 51, 59, 108, 127]

In the present study the heaviest hydrocarbon that has been considered is propane. Considering the ranges listed in Tab. 6.1, the compositions of Tab. 6.2 have been used for a first set of numerical simulations. The isobaric evolution with temperature of density, specific heat at constant pressure c_p, the dynamic viscosity μ and thermal conductivity k are shown for the mixtures of Tab. 6.2 in Fig. 6.2 (these graphics have been obtained with the models presented in Chap. 2). Also pure methane curves has been reported for the sake of comparison. The temperature range goes from low subcritical to high supercritical values, whereas the inlet pressure is 13 MPa which corresponds to a supercritical value for all the mixtures. From a qualitative point of view the curves of Fig. 6.2 are similar to each other but in fact there are differences as large as 20%. The purpose of the work is precisely to investigate how these differences could influence a heated channel flow.

The mixtures of Tab. 6.2 are only representative of typical LNG composition and do not give a complete overview. A better understanding of LNG behavior for varying composition can be obtained analyzing the influence of each species taken individually as the non-methane part of the LNG mixture. To reach this goal, different binary mixtures $CH_4 - X$ are taken into consideration, where X is either ethane, propane or nitrogen. For each of the three binary mixtures four compositions have been considered with methane molar fraction being 80%, 85%, 90% and 95%.

	CH_4	C_2H_6	C_3H_8	N_2
MIX 1	92	4.0	2.2	1.8
MIX 2	86	9.5	4.0	0.5
MIX 3	93	5.0	1.5	0.5
MIX 4	88	5.0	2.0	5.0

Table 6.2: Molar fraction (in percentage) of the species in different LNG mixtures

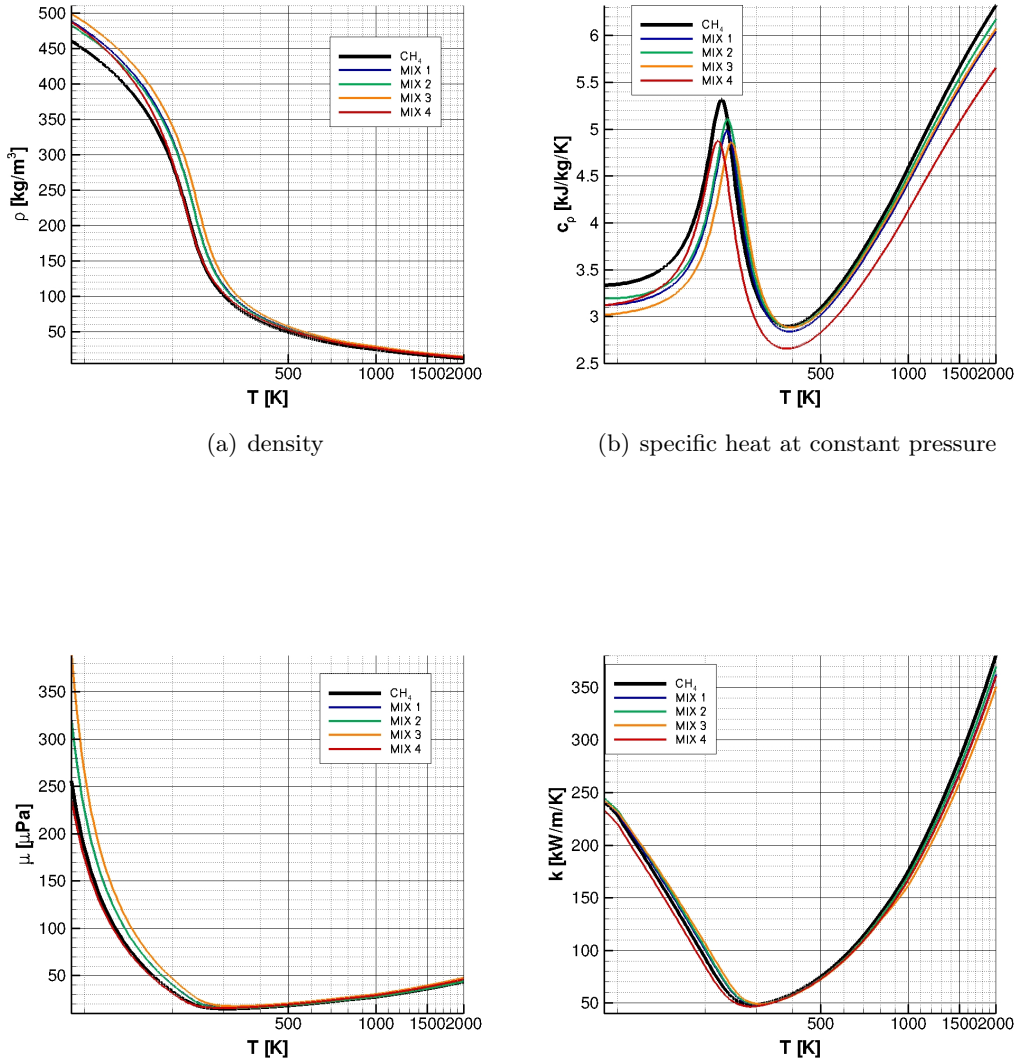

(a) density

(b) specific heat at constant pressure

(c) dynamic viscosity

(d) thermal conductivity

Figure 6.2: Density, specific heat at constant pressure, dynamic viscosity and thermal conductivity for the different LNG compositions of Tab.6.2 and for pure methane. Constant pressure $p = 13$ MPa.

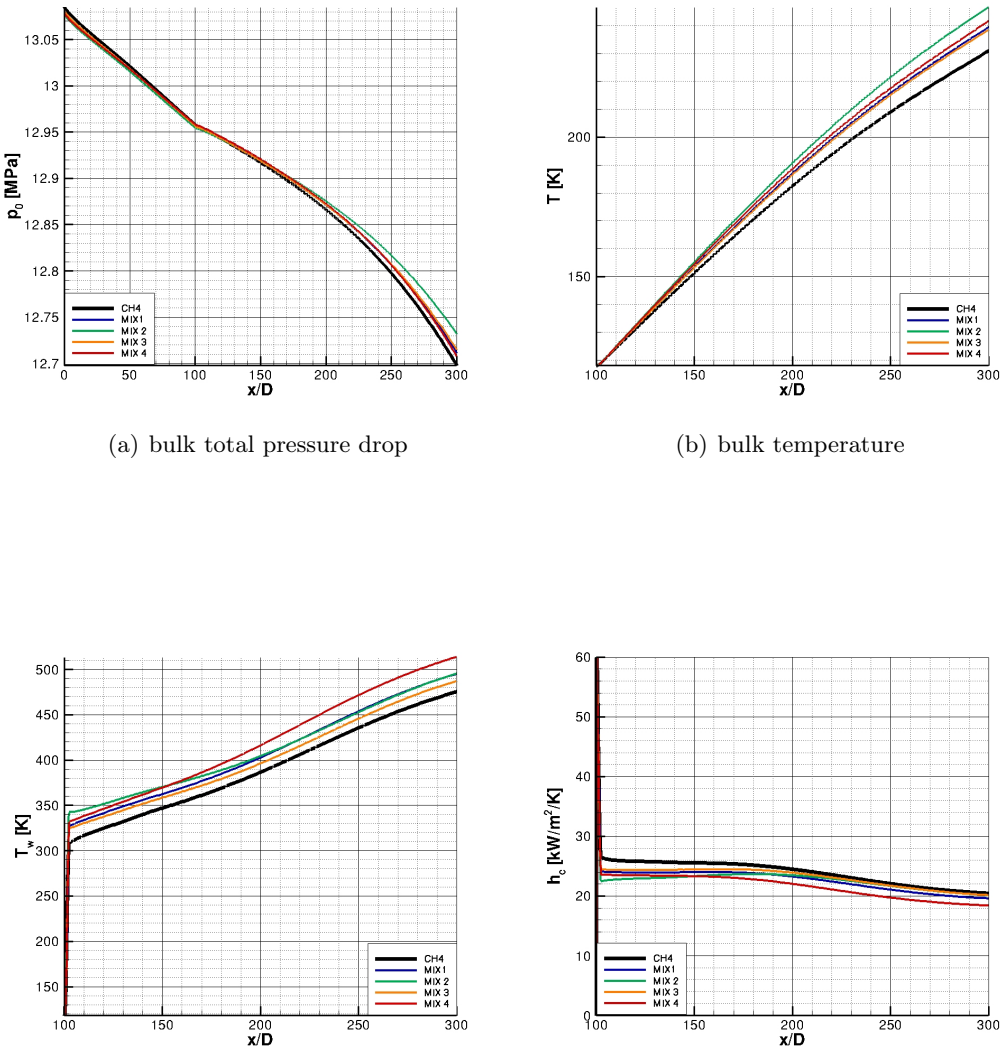

(a) bulk total pressure drop

(b) bulk temperature

(c) wall temperature

(d) convective heat transfer coefficient

Figure 6.3: Heated channel flow with the different LNG compositions of Tab. 6.2 and with pure methane.

6.2 Results

6.2.1 LNG mixtures

The results obtained for the heated channel flow considering LNG compositions of Tab. 6.2 are shown in Fig. 6.3. Before analyzing the results it has to be noted that the inlet bulk total pressure p_0 is slightly different for the different compositions (Fig. 6.3(a)): this is due to the fact that the static pressure, static temperature and mass flow rate are the same for all the cases, hence inlet density and inlet velocity differ and thus p_0. In particular inlet velocity of pure methane is greater than that of the LNG mixtures which are characterized by a greater density.

The computed bulk total pressure (Fig.6.3(a)) has a change in the trend for $x =$ 100 D corresponding to the beginning of the heated zone. In fact, in the adiabatic part of the channel the p_0 decrease only depends on the wall friction, whereas in the heated part (100 D $< x <$ 300 D) also the heat flux contributes. The p_0 behavior is similar for all the LNG compositions but the values are slightly different. This can be observed also in Fig. 6.4, where the p_0 drop in % of the inlet total pressure is reported along the channel. It appears that globally the greater total drop is found for the methane case, whereas the drops for the LNG mixtures cases are 5% to 10% smaller. Reducing the pressure drops in the cooling channels is one of the main aspects in a design phase: for an assigned chamber pressure that has to be reached the losses in the cooling channels influence the turbopump design and hence all the system. From this point of view the lower pressure drops of the LNG mixtures compared to methane can be considered a positive property of LNG.

Bulk and wall temperatures are reported in Figs. 6.3(b) and 6.3(c) only in the

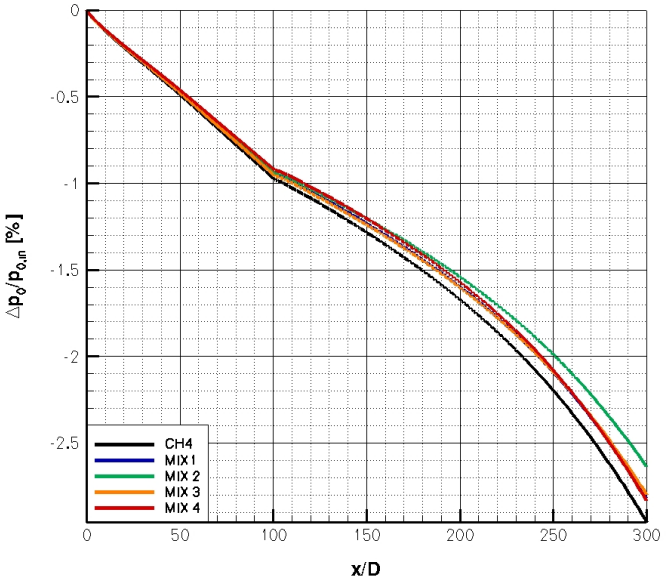

Figure 6.4: bulk total pressure drop

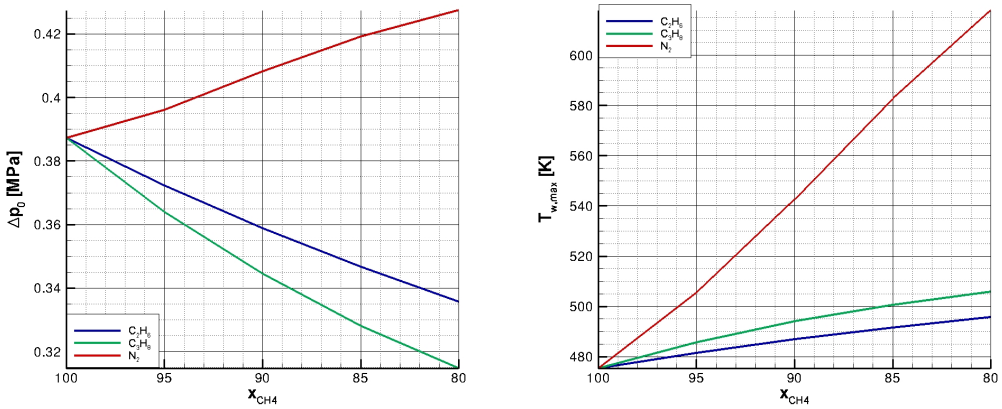

(a) bulk total pressure

(b) maximum wall temperature

Figure 6.5: Total bulk pressure drop and maximum wall temperature for three different binary mixtures $CH_4 - X$ with x_{CH4} methane percentage molar fraction

heated part of the channel because in the adiabatic part the temperatures can be considered constant. Moreover, inlet temperature is one of the parameters set equal for all the test cases and for this reason all the temperature curves start from the same point in these figures. Due to the heat load the total enthalpy increase in the heated part of channel results in an increase in both the static enthalpy, and hence the static temperature, and the velocity. Because all the test cases are characterized by the same heat flux and mass flow rate, the increase in the total enthalpy can also be considered as a fixed parameter of the analysis. As a consequence different temperature increases can be related to the different thermodynamic and transport properties. Among the investigated mixtures in Fig. 6.3, the smaller increase in the bulk temperature is found for methane and this is primarily due to its greater c_p: bulk temperature for the LNG compositions are 3% to 7% greater. Also the wall temperature is smaller for pure methane: the greater difference is found at the channel exit where LNG wall temperature is 4% to 8% greater than the methane wall temperature. To describe the relation between T, T_w and the heat transfer capabilities, the convective heat transfer coefficient h_c, is reported in Fig. 6.3(d)[1]. In the present discussion the h_c is in fact the difference between wall and bulk temperature because the same heat flux is imposed for all the cases. From Fig. 6.3(d) it appears that among the investigated compositions the pure methane case has always the greater h_c along the channel. This result permits to conclude that in the present conditions the heat transfer efficiency decreases passing from pure methane to LNG. However, it is interesting to observe how the h_c values for methane and for the mixtures *MIX 1*, *MIX 2* and *MIX 3*

[1] As explained in Chapter 1 the heat transfer coefficient h_c is useful to compare the heat transfer efficiency of different coolant flows. In fact for an assigned temperature difference $(T_w - T)$ the greater h_c the higher the heat flux that can be absorbed by the coolant flow, or for an assigned heat flux and bulk temperature, the higher h_c the lower the corresponding T_w, which is a critical quantity that has to satisfy cooling system constraints. The limit to the higher acceptable T_w is set by either structural requirements or thermal cracking temperature, depending both on the used propellant and on the wall channel material features

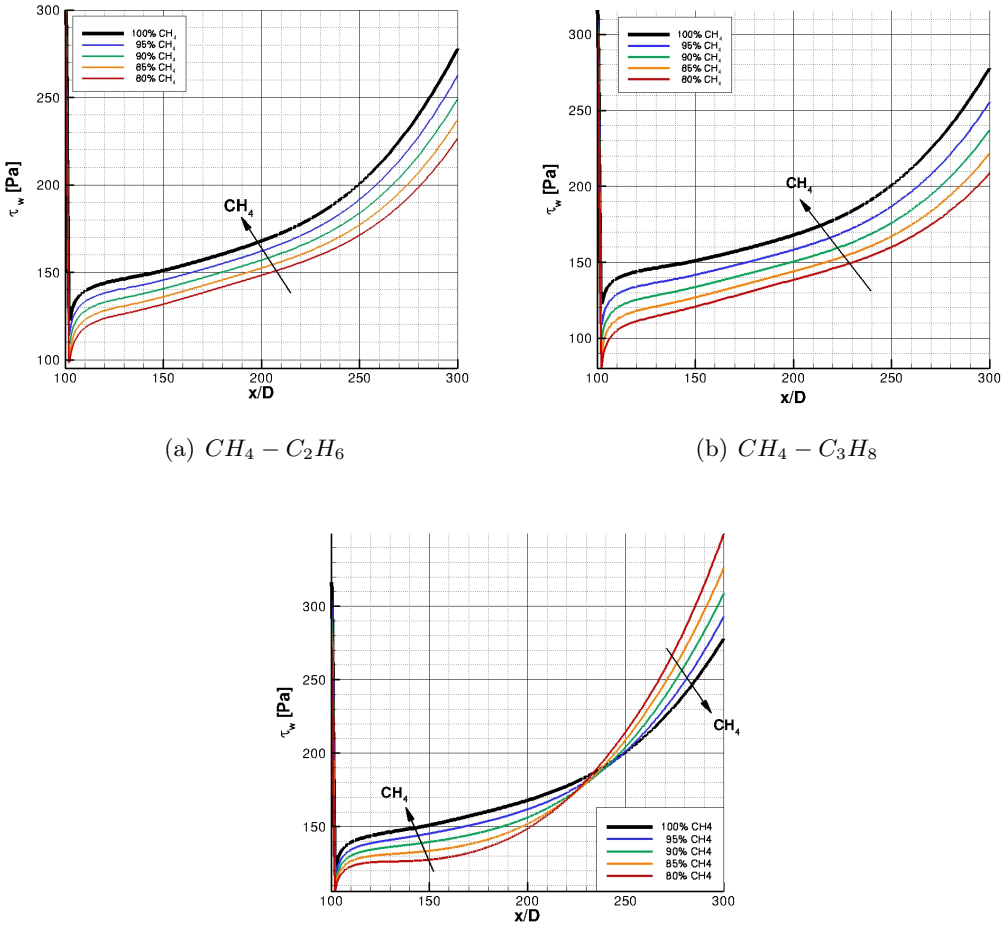

(a) $CH_4 - C_2H_6$

(b) $CH_4 - C_3H_8$

(c) $CH_4 - N_2$

Figure 6.6: evolution along the channel length of the wall shear stress for $CH_4 - C_3H_8$ and $CH_4 - N_2$ binary mixtures

converge toward the channel exit, whereas this is not the case for the mixture *MIX 4*. The main difference between *MIX 4* of Table 6.2 and the others mixtures is the molar fraction of nitrogen which is higher for *MIX 4*. Hence one explanation of the h_c behavior toward the channel exit could be found in the different nitrogen nature to respect to the other species which are hydrocarbons. This will be further discussed in the following.

As a matter of fact, from the results presented in Fig. 6.3 it can be inferred that LNG composition influences both the pressure drop and the heat transfer behavior and this cannot be neglected in the design of a regenerative cooling system.

6.2.2 Binary mixtures: CH_4-N_2, CH_4-C_2H_6, CH_4-C_3H_8

From the above discussed results only major differences between pure methane and LNG can be put in evidence and it is difficult to compare the LNG compositions

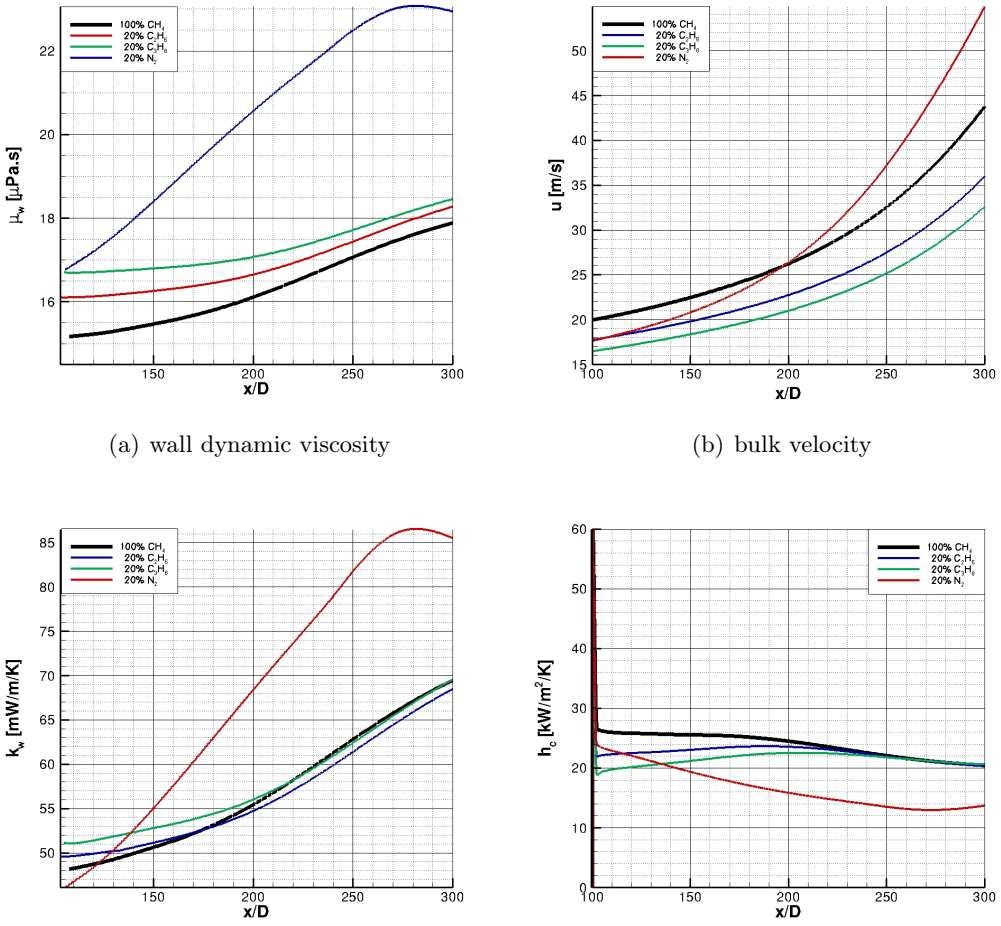

(a) wall dynamic viscosity

(b) bulk velocity

(c) wall thermal conductivity

(d) heat transfer coefficient

Figure 6.7: Evolution along the channel length of wall dynamic viscosity, the bulk velocity, the wall thermal conductivity and the heat transfer coefficients. Fluid: CH_4 and binary mixtures with 80% mole fraction of CH_4

one to each other. On the contrary the numerical simulations carried out with the binary mixtures presented in Sec. 6.1.2 are useful to understand the role of each species in the LNG heat transfer behavior. The results of the binary mixtures are summarized in Figs. 6.5: the two graphics depict the total bulk pressure drop Δp_0 between the outlet and the inlet of the channel and the maximum wall temperature $T_{w,max}$ reached along the channel as a function of the methane molar fraction in the binary mixture. A first comment to Fig. 6.5 is that nitrogen binary mixtures behave differently than the others: this could be expected because of the different chemical nature of nitrogen if compared with the other investigated species which are hydrocarbons similar to methane. The Δp_0 increases with the nitrogen molar fraction, whereas it decreases with ethane and propane molar fractions. This could be partially explained considering the wall shear stress τ_w evolution shown in Fig. 6.6: for propane and ethane mixtures τ_w decreases with the methane molar fraction. On

the other hand a different situation is observed for the nitrogen binary mixtures in the last part of heated channel where τ_w is greater for the mixtures with more nitrogen. Finally, with regard to the total pressure drop, Fig. 6.5(a) shows that for the same methane molar fraction the binary mixtures with ethane give a Δp_0 closer to the pure methane than the other mixtures.

To find an explanation in the different wall shear stress behavior for the nitrogen it is useful to remind that it depends on the wall viscosity and velocity gradient. For this purpose the evolution of the dynamic viscosity at wall and of the bulk velocity are reported in Fig. 6.7 for the different binary mixtures with 80% molar fraction of methane. The wall viscosity of all the mixtures is greater than the pure methane one, for all the thermodynamic conditions arising along the channel. Nevertheless, a greater difference is found for the nitrogen mixture. Moreover analyzing the velocity plot (Fig. 6.7(b)) it comes out that all the mixtures have a lower inlet velocity than methane, and this has been justified in Sec. 6.2.1. However, the bulk velocity of the nitrogen binary mixture becomes greater than the pure methane one in the second half of the channel. Conversely the bulk velocity for ethane and propane mixtures remains lower than methane velocity all along the channel, and increases with a similar trend. The nitrogen mixture velocity behavior explains why the wall shear stress evolution with nitrogen molar fraction (Fig. 6.6(c)) changes in the second half of the channel.

The above described behavior of the velocity is related with the heat transfer capabilities. Indeed also for the heat transfer characteristics nitrogen mixtures behave differently from the others. From Fig. 6.5(b) it appears that the maximum wall temperature reached along the channel always increases moving away from pure methane. Nevertheless, the influence of the nitrogen molar fraction is clearly greater: the wall temperature difference with respect to the pure methane is about 30% for the 20% nitrogen case, whereas only 4% and 6% for the 20% ethane and 20% propane cases, respectively. The fact that methane is more efficient as a coolant than the investigated mixtures is also illustrated in Fig. 6.8: the h_c of pure methane is the greatest all along the channel. Moreover, nitrogen mixtures show the lower cooling capabilities which explain the corresponding greater increase in the temperature if compared with ethane and propane mixtures (see Fig. 6.5(b)). This also explains the greater increase in the bulk velocity shown in Fig. 6.7(b). In fact the increase in the velocity is strictly related with the decrease of the density caused by the increase in the temperature. On another hand it is interesting to observe that toward the channel exit the ethane and propane mixtures h_c converge toward the same value as the methane: the differences between the curves after $x = 250$ D are lower than 1% as can be observed in Fig. 6.7(d). This behavior can be related to the transport properties of these mixtures which at high temperatures are much closer to each other than at low temperatures. This is confirmed by the evolution of the wall thermal conductivity and dynamic viscosity along the channel for the different binary mixtures with 80% molar fraction of methane shown in Figs. 6.7(a)-6.7(c). In these figures, toward the channel exit, the wall transport properties of ethane, propane mixtures and pure methane converge toward the same value, whereas the nitrogen ones behaves differently. It can concluded that increasing the temperature the percentage of ethane and propane less and less affects heat transfer capability of LNG mixtures, whereas this is not the case for the influence of nitrogen which reduces significantly

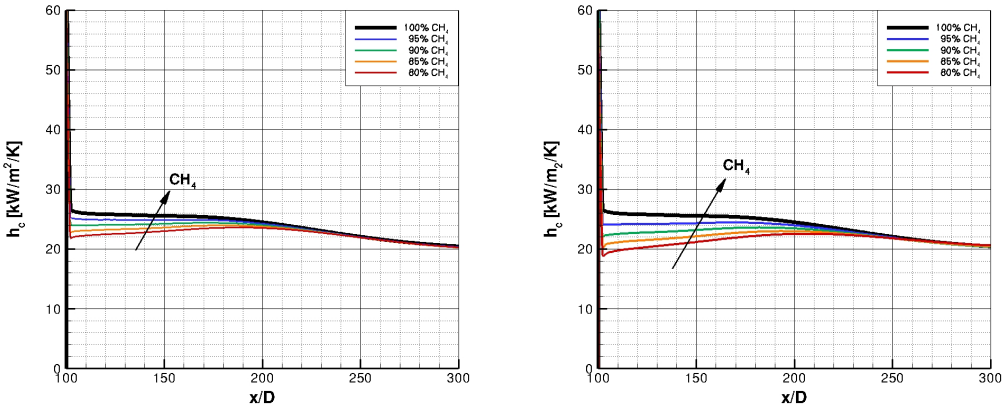

(a) $CH_4 - C_2H_6$

(b) $CH_4 - C_3H_8$

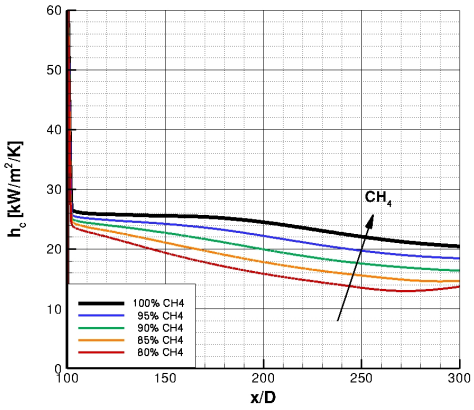

(c) $CH_4 - N_2$

Figure 6.8: evolution along the channel length of the heat transfer coefficient for $CH_4 - C_2H_6$, $CH_4 - C_3H_8$ and $CH_4 - N_2$ binary mixtures

the LNG mixtures cooling capability.

6.3 Conclusions

A parametric numerical study has been carried out to evaluate the influence of the LNG composition on the heat transfer behavior in the cooling channels of a regeneratively cooled liquid rocket engine. Methane, ethane, propane and nitrogen have been considered as components of LNG mixtures. The 2D axisymmetric test case of all the simulations was a straight channel with a circular cross section, uniformly heated. Comparisons have been made between different typical LNG compositions, and also between binary mixtures to investigate the effect of each species besides methane. The bulk total pressure drop between the end and the inlet of the channel has been analyzed: ethane and propane diminish it, and propane more than ethane. On the contrary increasing the molar fraction of nitrogen causes an increase in the total pressure drop. Nevertheless due to the low amount of nitrogen typically present in LNG and hence in the analyzed compositions in the present study, it results that the total pressure drop is greater for methane than for LNG. The investigation on the cooling capabilities has put in evidence a great influence of nitrogen: increasing the nitrogen molar fraction causes a clear increase in the wall temperature. Also the presence of ethane and propane slightly reduces the heat transfer capabilities of the coolant flow; however these differences become less important as the fluid temperature increases.

Chapter 7

Heat Transfer Deterioration of Methane and LNG

The knowledge of the different thermodynamic phenomena that could affect the propellant flow in the cooling channels of a liquid rocket engine is of particular interest, as discussed in Chapter 1. This is especially important in the case of engines based on an expander cycle for which the performance is strictly connected with the heat transfer characteristics in the cooling channels. In this framework, it has to be taken into account that the liquid propellants can flow in those channels at supercritical pressures and in the neighborhood of the critical point. In such conditions the strong property variations could change the heat transfer capabilities of the propellants. The main goal of the work presented in this chapter is to investigate the heat transfer to liquid methane in conditions close to those expected for a liquid rocket engine: the purpose is to analyze the influence of the thermodynamic properties variations on the coolant flow and its features, with attention on the heat transfer deterioration that can affect a transcritical fluid (see Chap. 1). To purse this objective the numerical model for the PNS equations presented in Chap. 4 together with the thermophysical models presented in Chap. 2 have been used. In fact, as it has been pointed out in Chap. 5, using the developed PNS solver is particularly suitable to parametric analysis, with a negligible loss of precision in physical modeling with respect to full Navier-Stokes solvers. Moreover, the code has been validated against experimental data of supercritical hydrogen with heat transfer deterioration, demonstrating its capability to accurately describe this thermodynamic phenomena. In the following a set of computations of methane heated in conditions similar to those that could occur in cooling channels of an expander cycle engine are presented and the possible heat transfer deterioration is emphasized. Further parametric analyzes are carried out to investigate the deterioration heat transfer onset and the conditions that most influence the phenomenon. Finally LNG mixtures presented in the previous Chap. 6 has been considered and the effect of the composition over the heat transfer deterioration is investigated.

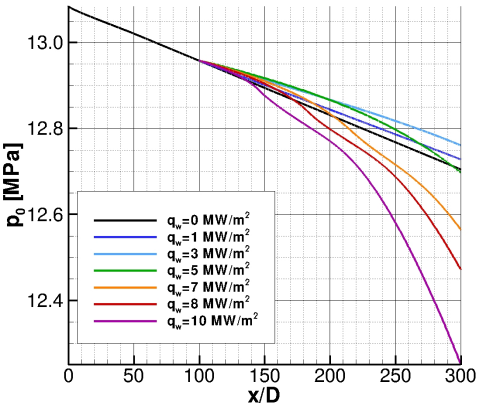

(a) bulk total pressure

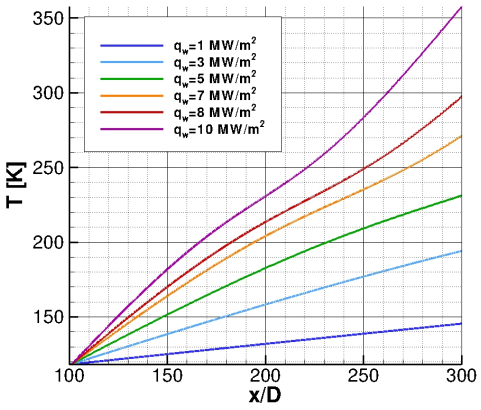

(b) bulk temperature

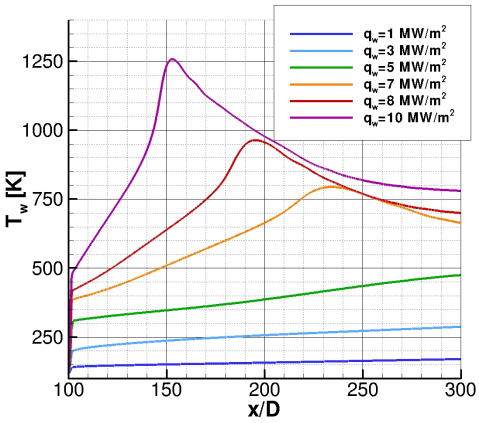

(c) wall temperature

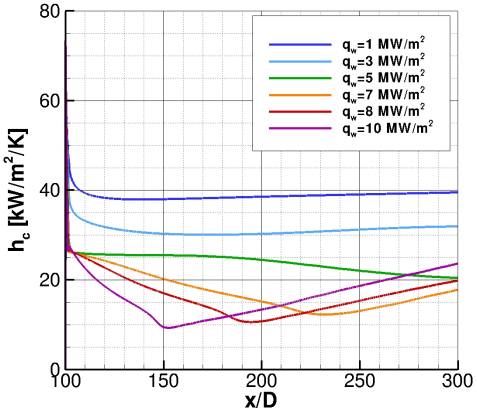

(d) convective heat transfer coefficient

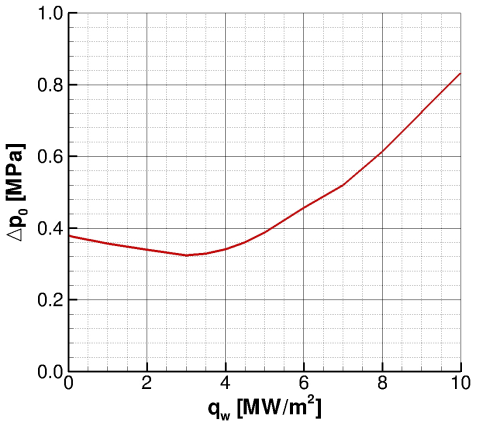

(e) total bulk pressure drop varying with the enforced heat load

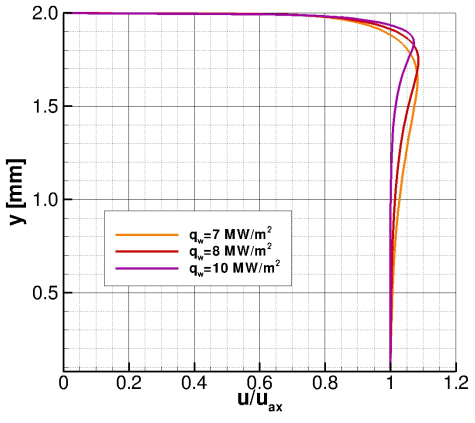

(f) M-shaped u profile

Figure 7.1: Methane flow in heated channels with a constant heat load.

7.1 Methane Flow in Heated Channels

7.1.1 Constant heat load

To investigate the capabilities of methane as a coolant in a rocket engine, different numerical simulations have been carried out on the same 2D axisymmetric geometry used for the investigation on LNG composition of Chap. 6. It is a straight channel with a circular cross section of diameter $D = 4$ mm (see Fig. 6.1). In the first 100 diameters no heat flux is applied so as to obtain a developed flow before heating in the last 200 diameters with a constant heat load q_w. The parametric study has been carried out keeping constant the following parameters:

- inlet pressure $p_{in} = 13$ MPa
- inlet temperature $T_{in} = 118$ K
- mass flow rate per unit area $G = 8500$ kg/s/m^2

whereas the heat load has been changed for each computation, varying from zero up to 10 MW/m^2. Both the geometry and the boundary conditions have been selected so as to get thermodynamic conditions close to those expected in a rocket engine cooling channel. In particular, the work of Schuff et al. [139], which is a system study for a LOX/Methane expander cycle engine, has been used again as a reference for this purpose. The results have been analyzed considering the main performance parameters of interest in a cooling system analysis. Therefore attention has been devoted principally to the pressure drop and the cooling capabilities through the heat transfer coefficient h_c The definition of h_c. Note that in the present discussion h_c is in fact the difference between wall and bulk temperature because a constant heat flux is enforced along the channel length. The computed evolution of the bulk total pressure p_0, the bulk temperature T, the wall temperature T_w and the convective heat transfer coefficient h_c is shown in Figs. 7.1(a)-7.1(d). The bulk total pressure p_0 evolution refers to the whole channel length (Fig. 7.1(a)), whereas bulk and wall temperatures, and the heat transfer coefficient evolution are only shown for the heated part of the channel because in the adiabatic part the temperatures can be considered constant and h_c is not defined (Figs. 7.1(b), 7.1(c) and 7.1(d)). The total bulk pressure behavior presented in Fig. 7.1(a) shows the close relationship between the pressure drop and the heat flux. For the lower heat fluxes increasing the heat flux reduces the pressure drop. This happens also for the higher heat fluxes in the first part of channel, where the temperatures are still very low. In fact, methane enters the channel with a supercritical pressure and a subcritical temperature. In these thermodynamic conditions it is quite similar to an incompressible fluid and, accordingly, the pressure drop is directly related to wall friction and hence to viscosity which, for subcritical temperatures, decreases as temperature increases (see Fig. 2.11 in Chap. 2). The situation changes when the fluid compressibility starts growing: in this case the temperature increase yields a density reduction, a velocity increase and, as a consequence, a pressure drop increment. This is also summarized in Fig. 7.1(e) where the evolution of the pressure drop with the heat flux is shown: it results that for this specific test case for heat fluxes smaller than 3 MW/m^2 the pressure drop decreases with q_w, whereas for higher heat fluxes the trend changes and a higher heat flux generates a higher pressure drop.

A change in the temperature behavior for heat fluxes higher than 3 MW/m^2 is also found (Figs. 7.1(b)-7.1(c)). For the smaller heat fluxes both the bulk and the wall temperatures smoothly increase along the channel, whereas for the higher heat fluxes T_w exhibits a peak and in the same axis location T changes trend: these are the consequences of the heat transfer deterioration phenomenon. In fact, in the same axial location the heat transfer coefficient has a minimum (Fig. 7.1(d)).

The heat transfer deterioration is a phenomenon which occurs when a subcritical temperature channel flow is sharply heated up. The high temperature gradients in the channel section leads to the formation of a layer of low density fluid near the wall, where the temperature is supercritical, which has low heat transfer capabilities, whereas the core of the flow is still cold and slow (see Chapter 1). As a consequence the velocity profile has the particular M-shaped profile which can be observed in Fig. 7.1(f) where the velocity profiles in the wall temperature peak section are reported. The velocity gradient is zero close to the wall and this implies a reduction of turbulent diffusion, and thus a wall thermal insulation which also contributes to deteriorate the heat transfer. If the flow is further heated up, the bulk temperature finally exceeds the pseudocritical temperature T_{ps} (the temperature at which specific heat at constant pressure c_p has a maximum at a specified pressure: see Chap. 1). Once T_{ps} is exceeded the flow velocity grows, h_c increases accordingly (Fig. 7.1(d)) and thus the wall temperature decreases. From a phenomenological point of view, the heat transfer deterioration phenomenon has been investigated in the literature, but no clear indication about the flow conditions for its onset has been given. This set of computations suggest that the heat transfer to methane used as a coolant in a regenerative cooling system has to be carefully studied. In particular, it has to be further investigated to understand which are the parameters that have to be taken into consideration to control the deterioration phenomenon.

7.1.2 Varying heat load in the axial direction

The previous set of computations has emphasized a deterioration of the heat transfer for constant heat fluxes greater than 5 MW/m^2. However, it has to be considered that the heat load is not constant along a cooling channel. In fact, it varies along the nozzle with a maximum in the proximity of the throat, hence a variable heat flux computation has also been carried out. The variable heat flux along the chamber computed by Betti et al. [103] has been considered as a reference for this purpose, with a suitable reduction to take into account for the different mass flow rate and channel geometry considered in the present study. The test case described in Fig. 6.1 has been considered again except for the length of the heated part of the channel which has been reduced to 63.5 cm corresponding with 158.75 diameters. The enforced heat flux is reported in Fig. 7.2(a) and the resultant wall temperature is shown in Fig. 7.2(b). As can be observed the wall temperature evolution along the channel follows the heat flux behavior and exhibits a peak where q_w has its maximum. The values reached by T_w are as high as 1930 K, which can not only be explained by the high heat flux but is also a consequence of the heat transfer deterioration that occurs in that region and that brings an abrupt drop of the heat transfer coefficient (Fig. 7.2(b)). The deterioration is also proved by the M-shaped velocity profile in the x station of the T_w peak, shown in Fig. 7.2(c) (number 2). Also a velocity profile upstream of the T_w peak location (number 1) and downstream (number 3) are reported in the

same figure for the sake of comparison (the corresponding x locations are indicated in Fig. 7.2(b)).

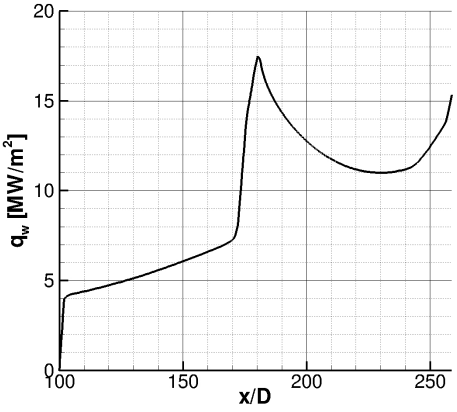

(a) enforced heat flux

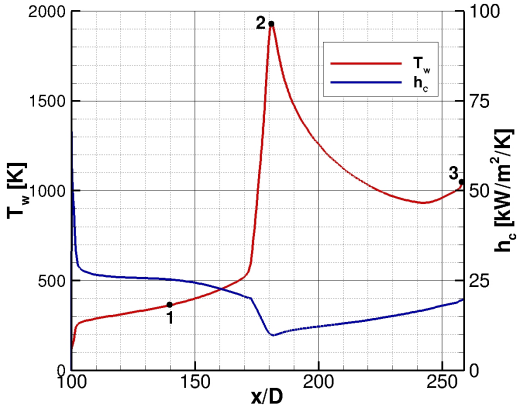

(b) T_w and h_c

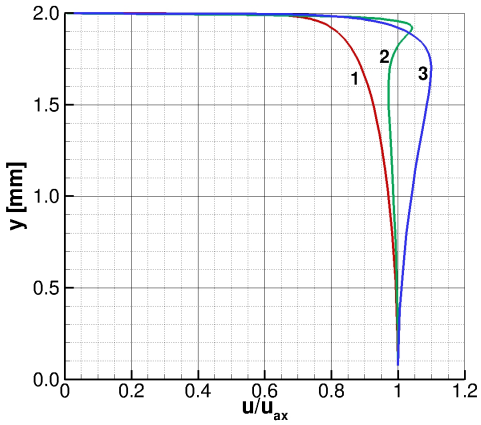

(c) u profile at different x section indicated by the points in (b)

Figure 7.2: Methane channel flow with a variable heat load.

Slightly downstream the T_w peak location the bulk temperature becomes greater than the pseudocritical temperature. As a consequence, the fluid reaches a gas-like state, its velocity increases and hence the heat transfer coefficient grows up again. Moreover, once the throat region is passed q_w decreases and therefore the wall temperature decreases until a value of 1000 K at the end of the channel. The above results make evident that in a regenerative cooling system with methane, the heat transfer deterioration is a concern and that if it occurs it could lead to unacceptable wall temperature.

7.2 The heat transfer deterioration analysis

When a supercritical fluid is heated up and passes through the pseudocritical temperature, a pseudo phase change occurs (see Chapter 1). This can bring to the heat transfer deterioration, in particular in case of high heat fluxes and low mass flow rate. This phenomenon has been studied in the literature both experimentally and numerically. The results obtained show that the heat transfer deterioration is mainly driven by the following parameters: the ratio between the heat flux and the mass flow rate per unit area (q_w/G), the inlet pressure and the inlet temperature (see Chap. 1). However, the flow conditions under which heat transfer deteriorates have not been fully clarified. Moreover as each substance behaves differently in the near-critical state, suitable studies must be performed for every single fluid of interest. For these reasons a parametric study is presently carried out to investigate the onset of heat transfer deterioration for methane. The parameters that have been considered are the inlet pressure p_{in}, the inlet temperature T_{in} and the ratio between the heat flux and the mass flow rate per unit area (q_w/G). In the following the influence of each parameter is analyzed separately. The parametric study is carried out considering the same test case of Section 7.1.

7.2.1 Inlet temperature

This first parametric set has been obtained keeping constant $G = 8500$ kg/m^2/s, $p_{in} = 13$ MPa, q_w and varying the inlet temperature from a subcritical temperature of $T_{in} = 110$ K up to a supercritical temperature of $T_{in} = 250$ K. Considering that at the inlet pressure ($p_{in} = 13$MPa) the pseudocritical temperature is of $T_{ps} = 227.3$ K, the investigated inlet temperature range goes from $T_{in} < T_{ps}$ up to $T_{in} > T_{ps}$. Two heat fluxes have been considered: $q_w = 5$ MW/m^2 that for $T_{in} = 118$ K is a non deteriorated test case and $q_w = 7$ MW/m^2 that for $T_{in} = 118$ K is a deteriorated test case, as shown in Section 7.1. The results of computations are shown in Fig. 7.3 for the wall temperature and heat transfer coefficient. For $T_{in} = 250$ K, which is the only supercritical temperature among the investigated inlet temperatures, a normal heat transfer is observed for both the heat fluxes. Indeed the temperature always increases, while the h_c initially decreases because of the formation of the thermal boundary layer, and then always increases. The behavior is different for all the other inlet temperatures which are subcritical. For the higher heat flux the heat transfer is deteriorated and the wall temperature exhibits a peak at the same axis location where h_c reaches a minimum value (Fig. 7.3). On another hand for the lower heat flux the behavior is similar to the $T_{in} = 250$ K case and the heat transfer is not deteriorated, due to the fact that for $T < T_{ps}$ the fluid is more similar to a liquid whereas for $T > T_{ps}$ is more like a gas. This different behavior between inlet supercritical and subcritical temperatures at high heat fluxes confirms that the heat transfer deterioration phenomenon can occur only when the inlet temperature is subcritical.

It is interesting to observe in Fig. 7.3(a) how, for the deteriorated cases, increasing the inlet temperature decreases the T_w peak and brings its position upstream along the channel axis. It has to be noticed that because G and p_{in} are assigned, a different T_{in} corresponds to a different inlet flow velocity. More precisely the higher T_{in}, the higher the inlet velocity, and thus the higher the pressure drop. Moreover, the

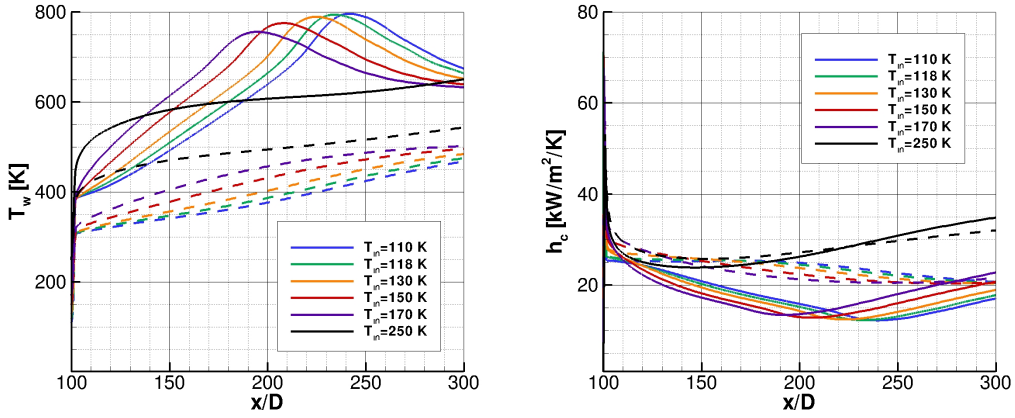

(a) wall temperature

(b) heat transfer coefficient

Figure 7.3: Heated channel flows with $p_{in} = 13$ MPa, $G = 8500$ kg/m^2/s, $q_w = 5$ MW/m^2 (dashed line) or $q_w = 7$ MW/m^2 (solid line) for different inlet temperatures.

greater subcritical inlet temperatures, the closer to the pseudocritical temperature. For both the reasons (higher inlet temperature and the consequent increase of pressure drop), the higher T_{in}, the earlier the pseudocritical temperature is reached along the channel. This is made evident in Fig. 7.4(a) where the bulk pressure (dashed line) is plotted together with the bulk constant pressure specific heat (solid line), which exhibits a peak when the pseudocritical temperature is reached. Increasing the inlet temperature the c_p peak moves toward the channel entrance, and so does the wall temperature peak (Fig. 7.3(a)). Moreover the c_p slightly diminishes increasing T_{in}. The reason is that despite the highest pressure drop of the higher inlet temperature test cases, for the cases with lower T_{in} a longer way is necessary to reach the pseudocritical temperature. As a consequence the pseudocritical condition is reached for a smaller pressure and hence the c_p peak is higher. This is summarized in Fig. 7.4(b) where the maximum wall temperature, and the pressure at which the pseudo-phase change occurs (p_{ps}) for the different test cases are reported varying the inlet temperature. Here again it appears that increasing T_{in} the maximum wall temperature decreases and p_{ps} increases. The higher maximum wall temperature for the lower inlet temperature can be explained considering that because the passage from the pseuodcritical temperature occurs when the pressure is lower than in the other cases, the gradients of all the thermodynamic variables are greater in each section, and this contributes to the insulation of the wall. This effect can be observed in Fig. 7.4(c), where the density profiles are shown in the sections of the T_w peak for each test case, and the lower the T_{in}, the higher the density gradient. Also the M-shaped u profile are reported in Fig. 7.4(d). Here just a little effect is observed since decreasing the inlet temperature just slightly accentuates the M-shape.

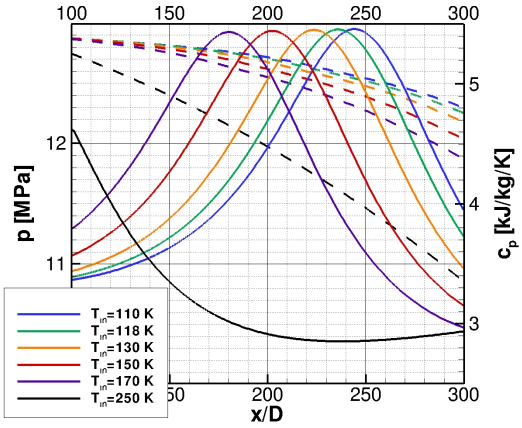

(a) pressure and constant pressure specific heat

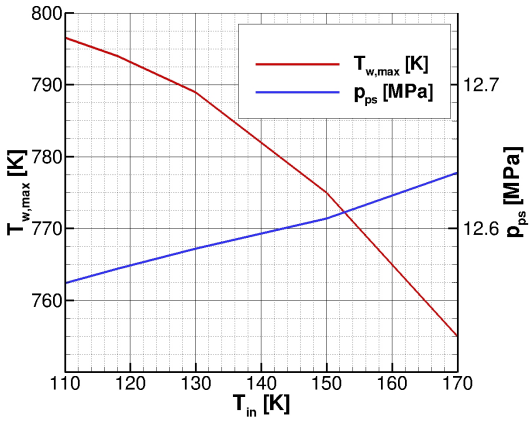

(b) maximum wall temperature and pressure at pseudo-critical temperature

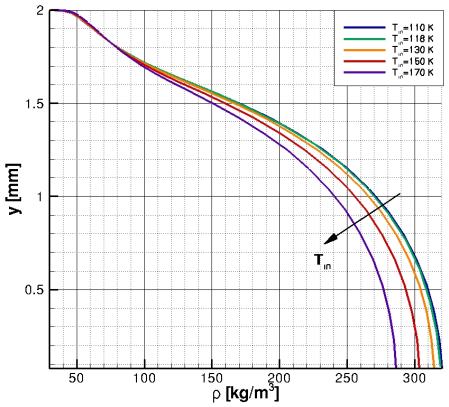

(c) density profile

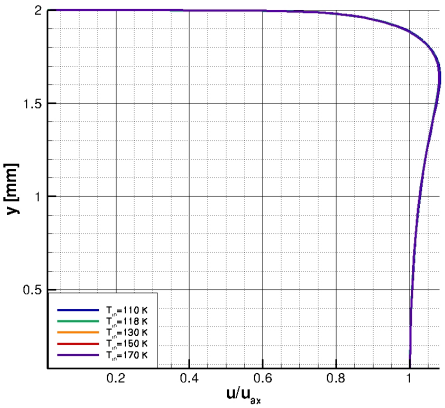

(d) normalized u profile

Figure 7.4: Heated channel flows with $p_{in} = 13$ MPa, $G = 8500$ kg/m^2/s and $q_w = 7$ MW/m^2 for different inlet temperatures.

7.2.2 Inlet pressure

Three different inlet pressures have been considered, $p_{in} = 8, 10, 13$ MPa, keeping constant the other parameters $G = 8500$ kg/m^2/s, $T_{in} = 118$ K, $q_w = 5$ MW/m^2. The results are shown in Fig. 7.5 for different bulk and wall variables. For the lower pressure of $p_{in} = 8$ MPa the heat transfer deteriorates and thus the wall temperature exhibits a peak (Fig. 7.5(a)) which corresponds to a minimum of the heat transfer coefficient, while for the other two pressure levels the phenomenon does not appear. The main reason of the pressure influence can be deduced from Fig. 7.5(b) where the bulk c_p and temperature are reported along the channel. For all the pressure levels considered the incoming total heat is sufficient to make the temperature become larger than the pseudocritical value (which increases with the pressure) as demonstrated by the peaks in the c_p curves. Nevertheless, when the pressure decreases toward the

critical value ($p_c = 4.5992$ MPa) the c_p peak sharply increases and the passage from a liquid like to a gas like state becomes more and more abrupt: this is why the c_p curve for the 8 MPa pressure case in Fig. 7.5(b) is steeper and reaches a higher value. Also in the y direction the gradients of the thermodynamic variables are larger for lower pressures as depicted in Fig. 7.5(c) for the c_p profile in section $x/D = 253$. These sudden changes in the thermodynamic variables lead to the formation of the insulating gas film near the wall which deteriorates the heat transfer.

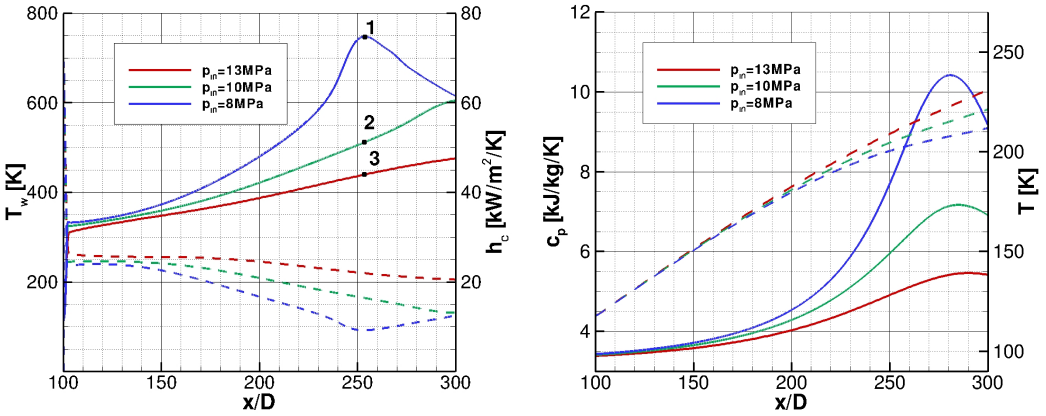

(a) wall temperature and heat transfer coefficient (b) bulk temperature and constant pressure specific heat

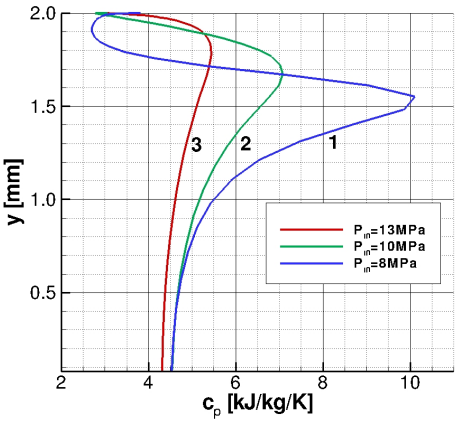

(c) constant pressure specific heat profile at x/D=253 corresponding to Fig.7.5(a)

Figure 7.5: Heated channel flows with $T_{in} = 118$ K, $G = 8500$ kg/m^2/s, $q_w = 5$ MW/m^2 for different inlet supercritical pressures.

7.2.3 Heat flux to specific mass flow rate ratio

The ratio between the heat flux and the mass flow rate per unit area[1] (q_w/G) (J/kg) is directly related with the streamwise gradient of the bulk total enthalpy per unit mass dh_0/dx of the coolant flow by the relation:

$$\frac{q_w}{G} = \frac{1}{4} D \frac{dh_0}{dx} \tag{7.1}$$

In the literature the ratio (q_w/G) is considered an indicator for the heat transfer deterioration: if the inlet flow temperature is subcritical and $(q_w/G) > (q_w/G)_{tr}$ the heat transfer will be deteriorated, with $(q_w/G)_{tr}$ being a threshold value depending on the coolant inlet pressure and temperature [140]. Recently Grabezhnaya and Kirillov [156] have identified the following generic relation for the threshold parameter:

$$(q_w/G)_{tr} = 600(M_{H_2O}/M),\ \text{J/kg} \tag{7.2}$$

with M and M_{H_2O} being respectively the fluid and water molar weights. Thus for methane, considering that it is $(M_{H_2O}/M_{CH_4}) = 18/16$, according to Eq. (7.2) it should be $(q_w/G)_{tr} = 675$ J/kg. To verify the validity of this relation for methane and also better understand the meaning of this threshold parameter, the computations summarized in Tab. 7.1 have been carried out: two values of the ratio q_w/G have been considered, corresponding to a non deteriorated case and to a deteriorated case, respectively. Both G and q_w have been varied keeping constant the inlet pressure ($p_{in} = 13$ MPa) and the inlet temperature ($T_{in} = 118$ K), and as a consequence also the inlet density. Therefore each test has a different inlet velocity.

(q_w/G) [J/kg]	Test	q_w [MW/m^2]	G [kg/m^2/s]
588	TC 1.1	3.75	6375
	TC 1.2	5.00	8500
	TC 1.3	6.25	10625
	TC 1.4	7.50	12750
823	TC 2.1	5.25	6375
	TC 2.2	7.00	8500
	TC 2.3	8.75	10625
	TC 2.4	10.5	12750

Table 7.1: Test cases analyzed in the (q_w/G) parametric study.

The wall temperature and heat transfer coefficients obtained for all the test cases of Tab. 7.1 are shown in Fig. 7.6: the test cases with the same ratio (q_w/G) exhibit a similar behavior. In particular for $(q_w/G) = 823$ J/kg the heat transfer is deteriorated, whereas this is not the case for $(q_w/G) = 588$ J/kg: this is in agreement with Eq. (7.2). Nevertheless the entity of the deterioration is different for the different test cases: the higher G and q_w, the higher the maximum wall temperature and the lower the h_c. This can be related to the difference in the pressure along the channel between one case and another. In fact because the inlet thermodynamic conditions

[1] The mass flow rate per unit area is referred as specific mass flow rate

are equal for all the tests (same p_{in}, T_{in} and hence ρ_{in}) the higher mass flow rate cases have a higher inlet velocity, and as a consequence experience a higher pressure drop along the channel. This is shown in Fig. 7.7 where for a same (q_w/G) the higher G test case (square symbols) undergoes a higher pressure drop than the other. As it has been demonstrated in Section 7.2.2 the pressure is an important parameter in the heat transfer deterioration and this is also shown by the present results: a lower pressure for a same (q_w/G) can make the deterioration occur (see Fig. 7.5).

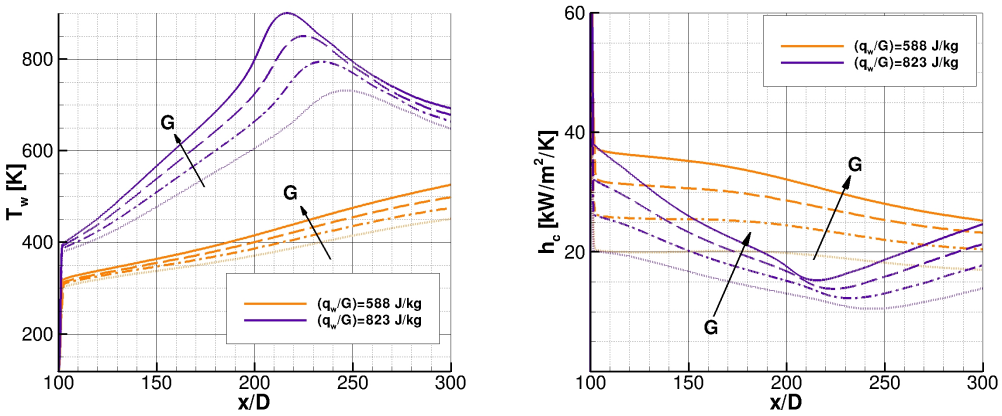

(a) wall temperature

(b) heat transfer coefficient

Figure 7.6: Heated channel flows with $T_{in} = 118$ K, $p_{in} = 13$ MPa for different (q_w/G) ratio.

From this analysis it is possible to conclude that for the investigated inlet pressure of $p_{in} = 13$ MPa the criteria of Eq. (7.2) can give an indication for the onset of the deteriorated heat transfer of methane. Moreover, it is possible to assert that $(q_w/G)_{tr}$ decreases if the inlet pressure decreases. More computations for different inlet pressures and for more (q_w/G) should permit to find a correlation for $(q_w/G)_{tr}$ as a function of pressure.

The above criteria on heat transfer deterioration onset is related to the bulk total enthalpy streamwise gradient, as expressed by Eq. (7.1): for a given diameter and mass flow rate a locally high dh_0/dx can deteriorate the heat transfer. To better understand this feature two more test cases are carried out. Actually they correspond with the two cases TC 1.2 (non deteriorated) and TC 2.2 (deteriorated) of Tab. 7.1 except that a longer channel is considered with a length of 500 D instead of 300 D. These two test cases have the same mass flow rate and different heat fluxes $q_{w1} = 5$ MW/m^2 (TC 1.2) and $q_{w2} = 7$ MW/m^2 (TC 2.2). The results for the two test cases are compared in Fig. 7.8. For TC 2.2 the heat transfer deteriorates and T_w reaches a peak for $x_2 = 233.5$ D: the total amount of heat received by the fluid when it reaches $x = x_2$ is proportional to the product of q_{w2} and $L_2 = x_2 - x_{in}$, with $x_{in} = 100$ D unheated length. Therefore, the same total amount of heat is received by the TC 1.2 flow in a longer length, which is reached at $x_1 = 287.6$ D. Nevertheless for this lower heat flux no deterioration is present: the wall temperature always increases along the channel length. This last comparison demonstrates the

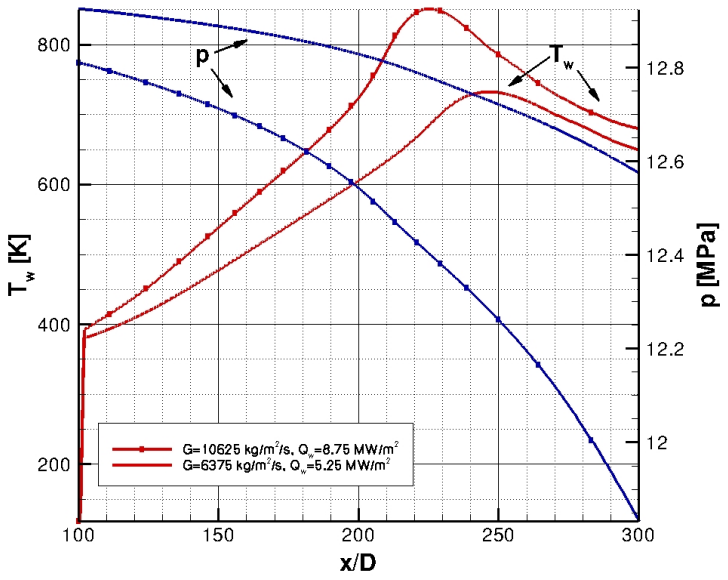

Figure 7.7: Bulk pressure and wall temperature for two test cases with different G and the same $q_w/G = 823$ J/kg. Entrance thermodynamic conditions: $T_{in} = 118$ K, $p_{in} = 13$ MPa

fact that what most influences the heat transfer deterioration is the gradient of the total enthalpy given to the fluid (dh_0/dx) rather than the total amount of power: that is for a same amount of power absorbed by a fluid, the smaller is the length the higher the probability that deterioration occurs.

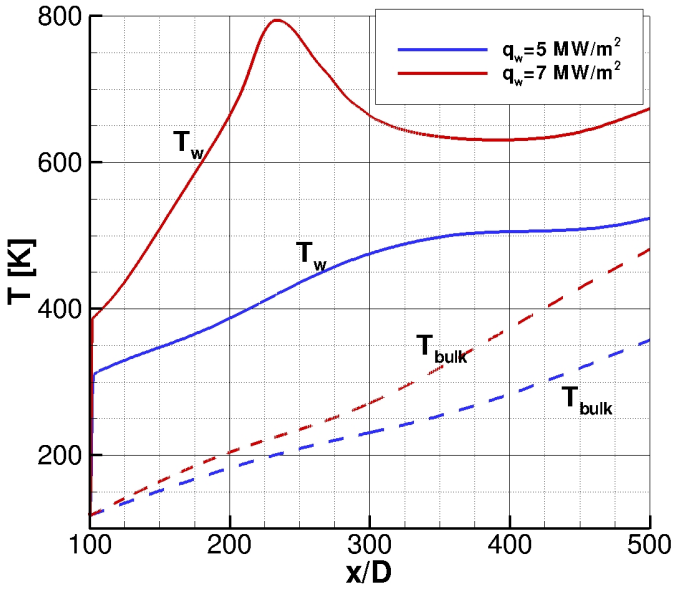

Figure 7.8: Comparison for two heat fluxes test cases with $q_{w1} = 5\text{MW/m}^2$ and $q_{w2} = 7\text{MW/m}^2$.

7.3 Heat transfer deterioration with LNG

In Chap. 6 an investigation of the LNG composition effect over the cooling capabilities has been carried out. The same mixtures are also considered in the present chapter focusing on the heat transfer deterioration. The composition are reported in Tab. 7.2. The aim is to compare the behavior of the LNG mixtures with respect to pure methane in a regime of deteriorated heat transfer.

	x_{CH4} [%]	x_{C2H6} [%]	x_{C3H8} [%]	x_{N2} [%]	M_{MIX} [kg/mol]	$(q_w/G)_{tr}$ [J/kg]
MIX 1	92	4.0	2.2	1.8	17.44	619.27
MIX 2	86	9.5	4.0	0.5	18.56	581.90
MIX 3	93	5.0	1.5	0.5	17.22	627.10
MIX 4	88	5.0	2.0	5.0	17.90	603.35

Table 7.2: Parameters of the LNG mixtures: composition (molar fractions in percentage), molar weight and threshold value for deterioration

With reference to section 7.2.3 the same two ratios q_w/G investigated for pure methane are presently taken into consideration, that is $q_w/G = 588$ J/kg and $q_w/G = 823$ J/kg. In particular the mass flow rate is the same for the two ratios, namely

$G = 8500$ kg/s/m^2, whereas two different heat fluxes are analyzed, namely $q_w = 5$ and 7 MW/m^2. The inlet pressure and temperature are the same of all the other test cases: $T_{in} = 118$ K and $p_{in} = 13$ MPa.

The results are shown in Fig. 7.9 in terms of wall temperature, bulk temperature, heat transfer coefficient and bulk pressure. In the same figure are also shown the results for pure methane with the aim to carry out a comparison. Note that the test cases with $q_w = 5$ MW/m^2 are those analyzed in Chap. 6 and are here reported to discuss the heat transfer deterioration.

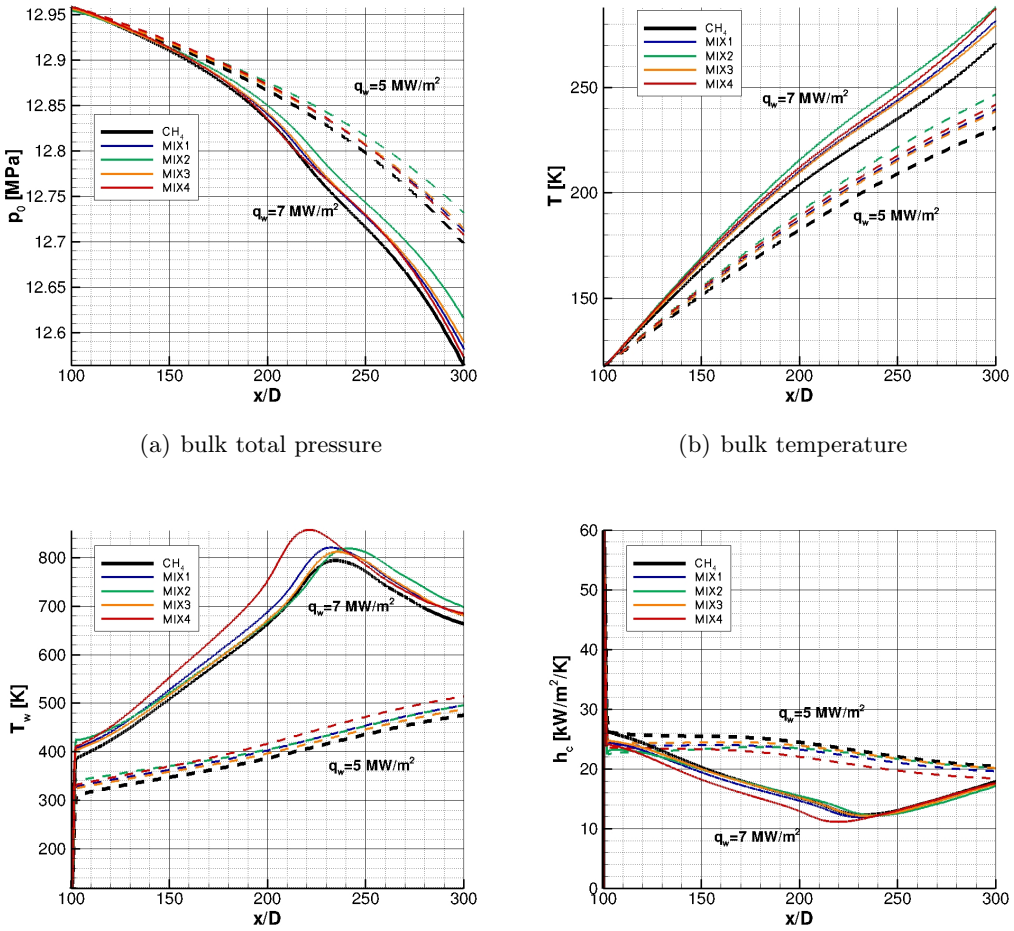

(a) bulk total pressure

(b) bulk temperature

(c) wall temperature

(d) heat transfer coefficient

Figure 7.9: Heated channels with LNG mixture of Tab. 6.2 and pure methane. Test conditions: p_{in}=13 MPa, T_{in}=118 K, G=8500 kg/s/m^2. Heat fluxes: $q_w = 5$ and $q_w = 7$ MW/m^2

As it could be expected the same qualitative behavior is found for pure methane and for all the LNG mixtures because of the similarities in the thermophysical properties. Precisely the test cases with the lower q_w/G are non deteriorated whereas for the higher q_w/G the deterioration heat transfer phenomena is present. Being the molar weight of the LNG mixtures near the pure methane one, also their threshold q_w/G

value, according to Eq. (7.2), are around that of pure methane. This is confirmed by the calculated values of the molar weights and of threshold parameters reported in Tab. 7.2 for each mixture. All the threshold values are contained in the range between the two investigated ratios (588 and 823 J/kg) except the threshold value of MIX 2. Indeed for MIX 2 it is $(q_w/G)_{tr} = 581.9$ J/kg which is just slightly smaller than the lower considered ratio of $q_w/G = 588$ J/kg. Therefore, if Eq. (7.2) was exactly verified the test case of MIX 2 with $q_w/G = 588$ J/kg should present the heat transfer deterioration phenomena. However this is not the case. In fact Eq. (7.2) is an empirical formula obtained from experimental data on water in certain particular pressure conditions. As a consequence, it can only give a rough approximation of the threshold value.

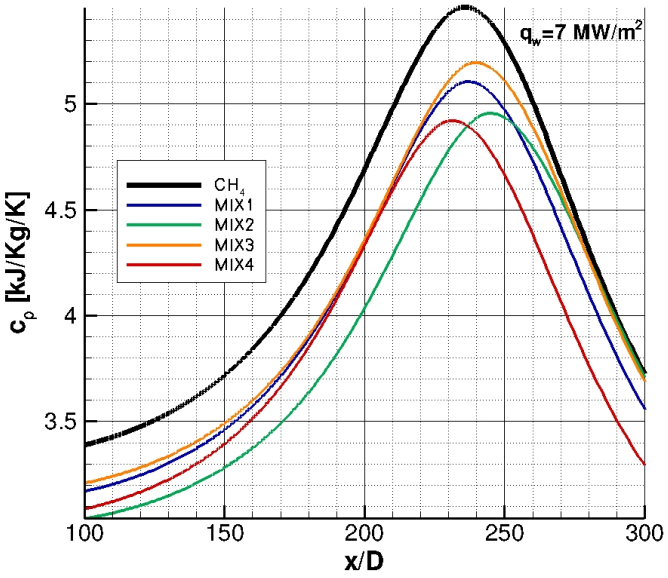

Figure 7.10: Bulk c_p along the channel for different LNG and pure methane test case for heat transfer deterioration ($q_w = 7$ MW/m^2)

From a quantitative point of view the percentage differences between pure methane and the LNG mixtures are of the same order of magnitude in the deteriorated and non deteriorated cases. Namely the differences are up to 8% on the temperatures and 10% on the drop of the total pressure. Despite of that, it has to be considered that in the wall temperature peak region an increment of 8% could be important in terms of absolute values. As can be observed in Fig. 7.9(c) the difference in the peak value of the wall temperature are up to 60 K between pure methane and the LNG mixtures. Also the position of the peak along the channel axis slightly changes from a mixture to another. The reason is that the thermodynamic conditions at which occurs the pseudo phase change varies with the composition. In addition it has been shown in Chapter 6 that the LNG composition influences both the cooling capabilities and the pressure drops along the channel. As a consequence of the above mentioned aspects for the different LNG mixtures the pseudo phase change occurs at different locations

along the channel. This can be observed in Fig. 7.10 where the bulk c_p is reported for the higher q_w/G. The c_p peak, corresponding with the heat transfer deterioration, is positioned at different locations. Moreover its entity is different. In particular it is higher for pure methane, whereas among the investigated mixtures MIX 4 has the lower c_p. The lower c_p of MIX 4 explains the higher value in the wall temperature.

Further parametric studies should permit to understand the influence of each LNG component on the phenomenon. Nevertheless it can concluded that, in first approximation, the results obtained for the methane deterioration can be extended on LNG.

7.4 Conclusions

Heat transfer to methane in a regenerative cooling system has been investigated. Computations referring to conditions close to those which can be expected in cooling channels of liquid rocket engines based on expander cycle have emphasized that if coolant is methane it could be subjected to the heat transfer deterioration. Therefore, parametric studies have been carried out to understand the methane heat transfer deterioration and to see what are the parameters that have to be controlled if the deterioration is to be avoided. These studies have emphasized that the heat transfer deterioration is a phenomenon that can affect fluids with a subcritical temperature that are suddenly heated up and then go over the pseudocritical temperature: the steep gradients of density and velocity bring to the heat transfer deterioration. For a given inlet pressure and temperature the deterioration occurs if the ratio (q_w/G) is greater than a critical value which corresponds to a threshold value in the total enthalpy streamwise gradient dh_0/dx, or, for a certain amount of power that the fluid must absorb, to a minimum heated length. Results show that for the present investigated thermodynamic conditions the threshold value for heat transfer deterioration agrees with the value of $(q_w/G)_{tr} = 675$ J/kg found in the literature. However, further investigations are necessary to evaluate the pressure sensitivity of this parameter, and eventually to find a correlation of more general validity. In fact, the present computations have shown a significant influence of the pressure on the phenomenon: decreasing the pressure the deterioration occurs for lower (q_w/G), because of the higher variations in all the thermophysical properties seen by the fluid when it passes from a liquid-like to a gas-like state. Also the inlet temperature influences the deterioration: decreasing the inlet temperature for a same inlet pressure and $(q_w/G) > (q_w/G)_{tr}$ moves the wall temperature peak downstream and increases its value. Finally also computations on heat transfer deterioration with LNG mixtures have been carried out. The parameters that characterize the heat transfer deterioration are strongly related with the thermophysical properties. Therefore, slight differences have been found comparing LNG with pure methane. Nevertheless, it can concluded that, at least as a first approximation, the results obtained with pure methane can be extended to the investigated LNG mixtures, whereas if an accurate estimation of the deterioration phenomenon onset is needed, studies focusing on the particular composition must be carried out.

.

Conclusions

The large interest in using methane or the cheaper LNG as a fuel in LRE has brought the need to study their behavior in cooling channels. The two main objectives were to understand the differences between LNG and pure methane and to investigate on the possible heat transfer deterioration. To reach this goal two main aspects have initially been taken into consideration, namely the selection of suitable thermophysical models and the development of a suitable numerical tool.

A large literature review has been done on the available EoS and transport property models for mixtures of real fluid. This survey has led to select the GERG EoS, that has been developed precisely for natural gas mixtures, as the most accurate available model for the wide range of thermodynamic conditions of interest. This EoS belongs to the family of Helmholtz free energy based models. On the other hand the transport property models that have been selected are based on the extended corresponding states theory which relies on accurate models for viscosity and conductivity for each species. These thermophysical models are used at low temperatures and are smoothly connected to perfect gas models used at high temperatures. The correct implementation of thermophysical models has been verified by comparison with the data of the National Institute of Standard and Technology. An important characteristic of the selected models is that they permit to treat both mixtures and single species with a high level of accuracy. Moreover, the mixture models smoothly converge towards the pure species models, which is an essential feature to compare LNG and pure methane.

A numerical code has been developed for the heated channel flows of interest. In particular, a space marching approach has been selected. In fact the geometries of the channels and the flow features permit to adopt an analytical description based on the parabolized Navier-Stokes equations. More precisely the parabolized form of the Reynolds Navier-Stokes equations have been considered. An eddy viscosity hypothesis has been used and the problem has been closed with the one equation model of Spalart-Allmaras. In regards to this, the convection-diffusion equation of Spalart-Allmaras for the turbulent viscosity has been suitably modified to account for the PNS hypothesis.

Analytical studies have demonstrated that the Eulerian part of considered PNS system of equations is hyperbolic. As a consequence, a numerical scheme based on the existence of the characteristic directions has been used. Indeed, the developed code is based on a finite volume approach with a Godunov-type scheme. In such scheme upwinding relies on the resolution of Riemann problems. Actually, the Riemann solver is the core of a Godunov-type scheme. For the present code an approximate Riemann solver has been developed. It is the Roe's Riemann solver suitably modified

for the PNS and to consider a generic EoS, which indeed appears in an implicit form. Therefore any kind of EoS can be used.

The developed numerical code has permitted to carry out simulations on turbulent flows in channels with an high ratio L/D (L ∼m and D ∼ mm), enforcing high heat fluxes up to 10 MW/m^2, ensuring a highly accurate description of all the changes in the thermophysical properties. Moreover, because the flow has a very low Mach number and the channel entrance (∼ 0.01) and high compressibility, the suitability of the present numerical model to fulfill the objectives of the study has been demonstrated and discussed.

The numerical model has been validated considering two different aspects. First comparisons with results that can be obtained with a Full Navier Stokes solver has been done. The small differences between the results justify the use of PNS. Then, a validation has been carried out with experimental data available from a test case of hydrogen with heat transfer deterioration which is precisely the thermodynamic phenomenon that has to be studied with methane and LNG. Results show a quite good agreement of numerical and experimental data.

With the validated numerical model two studies have been done. First attention has been devoted on the differences between LNG and pure methane. Typical LNG mixtures have been considered and differences of the order of 5% are found in the pressure drops, and 8% in the temperature fields. Further investigations on different binary mixtures have permitted to put in evidence the influence of each component on the mixture. The results have shown that nitrogen has a higher influence being the only species investigated which is not a hydrocarbon. Propane and ethane have a lower influence. Moreover the influence of propane and ethane decreases when the temperature increases, that is along the channel. The reason of this behavior is that the thermophysical properties of propane, ethane and methane converge towards the high temperatures regime which is described by models of perfect gas.

Pure methane has then be considered in channels with different levels of heat fluxes. This parametric study has put in evidence the risk of the deterioration of the heat transfer in cooling channels. Consequently, the heat transfer deterioration has been deeply studied for methane. Several parametric series of simulations have been done varying inlet pressure, inlet temperature and the ratio between the heat flux and the specific mass flow rate. It has been shown that the deterioration phenomenon is usually caused by an excess of power enforced to the coolant in a certain channel length. This limit is represented by a threshold value of the ratio of heat flux to specific mass flow rate. For a value of the ratio smaller than a threshold value a normal heat transfer occurs. Conversely for values larger than the threshold value and inlet temperature lower than the pseudocritical value, the heat transfer is deteriorated. The reason is that high variations of all the thermophysical properties bring to very high gradients in the transverse directions which cause an insulation of the wall, thus bringing to a reduction of the cooling capabilities. The threshold value of heat flux to specific mass flow rate is a decreasing function of the pressure which means that the near the pressure to the critical pressure the higher the risk of the deterioration. In fact, decreasing the pressure towards the critical value brings an increase in the rate of change of thermodynamic properties with temperature. As a consequence, the gradients of the flow properties in the transverse direction are steeper and hence the heat transfer can be subjected to a deterioration.

Finally a comparison between LNG mixtures and methane has been carried out in case of a deterioration of the heat transfer. It has been shown that the qualitative behavior is similar for LNG and methane. As a consequence the results obtained for methane can be, in first approximation, extended to LNG. However, dedicated studies should be carried out if precise information are needed. In fact, the comparison shows that the chemical nature of the coolant clearly influences the deterioration phenomenon and specific correlations of heat flux to specific mass flow rate ratio with pressure can be found for each fluid, or mixtures of fluid, of interest.

The developed numerical approach has demonstrated to be a valid tool to carry out parametric studies on cooling channels in a simple way and with a low computational cost. Further studies could be carried out with this approach. Among which it could be interesting to find a precise correlation of the threshold parameter with pressure for different propellants and mixtures, and eventually a correlation in terms of reduced parameters (T/T_c, p/p_c). Another interesting application is the validation of existent semi empirical correlations for heat transfer. Finally, the numerical model can be extended to study other aspects of the cooling channels. For example, a model for the roughness of the wall could be added as boundary condition.

Appendix A

Thermodynamic basic principles and definitions

A.1 Critical point

The phase passage between liquid and vapor results form the balance between pressure forces and thermal energy of the particles involved. In fact, if the pressure is increased at constant temperature, the thermal agitation does not change while the attraction force between the particles increases. This finally yields to the formation of new bounds and hence to a phase passage. However, if the temperature is greater than a threshold value the kinetic energy of the particles is so high that the bounds cannot be created even for very high pressures. In other words, this means that the phase passage cannot occur. The above threshold temperature is the critical temperature T_c of the fluid. The corresponding saturation pressure is the critical pressure p_c. The critical density ρ_c is the density which corresponds to T_c and p_c. For a pure fluid the critical state is unique and the following tow thermodynamic relations are verified in the critical point:

$$\begin{cases} \left(\dfrac{\partial p}{\partial \rho}\right)_T = 0 \\ \\ \left(\dfrac{\partial^2 p}{\partial \rho^2}\right)_T = 0 \end{cases} \tag{A.1}$$

The critical point strongly depends on the chemical nature of the fluid. The lower the interaction forces between the particles the lower the T_c. For instance, the helium critical temperature is very low, $T_{c,He} = 5.25$ K, whereas water as a much higher critical temperature of $T_{c,H2O} = 647.25$ K. To summarize, the critical temperature is the maximum temperature at which can exist the equilibrium between liquid an vapor phases, and the critical pressure is the limit value of the saturation pressure. The difference between vapor and gas comes from the above definition. Indeed, a vapor has a gaseous phase and a temperature lower than T_c. As a consequence a vapor can undergo a phase change to liquid phase by compression. Conversely, a gas has a temperature greater than the critical value and hence cannot become liquid by compression. As a consequence, at temperature greater than the critical

value the fluid can exist only in one phase and is called "supercritical". Similarly the critical pressure is the greater pressure at which can occur the phase passage between liquid and vapor. Therefore also a "supercritical pressure" fluid cannot undergo phase change. However, a distinction is usually done between temperature lower or greater than the T_c. Indeed at $p > p_c$ and $T < T_c$ the fluid is referred as a *compressed fluid*. It is characterized by an high density and a very low compressibility which make it similar to a liquid. For this reason it is common use to say that the fluid has a *liquid-like* behavior. If the temperature is increased keeping the pressure at a supercritical level, all the fluid properties undergo gradually changes. Even thought no phase change occurs, the fluid gradually pass form a liquid-like fluid to a gas-like fluid, thus it undergoes what can be called a *pseudo phase change*. In fact its density strongly decreases while its compressibility increases. In particular these changes are very large around a temperature called *pseudocritical temperature* (T_{ps}). Precisely T_{ps} is the temperature at which the specific heat at constant pressure has a peak. Increasing the pressure the peak occurs at a greater pseudocritical temperature and has a lower intensity [83]. In fact the peak temperature is called pseudocritical in analogy with the critical point where the c_p reaches an infinite value.

A.2 The corresponding states principle

The compressibility factor Z is a measure of a fluid identity with respect to the perfect gas law representation:

$$Z = \frac{p}{\rho R T} \tag{A.2}$$

indeed $Z = 1$ for a perfect gas. Reduced pressure and temperature with respect to the critical parameters are defined as follows:

$$p_r = \frac{p}{p_c} \qquad T_r = \frac{T}{T_c} \tag{A.3}$$

whereas for the density the value corresponding with critical temperature and pressure by the perfect gas law is selected as reducing parameter hence giving:

$$\rho_r = \frac{\rho R T_c}{p_c} \tag{A.4}$$

With the above definition the compressibility factor can also been expressed as:

$$Z = \frac{p_r}{\rho_r T_r} \tag{A.5}$$

The Van der Walls corresponding states principle states that any gas at the same T_r and p_r should have the same compressibility:

$$Z = Z(T_r, p_r) \tag{A.6}$$

This principle falls when applied to complex gases, in particular molecules with strong dipolar momentum and no spherical geometry. Hence a third parameter is introduced

in the corresponding state principle. One possible third parameter is the compressibility factor at critical conditions:

$$Z_c = \frac{p_c}{\rho R T_c} \tag{A.7}$$

Another, more physical third parameter is the acentric factor ω_a. The acentric factor ω_a gives an indication of the deviation from spherical symmetry in a molecule and is defined as:

$$\omega_a = -log_{10}\left(\frac{p_s}{p_c}\right) - 1 \qquad \text{at} \qquad \frac{\mathrm{T}}{\mathrm{T_c}} = 0.7 \tag{A.8}$$

where p_s is the saturation pressure. For *simple fluids* characterized by a spherical symmetry of the molecules, the acentric factor is zero. Hence the three parameter corresponding states principle states that any fluid with the same acentric factor should have the same compressibility factor at a given T_r and p_r:

$$Z = Z^0 + \omega_a Z^1 \tag{A.9}$$

where Z^0 and Z^1 are functions of the reduced temperature and pressure only. Z^0 is the compressibility factor of a simple fluid ($\omega_a = 0$) whereas Z^1 accounts for the deviation of real fluids from simple fluids.

The corresponding states principle can be extended to mixtures introducing pseudocritical properties, which are suitable combinations of the critical parameters of each component. Pseuodocritical parameters have not the same physical meaning of single species critical parameters. Rather they are defined such that the PVT behavior of the mixture is the same as that of a pure component whose T_c and p_c are equal to the pseuodcritical properties of the mixtures. Several mixing rules can be found in literature to define pseudocritical values. For example simple rules are [130]:

$$\begin{aligned} T_{cm} &= \sum_j x_j T_{cj} \\ p_{cm} &= \frac{R\left(\sum_j x_j Z_{cj}\right) T_{cm}}{\sum_j x_j (1/\rho_{cj})} \\ \omega_{am} &= \sum_j x_j \omega_{aj} \end{aligned} \tag{A.10}$$

A.3 Mixing rules

A mixture rule is an equation which gives an average of pure component properties: the aim is to obtain a value which can characterize the mixture so as to extend thermophysical models developed for pure fluids. Hence a mixture rule expresses a parameter in terms of composition and pure component parameters [130]:

$$Q_m = \sum_i \sum_j x_i x_j Q_{ij} \tag{A.11}$$

If $i = j$, Q_{ij} is the property of the pure component i (for example the critical temperature T_{ci}. Whereas if $i \neq j$ combining rules are necessary to provide Q_{ij} and the simpler are the Van der Walls combining rules:

- *arithmetic mean*

$$Q_{ij} = \frac{Q_{ii} + Q_{jj}}{2} \qquad \Rightarrow \qquad Q_m = \sum_i x_i Q_i \tag{A.12}$$

- *geometric mean*

$$Q_{ij} = (Q_{ii} \cdot Q_{jj})^{1/2} \qquad \Rightarrow \qquad Q_m = \left(\sum_i x_i Q_i \right)^2 \tag{A.13}$$

To improve Van der Walls mixing rules a binary interaction parameter k_{ij} is introduced for $i \neq j$. Four typical combining rules are:

$$\begin{aligned} Q_{ij} &= k_{ij} \frac{Q_{ii} + Q_{jj}}{2} \qquad k_{ii} = 1 \\ Q_{ij} &= k_{ij} (Q_{ii} \cdot Q_{jj})^{1/2} \qquad k_{ii} = 1 \\ Q_{ij} &= (1 - k_{ij}) \frac{Q_{ii} + Q_{jj}}{2} \qquad k_{ii} = 0 \\ Q_{ij} &= (1 - k_{ij}) (Q_{ii} \cdot Q_{jj})^{1/2} \qquad k_{ii} = 0 \end{aligned} \tag{A.14}$$

Interaction parameters are derived from experimental data for all possible considered binary pairs: they are usually independent from temperature, pressure and composition.

A.4 Helmholtz free energy

The Helmholtz free energy a is a state function defined as:

$$a = e - Ts \tag{A.15}$$

with e internal energy, T temperature and s entropy. The corresponding differential is:

$$da = de - Tds - sdT \tag{A.16}$$

Let us recall the thermodynamic first principle:

$$de + pdv - Tds = 0 \tag{A.17}$$

with $v = 1/\rho$ specific volume. Hence form Eqs. (A.16-A.17) it follows that for $T = const$ and $v = const$:

$$da = 0 \tag{A.18}$$

which means that a reaches an equilibrium condition. Indeed the Helmholtz free energy is a thermodynamic potential at constant temperature and specific volume. An equation of state based on the Helmholtz free energy is a fundamental equation: any thermodynamic property can be obtained by thermodynamic derivatives of a. For example replacing Eq. A.17 in Eq. A.16 yields:

$$da = -pdv - sdT \tag{A.19}$$

from which pressure and entropy expressions follow:

$$\begin{aligned} p &= -\left(\frac{\partial a}{\partial v}\right)_T \\ s &= -\left(\frac{\partial a}{\partial T}\right)_v \end{aligned} \tag{A.20}$$

GERG equation presented in Chapter 2 provides the reduced Helmholtz free energy $\overline{a} = a/RT$. For simplicity the overbar is omitted and in the following a states for the reduced Helmholtz free energy. Using Eq. (A.20) and other basic thermodynamic relations listed in Table A.1 can be derived.

Property	**Expression**
Pressure	$\frac{p}{\rho RT} = 1 + \delta a_\delta^r$
Entropy	$\frac{s}{R} = \tau \frac{\partial a}{\partial \tau} - a$
Internal Energy	$\frac{u}{RT} = \tau a_\tau$
Enthalpy	$\frac{h}{RT} = \tau a_\tau + 1 + \delta a_\delta^r$
Constant volume specific heat	$\frac{c_v}{R} = -\tau^2 a_{\tau\tau}$
Constant pressure specific heat	$\frac{c_p}{R} = \frac{c_v}{R} - \frac{(1 + \delta a_\delta^r - \delta\tau a_{\delta\tau}^r)^2}{1 + 2\delta a_\delta^r + \delta^2 a_{\delta\delta}^r}$
Sound speed	$\frac{w_s}{\sqrt{RT}} = 1 + 2\delta a_\delta^r + \delta^2 a_{\delta\delta}^r - \frac{(1 + \delta a_\delta^r - \delta\tau a_{\delta\tau})^2}{c_v/R}$

Table A.1: Thermodynamic properties from Helmholtz free energy derivatives

Also derivatives of pressure with respect to temperature and density can be obtained:

$$\begin{aligned} \left(\frac{\partial p}{\partial T}\right)_\rho &= \rho R(1 + \delta_\delta^r - \delta\tau a_{\delta\tau}^r) \\ \left(\frac{\partial p}{\partial \rho}\right)_T &= RT(1 + 2\delta a_\delta^r + \delta^2 a_{\delta\delta}^r) \end{aligned} \tag{A.21}$$

All other properties of interest can be derived from the derivatives listed above using the following basic relation:

$$\left(\frac{\partial z}{\partial x}\right)_y = \frac{\left(\frac{\partial z}{\partial \rho}\right)_T \left(\frac{\partial y}{\partial T}\right)_\rho - \left(\frac{\partial z}{\partial T}\right)_\rho \left(\frac{\partial y}{\partial \rho}\right)_T}{\left(\frac{\partial x}{\partial \rho}\right)_T \left(\frac{\partial y}{\partial T}\right)_\rho - \left(\frac{\partial x}{\partial T}\right)_\rho \left(\frac{\partial y}{\partial \rho}\right)_T} \tag{A.22}$$

where x, y and z are three thermodynamic variables. For example the derivatives of density with respect to pressure and temperature can be provided using this relation:

$$\begin{aligned} \left(\frac{\partial \rho}{\partial p}\right)_T &= 1 \Big/ \left(\frac{\partial p}{\partial \rho}\right)_T \\ \left(\frac{\partial \rho}{\partial T}\right)_p &= \left(\frac{\partial p}{\partial T}\right)_\rho \Big/ \left(\frac{\partial p}{\partial \rho}\right)_T \end{aligned} \tag{A.23}$$

Appendix B

Tables of coefficient for the EoS and transport property models

In the following are reported the coefficients for the EoS and transport properties models presented in Chapter 2 to describe mixtures of real fluids for supercritical pressures. The five species considered are: methane (CH_4), nitrogen (N_2), ethane (C_2H_6) and propane (C_3H_8).

Species	Coeff	Temperature range 200-1000 K	Temperature range 1000-6000 K
CH_4	a_1	$-1.766850998 \cdot 10^{+05}$	$3.730042760 \cdot 10^{+06}$
	a_2	$2.786181020 \cdot 10^{+03}$	$-1.383501485 \cdot 10^{+04}$
	a_3	$-1.202577850 \cdot 10^{+01}$	$2.049107091 \cdot 10^{+01}$
	a_4	$3.917619290 \cdot 10^{-02}$	$-1.961974759 \cdot 10^{-03}$
	a_5	$-3.619054430 \cdot 10^{-05}$	$4.727313040 \cdot 10^{-07}$
	a_6	$2.026853043 \cdot 10^{-08}$	$-3.728814690 \cdot 10^{-11}$
	a_7	$-4.976705490 \cdot 10^{-12}$	$1.623737207 \cdot 10^{-15}$
	a_8	$-2.331314360 \cdot 10^{+04}$	$7.532066910 \cdot 10^{+04}$
	a_9	$8.904322750 \cdot 10^{+01}$	$-1.219124889 \cdot 10^{+02}$
N_2	a_1	$+2.210371497 \cdot 10^{+04}$	$+5.877124060 \cdot 10^{+05}$
	a_2	$-3.818461820 \cdot 10^{+02}$	$-2.239249073 \cdot 10^{+03}$
	a_3	$+6.082738360 \cdot 10^{+00}$	$+6.066949220 \cdot 10^{+00}$
	a_4	$-8.530914410 \cdot 10^{-03}$	$-6.139685500 \cdot 10^{-04}$
	a_5	$+1.384646189 \cdot 10^{-05}$	$+1.491806679 \cdot 10^{-07}$
	a_6	$-9.625793620 \cdot 10^{-09}$	$-1.923105485 \cdot 10^{-11}$
	a_7	$+2.519705809 \cdot 10^{-12}$	$+1.061954386 \cdot 10^{-15}$
	a_8	$+7.108460860 \cdot 10^{+02}$	$+1.283210415 \cdot 10^{+04}$
	a_9	$-1.076003744 \cdot 10^{+01}$	$-1.586640027 \cdot 10^{+01}$

Table B.1: Coefficients of the caloric equation of state for methane and nitrogen (Eqs. (2.24)–(2.26)).

Species	Coeff	Temperature range 200-1000 K	Temperature range 1000-6000 K
C_2H_6	a_1	$-1.862044161 \cdot 10^{+05}$	$+5.025782130 \cdot 10^{+06}$
	a_2	$+3.406191860 \cdot 10^{+03}$	$-2.033022397 \cdot 10^{+04}$
	a_3	$-1.951705092 \cdot 10^{+01}$	$+3.322552930 \cdot 10^{+01}$
	a_4	$+7.565835590 \cdot 10^{-02}$	$-3.836703410 \cdot 10^{-03}$
	a_5	$-8.204173220 \cdot 10^{-05}$	$+7.238405860 \cdot 10^{-07}$
	a_6	$+5.061135800 \cdot 10^{-08}$	$-7.319182500 \cdot 10^{-11}$
	a_7	$-1.319281992 \cdot 10^{-11}$	$+3.065468699 \cdot 10^{-15}$
	a_8	$-2.702932890 \cdot 10^{+04}$	$+1.115963950 \cdot 10^{+05}$
	a_9	$+1.298140496 \cdot 10^{+02}$	$-2.039410584 \cdot 10^{+02}$
C_3H_8	a_1	$-2.433144337 \cdot 10^{+05}$	$5.608128010 \cdot 10^{+05}$
	a_2	$4.656270810 \cdot 10^{+03}$	$-8.371504740 \cdot 10^{+02}$
	a_3	$-2.939466091 \cdot 10^{+01}$	$2.975364532 \cdot 10^{+00}$
	a_4	$1.188952745 \cdot 10^{-01}$	$1.252249124 \cdot 10^{-03}$
	a_5	$-1.376308269 \cdot 10^{-04}$	$9.471216940 \cdot 10^{-07}$
	a_6	$8.814823910 \cdot 10^{-08}$	$-9.575405230 \cdot 10^{-11}$
	a_7	$-2.342987994 \cdot 10^{-11}$	$4.009672880 \cdot 10^{-15}$
	a_8	$-3.540335270 \cdot 10^{+04}$	$1.455582459 \cdot 10^{+05}$
	a_9	$1.841749277 \cdot 10^{+02}$	$-2.818374734 \cdot 10^{+02}$

Table B.2: Coefficients of the caloric equation of state for ethane and propane (Eqs. (2.24)–(2.26)).

k	$n^0_{i,k}$	$\theta^0_{i,k}$	k	$n^0_{i,k}$	$\theta^0_{i,k}$
		Methane			
1	19.597538587	–	5	0.004600000	0.936220902
2	-83.959667892	–	6	8.744320000	5.577233895
3	3.000880000	–	7	4.469210000	5.722644361
4	0.763150000	4.306474465			
		Nitrogen			
1	11.925182741	–	5	-1.060440000	-2.844425476
2	-16.118762264	–	6	2.033660000	1.589964364
3	2.500020000	–	7	0.013930000	1.121596090
4	2.044520000	3.022758166			
		Ethane			
1	24.675465518	–	5	1.2372200000	0.731306621
2	–77.42531376	–	6	13.197400000	3.378007481
3	3.0026300000	–	7	-6.019890000	3.508721939
4	4.3393900000	1.831882406			
		Propane			
1	31.602934734	–	5	3.197000000	0.543210978
2	-84.463284382	–	6	19.192100000	2.583146083
3	3.029390000	–	7	-8.372670000	2.777773271
4	6.605690000	14.461722565			

Table B.3: Coefficients and parameters of a^0_i of Eq. (2.31) for the considered 4 species.

k	$n_{i,k}$	$c_{i,k}$	$d_{i,k}$	$t_{i,k}$
1	$0.57335704239162 \cdot 10^{+0}$	-	1	0.125
2	$-0.26760687523730 \cdot 10^{-1}$	-	1	1.125
3	$0.23405291833916 \cdot 10^{+0}$	-	2	0.375
4	$-0.21947376343441 \cdot 10^{+0}$	-	2	1.125
5	$0.16369201404128 \cdot 10^{-1}$	-	4	0.625
6	$0.15004406389280 \cdot 10^{-1}$	-	4	1.500
7	$0.98990489492918 \cdot 10^{-1}$	1	1	0.625
8	$0.58382770929055 \cdot 10^{+0}$	1	1	2.625
9	$0.74786867560390 \cdot 10^{+0}$	1	1	2.750
10	$0.30033302857974 \cdot 10^{+0}$	1	2	2.125
11	$0.20985543806568 \cdot 10^{+0}$	1	3	2.000
12	$0.18590151133061 \cdot 10^{-1}$	1	6	1.750
13	$0.15782558339049 \cdot 10^{+0}$	2	2	4.500
14	$0.12716735220791 \cdot 10^{+0}$	2	3	4.750
15	$0.32019743894346 \cdot 10^{-1}$	2	3	5.000
16	$0.68049729364536 \cdot 10^{-1}$	2	4	4.000
17	$0.24291412853736 \cdot 10^{-1}$	2	4	4.500
18	$0.51440451639444 \cdot 10^{-2}$	3	2	7.500
19	$0.19084949733532 \cdot 10^{-1}$	3	3	14.000
20	$0.55229677241291 \cdot 10^{-2}$	3	4	11.500
21	$0.44197392976085 \cdot 10^{-2}$	6	5	26.000
22	$0.40061416708429 \cdot 10^{-1}$	6	6	28.000
23	$0.33752085907575 \cdot 10^{-1}$	6	6	30.000
24	$0.25127658213357 \cdot 10^{-2}$	6	7	26.000

Table B.4: Coefficients and exponents of a_i^r of Eq. (2.34) for **Methane**. $K_{Pol,i}$=6, $K_{Exp,i}$=18

k	$n_{i,k}$	$c_{i,k}$	$d_{i,k}$	$t_{i,k}$
1	0.59889711801201 $\cdot 10^{+0}$	-	1	0.125
2	-0.16941557480731 $\cdot 10^{+1}$	-	1	1.125
3	0.24579736191718 $\cdot 10^{+0}$	-	2	0.375
4	-0.23722456755175 $\cdot 10^{+0}$	-	2	1.125
5	0.17954918715141 $\cdot 10^{-1}$	-	4	0.625
6	0.14592875720215 $\cdot 10^{-1}$	-	4	1.500
7	0.10008065936206 $\cdot 10^{+0}$	1	1	0.625
8	0.73157115385532 $\cdot 10^{+0}$	1	1	2.625
9	-0.88372272336366$\cdot 10^{+0}$	1	1	2.750
10	0.31887660246708 $\cdot 10^{+0}$	1	2	2.125
11	0.20766491728799 $\cdot 10^{+0}$	1	3	2.000
12	-0.19379315454158$\cdot 10^{-1}$	1	6	1.750
13	-0.16936641554983$\cdot 10^{+0}$	2	2	4.500
14	0.13546846041701 $\cdot 10^{+0}$	2	3	4.750
15	-0.33066712095307$\cdot 10^{-1}$	2	3	5.000
16	-0.60690817018557$\cdot 10^{-1}$	2	4	4.000
17	0.12797548292871 $\cdot 10^{-1}$	2	4	4.500
18	0.58743664107299 $\cdot 10^{-2}$	3	2	7.500
19	-0.18451951971969$\cdot 10^{-1}$	3	3	14.000
20	0.47226622042472 $\cdot 10^{-2}$	3	4	11.500
21	-0.52024079680599$\cdot 10^{-2}$	6	5	26.000
22	0.43563505956635 $\cdot 10^{-1}$	6	6	28.000
23	-0.36251690750939$\cdot 10^{-1}$	6	6	30.000
24	-0.28974026866543$\cdot 10^{-2}$	6	7	16.000

Table B.5: Coefficients and exponents of a_i^r of Eq. (2.34) for **Nitrogen**. $K_{Pol,i}$=6, $K_{Exp,i}$=18

k	$n_{i,k}$	$c_{i,k}$	$d_{i,k}$	$t_{i,k}$
1	0.63596780450714 $\cdot 10^{+0}$	-	1	0.125
2	-0.17377981785459 $\cdot 10^{+1}$	-	1	1.125
3	0.28914060926272 $\cdot 10^{+0}$	-	2	0.375
4	-0.33714276845694 $\cdot 10^{+0}$	-	2	1.125
5	0.22405964699561 $\cdot 10^{-1}$	-	4	0.625
6	0.15715424886913 $\cdot 10^{-1}$	-	4	1.500
7	0.11450634253745 $\cdot 10^{+0}$	1	1	0.625
8	0.10612049379745 $\cdot 10^{+1}$	1	1	2.625
9	-0.12855224439423 $\cdot 10^{+1}$	1	1	2.750
10	0.39414630777652 $\cdot 10^{+0}$	1	2	2.125
11	0.31390924682041 $\cdot 10^{+0}$	1	3	2.000
12	-0.21592277117247 $\cdot 10^{-1}$	1	6	1.750
13	-0.21723666564905 $\cdot 10^{+0}$	2	2	4.500
14	-0.28999574439489 $\cdot 10^{+0}$	2	3	4.750
15	0.42321173025732 $\cdot 10^{+0}$	2	3	5.000
16	0.46434100259260 $\cdot 10^{-1}$	2	4	4.000
17	-0.13138398329741 $\cdot 10^{+0}$	2	4	4.500
18	0.11492850364368 $\cdot 10^{-1}$	3	2	7.500
19	-0.33387688429909 $\cdot 10^{-1}$	3	3	14.000
20	0.15183171583644 $\cdot 10^{-1}$	3	4	11.500
21	-0.47610805647657 $\cdot 10^{-2}$	6	5	26.000
22	0.46917166277885 $\cdot 10^{-1}$	6	6	28.000
23	-0.39401755804649 $\cdot 10^{-1}$	6	6	30.000
24	-0.32569956247611 $\cdot 10^{-2}$	6	7	16.000

Table B.6: Coefficients and exponents of a_i^r of Eq. (2.34) for **Ethane**. $K_{Pol,i}$=6, $K_{Exp,i}$=18

k	$n_{i,k}$	$c_{i,k}$	$d_{i,k}$	$t_{i,k}$
1	0.10403973107358 $\cdot 10^{+1}$	-	1	0.250
2	-0.28318404081403$\cdot 10^{+1}$	-	1	1.125
3	0.84393809606294 $\cdot 10^{+0}$	-	1	1.500
4	-0.76559591850023$\cdot 10^{-1}$	-	2	1.375
5	0.94697373057280 $\cdot 10^{-1}$	-	3	0.250
6	0.24796475497006 $\cdot 10^{-3}$	-	7	0.875
7	0.27743760422870 $\cdot 10^{+0}$	1	2	0.625
8	-0.43846000648377$\cdot 10^{-1}$	1	5	1.750
9	-0.26991064784350$\cdot 10^{+0}$	2	1	3.625
10	-0.69313413089860$\cdot 10^{-1}$	2	4	3.625
11	-0.29632145981653$\cdot 10^{-1}$	3	3	14.50
12	0.14040126751380 $\cdot 10^{-1}$	3	4	12.00

Table B.7: Coefficients and exponents of a_i^r of Eq. (2.34) for **Propane**. $K_{Pol,i}$=6, $K_{Exp,i}$=6

k	$d_{ij,k}$	$t_{ij,k}$	$n_{ij,k}$	$\eta_{ij,k}$	$\epsilon_{ij,k}$	$\beta_{ij,k}$	$\gamma_{ij,k}$
			Methane-Nitrogen				
			F_{ij} = 1.0,K$_{Pol,ij}$=2, K$_{Exp,ij}$=7				
1	1	0.000	-0.98038985517335 $\cdot 10^{-2}$	-	-	-	-
2	4	1.850	0.42487270143005 $\cdot 10^{-3}$	-	-	-	-
3	1	7.850	-0.34800214576142 $\cdot 10^{-1}$	1.000	0.500	1.000	0.500
4	2	5.400	-0.13333813013896 $\cdot 10^{+0}$	1.000	0.500	1.000	0.500
5	2	0.000	-0.11993694974627 $\cdot 10^{-1}$	0.250	0.500	2.500	0.500
6	2	0.750	0.69243379775168 $\cdot 10^{-1}$	0.000	0.500	3.000	0.500
7	2	2.800	-0.31022508148249 $\cdot 10^{+0}$	0.000	0.500	3.000	0.500
8	2	4.450	0.24495491753226 $\cdot 10^{+0}$	0.000	0.500	3.000	0.500
9	3	4.250	0.22369816716981 $\cdot 10^{+0}$	0.000	0.500	3.000	0.500
			Methane-Ethane				
			F_{ij} = 1.0,K$_{Pol,ij}$=2, K$_{Exp,ij}$=10				
1	3	0.650	-0.80926050298746 $\cdot 10^{-3}$	-	-	-	-
2	4	1.550	-0.75381925080059 $\cdot 10^{-3}$	-	-	-	-
3	1	3.100	-0.41618768891219 $\cdot 10^{-1}$	1.000	0.500	1.000	0.500
4	2	5.900	-0.23452173681569 $\cdot 10^{+0}$	1.000	0.500	1.000	0.500
5	2	7.050	0.14003840584586 $\cdot 10^{+0}$	1.000	0.500	1.000	0.500
6	2	3.350	0.63281744807738 $\cdot 10^{-1}$	0.875	0.500	1.250	0.500
7	2	1.200	-0.34660425848809 $\cdot 10^{-1}$	0.750	0.500	1.500	0.500
8	2	5.800	-0.23918747334251 $\cdot 10^{+0}$	0.500	0.500	2.000	0.500
9	2	2.700	0.19855255066891 $\cdot 10^{-2}$	0.000	0.500	3.000	0.500
10	3	0.450	0.61777746171555 $\cdot 10^{+1}$	0.000	0.500	3.000	0.500
11	3	0.550	-0.69575358271105 $\cdot 10^{+1}$	0.000	0.500	3.000	0.500
12	3	1.950	0.10630185306388 $\cdot 10^{+1}$	0.000	0.500	3.000	0.500

Table B.8: Parameters, coefficients and exponents of a_{ij}^r of Eq.(2.35) for the binary mixtures taken into account. The values of F_{ij} equal zero for all other binary combinations.

k	$d_{ij,k}$	$t_{ij,k}$	$n_{ij,k}$	$\eta_{ij,k}$	$\epsilon_{ij,k}$	$\beta_{ij,k}$	$\gamma_{ij,k}$
			Methane-Propane				
			$F_{ij} = 1.0$,K$_{Pol,ij}$=5, K$_{Exp,ij}$=4				
1	3	1.850	0.13746429958576 $\cdot 10^{-1}$	-	-	-	-
2	4	3.950	-0.74425012129552 $\cdot 10^{-2}$	-	-	-	-
3	1	0.000	-0.45516600213685 $\cdot 10^{-2}$	-	-	-	-
4	2	1.850	-0.54546603350237 $\cdot 10^{-2}$	-	-	-	-
5	2	3.850	0.23682016824471 $\cdot 10^{-2}$	-	-	-	-
6	2	5.250	0.18007763721438 $\cdot 10^{0}$	0.25	0.50	0.750	0.500
7	2	3.850	-0.44773942932486 $\cdot 10^{0}$	0.25	0.50	1.000	0.500
8	2	0.200	0.19327374888200 $\cdot 10^{-1}$	0.00	0.50	2.000	0.500
9	2	6.500	-0.30632197804624 $\cdot 10^{0}$	0.00	0.50	3.000	0.500
			Nitrogen-Ethane				
			$F_{ij} = 1.0$,K$_{Pol,ij}$=3, K$_{Exp,ij}$=3				
1	2	0.000	-0.47376518126608 $\cdot 10^{+0}$	-	-	-	-
2	2	0.050	0.48961193461001 $\cdot 10^{+0}$	-	-	-	-
3	3	0.000	-0.57011062090535 $\cdot 10^{-2}$	-	-	-	-
4	1	3.650	-0.19966820041320 $\cdot 10^{+0}$	1.000	0.500	1.000	0.500
5	2	4.900	-0.69411103101723 $\cdot 10^{+0}$	1.000	0.500	1.000	0.500
6	2	4.450	0.69226192739021 $\cdot 10^{+0}$	0.875	0.500	1.250	0.500
			Ethane-Propane				
			$F_{ij} = 0.130424765150$,K$_{Pol,ij}$=10, K$_{Exp,ij}$=0				
1	1	1.000	0.25574776844118 $\cdot 10^{+1}$	-	-	-	-
2	1	1.550	-0.79846357136353 $\cdot 10^{+1}$	-	-	-	-
3	1	1.700	0.47859131465806 $\cdot 10^{+1}$	-	-	-	-
4	2	0.250	-0.73265392369587 $\cdot 10^{+0}$	-	-	-	-
5	2	1.350	0.13805471345312 $\cdot 10^{+1}$	-	-	-	-
6	3	0.000	0.28349603476365 $\cdot 10^{+0}$	-	-	-	-
7	3	1.250	-0.49087385940425 $\cdot 10^{+0}$	-	-	-	-
8	4	0.000	-0.10291888921447 $\cdot 10^{+0}$	-	-	-	-
9	4	0.700	0.11836314681968 $\cdot 10^{+0}$	-	-	-	-
10	4	5.400	0.55527385721943 $\cdot 10^{-4}$	-	-	-	-

Table B.9: Parameters, coefficients and exponents of a_{ij}^{r} of Eq.(2.35) for the binary mixtures taken into account. The values of F_{ij} equal zero for all other binary combinations.

Mixture $i-j$	$\beta_{\nu,ij}$	$\gamma_{\nu,ij}$	$\beta_{T,ij}$	$\gamma_{T,ij}$
CH_4-N_2	0.998721377	1.013950311	0.998098830	0.979273013
CH_4-C_2H_6	0.997547866	1.006617867	0.996336508	1.049707697
CH_4-C_3H_8	1.004827070	1.038470657	0.989680305	1.098655531
N_2-C_2H_6	0.978880168	1.042352891	1.007671428	1.098650964
N_2-C_3H_8	0.974424681	1.081025408	1.002677329	1.002677329
C_2H_6-C_3H_8	0.997607277	1.003034720	0.996199694	1.014730190

Table B.10: Binary parameters of the reducing functions for density and temperature (Eq.(2.36)).

Species	Formula	$\Delta H_{0,i}$ [J/kg]	$\Delta S_{0,i}$ [J/kg/K]
Methane	CH_4	-74600	11617.125
Nitrogen	N_2	0	6839.79074
Ethane	C_2H_6	-83851.544	7623.00439
Propane	C_3H_8	-104680	6130.07218

Table B.11: Enthalpy and entropy at the reference state $T = 298.15$ K and $p = 1.01325 \cdot 10^5$ Pa

Species	Formula	ρ_c [mol/dm^3]	T_c [K]	W [g·mol^{-1}]
Methane	CH_4	10.139342719	190.5640	16.042460
Nitrogen	N_2	11.183900000	126.1920	28.01340
Ethane	C_2H_6	6.870854540	305.3220	30.06904
Propane	C_3H_8	5.000043088	369.8250	44.09562

Table B.12: Critical parameters and molar masses of the 4 species of interest

Species	Coeff	Temperature range 200-1000 K	Temperature range 1000-5000 K
CH_4	$a_{\mu,1}$	$+0.57643622 \cdot 10^{+0}$	$+0.66400044 \cdot 10^{+0}$
	$a_{\mu,2}$	$-0.93704079 \cdot 10^{+2}$	$+0.10860843 \cdot 10^{+2}$
	$a_{\mu,3}$	$+0.86992395 \cdot 10^{+3}$	$-0.76307841 \cdot 10^{+4}$
	$a_{\mu,4}$	$+0.17333347 \cdot 10^{+1}$	$+0.10323984 \cdot 10^{+1}$
CO_2	$a_{\mu,1}$	$+0.51137258 \cdot 10^{+00}$	$+0.63978285 \cdot 10^{+00}$
	$a_{\mu,2}$	$-0.22951321 \cdot 10^{+03}$	$-0.42637076 \cdot 10^{+02}$
	$a_{\mu,3}$	$+0.13710678 \cdot 10^{+05}$	$-0.15522605 \cdot 10^{+05}$
	$a_{\mu,4}$	$+0.27075538 \cdot 10^{+01}$	$+0.16628843 \cdot 10^{+01}$
CO	$a_{\mu,1}$	$+0.62526577 \cdot 10^{+00}$	$+0.87395209 \cdot 10^{+00}$
	$a_{\mu,2}$	$-0.31779652 \cdot 10^{+02}$	$+0.56152222 \cdot 10^{+03}$
	$a_{\mu,3}$	$-0.16407983 \cdot 10^{+04}$	$-0.17394809 \cdot 10^{+06}$
	$a_{\mu,4}$	$+0.17454992 \cdot 10^{+01}$	$-0.39335958 \cdot 10^{+00}$
O_2	$a_{\mu,1}$	$+0.60916180 \cdot 10^{+00}$	$+0.72216486 \cdot 10^{+00}$
	$a_{\mu,2}$	$-0.52244847 \cdot 10^{+02}$	$+0.17550839 \cdot 10^{+03}$
	$a_{\mu,3}$	$-0.59974009 \cdot 10^{+03}$	$-0.57974816 \cdot 10^{+05}$
	$a_{\mu,4}$	$+0.20410801 \cdot 10^{+01}$	$+0.10901044 \cdot 10^{+01}$
H_2O	$a_{\mu,1}$	$+0.50019557 \cdot 10^{+00}$	$+0.58988538 \cdot 10^{+00}$
	$a_{\mu,2}$	$-0.69712796 \cdot 10^{+03}$	$-0.53769814 \cdot 10^{+03}$
	$a_{\mu,3}$	$+0.88163892 \cdot 10^{+05}$	$+0.54263513 \cdot 10^{+05}$
	$a_{\mu,4}$	$+0.30836508 \cdot 10^{+01}$	$+0.23386375 \cdot 10^{+01}$

Table B.13: Coefficients for the expression of the perfect gas contribution to viscosity (2.41).

Species	Coeff	Temperature range 200-1000 K	Temperature range 1000-5000 K
CH_4	$a_{k,1}$	$+0.10238177 \cdot 10^{+1}$	$+0.77485028 \cdot 10^{+0}$
	$a_{k,2}$	$-0.31092375 \cdot 10^{+3}$	$-0.40089627 \cdot 10^{+3}$
	$a_{k,3}$	$+0.32944309 \cdot 10^{+5}$	$-0.46551082 \cdot 10^{+5}$
	$a_{k,4}$	$+0.67787437 \cdot 10^{+0}$	$+0.25671481 \cdot 10^{+1}$
CO_2	$a_{k,1}$	$+0.48056568 \cdot 10^{+00}$	$+0.69857277 \cdot 10^{+00}$
	$a_{k,2}$	$-0.50786720 \cdot 10^{+03}$	$-0.11830477 \cdot 10^{+03}$
	$a_{k,3}$	$+0.35088811 \cdot 10^{+05}$	$-0.50688859 \cdot 10^{+05}$
	$a_{k,4}$	$+0.36747794 \cdot 10^{+01}$	$+0.18650551 \cdot 10^{+01}$
CO	$a_{k,1}$	$+0.85439436 \cdot 10^{+00}$	$+0.88407146 \cdot 10^{+00}$
	$a_{k,2}$	$+0.10573220 \cdot 10^{+03}$	$+0.13357293 \cdot 10^{+03}$
	$a_{k,3}$	$-0.12347848 \cdot 10^{+05}$	$-0.11429640 \cdot 10^{+05}$
	$a_{k,4}$	$+0.47793128 \cdot 10^{+00}$	$+0.24417019 \cdot 10^{+00}$
O_2	$a_{k,1}$	$+0.77229167 \cdot 10^{+00}$	$+0.68463210 \cdot 10^{+01}$
	$a_{k,2}$	$-0.58933377 \cdot 10^{+04}$	$+0.12210365 \cdot 10^{+01}$
	$a_{k,3}$	$+0.90917351 \cdot 10^{+00}$	$+0.29124182 \cdot 10^{+03}$
	$a_{k,4}$	$-0.79650171 \cdot 10^{+05}$	$+0.64851631 \cdot 10^{-01}$
H_2O	$a_{k,1}$	$+0.10966389 \cdot 10^{+01}$	$+0.39367933 \cdot 10^{+00}$
	$a_{k,2}$	$-0.55513429 \cdot 10^{+03}$	$-0.22524226 \cdot 10^{+04}$
	$a_{k,3}$	$+0.10623408 \cdot 10^{+06}$	$+0.61217458 \cdot 10^{+06}$
	$a_{k,4}$	$-0.24664550 \cdot 10^{+00}$	$+0.58011317 \cdot 10^{+01}$

Table B.14: Coefficients for the expression of the perfect gas contribution to thermal conductivity (2.42).

Appendix C

Elliptic, parabolic, hyperbolic differential equations

To introduce the concept of elliptic, hyperbolic, parabolic is it useful to consider the one dimensional simplified convection diffusion equation [58]:

$$\frac{\partial u}{\partial t} + a(u)\frac{\partial u}{\partial x} = \alpha \frac{\partial^2 u}{\partial x^2} \tag{C.1}$$

where $a(u)$ is the x component of the convection velocity and α is a diffusion coefficient. [1] It can be demonstrated that the solution of Eq. (C.1) has the following form:

$$u(x,t) = \hat{u} e^{-\alpha k^2 t} e^{ik(x-at)} \tag{C.2}$$

If a is real and $\alpha > 0$ Eq. (C.2) is a wave of amplitude $\hat{u}$, propagating with a velocity a and damped due to the diffusion coefficient α [2]. k is the wave number $k = 2\pi/\lambda$ with λ wavelength.

The approach of searching wave like solutions can be extended also to a system of quasi-linear partially differential equations (PDE). A system of PDE is then said to be:

- *hyperbolic* if its homogeneous part admits wave-like solutions;
- *parabolic* if its homogeneous part admits damped wave-like solutions;
- *elliptic* if its homogeneous part does not admit wave-like solutions.

These concepts can be applied also to second order PDE systems. In fact it can be demonstrated that every second order PDE system can be transformed into a first order system. Hence also the Navier-Stokes equations can be analyzed under this point of view. In particular this is done considering the quasilinear form of the Navier-Stokes equations and analyzing the eigenvalues of Jacobian matrix of the system as done in Chap. 3 for the PNS system.

[1] If the x-projection of the momentum equation is considered in absence of pressures and external forces, u is the velocity and $a(u) = u$. The convection-diffusion equation becomes the well-known Burgers equation. Burgers equation plays an important role since it contains the full convective non linearity of the flow equations

[2] The amplitude is dumped by a factor αk^2 in the time unit

Appendix D

Vigneron parameter

The 2D Eulerian PNS system is considered:

$$\frac{\partial \overline{\mathbf{F}}_\mathbf{e}}{\partial x} + \frac{\partial \mathbf{G}_\mathbf{e}}{\partial y} = 0 \tag{D.1}$$

where the two dimensional Eulerian fluxes are given by:

$$\overline{\mathbf{F}}_\mathbf{e} = \begin{Bmatrix} \rho u \\ \rho u^2 + \omega p \\ \rho u v \\ \rho u h_0 \end{Bmatrix} \qquad \mathbf{G}_\mathbf{e} = \begin{Bmatrix} \rho v \\ \rho u v \\ \rho v^2 + p \\ \rho v h_0 \end{Bmatrix} \tag{D.2}$$

The system (D.1) can be written in quasi linear form introducing the Jacobian matrix of the fluxes with respect to the primitive variable vector $\mathbf{V}$ defined by:

$$\mathbf{V} = \begin{Bmatrix} \rho \\ u \\ v \\ p \end{Bmatrix} \tag{D.3}$$

The Jacobian matrix of the fluxes are:

$$\mathbf{B} = \frac{\partial \overline{\mathbf{F}}_\mathbf{e}}{\partial \mathbf{V}} = \begin{pmatrix} u & \rho & 0 & 0 \\ u^2 & 2\rho u & 0 & \omega \\ uv & \rho v & \rho u & 0 \\ u(h_0 + \rho h_\rho) & \rho(h_0 + u^2) & \rho u v & \rho u h_p \end{pmatrix} \tag{D.4}$$

$$\mathbf{C} = \frac{\partial \mathbf{G}_\mathbf{e}}{\partial \mathbf{V}} = \begin{pmatrix} v & 0 & \rho & 0 \\ uv & \rho v & \rho u & 0 \\ v^2 & 0 & 2\rho v & 1 \\ v(h_0 + \rho h_\rho) & \rho u v & \rho(h_0 + v^2) & \rho v h_p \end{pmatrix} \tag{D.5}$$

Hence defining the matrix $\mathbf{A} = \mathbf{B^{-1}C}$ the system (D.1) can be written in a quasi linear form:

$$\frac{\partial \mathbf{V}}{\partial x} + \mathbf{A}\frac{\partial \mathbf{V}}{\partial y} = 0 \tag{D.6}$$

To understand the mathematical nature of this system, **A** eigenvalues must be calculated solving the equation:

$$det(\mathbf{A} - \lambda\mathbf{I}) = 0 \tag{D.7}$$

where **I** is the identity matrix and λ the generic eigenvalue, which is equivalent to:

$$det(\mathbf{C} - \lambda\mathbf{B}) = 0 \tag{D.8}$$

and thus to:

$$\begin{pmatrix} v-\lambda u & -\lambda\rho & \rho & 0 \\ uv-\lambda u^2 & \rho v - 2\lambda\rho u & \rho u & \lambda\omega \\ v^2-\lambda uv & -\lambda\rho v & 2\rho v - \lambda\rho u & 1 \\ (v^2-\lambda u)(h_0+\rho h_\rho) & \rho uv - \lambda\rho(h_0+u^2) & \rho(h_0+v^2)-\lambda\rho uv & \rho(v-\lambda u)h_p \end{pmatrix} = 0 \tag{D.9}$$

To solve the 4^{th} order Eq. (D.9) for λ, two thermodynamic parameters are introduced for the clarity of notation:

$$\hat{x} = \rho h_p \qquad \hat{y} = \rho h_\rho \tag{D.10}$$

It is helpful to introduce also a third parameter $z = v - \lambda u$. With these notations the eigenvalues problem of Eq. D.9 becomes:

$$\rho^2 z^2\{[(\hat{x}-\omega)u^2 + \omega y]\lambda^2 - [2x - (\omega+1)]uv\lambda + [\hat{y} + (\hat{x}-1)v^2]\} = 0 \tag{D.11}$$

Two eigenvalues are obtained from

$$z = u - \lambda v = 0 \tag{D.12}$$

which are

$$\lambda_{1,2} = \frac{v}{u} \tag{D.13}$$

The two other eigenvalues are obtained solving the second order equation in λ between brace brackets in Eq. (D.11), and are:

$$\lambda_{3,4} = \frac{[2\hat{x} - (\omega+1)]uv \pm \sqrt{\Delta}}{2[(\hat{x}-\omega)u^2 + \omega\hat{y}]} \tag{D.14}$$

with Δ given by:

$$\Delta = (\omega-1)^2u^2v^2 - 4[(\hat{x}-\omega)u^2 + \omega(\hat{x}-1)v^2]\hat{y} - 4\omega\hat{y}^2 \tag{D.15}$$

The system is hyperbolic if all the eigenvalues are real. $\lambda_{1,2}$ are always real and are defined if $u \neq 0$. The others two eigenvalues $\lambda_{3,4}$ are real if Δ is positive and hence its sign must be investigated. First the hypothesis $u \gg v$ can be used to simplify its expression, neglecting the terms multiplied by the crosswise velocity v thus yielding to:

$$\Delta \backsimeq -4y[(\hat{x}-\omega)u^2 + \omega\hat{y}] \tag{D.16}$$

At this point it is convenient to express $\hat{x}$ and $\hat{y}$ as functions of the speed of sound w_s and the internal energy derivative $e_p = \left(\frac{\partial e}{\partial p}\right)_\rho$. The relation between enthalpy and internal energy can be expressed by:

$$dh = de + d(\frac{p}{\rho}) \tag{D.17}$$

from which follows

$$\left(\frac{\partial h}{\partial p}\right)_{\rho} = \left(\frac{\partial e}{\partial p}\right)_{\rho} + \frac{1}{\rho} \tag{D.18}$$

Hence for $\hat{x}$ it results that:

$$\hat{x} = \rho e_p + 1 \tag{D.19}$$

Combining the first and second thermodynamic principles yields to the well known differential relations:

$$\begin{aligned} dh &= Tds + \frac{dp}{\rho} \\ de &= Tds - pd\frac{1}{\rho} \end{aligned} \tag{D.20}$$

from which follows:

$$\begin{aligned} \left(\frac{\partial h}{\partial \rho}\right)_{\rho} &= T\left(\frac{\partial s}{\partial \rho}\right)_{p} \\ \left(\frac{\partial e}{\partial p}\right)_{\rho} &= T\left(\frac{\partial s}{\partial p}\right)_{\rho} \end{aligned} \tag{D.21}$$

Moreover Maxwell relation implies that:

$$\left(\frac{\partial p}{\partial s}\right)_{\rho}\left(\frac{\partial s}{\partial \rho}\right)_{p}\left(\frac{\partial \rho}{\partial p}\right)_{s} = -1 \qquad \rightarrow \qquad \left(\frac{\partial p}{\partial s}\right)_{\rho}\left(\frac{\partial s}{\partial \rho}\right)_{p} = -w_s^2 \tag{D.22}$$

Combining Eqs (D.22) and (D.21) it results that:

$$\left(\frac{\partial h}{\partial \rho}\right)_{\rho} = -w_s^2\left(\frac{\partial e}{\partial p}\right)_{\rho} \tag{D.23}$$

where w_s is as usual the speed of sound. From this last relations follows:

$$\hat{y} = -\rho w_s^2 e_p \tag{D.24}$$

Thus the sign of $\hat{y}$ is related to the sign of the internal energy derivative with respect to pressure at constant density which can also be expressed applying the chain rule as:

$$\left(\frac{\partial e}{\partial p}\right)_{\rho} = \left(\frac{\partial e}{\partial T}\right)_{\rho}\left(\frac{\partial p}{\partial T}\right)_{\rho} \tag{D.25}$$

The specific heat at constant volume is a positive quantity defined by:

$$c_v = \left(\frac{\partial e}{\partial T}\right)_{\rho} \tag{D.26}$$

and introducing it in Eq. (D.25) gives:

$$\left(\frac{\partial e}{\partial p}\right)_{\rho} = \frac{c_v}{\left(\frac{\partial p}{\partial T}\right)_{\rho}} \tag{D.27}$$

D. Vigneron parameter

The derivative $\left(\frac{\partial p}{\partial T}\right)_\rho$ is a positive quantity for any generic equation of state. To confirm this obvious statement the computed above derivative with the thermodynamic models presented in Chap. 2 is reported in Fig. D.1 versus temperature for different supercritical pressures. The temperature range covers different regimes going from liquid-like conditions to perfect gas, and the quantity is always positive.

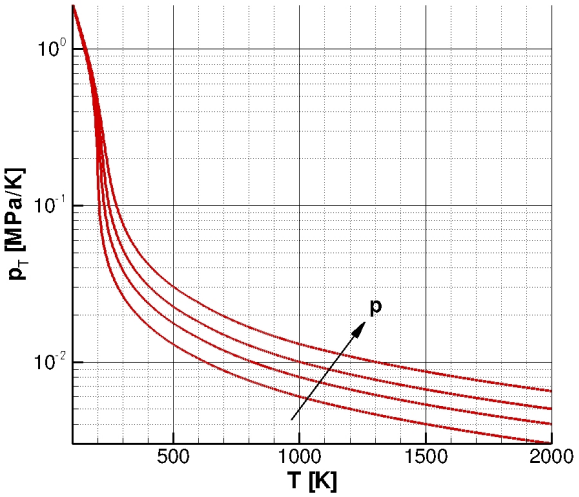

Figure D.1: Evolution of $\left(\frac{\partial p}{\partial T}\right)_\rho$ with the temperature for different supercritical pressures (6 MPa< p <13 MPa) for methane (logarithmic scale).

The previous conditions imply that $\hat{y} < 0$. Thus Δ is positive if the term between square brackets in Eq. (D.16) is positive. Replacing $\hat{x}$ and $\hat{y}$ with Eqs (D.19-D.24) this conditions is:

$$(\rho e_p + 1 - \omega)u^2 - \omega w_s^2 \rho e_p > 0 \tag{D.28}$$

which reduces to the following condition for ω:

$$\omega < \frac{[1 + \rho e_p]M_x^2}{M_x^2 + \rho e_p} \tag{D.29}$$

where $M_x = u/w_s$ is the Mach number in the streamwise direction. This condition is equivalent with the perfect gas one if γ is replaced with an equivalent parameter defined by:

$$\overline{\gamma} = 1 + \frac{1}{\rho e_p} \tag{D.30}$$

The derivative e_p is always positive and hence it results that the right hand side of Eq. (D.29) is always positive. Moreover, it is an increasing function of the Mach number and it tends towards zero when $M_x \to 0$.

Appendix E

Grid generation

In a numerical code the generation of a suitable computational grid is mandatory to obtain accurate solutions. Two main points must be addressed to create a grid. The first requirement is to have a clustered grid where the gradients are higher. Dealing with channel flows the grid should be clustered near the wall where the no-slip condition causes high velocity gradients. The second requirement is related to the turbulence model. RANS with Spalart-Allmaras closure model implies an integration *up to the wall*. This means that also the thin laminar sublayer should be captured by the grid. To identify the viscous sublayer it is useful to refer to the logarithmic coordinates defined as:

$$u^+ = u/u_\tau \qquad y^+ = y/y_\tau \tag{E.1}$$

u_τ is the friction velocity and y_τ is characteristic length defined as:

$$u_\tau = \sqrt{\frac{\tau_w}{\rho}} \qquad y_\tau = \frac{\nu}{u_\tau} \tag{E.2}$$

where τ_w is the wall shear stress. Typically the viscous sublayer is bounded in the region between the wall and $y^+ = 5$. Therefore to obtain an accurate description of this region the first grid point from the wall should at least correspond to $y^+ = 1$.

In the present work a hyperbolic tangent stretching function has been used to generate the grid:

$$st = \frac{\tanh(AH \cdot z)}{\tanh(AH)} \tag{E.3}$$

where $AH > 1$ is a parameter and z is the independent variable. For $z \subset [0, 1]$ this function varies in the range $[0, 1]$. The above function is reported in Fig. (E.1) for several values of the parameter AH.

For example we can consider a two dimensional axisymmetric case. The computational domain is represented in Fig. 4.5. A grid must be generated for the generic section. Only one cell is considered in the tangential direction. Whereas a N cells grid is generated for the radial direction. This grid must be clustered going from the symmetry axis towards the wall. Using the stretching function of Eq. (E.3) the grid can be generated according to:

$$y_{j+1/2} = \frac{D}{2}\frac{\tanh(AH \cdot \frac{j}{N})}{\tan(AH)} \qquad j = \{0, \cdots, N\} \tag{E.4}$$

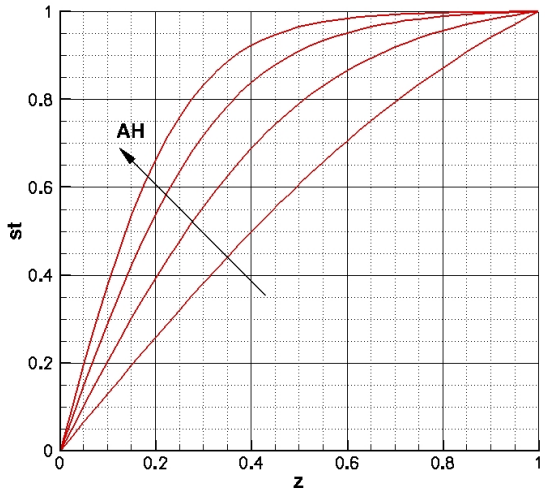

Figure E.1: Stretching function of Eq. (E.3) used in the grid generation

where N is as usual the number of the cells in the y direction. Increasing the parameter AH the grid is clustered near the wall. Therefore a suitable AH can be chosen so as to verify the required condition on $y^+ < 1$ at the cell near the wall. The projection of the grid on a plane passing from the symmetry axis is reported in Fig. (E.2).

Figure E.2: Projection of the two dimensional axysimmetric grid a plane containing the symmetry axis

Appendix F

Bulk properties

Bulk variables are useful in channel to have a global point of view over the solution. Moreover semi-empirical correlation for channels are based on bulk properties. It is important to give clear and coherent definitions of these averages. In the present study bulk properties are calculated starting from the definitions of bulk total enthalpy and bulk pressure:

$$\begin{aligned} p_b &= \frac{1}{A}\int_A p dS \\ h_{0,b} &= \frac{1}{\dot{m}}\int_A \rho u h_0 dS \end{aligned} \tag{F.1}$$

where A is the crosswise section and $\dot{m}$ the mass flow rate defined as:

$$\dot{m} = \int_A \rho u dS \tag{F.2}$$

The quantities without subscript appearing in the integral depend on (x, y, z) whereas bulk properties by definition only depend on the streamwise position x. Once p_b, h_0 and $\dot{m}$ have been evaluated the bulk density ρ_b is calculated with an iteration process: in fact there is only one density value which together with the given bulk pressure correspond to the given bulk total enthalpy. Namely bulk density and pressure must verify the following equations:

$$\begin{cases} h_b = h(\rho_b, p_b) \\ h_b = h_{0,b} - 0.5\left(\dfrac{\dot{m}}{\rho A}\right)^2 \end{cases} \tag{F.3}$$

The other bulk thermodynamic and transport properties are calculated using the EOS and transport properties equations in the thermodynamic state (ρ_b, p_b), whereas the bulk velocity is simply given by:

$$u_b = \frac{\dot{m}}{\rho_b A} \tag{F.4}$$

Bibliography

[1] NIST, National Institute of Standards and Technology, http://webbook.nist.gov/chemistry/fluid/.

[2] http://w3.pppl.gov/ntcc/PSPLINE/.

[3] NETL, National Energy Technology Laboratory, http://www.netl.doe.gov/.

[4] *Numerical Methods for Conservation Laws.* Birkäuser, 1992.

[5] Ideal-gas thermodynamic properties for natural-gas applications. *Int. J. Thermophysics*, 16:1381–1391, 1995.

[6] *Verification and Validation in Computational Sciences end Engineering.* Hermosa Publishers, 1998.

[7] *Riemann Solvers and Numerical Methods for Fluid Dynamics, A Practical Introduction.* Springer, 1999.

[8] *Turbulent Flows.* Cambridge University Press, 2000.

[9] Lng interchangeability/gas quality: Results of the national energy technology laboratory's research for the ferc on natural gas quality and interchangeability. Report, U.S. Department of Energy National Energy Technology Laboratory, 2007.

[10] S. Acharya. Pressure-based finite-volume methods in computational fluid dynamics. *Journal of Heat Transfer*, 129:407–424, 2007.

[11] A.Fröhlich, H. Immich, F. LeBail, and M. Popp. Three-dimensional flow analysis in rocket engine coolant channel of high depth/width ratio. AIAA Paper 1991-2183, 1991. 27th AIAA/ASME/SAE/ASEE Joint Propulsion Conference.

[12] M. Benedict, G. Webb, and L. Rubin. An empirical equation for thermodynamic properties of light hydrocarbons and their mixtures. *Journal of Chemical Physics*, 8:334–345, April 1940.

[13] P. Birken and A. Meister. On low mach number preconditioning of finite volume schemes. *Proceedings in Applied Mathematics and Mechanics*, 5:759–760, 2005.

[14] P. Bishnoi and D. Robinson. New mixing rules for the bwr parameters to predict mixture properties. *The Canadian Journal of Chemical Engineering*, 50:101–107, February 1972.

[15] A. Boushehri, J. Bzowski, J. Kestin, and E. Mason. Equilibrium and transport properties of eleven polyatomic gases at low density. *Journal of Physical and Chemical Reference Data*, 16:445–467, 1987.

[16] W. Briley. Numerical methods for predicting three-dimensional steady viscous flow in ducts. *Journal of Computational Physics*, 14:8–28, 1974.

[17] W. Briley and H. McDonald. Three-dimensional viscous flows with large secondary velocity. *Journal of Fluid Mechanics*, 144:47–77, 1984.

[18] C. Brown. Conceptual investigations for a methane-fueled expander rocket engine. AIAA Paper 2004-4210, 2004. 40th AIAA/ASME/SAE/ASEE Joint Propulsion Conference and Exhibit, Fort Lauderdale, Florida.

[19] P. BuelowJ.C., J. Tannehill, J. Ievalts, and L. Lawrence. Three-dimensional, upwind, parabolized navier-stokes code for chemically reacting flows. *Journal of Thermophysics and Heat Transfer*, 5(3):274–283, 1991.

[20] C. Burg and T. Erwin. Application of richardson extrapolation to the numerical solution of partial differential equations. *Numerical Methods for Partial Differential Equations*, 25(4):810–832, 2008.

[21] H. Burkhardt, M. Sippel, A. Herbertz, and J. Klevanski. Comparative study of kerosene and methane propellant engine for reusable liquid booster stages. *4th international conference on launcher technology "Space Launcher Liquid Propulsion", Liège*, 2002.

[22] H. Burkhardt, M. Sippel, A. Herbertz, and J. Klevanski. Comparative study of kerosene and methane propellant engines for reusable liquid booster stages. Technical report, 2002. 4th International Conference on Launcher Technology "Space Launcher Liquid Propulsion".

[23] P. Caisso, A. Souchier, C. Rothmund, P. Alliot, C. Bonhomme, W. Zinner, R. Parsley, T. Neill, S. Forde, R. Starke, W. Wang, M. Takahashi, M. Atsumi, and D. Valentian. A liquid propulsion panorama. *Acta Astronautica*, 65:1723–1737, 2009.

[24] S. Catris and B. Aupoix. Density corrections for turbulence models. *Aerospace Science Technology*, 4:1–11, 2000.

[25] C.Dang and E.Hihara. In-tube cooling heat transfer of supercritical carbon dioxide. part 1. experimental measurement. *International Journal of Refrigeration*, 27:736–747, 2004.

[26] X. Cheng, B. Kuang, and Y. Yang. Numerical analysis of heat transfer in supercritical water cooled flow channels. *Nuclear Engineering and Design*, 237(3):240–252, 2007.

[27] X. Cheng, T. Schulenberg, and F. Karlsruhe. Heat transfer at supercritical pressures: Literature review and application to an hplwr. Forschungszentrum Karlsruhe FZKA 6609, 2001.

[28] R. Chilukuri and R. Pletcher. Numerical solutions to the partially parabolized navier-stokes equations for developing flow in a channel. *Numerical Heat Transfer*, 3:169–188, 1980.

[29] Y. Choi and C. Merkle. The application of preconditioning in viscous flows. *Journal of Computational Physics*, 105:207–223, 1993.

[30] C. Conrado and V. Vesovic. The influence of chemical composition on vaporisation of lng and lpg on unconfined water surfaces. *Chemical Engineering Science*, 55:4549–4562, 2000.

[31] R. Cook. Methane heat transfer investigation. NASA CR-171051, June 1984.

[32] J. W. Cornelisse, H. F. R. Schoyer, and K. F. Wakker. *Rocket Propulsion and Spaceflight*. Butterworth-Heinemann, 2007.

[33] A. Crocker and S. Peery. System sensitivity studies of a lox/methane expander cycle rocket engine. AIAA Paper 1998-3674, 1998. 34th AIAA/ASME/SAE/ASEE Joint Propulsion Conference and Exhibit.

[34] R. Cross. Combustion performance and heat transfer characterization of lox/hydrocarbon type propellants. Report CR160874, Aerojet Liquid Rocket Company, August 1980. prepared for National Aeronautics and Space Administration.

[35] D. D'Ambrosio and R. Marsilio. A numerical method for solving the three-dimensional parabolized navier-stokes equations. *Computers and Fluids*, 26(6):587–611, 1997.

[36] J. T. D.K. Prabhu. Numerical solution of space shuttle orbiter flowfield including real-gas effects. *Journal of Spacecraft*, 23(3):264–272, 1986.

[37] A. Domaschenko, A. Dovbish, R. Darbinyan, A. Lyapin, and V. Peredle'skii. Analysis of liquefied methane production technology depending on methane purity and production volume. *Journal of Petroleum Science and Engineering*, 40(3):145–148, 2004.

[38] A. Domaschenko and Y. Kondrashkov. Technology of quality control of liquefied methane-a fuel for space rocket systems. *Journal of Petroleum Science and Engineering*, 39(11):656–661, 2003.

[39] Z. Duan and J. Hu. A new cubic equation of state and its applications to the modeling of vapor-liquid equilibria and volumetric properties of natural fluids. *Geochimica et Cosmochimica Acta*, 68(14):2997–3009, 2004.

[40] J. Estla-Uribe and J. Jaramillo. Generalized virial equation of state for natural gas systems. *Fluid Phase Equilibria*, 231:84–98, 2005.

[41] M. Farzaneh-Gord, A. Khamforoush, S. Hashemi, and H. P. Namin. Computing thermal properties of natural gas by utilizing aga8 equation of state. *International Journal of Chemical Engineering and Applications*, 1(1):20–24, June 2010.

[42] D. Friend, J. Ely, and H. Ingham. Thermophysical properties of methane. *J. Phys. Chem. Ref. Data*, 18(2):583–638, 1989.

[43] D. Friend, H. Ingham, and J. Ely. Thermophysical properties of ethane. *J. Phys. Chem. Ref. Data*, 20(2):275–347, 1991.

[44] R. Gerbsch and R. Agarwal. Solution of the parabolized navier-stokes equations for three-dimensional real-gas flows using osher's upwind scheme. AIAA Paper 1991-0248, 1991. 29th Aerospace Science Meeting, January 7-10, Reno, Nevada.

[45] A. Giovanetti, L. Spadaccini, and E. Szetela. Deposit formation and heat-transfer characteristics of hydrocarbon rocket fuels. NASA CR-168277, 1983.

[46] M. Gitterman. Hydrodynamics of fluids near a critical point. *Reviews of Modern Physics*, 50(1):85–106, 1978.

[47] T. Govindan, W. Briley, and H. McDonald. General three-dimensional viscous primary/secondary flow analysis. *AIAA Journal*, 29(3):361–370, 1991.

[48] H. Griem. A new procedure for the prediction of forced convection heat transfer near- and supercritical pressure. *Heat and Mass Transfer*, 31:301–305, 1996.

[49] H. Guillard and C. Viozat. On the behavior of upwind schemes in the low mach number limit. *Computers and Fluids*, 28:63–86, 1999.

[50] O. Haidn. Advanced rocket engines. In advances on propulsion technology for high-speed aircraft. educational notes rto-en-avt-150, paper 6, 2008.

[51] P.-G. Han, S.-W. Lee, K.-H. Kim, and Y. Yoon. Performance analysis of the thrust chamber in liquid rocket engine using liquefied natural gas as a fuel. AIAA Paper 2004-3860, 2004. 40th AIAA/ASME/SAE/ASEE Joint Propulsion Conference and Exhibit, 11-14 July 2004, Fort Lauderdale, Florida.

[52] H.Bilj and P.Wesseling. A numerical method for the computation of compressible flows with low mach number regions. *Computational Fluid Dynamics*, 1996.

[53] S. He, W. Kim, and J. Bae. Assessment of performance of turbulence models in predicting supercritical pressure heat transfer in a vertical tube. *International Journal of Heat and Mass Transfer*, 51:4659–4675, 2008.

[54] R. Hendricks, R. Graham, Y. Hsu, and R. Friedman. Experimental heat-transfer results for cryogenic hydrogen flowing in tubes at subcritical and supercritical pressures to 800 pounds per square inch absolute. NASA TN D-3095, 1966.

[55] R. Hendricks, R. Simoneau, and R. Friedman. Heat transfer characteristics of cryogenic hydrogen from 1000 to 2500 psia flowing upward in uniformly heated straight tubes. NASA TN D-2977, 1965.

[56] K. Higashino, M. Sugioka, T. Kobayashi, R. Minato, and Y. Maru. Fundamental study on coking characteristics of lng rocket engines. AIAA Paper 2008-4753, 2008. 44th AIAA/ASME/SAE/ASEE Joint Propulsion Conference.

[57] K. Higashino, M. Sugioka, T. Kobayashi, R. Minato, Y. Maru, Y. Sasayama, M. Otsuka, T. Makino, and H. Sakaguchi. Fundamental study on coking characteristics of lng rocket engines. AIAA Paper 2008-4753, 2008. 44th AIAA/ASME/SAE/ASEE Joint Propulsion Conference and Exhibit, 21-23 July 2008, Hartford, CT.

[58] C. Hirsch. *Numerical Computation of Internal and External Flows: The Fundamentals of Computational Fluid Dynamics, Second Edition.* Pitman, 1979.

[59] D. Hissong. Keys to modeling lng spills on water. *Journal of Hazardous Materials*, 140:465–477, 2007.

[60] N. H.Negishi, Y.Daimon. Numerical investigation of supercritical coolant flow in liquid rocket engine. AIAA Paper 2010-6888, 2010. 46th AIAA/ASME/SAE/ASEE Joint Propulsion Conference.

[61] Y.-X. Hua, Y.-Z. Wang, and H. Meng. A numerical study of supercritical forced convective heat transfer of n-heptane inside a horizontal miniature tube. *The Journal of Supercritical Fluids*, 52:36–46, 2010.

[62] M. Huber and J. Ely. Prediction of viscosity of refrigerants and refrigerant mixtures. *Fluid Phase Equilibria*, 80:239–248, 1992.

[63] M. Huber, D. Friend, and J. Ely. Prediction of thermal conductivity of refrigerants and refrigerant mixtures. *Fluid Phase Equilibria*, 80:249–261, 1992.

[64] J. Hulka and G. Jones. Performance and stability analyses of rocket thrust chambers with oxygen/methane propellants. Technical report, July 2010.

[65] R. Jacobsen and R. Stewart. Thermodynamic properties of nitrogen including liquid and vapor phases from 63 k to 2000 k with pressures to 10,000 bar. *Journal of Physical and Chemical Reference Data*, 2(4):757–922, 1973.

[66] K. Javadi, M. Darbandi, and M. Taeibi-Rahni. Three dimensional compressible-incompressible tubulent flow simulation using a pressure-based algorithm. *Computers and Fluids*, 37:747–766, 2008.

[67] H. Jung, C. Merkle, R. Schuff, and W. Anderson. Detailed flowfield predictions of heat transfer to supercritical fluids in high aspect ratio channels. AIAA Paper 2007-5548, July 2007. 43rd AIAA/ASME/SAE/ASEE Joint Propulsion Conference.

[68] N. Kafengauz. Heat transfer to turbulent stream in pipes under supercritical pressures. *Inzhenerno-Fizicheskii Zhurnal*, 44(1):9–12, 1981.

[69] K. Karki and S. Pantakar. Pressure based calculation procedure for viscous flows at all speeds in arbitrary configurations. *AIAA Journal*, 27:1167–1174, 1989.

[70] K. E. . K.E. Tsiolkovsky. The exploration of cosmic space by means of reaction devices. *The Science Review*, 5, 1903.

[71] R. Klein. Semi-implicit extension of a godunov-type scheme based on low mach number asymptotic i: One-dimensional flow. *Journal of Computational Physics*, 121:213–237, 1995.

[72] S. A. Klein, M. O. McLinden, and A. Laesecke. An improved extended corresponding states method for estimation of viscosity of pure refrigerants and mixtures. *International Journal of Refrigeration*, 20(3):208–217, 1997.

[73] I. Klepikov, B. Katorgin, and V. Chvanov. The new generation of rocket engines, operating by ecologically safe propellant "liquid oxygen and liquified natural gas (methane)". *Aerotecnica The Journal of Aerospace Science, Technology and Systems*, 41(4-10):209–217, 1997.

[74] O. Knab, A. Fröhlich, D. Wennerberg, and W. Haslinger. Advanced cooling circuit layout for the vinci expander cycle thrust chamber. AIAA Paper 2002-4005, 2002. 38th AIAA/ASME/SAE/ASEE Joint Propulsion Conference.

[75] J. Korte. An explicit upwind algorithm for solving the parabolized navier-stokes equations. NASA TP 3050, 1991.

[76] S. Koshizuka, N.Takano, and Y. Oka. Numerical analysis of deterioration phenomena in heat transfer to supercritical water. *International Journal of Heat and Mass Transfer*, 38(16):3077–2084, 1995.

[77] J. Kreskovsky, W. Briley, and H. McDonald. Analysis and computational of three-dimensional flow in strongly curved ducts. Computers in flow predictions and fluid dynamics experiments, 1981.

[78] A. Kumar and A. Henni. Three-parameter cubic equation of state for pure components of heavy oils. *The Canadian Journal of Chemical Engineering*, 89:869–878, 2011.

[79] O. Kunz, R. Klimeck, W. Wagner, and M. Jaeschke. The gerg-2004 wide-range equation of state for natural gases and other mixtures. Technical report, GERG TM15, 2007.

[80] S. Lawrence and J. Tannehill. Upwind algorithm for the parabolized navier-stokes equations. *AIAA Journal*, 27(9):1175–1183, 1989.

[81] F. LeBail and M. Popp. Numerical analysis of high aspect ratio cooling passage flow and heat transfer. AIAA Paper 1993-1829, June 1993. 29th AIAA/ASME/SAE/ASEE Joint Propulsion Conference.

[82] B. Lee and M. Kesler. A generalized thermodynamic correlation based on three-parameter corresponding states. *American Institute of Chemical Engineering Journal*, 21:510–527, 1975.

[83] S. Lee and J. Howell. Turbulent developing convective heat transfer in a tube for fluids near the critical point. *International Journal of Heat and Mass Transfer*, 41(10):1205–1218, 1998.

[84] Z. Lei. Thermoacoustic convection and transport in supercritical fluids under normal and micro-gravity conditions. Phd thesis, drexel university, 2009.

[85] E. Lemmon and R. Jacobsen. Viscosity and thermal conductivity equations for nitrogen, oxygen, argon, and air. *International Journal of Thermophysics*, 25(1):21–69, 2003.

[86] E. W. Lemmon and R. T. Jacobsen. A generalized model for the thermodynamic properties of mixtures. *International Journal of Thermophysics*, 20(3):825–835, 1999.

[87] R. Levy, W. Briley, and H. McDonald. Viscous primary/secondary flow analysis for use with nonorthogonal coordinate systems. AIAA Paper 83-0556, 1983. 21st Aerospace Science Meeting, January 10-13, Reno, Nevada.

[88] K. Liang, B. Yang, and Z. Zhang. Investigation of heat transfer and coking characteristics of hydrocarbon fuels. *Journal of Propulsion and Power*, 14:789–796, 1998.

[89] J. Locke and D. Landrum. Uncertainty analysis of heat transfer to supercritical hydrogen in cooling channels. AIAA Paper 2005-4303, 2005. 41th AIAA/ASME/SAE/ASEE Joint Propulsion Conference and Exhibit.

[90] J. Locke and D. Landrum. Study of heat transfer correlations for supercritical hydrogen in regenerative cooling channels. *Journal of Propulsion and Power*, 24(1):94–103, 2008.

[91] J. Locke, S. Pal, and R. Woodward. Chamber wall heat flux measurements for a lox/ch4 uni-element rocket. AIAA Paper 2007-5547, 2007. 43th AIAA/ASME/SAE/ASEE Joint Propulsion Conference and Exhibit.

[92] J. Lux and O. Haidn. Flame stabilization in high-pressure liquid oxygen/methane rocket engine combustion. *Journal of Propulsion and Power*, 25(1):15–23, 2009.

[93] K. Marsh, R. Perkins, and M. Ramires. Measurement and correlation of the thermal conductivity of propane from 86 k to 600 k at pressures to 70 mpa. *Journal of Chemical and Engineering Data*, 47:932–940, 2002.

[94] B. J. McBride and S. Gordon. *Computer Program for Calculation of Complex Chemical Equilibrium Compositions and Applications: I. Analysis.* National Aeronautics and Space Administration, Lewis Research Center, Cleveland, Ohio 44135-3191, October 1994. Reference Publication, NASA RP-1311.

[95] B. J. McBride and S. Gordon. *Computer Program for Calculation of Complex Chemical Equilibrium Compositions and Applications: II. User's Manual and Program Description.* National Aeronautics and Space Administration, Lewis Research Center, Cleveland, Ohio 44135-3191, June 1996. Reference Publication, NASA RP-1311.

[96] M. O. McLinden, S. A. Klein, and R. A. Perkins. An extended corresponding states model for the thermal conductivity of refrigerants and refrigerant mixtures. *International Journal of Refrigeration*, 23:43–63, 2000.

[97] J. Mellish. Low thrust chemical rocket engine study. NASA CR-165276, March 1981.

[98] C. Merkle. Computation of flows with arbitrary equations of state. *AIAA Journal*, 36(4):515–521, 1998.

[99] C. Merkle, D. Li, and V. Sankaran. Analysis of regen cooling in rocket combustors. Technical report, May 2004. JANNAF Propulsion Conference.

[100] M. L. Meyer. Electrically heated tube investigation of cooling channel geometry effects. AIAA Paper 95-2500, 1995. 31st AIAA/ASME/SAE/ASEE Joint Propulsion Conference and Exhibit.

[101] J. Mitchell and J. Gregory. Space storable regenerative cooling investigation. NASA CR-72341, July 1968.

[102] M. Mohseni and M. Bazargan. The effect of the low reynolds number k-e turbulence models on simulations of the enhances and deteriorated convective heat transfer to the supercritical fluid flows. *Heat Mass Transfer*, 2010.

[103] F. M.Pizzarelli, B.Betti. Coupled analysis of hot-gas and coolant flows in lox/methane thrust chambers. In *4th European Conference for aerospace sciences*. St Petersburg, Russia, July 2011.

[104] B. Muller. Low mach number asymptotics of the navier-stokes equations and numerical implications. Lecture series, von karman institute for fluid dynamics, March 1999.

[105] C.-D. Munz, S. Roller, R. Klein, and K. Geratz. The extension of incompressible flow solvers to the weakly compressible regime. *Computers and Fluids*, 32:173–196, 2003.

[106] J. Murthy and S. Patankar. A partially parabolic calculation procedure for duct flows in irregular geometries. part i: Formulation. *Numerical Heat Transfer*, 16:1–15, 1989.

[107] M. Naraghi, S. Dunn, and D. Coats. Dual regenerative cooling circuits for liquid rocket engines. Aiaa paper. 42th AIAA/ASME/SAE/ASEE Joint Propulsion Conference.

[108] K. Nasrifar and O. Bolland. Prediction of thermodynamic properties of natural gas mixtures using 10 equations of state including a new cubic two-constant equation of state. *Journal of Petroleum Science and Engineering*, 51:253–266, 2006.

[109] J. Nathmann, J. Niehaus, and J. Sturgis. Preliminary study of heat transfer correlation development and pressure loss behavior in curved high aspect ratio coolant channels. AIAA Paper 2008-5240, 2008. 44th AIAA/ASME/SAE/ASEE Joint Propulsion Conference and Exhibit.

[110] H. Negishi and Y. Daimon. Flowfield and heat transfer characteristics of cooling channel flows in a subscale thrust chamber. AIAA Paper 2011-5844, 2011. 47th AIAA/ASME/SAE/ASEE Joint Propulsion Conference and Exhibit.

[111] Y. Noguchi, K. Taya, T. Hirai, A. Yui, and T. Makino. Conceptual design of a lox/lng rocket engine for a space tourism vehicle. AIAA Paper 2009-5138, 2009. 45th AIAA/ASME/SAE/ASEE Joint Propulsion Conference and Exhibit, 2-5 August 2009, Denver, Colorado.

[112] G. Olchowy and J. Sengers. A simplified representation for the thermal conductivity of fluids in the critical region. *International Journal of Thermophysics*, 10:417–426, 1989.

[113] D. Palko and H. Anglart. Theoretical and numerical study of heat transfer deterioration in high performance light water reactor. *Science and Technology of Nuclear Installations*, 2008.

[114] S. Pantakar. *Numerical Heat Transfer and Fluid Flow*. McGraw-Hill, 1980.

[115] J. D. Parker, J. H. Boggs, and E. F. Blick. *Introduction to fluid mechanics and heat transfer*. Addison-Wesley Publishing Company, 1969.

[116] D. K. Parris and B. Landrum. Effect of tube geometry on regenerative cooling performance. AIAA Paper 2005-4301, 2005. 41th AIAA/ASME/SAE/ASEE Joint Propulsion Conference and Exhibit.

[117] S. Patankar and D. Spalding. A calculation procedure for heat, mass and momentum transfer in three-dimensional parabolic flows. *International Journal of Heat and Mass Transfer*, 15:1787–1806, 1972.

[118] D. Peng and D. Robinson. A new two-constant equation of state. *Ind. Eng. Chem. Fundam.*, 15(1):59–64, 1976.

[119] I. Pioro and R. Duffey. Experimental heat transfer in supercritical water flowing inside channels (survey). *Nuclear Engineering and Design*, 235:2407–2430, 2005.

[120] I. Pioro, H. Khartabil, and R. Duffey. Heat transfer to supercritical fluids flowing in channels - empirical correlations (survey). *Nuclear Engineering and Design*, 230(1-3):69–91, 2004.

[121] M. Pizzarelli, F. Nasuti, and M. Onofri. Cfd analysis of curved cooling channel flow and heat transfer in rocket engines. AIAA Paper 2010-6722, 2010. 46th AIAA/ASME/SAE/ASEE Joint Propulsion Conference and Exhibit.

[122] M. Pizzarelli, F. Nasuti, R. Paciorri, and M. Onofri. Numerical analysis of three-dimensional flow of supercritical fluid in asymmetrically heated channels. *AIAA Journal*, 47(11), Nov. 2009.

[123] M. Pizzarelli, A. Urbano, and F. Nasuti. Numerical analysis of deterioration in heat transfer to near-critical rocket propellants. *Numerical Heat Transfer, Part A: Applications*, 57:297–314, 2010.

[124] M. Pougare and B. Lakshminarayana. A space-marching method for viscous incompressible internal flows. *Journal of Computational Physics*, 64(2):389–415, 1986.

[125] D. Preclik, G. Hagemann, O. Knab, C. Mäding, and D. Haeseler. Lox/hydrocarbons preparatory thrust chamber technology activities in germany. AIAA Paper 2005-4555, 2005. 41th AIAA/ASME/SAE/ASEE Joint Propulsion Conference and Exhibit.

[126] P.Tamamidis and D. G.Zhang. Comparison of pressure-based and artificial compressibility methods for solving 3d steady incompressible viscous flows. *Journal of Computational Physics*, 124:1–13, 1996.

[127] E. Querol, B. Gonzalez-Regueral, J. García-Torrent, and A. Ramos. Available power generation cycles to be coupled with the liquid natural gas (lng) vaporization process in a spanish lng terminal. *Applied Energy*, 88:2382–2390, 2011.

[128] S. E. Quinones-Cisneros and U. K. Deiters. Generalization of the friction theory for viscosity modeling. *J. Phys. Chem. B*, 110(2):12820–12834, 2006.

[129] A. Rabah and S. Mohamed. A new three parameter cubic equation of state. *Transactions C: Chemistry and Chemical Engineering*, 17(2):177–184, 2010.

[130] R. Reid, J. Prausnitz, and B. Poling. *The Properties of Gases and Liquids*. McGraw-Hill Book Company, 1987.

[131] R.F.Kelbaliev. Deterioration of heat transfer at supercritical pressures of a substance. *Journal of Engineering Physics and Thermophysics*, 74:416–420, 2001.

[132] P. Roe. Approximate riemann solvers, parameter vectors, and difference schemes. *Journal of Computational Physics*, 43:357–372, 1981.

[133] S. Roller and C.-D. Munz. A low mach number scheme based on multi-scale asymptotics. *Computer Visual Science*, 3:85–91, 2000.

[134] S. Rosenberg and M. Gage. Corrosion prevention in hydrocarbon-fueled booster engine combustion chamber liner. AIAA Paper 89-2738, 1989. 25th AIAA/ASME/SAE/ASEE Joint Propulsion Conference and Exhibit.

[135] S. Rosenberg and M. Gage. Corrosion prevention in copper combustion chamber liners of liquid oxygen/methane booster engines. AIAA Paper 90-2119, 1990. 26th AIAA/ASME/SAE/ASEE Joint Propulsion Conference and Exhibit.

[136] S. Rosenberg, M. Gage, G. Homer, and J. Franklin. Hydrocarbon-fuel/copper combustion chamber liner compatibility, corrosion, prevention and refurbishment. AIAA Paper 91-2213, 1991. 27th AIAA/ASME/SAE/ASEE Joint Propulsion Conference and Exhibit.

[137] S. Rubin and J. Tannehill. Parabolized/reduced navier-stokes computational techniques. *Annual Review of Fluid Mechanics*, 24:117–144, 1992.

[138] T. Sato, M. Sugiyama, K. Itoh, K. Mori, T. Fukunaga, M. Misawa, T. Otomo, and S. Takata. Structural difference between liquidlike and gaslike phases in supercritical fluid. *Physical Review E (Statistical, Nonlinear, and Soft Matter Physics)*, 78(5):051503:1–9, 2008.

[139] R. Schuff, M. Mayer, O. Sindiy, C. Ulrich, and S. Fugger. Integrated modeling and analysis for a lox/methane expander cycle engine: Focusing on regenerative cooling jacket design. AIAA Paper 2006-4534, 2006. 42nd AIAA/ASME/SAE/ASEE Joint Propulsion Conference.

[140] B. Shiralkar and P. Griffith. Deterioration in heat transfer to fluids at supercritical pressure and high heat fluxes. *ASME Journal of Heat Transfer*, 91(1):27–36, February 1969.

[141] G. Singla, P. Scouflaire, C. Rolon, and S. Candel. Transcritical oxygen/transcritical or supercritical methane combustion. *Proceedings of the Combustion Institute*, 30(2):2921–2928, 2005.

[142] S.M.Liao and T.S.Zhao. Measurements of heat transfer coefficients from supercritical carbon dioxide flowing in horizontal mini/micro channels. *Journal of Heat Transfer*, 124:413–420, 2002.

[143] G. Soave. Equilibrium constants from a modified redlich-kwong equation of state. *Chem. Eng. Scien.*, 27(6):1197–1203, 1972.

[144] P. Spalart and S. Allmaras. A one-equation turbulence model for aerodynamic flow. *La Recherche Aérospatiale*, 1:5–21, 1994.

[145] G. Sutton and O. Biblarz. *Rocket Propulsion Elements*. John Wiley and Sons, 2001.

[146] R. Svehla. Transport coefficients for the nasa lewis chemical equilibrium program. NASA TM 4647, 1995.

[147] J. Tannehill, D. Anderson, and R. H. Pletcher. *Computational Fluid Mechanics and Heat Transfer*. Taylor&Francis, 1984.

[148] J. Tannehill, P. Buelow, J. Ievalts, and S. Lawrence. Three-dimensional upwind parabolized navier-stokes code for real gas flows. *Journal of Spacecraft*, 27(2):150–158, 1989.

[149] M. Taylor. Correlation of local heat-transfer coefficients for single-phase turbulent flow of hydrogen in tubes with temperature ratio to 23. NASA TN D-4332, January 1968.

[150] D. Thunnissen, S. Guernsey, R. Baker, and R. Miyake. Advanced space storable propellants for outer planet exploration. AIAA Paper 2004-3488, 2004. 40th AIAA/ASME/SAE/ASEE Joint Propulsion Conference and Exhibit.

[151] R. Tillner-Roth and H. Baehr. An international standard formulation for the thermodynamic properties of 1,1,1,2-tetrafluoroethane (hfc-134a) for temperatures from 170 k to 455 k and pressures up to 70 mpa. *Journal of Physical and Chemical Reference Data*, 23(5):657–729, 1994.

[152] A. Tomboulides and S. Orszag. A quasi-two-dimensional benchmark problem for low mach number compressible codes. *Journal of Computational Physics*, 146:691–706, 1998.

[153] E. Turkel. Preconditioning techniques in computational fluid dynamics. *Annual Review of Fluid Mechanics*, 31:385–416, 1999.

[154] T.Yamashita, H.Mori, S.Yoshida, and M.Ohno. Heat transfer and pressure drop of a supercritical pressure fluid flowing in a tube of small diameter. *Memoirs of the Faculty of Engineering, Kyushu UNiversity*, 63(4):227–244, 2003.

[155] A. Urbano, M. Pizzarelli, and F. Nasuti. Numerical analysis of transcritical fluids heating in liquid rocket engine cooling channels. *Aerotecnica The Journal of Aerospace Science, Technology and Systems*, 87(4):100–110, 2009.

[156] P. V.A.Grabezhnaya. Heat transfer under supercritical pressures and heat transfer deterioration boundaries. *Thermal Engineering*, 53(4):296–301, 2006.

[157] J. Valderrama and A. Silva. Modified soave-redlich-kwong equations of state applied to mixtures containing supercritical carbon dioxide. *Korean Journal of Chemical Engineering*, 20(40):709–715, 2003.

[158] V. Vesovic, W. Wakeham, G. Olchowy, G. Sengers, J. Watson, and J. Millat. The transport properties of carbon dioxide. *Journal of Physical and Chemical Reference Data*, 19(3):763–808, 1990.

[159] Y. Vigneron, J. Rakich, and J. Tannehill. Calculation of supersonic viscous flow over delta wings with sharp subsonic leading edges. AIAA Paper 78-1137, 1978.

[160] E. Vogel, C. Kuchenmeister, and E. Bich. Reference correlation of the viscosity of propane. *J. Phys. Chem. Ref. Data*, 27(5):947–955, 1998.

[161] G. Volpe. Performance of compressible flow codes at low mach numbers. *AIAA Journal*, 31:49–56, 1993.

[162] G. Wadawadigi, J. Tannehill, and P. Buelow. Three-dimensional upwind parabolized navier-stokes code for supersonic combustion flowfileds. *Journal of Thermophysics and Heat Transfer*, 7(4):661–667, 1993.

[163] Y.-Z. Wang, Y.-X. Hua, and H. Meng. Numerical studies of supercritical turbulent convective heat transfer of cryogenic-propellant methane. *Journal of Thermophysics and Heat Transfer*, 24(3):490–500, 2010.

[164] J. Weiss and W. Smith. Preconditioning apllied to variable and constant density flows. *AIAA Journal*, 33(11):2050–2057, 1995.

[165] J. C. Wennerberg, W. E. Anderson, P. A. Haberlen, H. Jung, and C. L. Merkle. Supercritical flows in high aspect ratio cooling channels. AIAA Paper 2005-4302, 2005. 41th AIAA/ASME/SAE/ASEE Joint Propulsion Conference and Exhibit.

[166] J. C. Wennerberg, W. E. Anderson, R. Schuff, H. Jung, and C. L. Merkle. Study of simulated fuel flows in high aspect ratio cooling channels. AIAA Paper 2006-4708, 2006. 42th AIAA/ASME/SAE/ASEE Joint Propulsion Conference and Exhibit.

[167] A. Woschnak and M. Oschwald. Thermo and fluidmechanical analysis of high aspect ratio cooling channels. AIAA Paper 2001-3404, July 2001. 37th AIAA/ASME/SAE/ASEE Joint Propulsion Conference.

[168] J. A. Yagley, J. Feng, , and C. L. Merkle. The effect of aspect ratio on the effectiveness of combustor coolant passages. Technical report, July 1992.

[169] J. A. Yagley, J. Feng, , and C. L. Merkle. Cfd analyses of coolant channel flowfields. Technical report, 1993.

[170] B. A. Younglove. Thermophysical properties of fluids. i. argon, ethylene, parahydrogen, nitrogen, nitrogen trifluoride and oxygen. *J. Phys. and Chem. Ref. Data*, 11, 1982.

[171] B. A. Younglove and J. F. Ely. Thermophysical properties of fluids. ii. methane, ethane, propane, isobutane, and normal butane. *Journal of Physical and Chemical Reference Data*, 16(4), June 1987.

[172] R. Zubrin, B. Frankie, and T. Kito. Mars in-situ resource utilization based on the reverse water gas shift: Experiments and mission applications. AIAA Paper 97-2767, 1997. 33th AIAA/ASME/SAE/ASEE Joint Propulsion Conference and Exhibit.